Multiscale Investigation of Adsorption Phenomena for Adsorption Heat Transformer and Desalination

サガル, サレン

https://hdl.handle.net/2324/7157380

出版情報：Kyushu University, 2023, 博士（学術）, 課程博士
バージョン：
権利関係：

Multiscale Investigation of Adsorption Phenomena for Adsorption Heat Transformer and Desalination

A thesis submitted to the
Kyushu University
for the award of the degree

of

Doctor of Philosophy

by

Sagar Saren

Under the guidance of

Prof. Kyaw Thu

INTERDISCIPLINARY GRADUATE SCHOOL OF ENGINEERING SCIENCES
KYUSHU UNIVERSITY
6-1 KASUGA-KOEN, KASUGA-SHI, 816-8580, FUKUOKA, JAPAN
August 2023

Acknowledgments

I am deeply grateful to Associate Professor Kyaw Thu for accepting me as his doctoral student. In particular, I will always remember his effort in pushing my delayed application for the admission in the doctoral program. Under his expert guidance and mentorship, my research career has flourished. The rigorous discussions held at his office have been invaluable in helping me overcome doubts and generate new research ideas. Thanks to his insightful learning strategies and ongoing progress monitoring, I have been able to confidently pursue impactful research in an area beyond my academic background. In addition, he has provided countless valuable advice that has contributed to both my personal and professional growth, covering not only academic but also non-academic fronts. This thesis represents the culmination of his immense guidance and expertise.

I would like to extend my gratitude to Professor Takahiko Miyazaki for his invaluable support and guidance in my research journey. His critical opinions and advice, which he provided during our weekly/monthly research meetings, have been instrumental in improving the quality of my work. I am also thankful to Dr. Frantisek Miksik for his invaluable insights on my research activities. His critical review has substantially improved our manuscripts, both in terms of fundamental content and writing structure. Furthermore, his excellent interpersonal and conversational skills have inspired me to communicate my research more effectively during presentations. I would also like to thank Dr. Sourav Mitra for presenting me the opportunity to pursue my doctoral studies at Kyushu University. My prior experience in the adsorption field, gained during my master's studies under his supervision, enabled me to quickly adapt to my doctoral research theme. Also, I appreciate his suggestions for improving the manuscript of the journal paper.

I wish to thank Ms. Yamato Yuri, the secretary of TECS laboratory, for managing the necessary paperwork for the utilization of my JICA budget. Thus, I have been able to attend numerous conferences without worrying about the monetary constraints. I am also thankful to Mr. Takata for providing us the necessary instructions to carefully handle the laboratory instruments. I wholeheartedly appreciate the Student Affairs Division of the Chikushi campus for generously assisting with the smooth transition to this new country. I am further thankful to Matsuura Ranko-sensei, Ohto Aki-sensei, and Koyama-sensei of the Japanese language course at Kyushu University for helping me improve my Japanese language ability to communicate more effectively with the local community and participate in various activites.

I would like to express my gratitude to the Ministry of Education, Culture, Sports, Science and Technology (MEXT) Japan and Japan International Cooperation Agency (JICA) for generously awarding me the scholarship as part of the Innovative Asia doctoral program. I am also grateful to JICA for providing additional research funds, which enabled me to acquire the necessary resources for my research and attend various domestic and international conferences. Their support has been invaluable in allowing me to pursue my research goals and contribute to the academic community. I would like to extend my sincere appreciation to JICA for sponsoring my personal Japanese language classes, which helped me improve my Japanese communication skills.

Throughout my research journey at Kyushu University, my fellow lab members from diverse backgrounds and cultures have played an integral role in shaping my experiences. I am especially grateful for the contributions of Mr. Motaz Salama, who was not only an excellent labmate but also a wonderful neighbor during our time in the dormitory. Our discussions about our research, cultural traditions, and shared cuisine will always be treasured memories. Furthermore, I wish to thank Dr. Chairunnisa for being an awesome senpai, who kept an vibrant atmosphere in the laboratory. Her research presentations during the study and research meetings were a source of motivation for us all. I am also thankful to Dr. Perera for his tips and guidance to help me navigate my research journey. Mr. Haonan Chen, with whom I formed the new molecular simulation group, was also an invaluable partner, and I learned a great deal from him as we explored this new research direction together. I am also thankful to Mr. Hao Yu and Mr. Haonan for being a great companion while attending various academic conferences and workshops. I am really glad to have collaborated with Mr. Sang Won Seo on a research project and also learned about each other's cultures over our coffee sessions. Additionally, I am grateful to have become friends with Mr. Sannan Salabat Butt. Belonging from the neighboring countries, we could interact in our native language and help in each other's research related issues. Finally, I would like to extend my thanks to Mr. Kanta Kawagita, Mr. Hideaki Nakatsu, Mr. Kouki Mizobe, Mr. Mutebi Denis, Mr. Mojtaba Purjam, Mr. Yang Zhaosheng, Mr. Yang Cheng, Mr. Marco Lao, among others, for their camaraderie and support throughout my time at Kyushu University.

Lastly, I would like to express my deepest gratitude to my parents and my little sister, who stood by me during all my ups and downs in my research journey. They have been my source of happiness, inspiration, and a pillar of support and encouragement, without whom I could not have made it this far. Thus, I dedicate this thesis to my family.

Summary

Rampant emission of greenhouse gases in the atmosphere is the primary contributor to the global warming and climate change phenomena. The primary sources of these greenhouse gases include the fossil-fuel based power generation and its utilization in the conventional mechanical vapor compression and thermal desalination systems. Furthermore, the waste heat generated due to the thermal inefficiencies of the energy systems exacerbates the given crises. In order to mitigate these crises, the incessant switch to renewable energy and waste heat recovery for use in thermal systems are gaining importance. Adsorption-based thermal systems, including cooling and desalination applications, are becoming promising alternatives to the conventional energy-based thermal systems. The use of adsorption phenomena for these given applications is still at a developing stage. The primary research on the adsorption-based thermal systems encapsulates from material characterization to system-level performance optimization. Therefore, the adsorption phenomena can be investigated from microscopic to macroscopic perspectives. The present study concerns with the equilibrium adsorption phenomena, for which three types of studies are conducted: (i) molecular simulation, (ii) adsorbed phase thermodynamic property determination, and (iii) adsorption heat transformer cycle simulation.

The adsorption properties, viz., isotherm and isosteric heat of adsorption, are dependent upon the adsorbent material characteristics such as its pore size distribution and pore surface chemistry. Influence of these factors is evaluated by performing a Grand Canonical Monte Carlo (GCMC) simulation of the adsorption process. CO_2 adsorption in activated carbon is taken as an example for this simulation study. The activated carbon is modeled as graphite slit pore structures with or without surface functional groups. Three oxygen containing functional groups are considered, viz., carbonyl, hydroxyl, and carboxyl groups. The results indicate favorable impact of smaller pore size and the presence of functional groups on the low-pressure adsorption uptake and isosteric heat of adsorption. Furthermore, a GCMC simulation is performed for water adsorption in hydroxyl functional group-based graphite slit pore. This study elucidates the adsorbed phase formation process and the resultant adsorption isotherm shape.

The molecular level investigation of the adsorption phenomena is followed by the bulk thermodynamic property determination of the resultant adsorbed phase. Three properties are determined, viz., specific heat capacity, specific entropy, and specific enthalpy. The rigorous mathematical development of these properties is carried out considering the key variables of pressure, temperature, uptake, isosteric heat of adsorption, and gaseous phase properties. The path integrals present in the entropy formulation is calculated by choosing accurate reference uptake value and consistent reference entropy values between the gaseous phase and adsorbed phase. These thermodynamic properties are compared against the corresponding gaseous phase and saturated liquid phase values, to evaluate the relative behavior of the adsorbed phase with respect to the pure adsorbate property values.

Finally, an equilibrium cycle development of the heat upgrading adsorption heat transformer cycle (AHT) is performed. The heat upgrading cycles can elevate the low-grade heat source temperature to a higher value, for increasing its exergetic potential. Recently, these cycles are gaining attraction for its use in cooling, desalination, and power generation applications as opposed to the conventional adsorption-based thermal systems. However, given the relative scarcity in the available studies on the heat upgrading cycles, a detailed equilibrium performance evaluation for the AHT cycle is carried out. Non-linear optimization based mathematical model is developed for characterizing the non-isosteric preheating and precooling phases of the AHT cycle. The performance parameters are defined by the useful heat ratio (UHR) and condensation heat ratio (CHR), denoting the heat upgrading and desalination potentials, respectively. Detailed parametric evaluation of these performance parameters and the output adsorption heat amount is carried out with respect to operating temperature range, adsorber bed thermal mass, and type of adsorbent-adsorbate pair. This study is accompanied by the performance enhancement of the AHT cycle via an internal heat recovery scheme. Moreover, the theoretical maximum temperature lift of the AHT cycle is determined from both the reversible and irreversible thermodynamic process-based approaches. The ability to augment the desalination performance of an existing multi-effect distillation (MED) system is realized by the hybridization of the AHT cycle with the MED system. The resultant AHT-MED system elucidates a significant improvement in the performance ratio and water production rate as compared to the standalone MED system with the same working temperature range.

Table of Contents

List of Figures

List of Tables

List of Abbreviations

AAD	Average absolute deviation / %
AD	Adsorption Desalination
AHT	Adsorption heat transformer cycle
CHR	Condensation heat ratio / -
COP	Coefficient of performance
HR	Heat recovery
HTF	Heat transfer fluid
MED	Multi effect distillation
PR	Performance ratio
SCP	Specific cooling power / $\mathrm{J\,kg^{-1}}$
$SDWP$	Specific daily water production / $\mathrm{kg\,kg^{-1}\,d^{-1}}$
UHR	Useful heat ratio / -
WPR	Water production rate / $\mathrm{kg\,s^{-1}}$

List of symbols

Notations

A	Area / m^2
α	Thermal expansion coefficient / K^{-1}
b	Van der Waals volume / $\mathrm{m}^3\,\mathrm{mol}^{-1}$
c	Specific heat capacity / $\mathrm{J\,kg^{-1}\,K^{-1}}$
c_0	Maximum volumetric uptake / $\mathrm{m}^3\,\mathrm{kg}^{-1}$
c_p	Specific heat capacity at constant pressure / $\mathrm{J\,kg^{-1}\,K^{-1}}$
Δz	Thickness in the z-direction / Å
e	Specific heat per unit mass of adsorbent / $\mathrm{J\,kg^{-1}}$
E	Activation energy / $\mathrm{J\,mol^{-1}\,K^{-1}}$
Ex	Exergy / $\mathrm{J\,kg^{-1}}$
η	Efficiency / -
ϵ	Potential well depth / $\mathrm{J\,mol^{-1}}$
ε_0	Free space permittivity / $\mathrm{F\,m^{-1}}$
$\hat{G}$	Gibbs free energy / J
h	Specific enthalpy / $\mathrm{J\,kg^{-1}}$
$\hat{H}$	Enthalpy / J
h_{fg}	Heat of vaporization / $\mathrm{J\,kg^{-1}}$
k_B	Boltzmann constant / $\mathrm{J\,K^{-1}}$
L	Unit cell length / Å
m	Mass / kg
$\dot{m}$	Mass flow rate / $\mathrm{kg\,s^{-1}}$
μ	Chemical potential / $\mathrm{J\,kg^{-1}}$

n	Surface heterogeneity coefficient / -
N	Number of particles or molecules / -
P	Pressure / Pa
q_i	Partial charge of the $\mathrm{i^{th}}$ particle or molecule / 1.602×10^{-19} C
Q	Heat / J
$\dot{Q}$	Heat transfer rate / W
q_{st}	Isosteric heat of adsorption / $\mathrm{J\,kg^{-1}}$
r	Fraction of maximum possible heat recovery / -
R	Universal gas constant / $\mathrm{J\,mol^{-1}\,K^{-1}}$
r_c	Cutoff distance / Å
ρ_g	Gaseous phase density of the molecules / $\mathrm{Å^{-3}}$
s	Specific entropy / $\mathrm{J\,kg^{-1}\,K^{-1}}$
$\hat{S}$	Entropy / $\mathrm{J\,K^{-1}}$
T	Temperature / K
t_{cycle}	Time / s
U	Heat transfer coefficient / $\mathrm{W\,m^{-2}\,K^{-1}}$
U^{total}	Total intermolecular energy of the adsorption system / $\mathrm{J\,mol^{-1}}$
U^{vdW}	Van der Waals energy between two molecules / $\mathrm{J\,mol^{-1}}$
v	Specific volume / $\mathrm{m^3\,kg^{-1}}$
V_{pore}	Pore volume of the adsorbent / $\mathrm{Å^3}$
$\hat{V}$	Volume / $\mathrm{m^3}$
w	Uptake / $\mathrm{kg\,kg^{-1}}$
W	Work / J
X	Salinity / $\mathrm{kg\,kg^{-1}}$

Subscripts/Superscripts

a, ade	Adsorbed phase adsorbate
ad	Adsorption phase in the AHT cycle
ads	Adsorbent
Amb	Ambient
avg	Average

b	Normal boiling point
B_e	Brine generated due to flashing in the effect of MED
$cond$	Condenser
$Crit$	Critical point
cw	Cooling water
$cycle$	Cycle
D	Distillate vapor
D_f	Distillate vapor generated due to flashing in the effect of MED
D_{bd}	Distillate blowdown
D_c	Condensed distillate from effect
D_{cond}	Distillate from condenser of the MED system
D_{fb}	Distillate flash box
D_{fh}	Distillate feed heater
des	Desorption phase
e	Effect in the MED system
E	MED effect
$elec$	Electrostatic interaction
$evap$	Evaporator
F	Feed
g	Gaseous phase
H	Heat supply temperature
HX	Heat exchanger
in	Inlet
l	Liquid phase
L	Heat sink temperature
lat	Latent heat
M	Heat source temperature
max	Maximum
mb	Mixing box
out	Outlet
$prev$	Previous
pc	Precooling phase
ph	Preheating phase

pw	Potable water
rec	Recovery phase
s	Steam
sat	Saturation
sen	Sensible heat
sw	Seawater
$Trip$	Triple point
vdW	Van der Waals interaction
x, y, z	Directions

Chapter 1

Introduction

At present, the world is grappling with the negative effects of global warming and climate change, and the primary cause for this crisis is attributed to the release of greenhouse gases at a global scale. For example, the atmospheric concentration of carbon dioxide (CO_2), a major greenhouse gas, is increasing at an alarming rate. Quantitatively speaking, the CO_2 concentration is expected to elevate up to 500 ppm by the year 2050 and 800 ppm by year 2100 because of its rampant emission from the industrial exhaust [1]. Therefore, this occurrence poses the threat to increase the global atmospheric temperature by more than $1.5\,^{\circ}C$, the limiting temperature increase value set by the Paris Agreement [2]. Concomitantly, the surface temperature of the earth has risen by $1\,^{\circ}C$ in the last sixty years [3], owing to the increasing concentration of greenhouse gases including CO_2. Along with the emission of greenhouse gases, the waste heat generated from the industrial processes equally exacerbates the global warming phenomena [4]. The waste heat is defined as the energy generated in industrial processes which is released to the environment without necessary processing [5]. Statistically, the low-grade waste heat rejected amounts to as high as two-thirds of the primary energy supply in the USA, caused by the thermo-mechanical energy conversion losses [6]. This large amount of waste heat affects the global warming phenomena directly or indirectly, due to the severity of the inefficiencies in the thermal systems.

Another practical issue prevailing in the world is the scarcity of drinkable water [7]. The contributing factors can be listed as: (i) rapid urbanization and industrialization, (ii) population burst, (iii) surface water contamination caused by the industrial waste disposal, and (iv) climate change [8]. For decades, desalination has been prevalent as an established technique to eradicate the water scarcity issue. This technique is defined as the process of separating the salt from the saline water through the use of thermal and/or mechanical energy. The abundance of the saline water in the form of seawater makes the desalination possible to be implemented at a global scale. Moreover, technological advancements has resulted in a significant growth in the water desalination capacity [9]. Especially, the Middle East appears to encapsulate the largest market share of thermal energy driven desalination plants. The presence of large fossil fuel-based power plants as the driving energy source of the desalination plants has primarily contributed to this large desalination capacity [10]. The use of fossil fuel for satisfying this energy requirement exacerbates the global warming crisis. The use of renewable energy sources (e.g., solar energy, wind energy etc.) and the industrial waste heat for driving the thermal desalination system appears to be a viable solution. However, the low exergy content offered by these energy-sources results in poorer efficiency of the thermal systems compared to the ones using conventional energy sources.

The issues mentioned in the preceding discussion have led the researchers to pay attention toward developing new and clean technologies to abate the rampant greenhouse gas emission in the atmosphere, to increase the waste heat utilization, and to improve the performance of renewable energy-based thermal desalination systems. Along with these goals, the need for the efficient utilization of low-temperature heat source (waste heat and renewable energy), low-maintenance of the system, reduced required energy consumption, and economic viability have brought the adsorption based cooling and desalination technologies into the researchers' attention [11].

1.1 Adsorption phenomena

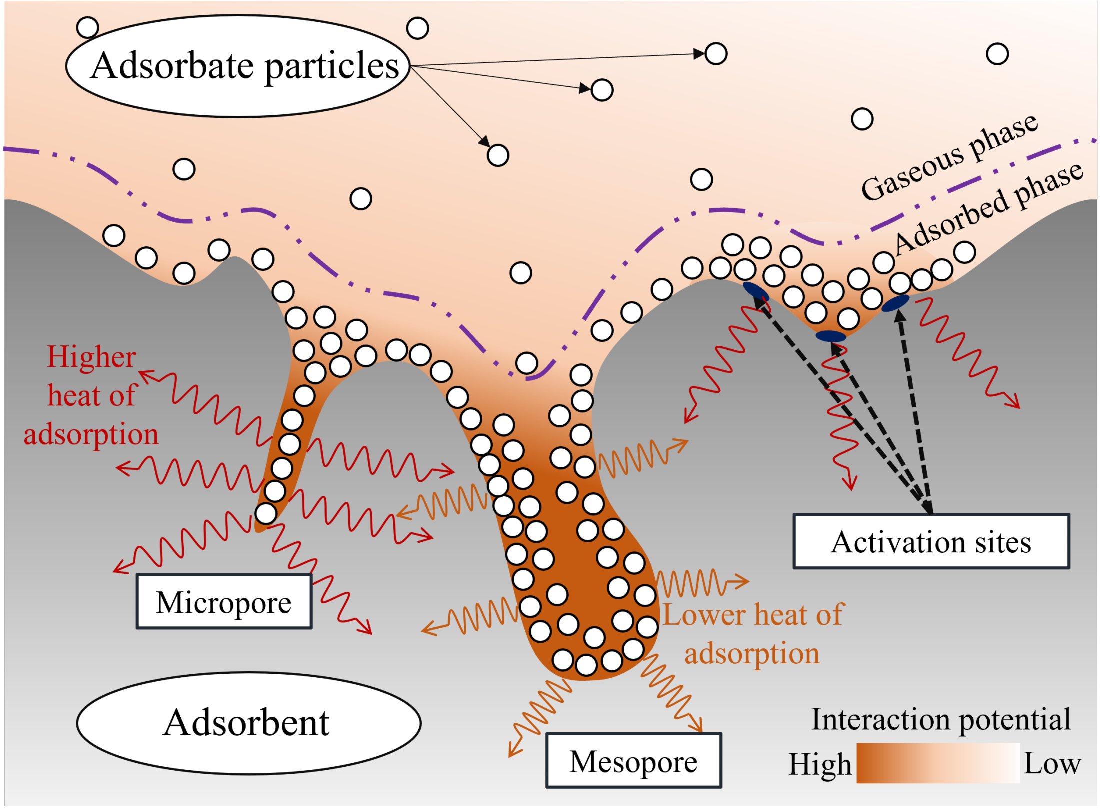

Figure 1.1: Schematic of the adsorption phenomena

Adsorption process refers to the adherence of the gas or liquid adsorbate particles onto the surface of a solid adsorbent material. Depending on the nature of interaction between the adsorbate and adsorbent materials, the adsorption process can be classified into physisorption and chemisorption processes. In a physisorption process, the van der

Waals and electrostatic interactions are present between the adsorbate and adsorbent surface molecules. The occurrence of chemical bond formation between the adsorbate and adsorbent molecules is absent in this process. In case of chemisorption, the adsorbate-adsorbent interaction occurs via chemical bond formation. The adsorption process is generally exothermic in nature. Therefore, the adherence of adsorbate molecules is accompanied by a release of energy, which is termed as the heat of adsorption. The amount of energy released is higher in chemisorption than the physisorption process. In Fig. 1.1, a schematic of the physisorption (hereby 'adsorption' is used interchangeably) process is depicted. The given adsorbent material consists of porous geometries and activation sites. Based on the dimension of the pores, the porous adsorbents can be classified as microporous (pore size $<$20 Å), mesoporous (20 Å-500 Å), and macroporous ($>$500 Å). The gaseous adsorbate particles are primarily adsorbed in the pores of the adsorbents. These pores offer a high magnitude of attractive interaction potential between the adsorbate-adsorbent particles. This higher interaction potential is attributed to the inverse relationship between the attractive van der Waals potential and the inter-particle distance. Thus, as the pore size decreases, the affinity to adsorb an adsorbate particle enhances. However, the capacity to adsorb adsorbate molecules reduces with the reduction in the pore size. Apart from the pore geometries, the activation sites also influence the overall affinity of the adsorbent material towards the adsorbate particles. These sites represent the chemical heterogeneity of the adsorbent surface. Generally, these sites are formed by doping or functionalizing components with higher interaction potential (primarily electrostatic) onto the adsorbent surface. Therefore, the structural and chemical characteristics of the adsorbent surface governs the adsorption process.

The resultant adsorption properties, viz., adsorption isotherm and isosteric heat of adsorption, are of primary interest for its use in characterization of the adsorption-based thermodynamic processes. The adsorption isotherm describes how the uptake, or the amount of adsorbate particles adsorbed onto the adsorbent surface, varies with respect to the pressure and temperature conditions of the adsorption process. The uptake value is directly and inversely proportional to pressure and temperature, respectively. The adsorption isotherm is determined at thermodynamic equilibrium or steady-state condition. The adsorption kinetics (dependent upon the diffusivity of the adsorbate particles) governs the time required to attain the equilibrium uptake value at a given pressure and temperature. The isosteric heat of adsorption characterizes the heat of adsorption released to adsorb a single adsorbate particle at thermodynamic equilibrium. These fundamental properties are used for development of the adsorption-based thermal systems for cooling and desalination. The thermodynamic cycles corresponding to these systems are represented using the pressure, temperature, and uptake values. Likewise, determination of the energetic performance parameters (e.g., specific cooling power, coefficient of performance, etc.) requires the isosteric heat of adsorption value of the given adsorbent-adsorbate pair.

Adherence of the adsorbate molecules onto the adsorbent surface leads to the formation of the adsorbed phase, as highlighted in Fig. 1.1. This adsorbed phase possesses distinct thermodynamic characteristics as opposed to the corresponding gaseous phase. These thermodynamic properties include specific heat capacity, entropy, enthalpy, internal energy, and Gibbs free energy. Calculation of these properties requires the use of classical thermodynamic principles such as Gibbs law, Maxwell relations, and Gibbs-Duhem relation. These properties are then expressed as functions of pressure, temperature, uptake, isosteric heat of adsorption, and the corresponding gaseous thermodynamic properties. Since, the adsorbed phase is manifested as the result of interaction between the adsorbate molecules and the solid adsorbent surface, the thermodynamic properties deviate from the condensed/liquid phase of the adsorbate. These thermodynamic properties are further used for modeling the heat and mass transfer processes of the adsorption-based systems and second law-based performance analysis of the said systems. Therefore, accuracy values of the adsorbed phase property are indispensable for thermodynamic evaluation of the adsorption process.

1.2 Adsorption cycles

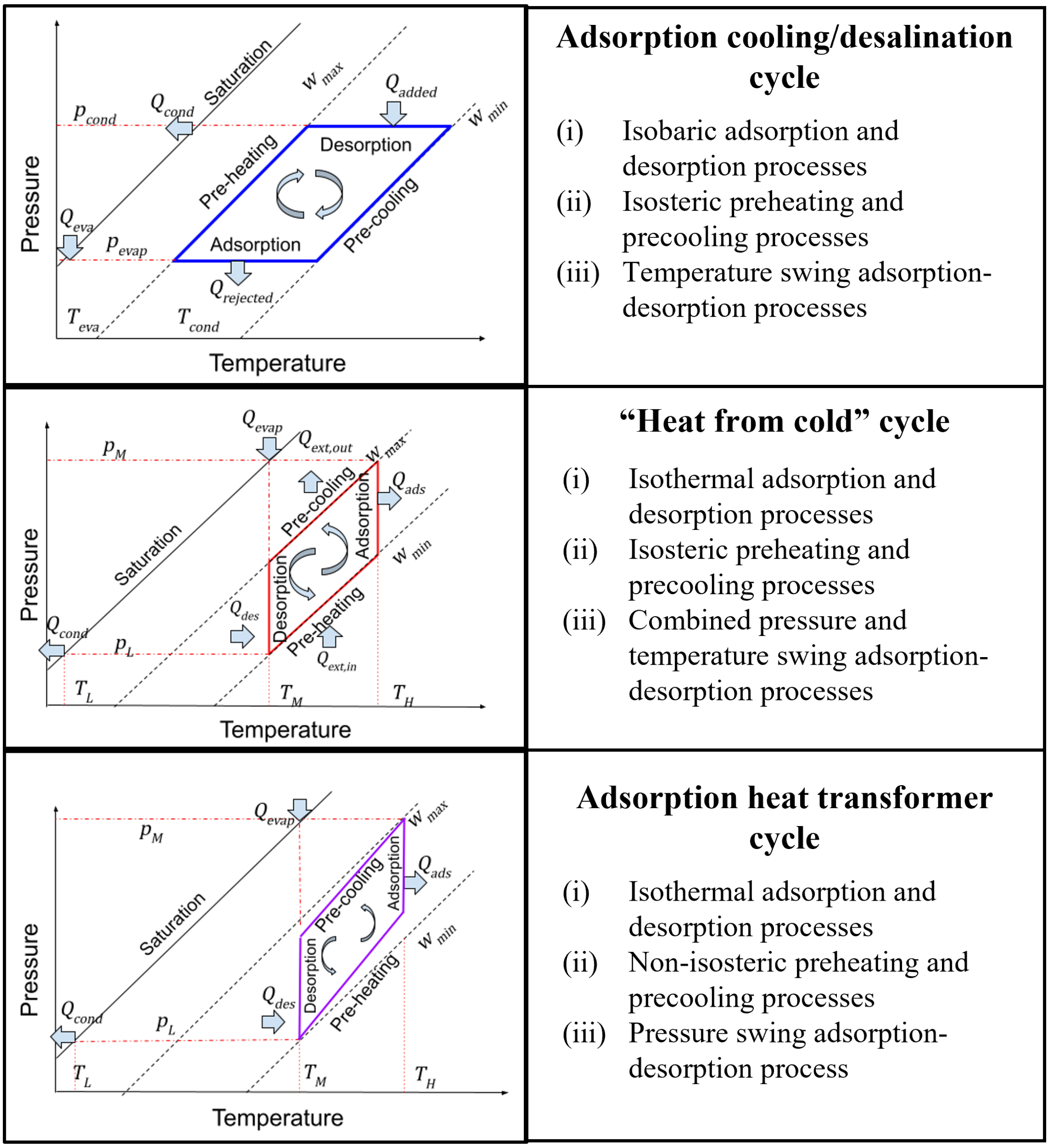

Adsorption cooling/desalination cycle

(i) Isobaric adsorption and desorption processes
(ii) Isosteric preheating and precooling processes
(iii) Temperature swing adsorption-desorption processes

“Heat from cold” cycle

(i) Isothermal adsorption and desorption processes
(ii) Isosteric preheating and precooling processes
(iii) Combined pressure and temperature swing adsorption-desorption processes

Adsorption heat transformer cycle

(i) Isothermal adsorption and desorption processes
(ii) Non-isosteric preheating and precooling processes
(iii) Pressure swing adsorption-desorption process

Figure 1.2: Three types of adsorption cycles depicted on the pressure-temperature-uptake plane

Fig. 1.2 displays three different adsorption cycles available in the literature. The specific characteristics of the cycles are also listed. All of these adsorption cycles consist of four distinct phases, viz., preheating, precooling, adsorption, and desorption phases. However, the nature of these phases vary across the different cycles. The adsorption cooling and desalination cycle has been established as a promising alternative to the fossil fuel-based energy consuming thermal systems such as mechanical vapor compression and thermal desalination systems. Typically, an adsorption cycle is configured with an evaporator, a condenser, and adsorber beds. The evaporator pressure is lower than the condenser pressure in the adsorption cooling cycle. The isobaric adsorption and desorption phases occur at the evaporator and condenser pressures, respectively. A regenerated adsorber bed contains low amount of adsorbed vapor (denoted as w_{min}) and remains at high temperature and pressure values. The precooling phase is initiated by extracting the heat from the adsorber bed to reduce its temperature. The pressure reduces accordingly in order to maintain the constant uptake value. During the precooling phase, there is no adsorbate mass flow in or out of the adsorber bed. After reaching the low evaporator pressure and an intermediate temperature, the flow of the adsorbate vapor is initiated by connecting the adsorber bed with the evaporator. Further reduction in the temperature leads to the adsorption of the incoming vapor from the evaporator in an isobaric manner, reaching the higher uptake value (w_{max}). Once, the bed reaches the adsorption temperature, the regeneration of the adsorber bed is proceeded. The corresponding phases involve increasing the pressure of the bed to reach the condenser pressure via regeneration heat supply, followed by the desorption of the bed via its connection with the condenser. The temperature levels of a typical adsorption cooling cycle are the evaporation temperature (5 °C to 15 °C), adsorption/condenser temperature (25 °C to 35 °C), and regeneration temperature (55 °C to 95 °C). The adsorption cooling cycle is driven by the temperature swing adsorption process, where variation in the temperature of the bed governs the cyclic change in the uptake values.

The following cycles as depicted in Fig. 1.2 include the heat upgrading "heat from cold" (HeCol) cycle and adsorption heat transformer (AHT) cycles. Unlike the adsorption cooling cycle, the HeCol and AHT cycles generate a heating effect with the help of low-temperature heat input. These cycles upgrade the said low-temperature heat source, which is typically characterized as the low-grade waste heat and renewable energy sources. In case of these heat upgrading adsorption cycles, the evaporator pressure is higher than the condenser pressure. At the initial state, the adsorber bed possesses a low pressure and temperature. The preheating phase is carried out by simultaneously increasing the temperature and pressure of the bed. The temperature of the adsorber bed is increased till the desired upgraded heat temperature value is attained. In case of HeCol cycle, this preheating process is isosteric in nature, which denotes that the uptake value remains constant during this phase. This behavior is similar to the preheating phase of the adsorption cooling cycle. Therefore, an external heat source is required for maintaining the constant uptake value in the HeCol cycle. However, in case of an AHT cycle, this preheating phase is carried out via the connection of the high pressure evaporator to the adsorber bed. Therefore, the temperature rise is attributed to the heat of adsorption released during the pressure swing adsorption process. As a result, the preheating process in an AHT cycle is non-isosteric in nature. After reaching the desired temperature and an intermediate pressure value, the adsorber bed is connected to the high pressure evaporator, which initiates the pressure swing adsorption process in the bed. Furthermore, the adsorption heat is extracted during this phase, to maintain the isothermal nature of the adsorption process. After reaching the evaporator pressure, the precooling and isothermal desorption phases follow, respectively. It can be seen that the primary driving force for these two cycles are the pressure swing adsorption process. It is noted that the studies on the application of pressure swing adsorption is primarily abundant for gas separation and sequestration processes. However, the available literature on the heat upgrading adsorption cycles are relatively scarce as compared to the adsorption cooling cycles.

1.3 Objectives

The primary aim of the thesis is to evaluate the adsorption phenomena from a multiscale perspective, which includes the molecular level adsorbent-adsorbate interactions, macroscopic thermodynamic property evaluation of the adsorbed phase, and system level characterization of the equilibrium adsorption cycle. A detailed description of the objectives are listed as follows:

(i) Delineating the effect of fundamental adsorbent material properties on the adsorption performance from a molecular perspective

(ii) Establishing accurate thermodynamic behavior of the adsorbed phase with respect to the known gaseous and liquid phases of the adsorbate gas.

(iii) Performing energetic performance evaluation of the bulk adsorption-based thermal systems under equilibrium condition.

1.4 Scope

These objectives are achieved via the following research scope and activities:

(i) **GCMC simulation:** Grand Canonical Monte Carlo simulation is performed for modeling the equilibrium adsorption process. The adsorption isotherm and isosteric heat of adsorption are found out for CO_2 and water vapor adsorption in activated carbon. Detailed parametric variation in these properties and adsorbed phase molecular configuration is performed with respect to the adsorbent material characteristics, viz., pore size distribution and functional groups.

(ii) **Adsorbed phase thermodynamic properties:** Detailed mathematical formulations are developed for the adsorbed phase thermodynamic properties using the classical thermodynamic principles. These properties include specific heat capacity, specific entropy, and specific enthalpy of the adsorbed phase. These values are compared against the corresponding gaseous and liquid phase property values at the same thermodynamic state.

(iii) **Performance evaluation of AHT cycle:** The fundamental heat and mass transfer model of the heat upgrading adsorption heat transformer cycle is developed considering equilibrium cycle condition. Parametric variation of the performance parameters such as useful heat ratio (UHR) and condensation heat ratio (CHR) are performed with respect to operating temperature values, adsorber bed design, and adsorption isotherm characteristics.

(iv) **Theoretical development of AHT cycle:** Theoretical model is developed for the internal heat recovery scheme implemented in equilibrium AHT cycle considering the heat exchanger effectiveness. The theoretical limiting heat recovery potential in terms of maximum possible temperature lift of the AHT cycle is determined. Reversible and irreversible process-based representation of the AHT cycle is undertaken for the given evaluation.

(v) **Hybridization of AHT with MED system:** The AHT cycle is hybridized with the multi-effect distillation (MED) system to improve its desalination performance in terms of performance ratio and water production rate.

Chapter 2

Literature Survey

In this chapter, a detailed overview of the existing literature on the adsorption-based studies is provided. The current review is divided into the fundamental aspects of the adsorption phenomena and the system-level adsorption-based application. The fundamental studies include the molecular aspect of the adsorption process, macroscopic thermodynamic properties of adsorbed phase, and adsorption-based cycle development. The system-level studies on the adsorption phenomena include the development and performance evaluation of the adsorption cooling and desalination systems, performance improvement of these systems via incorporating heat and mass recovery schemes, hybridization of the adsorption systems with the existing thermal desalination systems, and the basic analysis of the heat upgrading cycles.

2.1 Fundamental overview of adsorption phenomena

2.1.1 Molecular description of adsorption process

The molecular simulation techniques applied for characterizing the adsorption process include Density Functional Theory (DFT) [12], Grand Canonical Monte Carlo (GCMC) [13], and Molecular Dynamics (MD) [14] simulation methods. The DFT method is a part of *“ab initio”* computational frameworks, where the electronic-level descriptions are generated using the quantum mechanical principles. Therefore, no experimental data is required to characterize the intermolecular interactions [15]. The DFT technique has been used for simulating the adsorption of light gases (e.g., methane, CO_2, H_2, N_2, ethane, etc.). The adsorption properties that are obtained using this technique includes adsorption isotherm, isosteric heat of adsorption, and diffusion properties. Kessler et al. [16] proposed the use of a classical density functional theory (cDFT) based on the PC-SAFT equation of state to determine the adsorption isotherms of methane, ethane, n-butane, and nitrogen in the covalent organic frameworks (COF)-based adsorbents. Alonso et al. [17] proposed a combination of periodic density functional theory and dual-site Langmuir isotherm formulation to obtain the adsorption isotherms of pure gases, viz., CO_2,N_2, and SO_2 in the Mg-MOF-74 adsorbent. Grinev et al. [18] performed a DFT simulation to analyze the isosteric heat of adsorption behavior of the pure gas adsorption on graphite surface. Diffusion properties of the CO_2 and CH_4 molecular transport in the ZIF-8 adsorbent were obtained using the DFT method by Paudel et al. [19]. Despite the ability to model the adsorption process of light molecules, the DFT simulation technique is used for versatile purposes. Force field parameterization is defined as the determination of the coefficients in the empirical equations (e.g., L-J potential) to describe the intermolecular interactions. This parameterization for the adsorption simulation can be performed using the experimental isotherm data or data obtained from the first principle-based computational frameworks. Several studies are available for the use of DFT in obtaining the force field parameters of the L-J potential formulation. For instance, transferable force field was developed using DFT method for the hydrocarbon and small molecule adsorption in alkali metal exchanged zeolites [20] and silica zeolites [21]. Improved force field parameters were developed for hydrocarbon adsorption in MOFs compared to the traditionally used models [22, 23]. Furthermore, the partial charge distribution of the adsorbent materials (especially the MOFs and COFs) utilize the DFT-based algorithms. Instances of few such models can be listed as: (i) charges from electrostatic potentials (ESP) using a grid-based method (ChelpG) [24], (ii) Hirshfeld population analysis [25, 26], (iii) Bader's charge density analysis using the atoms in molecule (AIM) method [27, 28], (iv) repeating electrostatic potential extracted atomic charge method (REPEAT) [29], (v) density-derived electrostatic and chemical (DDEC) charges [30]. Finally, based on the experimental isotherm of the liquid N_2 at temperature 77 K or argon at 87 K, the DFT-based techniques are used to characterize the pore size distribution (PSD) of adsorbents. Few such applications are listed as follows: (i) non-local density functional theory (NLDFT) technique applied for N_2 and Ar adsorption in MCM-41 adsorbent [31], (ii) NLDFT method used for obtaining the PSD of amorphous polymer materials [32], (iii) 2-dimensional NLDFT method for PSD determination of biochars and activated carbons [33], (iv) Quenched solid density functional theory (QSDFT) technique applied for PSD determination of porous carbon produced via KOH activation of petroleum coke [34], (v) QSDFT applied for obtaining the PSD of microporous, mesoporous, and amorphous silica gel materials [35]. It can be observed from this discussion that the use of DFT is limited to characterizing the adsorption process of small molecules, and determining the adsorbent properties such as PSD and partial charge distribution. DFT method is computationally intensive for modeling adsorption of complex molecules (e.g., water and long-chain hydrocarbon) in larger simulation systems (e.g., $>$ 100 adsorbate molecules). Furthermore, the DFT-based simulation results in significant inaccuracies of the dispersive interaction parameters between the adsorbate and adsorbent molecules [36]. Hence, the statistical mechanics-based computational frameworks are generally utilized for adsorption simulation at these conditions.

GCMC is a reliable probabilistic tool (based on statistical mechanics principles) to determine the equilibrium adsorption properties, e.g., isotherm and isosteric heat of adsorption. This technique is used to simulate the adsorption of inert gases, non-polar and polar adsorbate gases in different kinds of adsorbents, which include zeolites, metal organic frameworks, activated carbon, covalent organic frameworks, and polymers. The studies on the GCMC technique further include analyzing the effects of pore size distribution and surface chemistry on the adsorption equilibrium properties, defining new database of force field parameters for certain adsorbent-adsorbate pair (e.g., TraPPE-Zeo force field for gas adsorption in zeolite [37]), high throughput screening (HTS) of MOFs for a given application (e.g., screening of Zr-oxide MOFs for CO_2 adsorption [38]), determining pore size distribution of the adsorbent [39] and last but not limited to characterizing the wetting behavior of the adsorbed phase (e.g., adsorbed CO_2 wetting on graphite surface [40]). A detailed overview on the use of GCMC for simulating adsorption processes in various materials are provided in Table 2.1.

Table 2.1: Existing studies on the application of Grand Canonical Monte Carlo simulation technique

Material pair	Properties evaluated	Remarks	Reference
Graphite + CH_4 and Kr	Excess loading, isosteric heat of adsorption, local density distribution, and radial distribution function	Delineated underlying transitions in the adsorbate loading and the generation of spikes in the profile of isosteric heat of adsorption. Two types of graphite models (homogeneous and corrugated anisotropy) were considered for defining the solid-fluid interactions.	[41]
M-MOF-74 (M = Mg, Ni, Co, Zn) + H_2	Isotherms, isosteric heat of adsorption, H_2 dipole distribution	The effect of partial charge distribution and polarizabilities of each atom in the MOF structure were investigated for H_2 adsorption. The order of H_2-metal interaction strength was found out to follow the sequence as: Ni-MOF-74 > Co-MOF-74 > Mg-MOF-74 > Zn-MOF-74	[42]
MOF-74-x series and nbo-MOFs + noble gases (Ar, Kr, Xe and Re)	Isotherm, isosteric heat of adsorption, Henry's constant	Reduced pore size of the adsorbent structure facilitated the gas uptake and Henry's constant. The identity of the metal ion present at the open metal sites didn't pose significant influence on the gas-metal interaction potential.	[43]
Siliceous zeolites + N_2 and Ar	Isotherm	Three types of zeolites were considered for simulation, viz., LTA, FAU, and MFI. N_2 adsorption was seen to initiate at lower relative pressure than Ar adsorption, attributed to the quadrupole moment of the N_2 molecule.	[44]
Porous Polymer Networks + Methane	Adsorption isotherm and isosteric heat	Database of 18,000 PPN chemical structures was developed and screened using GCMC technique for high deliverable capacity of methane. Cooperative methane-methane interactions were highlighted to be important parameter for high methane storage performance	[45]
Graphite + Methane	Surface excess density, isosteric heat, local density distribution, 2D radial distribution function	Simulation was carried out at temperatures between 50 K and 110 K. 2D phase transitions across the adsorption isotherm profile was delineated. The cusps and spikes in the isosteric heat were explained by the entropic and enthalpic contributions between the first and second layers of the adsorbed phase	[46]
HKUST-1 and MIL-101(Cr) + Methane	Adsorption uptake, isosteric heat of adsorption	Isotherms obtained from GCMC simulations overestimated the corresponding experimental uptake data. The adsorbate binding sites were identified in the MOF structures. Enrichment of open metal sites and reduction in the fraction of large pores were recommended in the development of precision adsorbents for improved adsorption performance.	[47]
Siliceous zeolites + Methane and CO_2	Adsorption uptake and selectivity	12 types of siliceous zeolites were considered for the adsorption of CH_4/CO_2 mixture using GCMC simulation technique. PCFF force field was recommended as the best model to define adsorbate interaction with zeolites.	[48]

Table 2.1 Continued: Existing studies on the application of Grand Canonical Monte Carlo simulation technique

Zeolites + CO_2	Adsorption isotherm, Henry coefficient, free energy landscape of adsorbed phase	156 geometrically diverse zeolite structures were incorporated to model the adsorption of pure component and mixture CO_2. Different force field model parameters for the L-J potential were compared. Inclusion of high pressure adsorption uptake values were suggested to be important in developing transferrable force field of the CO_2 adsorption.	[49]
Hybrid graphene oxide/MOF + CO_2	Adsorption uptake, selectivity	The enhancement in the CO_2 adsorption uptake values due to the presence of graphene oxide (GO) layer in the hybrid GO/MOF structures was realized using GCMC simulation. The high electrostatic potential with GO layer and small pore size distribution of Cu-BTC MOF were beneficial for low-pressure adsorption of CO_2 in the hybrid GO/Cu-BTC adsorbent.	[50]
Hybrid 2D graphene with ionic liquids + CO_2 and binary mixtures CO_2/CH_4, CO_2/N_2	Adsorption uptake, isosteric heat and selectivity	A hybridization of 2D graphene layers with ionic liquids was proposed for improved adsorption and separation of CO_2 gas. DFT-optimized structure revealed an increase interlayer spacing of the graphene due to the presence of ionic liquid's cation and anions, which increased the accessible pore size, thus improving the adsorption capacity of CO_2 adsorption.	[51]
MOF-801 + water	Adsorption isotherm	Structural defects were introduced in the MOF adsorbent. Missing organic linkers resulted in the presence of terminal H_2O/OH groups, which increased the hydrophilicity of the adsorbent by the enhanced hydrogen bond formation. Missing Zr-metal clusters engendered an increase in the pore size, which enhanced the water adsorption capacity.	[52]
Activated carbon fibre + water	Adsorbed phase density, isosteric heat of adsorption, radial distribution function	Origin of hysteresis was delineated using the difference in adsorbed water cluster formation during the adsorption and desorption phases. The larger pore size (1.1 nm) exhibited the hysteresis loop generation, unlike in the smaller pore size of 0.7 nm	[53]
Silicalite-1 + water	Adsorption isotherm, isosteric heat of adsorption	The isotherm results obtained from GCMC simulation deviated from the experimentally observed hydrophobicity of the silicalite adsorbent. Reduction in the dipole moment of water by reducing the partial charges of water was suggested for obtaining good agreement with the experimental results.	[54]

From the above discussion, the GCMC simulation technique is able to provide insight on a diverse set of adsorption equilibrium properties. However, the knowledge of dynamic behavior of the adsorption process is necessary to characterize practical adsorption process. Molecular Dynamics simulation technique is utilized to determine the diffusion properties of the adsorbate confined in the pore of the adsorbent. Few of such observed phenomena include:

(i) self-diffusivity determination of CO_2 adsorbate in coal adsorbent, which led to the permeability determination of coal via calculation of transport diffusivity [55]

(ii) observing cluster formation nature of the confined water molecules in activated carbon across the adsorption - desorption curve [56]

(iii) application of Terahertz frequency-domain spectra to evaluate different motions of adsorbed water molecules by studying the water configurations in MIL-101(Cr) adsorbent obtained from MD simulation [14].

For an improved validity of the simulation results with the corresponding experimental data, the GCMC and MD methods are often hybridized. An MD-based relaxation step is included in certain intervals of the GCMC simulation steps for faster achievement of the energetically minimized configuration of the adsorption system. Few such use cases are provided in these literatures [57, 58]. Apart from the GCMC and MD based molecular simulation techniques, there are few other methodologies available for simulating the adsorption phenomena such as Configurational Bias Monte Carlo (CBMC) [59], and Continuous Fractional Component Monte Carlo (CFCMC) simulation [60].

Adsorption of CO_2 and water in activated carbon

In this section, the adsorption of CO_2 and water adsorbates in the activated carbon using GCMC simulation is discussed. Activated carbon (AC) is a ubiquitous material for application in desiccant dehumidification and post-combustion adsorption-based carbon capture technologies. AC's desirability is attributed to its low production cost (e.g., ability to be produced from biomass), abundance of micropores and the presence of a wide PSD, and low-regeneration energy requirement. Therefore, the characterization of the adsorption performance of AC becomes indispensable for its application. As already discussed in the previous section, the GCMC technique is able to provide in-depth insight of the material characteristics relevant to its adsorption performance. Two of these main characteristics are PSD and surface chemistry. Therefore, a brief overview of the use of GCMC technique to witness the effect of these material properties on the equilibrium adsorption behavior is provided.

The adsorption isotherm shape and maximum uptake capacity of the adsorbent material are mostly influenced by the pore size distribution. Studies on adsorption at the molecular level in activated carbon generally use idealized models of the adsorbent, which may include slit pores made up of graphite walls [61–63], disordered carbon structures that create a range of pore sizes [64–66], cylindrical porous structures represented by carbon nanotubes [67], or a combination of these models. Slit-pore based graphite structure is the most convenient choice for modeling the adsorption process, due to the ease of parametric variation of the pore size. The excess adsorption isotherm trend of CO_2 in graphite slit-pore adsorbent was modeled using the GCMC simulation method, where this trend deviated from the monotonically rising uptake trend with the increasing pressure [68]. Along with the equilibrium adsorption uptake and heat of adsorption, specific observations can be made in the CO_2 adsorbed phase formation in the slit-pore graphite structures. Vishnyakov et al. [69] performed a GCMC and NLDFT calculation of CO_2 adsorption in slit-pore graphite having the pore size between 3 Å and 15 Å at 273.15 K. A general agreement between the adsorption uptake data was found between these two methods for the pore sizes ≤ 6.5 Å and ≥ 8.5 Å. At the intermediate pore sizes, a transition of the CO_2 adsorbed layer was observed in the GCMC simulation. This transition was modeled using a quantity named as density-orientation distribution, which indicated that the adsorbed molecules formed bi-layer configuration from a monolayer configuration between the given pore sizes. Similar study was performed by Samios et al. [70], with an additional determination of PSD of an AC sample by comparing the simulated and experimental isotherm data. Bhatia et al. [71] highlighted the rotation of the adsorbed CO_2 molecules from a parallel to perpendicular orientation in the slit-pore graphite with the increase in pore size. Accordingly, the formation of a third adsorbed layer with pore-surface perpendicular CO_2 molecules at the middle of the pore with pore size of 0.85 nm was observed. The high stability of the 'T'-shaped configuration of the CO_2 molecules was responsible for this excess layer generation. A continuously varying PSD was modeled by developing a wedge-pore graphite structure and the CO_2 adsorption was simulated using GCMC method in the study by Liu et al. [72]. Formation of stepwise adsorption isotherms were observed at subcritical temperature. The alternate packing between commensurate and incommensurate adsorbed phases was responsible for this phenomenon. The isotherm shape was further impacted by the presence of internal graphitic corrugations in the pore, which altered the uniformly varying PSD of the wedge-pore.

The effect of graphitic pore surface functionalization on the adsorption behavior is also widely studied. Generally, the functionalization can be achieved via either the presence of chemical compounds bonded to the graphitic carbon or the doping of impurities in graphite. In their research, Chen et al. [73] investigated how the performance of graphite in capturing CO_2 is impacted by the presence of P, S, O, and N-doped atoms on its surface, across a range of pressures and pore sizes. P-doped graphite was found to offer a high guest-host interaction potential, which resulted in its higher CO_2 adsorption uptake compared to the other doping elements. A GCMC simulation of CO_2/N_2 adsorption in nanoporous carbons consisting of edge-functionalized graphene sheets was carried out by Zhou et al. [74]. The N containing functional groups engendered an improved adsorption selectivity of CO_2 over N_2, due to the decreased net interaction potential between N-based functional groups and N_2. Alkali metals as the doping agent were found to be more effective in improving the CO_2 adsorption uptake capacity and CO_2/N_2 selectivity, compared to the aforementioned O, S, and N-doping of graphite structure [75]. Dang et al. [76] delineated the CO_2/CH_4adsorption behavior in brown coal using GCMC, MD, and DFT simulations. The coal molecular structure consisted of oxygen-containing (methoxy, ether, carbonyl, hydroxyl, and carboxylic), nitrogen, and sulfur-containing functional groups, which acted as strong adsorption sites for CO_2. Khosrowshahi et al. [77] investigated the effect of surface chemistry of the porous carbon C-700 on its CO_2 adsorption performance. Simultaneous presence of graphite-pyridinic nitrogen and carboxyl-hydroxyl groups were found to be the most influential factor impacting the adsorption kinetics. A high CO_2 adsorption uptake capacity was observed for the biomass derived AC, known as OC700, through experimental study by Ma et al. [78]. This behavior was further simulated using GCMC technique, where the AC was modeled as a 3-D random distribution of the graphene flakes containing oxygen-based functional groups on the graphene edges. Therefore, both the PSD and the FG effect were investigated and a relative contribution of 37 % and 63 % were determined for the resultant high uptake capacity, respectively. Similar observation was made by Wang et al. [79], where a hybird GCMC + MD simulation study was perfored for the CO_2 adsorption in AC. The surface chemistry appeared to dominate the textural properties of the adsorbent. Specifically, the COOH functional group exhibited significant increase in the CO_2 selectivity at low pressures, due to the higher electrostatic interactions between the CO_2 and adsorbent. A synergistic effect of narrow micropores and N-doped porous carbon was demonstrated using GCMC and DFT calculations by Wei et al. [80].

Apart from these experimentally observable parameters, viz., adsorption isotherm, isosteric heat of adsorption, selectivity of CO_2 from mixture of gases, and few additional molecular level adsorbed phase parameters were obtained in the literature. Cluster formation and wetting/non-wetting transition of the adsorbed CO_2 molecules on graphene surface was delineated using Molecular Dynamics (MD) and DFT techniques [40, 81]. Adsorption phase local density distribution and angular orientation of the adsorbed CO_2 molecules were also demonstrated using the GCMC simulation techniques [71]. These properties assist in explaining trends in the experimentally observable adsorption properties.

The use of GCMC simulation for characterizing the water adsorption process in graphite adsorbents are abundant in literature. Pristine slit-shaped carbon nanopores are inherently hydrophobic in nature. Ohba et al. [82] showed that a threshold relative pressure value existed till which these hydrophobic nanopores exhibited negligible adsorption uptake. Beyond this cutoff pressure, the adsorption occurred due to the nanoscale cluster formation of the water molecules, owing to the strong hydrogen bond formation among the H_2O molecules. Ohba et al. [53] further demonstrated that the variation in the water cluster formation in the graphite slit-pores lead to hysteresis loop in the adsorption-desorption isotherms, as the pore size increases. Striolo et al. [83] described the pore filling mechanism of water molecules in the hydrophobic carbon slit-pores. They observed that the relative pressure for capillary condensation reduced with the decrease in pore size from 2.0 nm to 0.7 nm, due to the increase in the isosteric heat of adsorption values. However, a 0.6 nm, this cutoff pressure showed a jump to the saturation pressure of water at the given temperature (298.15 K). This contrasting behavior was attributed to the containment of the water molecules in narrower region, giving rise to increased repulsive interactions. Similar conclusions were made by Liu and Monson [84], where they determined the cutoff pore size for the water capillary condensation to occur below its bulk saturation pressure. These studies used GCMC simulation technique to obtain the respective water adsorption behavior. It is to be noted that, the water adsorption isotherm shape in the hydrophobic graphite adsorbent exhibited a type V isotherm shape.

To enhance the hydrophilicity of the carbon-based adsorbents, surface heterogeneity needs to be introduced in the adsorbent pore. Generally, functional groups act as the hydrophilic center for the water molecules. Müller et al. [85] first introduced the use of activated sites to model the hydrophilic interaction of the graphite pores surface for the water adsorption process using GCMC method. They observed the formation of nucleation sites due to the strong interaction potential between the water molecule and the activated sites. Around these nucleation sites, three-dimensional water cluster formation was observed. Different types of pore filling mechanisms appeared depending upon the activated site density and spacing. McCallum et al. [86] demonstrated the impact on the water adsorption in the low-pressure region in the functional group containing functional groups. Both the acidic (e.g., carboxylic) and basic (e.g., pyrone) functional groups were considered for the adsorption analysis. An “effective single group” model was developed where each functional group could interact with a single water molecule. Adopting this technique, the GCMC simulation at very low relative pressures (≈ 0.003), a finite adsorption uptake was realized due to the interaction of water molecules with the energetic sites on the pore surface. Wongkoblap and Do [87] performed the GCMC simulation of water adsorption in a hydroxyl (OH) functional group-based graphite slit-pore. The concentration and position across the graphite box of the OH functional group were varied. High concentration and central position in the graphene surface of the OH FG was found to lower the onset of water adsorption. Unlike the study by McCallum et al. [86], here the OH group was able to interact with multiple water molecules. The hysteresis loop was still observed in the simulation results.

Liu et al. [88] performed GCMC simulation of water adsorption in graphite slit pore with the presence of various functional groups. These groups consisted of carbonyl, hydroxyl, carboxylic, amine, and nitrile. Significant decrease in the threshold pressure for the capillary condensation was observed with the presence of oxygen containing functional groups, especially hydroxyl and carboxyl groups. The strong dispersive and electrostatic interactions led to the increased adsorbent-adsorbate potential value. Therefore, with the increase in the density of the functional groups, the water cluster formation was inhibited. Consequently, water adsorption isotherm type transformed from type V to type I behavior, which is the characteristic of hydrophilic adsorbents such as silica gel and zeolites. This transition was associated with the change in the adsorbed phase formation from clustering to layering of the water molecules. Due to the transition into the type I isotherm behavior, the hysteresis loop also diminished with the increase in the density of functional groups. These configurational details of the adsorbed phase formation was obtained by calculating 2-D density and compressibility distribution from the results of the GCMC simulation. In an earlier study, Liu et al. [89] studied the development of the adsorption - desorption isotherm for water adsorption in hydroxyl (OH) containing graphite slit-pore. The steps involved in the adsorbed phase formation was described by carrying out the adsorption process on a homogeneously arranged OH groups grafted on two pore-mouths of the graphite slit-pore. The hysteresis loop formation was also observed using the GCMC simulation. The difference in the cluster generation around the functional groups between the adsorption and desorption phases was responsible for the hysteresis loop occurrence. In a subsequent study, the effect of bimodal pore size distribution of the graphite slit-pores with the OH functional groups was analyzed by Liu et al. [90]. The effect of pore connectivity was thoroughly investigated on the stepwise water adsorption isotherm behavior.

A comparative analysis among the different types of non-polar and polar adsorbate adsorption on graphene plane was conducted by Do et al. [91]. Water having the highest polarity among other polar molecules considered, exhibited a clustering phenomenon around the strong sites of the graphene. This analysis was carried out based on the Henry law constant and Monte Carlo simulation method. Takamatsu and Ohba [92] performed a GCMC simulation of water adsorption on five types of graphene-related materials. These materials comprised pristine graphene (only carbon atoms), hydrogenated graphene or graphane, and partially oxidized graphene or graphoxide (with 1 %, 3 % and 5 % oxygen atomic ratio). A comparison in the degree of hydrophobicity among these materials revealed the graphoxide with 5 % oxygen atomic ratio to possess the least hydrophobicity. Despite the increased potential well depth magnitude due to the presence of oxygen atom, the graphane is more hydrophobic than the graphene structure. This phenomenon was attributed to the restriction of the adsorbed water molecule orientation for the graphane structure. Kumar et al. [93] demonstrated the water adsorption behavior in N-doped graphite slit-pore and disordered N-doped porous carbon using GCMC simulation technique. Water nanowires/pillars and 3-D water clusters were formed at the nucleation sites induced by the N-doping sites of the carbon. This occurrence was stronger in case of slit-pore graphite adsorbent. The heterogeneity in the disordered porous carbon perturbed such nucleation phenomenon. An increase in the N-doping led to the increased water adsorption uptake at the low pressure.

2.1.2 Thermodynamic characterization

The molecular level investigation of the adsorption process sheds light on the theoretical aspects useful for adsorbent material design and characterization. However, such molecular level insight makes it challenging to obtain the broad macroscopic thermodynamic property values associated to the adsorption process. The description of the phase change process occurring during the adsorption phenomena in terms of macroscopic quantities such as enthalpy, entropy, specific heat capacity, etc. are indispensable for energetic performance evaluation of the bulk adsorption-based systems. Therefore, extensive research has been carried out on the thermodynamic behavior of the adsorption process. Here, a brief historical development of the thermodynamic quantities are highlighted.

Hill [94] and Everett [95] characterized the adsorption process thermodynamics extensively. Young and Crowell [96] summarized these studies to provide a coherent description of the adsorption mechanism. In these studies, the surface thermodynamics was incorporated to describe the adsorption phenomena, since the adsorption phenomena, specifically the physisorption process, occurs via the accumulation of the gaseous molecules on the solid surface of the adsorbent material. The two-dimensional equation of state of the adsorbed layer was described using its spreading pressure and the surface area. Spreading pressure was defined as a thermodynamic quantity representing the pressure exerted on the adsorbent surface solely due to the surface coverage of the adsorbed phase. Furthermore, the adsorbent was considered inert. The adsorbing gas was assumed to follow the ideal gas law. The spreading pressure was correlated with the thermodynamic property of the adsorbed phase, e.g., Helmholtz free energy (F). However, these models resulted in several inconsistencies: (i) spreading pressure cannot be determined via either experimental approach or molecular simulation technique, (ii) this molecular pressure quantity is undefined for the micropores where it deviates from the 2-dimensional adsorbent surface model. Myers [97] applied solution thermodynamics principles to describe the thermodynamic properties for the adsorption of gas mixtures in the microporous adsorbent such as isosteric heat, differential and integral enthalpy, entropy and specific heat capacity. The obtained formulations were shown to be independent of the spreading pressure which is invalid for the adsorption in micropores. An additional quantity named surface potential was proposed to represent the change in chemical potential of the adsorbent. In a subsequent study, Myers and Monson [98] developed the thermodynamic property correlations for the absolute and excess adsorption quantities. The absolute adsorption uptake refers to the total amount of gas present in the pore space of the adsorbent, whereas excess amount denotes only the adsorbed gas due bound to the pore surface of the adsorbent. The absolute adsorption properties are obtained by molecular simulation techniques, e.g., GCMC method. The excess quantities are found out using experimental study. Therefore, a bridge between the theoretical and experimental observations was developed via the adsorption thermodynamic properties in this study. Al-Muhtaseb et al. [99] developed analytical expressions based on the lattice statistics model to study the effect of surface heterogeneity and lateral interactions on the isosteric heat of adsorption and adsorbed phase heat capacity. Despite the theoretical rigor of the thermodynamic properties presented in these studies, the validity of these properties was scarcely addressed. Ismail et al. [100] used the foundations of statistical rate theory to derive the mathematical expressions for the thermodynamic properties (viz. specific volume of the adsorbed phase, q_{st}, c_{ade}, specific entropy and enthalpy). They validated the behavior of the obtained adsorbed phase thermodynamic properties via illustrating their boundaries with respect to gaseous and liquid phase properties. All the correlations were shown to depend upon the molecular partition function of the adsorbed phase, which was translated to the chemical potential of the adsorbed phase via the Langmuir isotherm assumption. This assumption corresponded to the representation of the surface coverage as the ratio of number of molecules and number of adsorption sites in a homogeneous potential distribution. However, when considering the adsorption process in an adsorbent with heterogeneous potential distribution, the given assumption becomes invalid. For these cases, the partition function information is required for the thermodynamic property correlations. However, obtaining this information requires additional statistical thermodynamic treatment of the adsorption system (e.g., molecular simulation). Therefore, a different route for determination of the thermodynamic properties of the adsorbed phase needs to be taken into consideration, whose derivation excludes the adsorption isotherm nature.

The adsorbed phase property correlations, derived from the classical thermodynamic relations, have been widely used in the existing literature. Chua et al. [101] derived the expressions for the thermodynamic property fields of single component adsorbent+adsorbate system as functions of pressure (P), temperature (T), and mass of the adsorbate (m_a). They elucidated a significant deviation in the specific heat capacity of the adsorbed phase from the corresponding gaseous and liquid phase values at a significantly higher pressure or lower temperature. The assumption of the equality between the gaseous phase and adsorbed phase specific heat capacities [97] was invalidated by the latest correlations by Chua et al. [101]. Chakraborty et al. carried out rigorous derivation of the isosteric heat of adsorption (q_{st}) [102] and specific heat capacity (c_{ade}) [103] for the adsorbed phase using classical thermodynamics. The formulation of q_{st} comprised the adsorbed phase specific volume (v_a) and the pressure differential with respect to temperature at constant uptake $\left(\frac{\partial P}{\partial T}\big|_w\right)$. The q_{st} formulation included the isotherm fitting coefficients, when the D-A isotherm equation was implemented. The resultant expression contained an additional gaseous phase pressure differential with respect to temperature. The c_{ade} was represented as the differential enthalpy of the adsorbed phase with respect to temperature at constant uptake $\left(\frac{\partial h_a}{\partial T}\big|_w\right)$, where h_a denotes the adsorbed phase specific enthalpy. This expression was further expanded in terms of the gaseous phase specific heat capacity ($c_{p,g}$) and the temperature differential of the q_{st}. The q_{st} differential is the primary difference between the c_{ade} expressions provided by Chakraborty et al. [103] and Chua et al. [101]). Subsequently, Chakraborty et al. [104] developed a complete thermodynamic model for the adsorbed phase using the classical thermodynamic relations such as Gibbs equations and Maxwell relations. The assumption of chemical equilibrium between the gaseous and the adsorbed phase was invoked to derive the correlation for adsorbed phase entropy (s_a). The specific enthalpy (h_a) formulation was derived using energy balance during the transition from gaseous phase to adsorbed phase.

Rahman et al. [105] used Clausius-Clapeyron equation for the q_{st} formulation, which invoked the ideal gas assumption. They considered the Dubinin-Astakhov (D-A) isotherm equation to represent the q_{st} formulation in terms of the D-A isotherm parameters. The adsorbed phase enthalpy was represented as the difference between the gaseous phase enthalpy and isosteric heat of adsorption in their study. Based on this formula for h_a, they carried out the temperature based differential of h_a to obtain the expression for c_{ade}. Different forms of c_{ade} formulation were obtained for the sub-critical and supercritical temperature operating condition. The isotherm coefficient containing q_{st} expressions derived by Chakraborty et al. [102] and Rahman et al. [105] differed by the presence of excess pressure differential in the formulation given by the former. These different q_{st} expressions and their resulting values were compared in the study by Fatin et al. [106], where the higher values of the Chakraborty et al. [102] correlation than of the Rahman et al. [105] were apparent. The studies on adsorbed phase thermodynamic formalism are summarized in Table 2.2, highlighting the key methodologies adopted and the corresponding limitations.

These thermodynamic correlations for the adsorbed phase properties were used to characterize the adsorption processes involving various adsorbent-adsorbate pairs. Saha et al. [107] performed a thermodynamic analysis of n-butane adsorption in pitch black activated carbon using the isosteric heat of adsorption and entropy/ enthalpy correlations obtained from the studies by Chakraborty et al. [102] and Chua et al. [101], respectively. Rahman et al. [108] used the c_{ade} correlation with ideal gas assumption in formulating the specific entropy and enthalpy for the adsorption of methane on carbonaceous materials based on Chakraborty et al.'s correlations [104]. Singh and Kumar [109] followed the study by Rahman et al. [108] to calculate the adsorbed phase thermodynamic properties for CO_2 - activated carbon material pair. They showed the variation in the c_{ade} characteristics (increasing/decreasing trend with increasing equilibrium pressure) according to the isotherm properties. The same correlations from the study by Rahman et al. [108] (q_{st},c_{ade}) and Chua et al. [101] (s_a,h_a) was used by Pal et al. [110] to perform the thermodynamic analysis of the adsorbed phase CO_2 generated on the biomass derived activated carbon. Rupam et al. [111] obtained the thermodynamic properties of the adsorbed phase for three different refrigerants and two types of activated carbon using the s_a and h_a correlations derived by Chakraborty et al. [104], with simplified correlations eliminating the pressure dependence of the respective properties. They compared different material pairs in terms of the respective properties with variation in the uptake and temperature. In their study, Rocky et al. [112] used thermodynamic property correlations to analyze the adsorption of CO_2 on a composite adsorbent made from activated carbon, polymerized ionic liquid, and PVA as binder. They employed a combination of the improved q_{st} model developed by Azahar et al. [106] and the enthalpy and entropy models proposed by Chua et al. [101]. Ye et al. [113] analyzed the adsorption of HFO-1234ze(E) in Maxsorb III activated carbon, where they delineated the adsorption entropy trend with respect to adsorption uptake. They used the entropy correlations based on the Gibbs free energy formulation ($\Delta G = \Delta H - T\Delta S$, $\Delta G = -RT\ln(P_{sat}/P)$). However, this correlation is valid in the Henry's law region [114], which indicates a linear relationship between the pressure and uptake values at the very low pressure condition. Taking this condition into consideration, Han et al. [115] observed the adsorbed phase entropy variation in the Henry's law region for the initial adsorption phenomena of various light gases and refrigerants on graphite/MOFs adsorbents. Dependence of adsorbent pore width and volume on the adsorbed phase entropy was elucidated in this study.

Table 2.2: Existing studies on adsorption thermodynamic formalism

Works	Methodology	Remarks/Limitations
Chua et al. [101]	The Integral and differential formulations for entropy, enthalpy, and internal energy were developed considering adsorbent and adsorbate as a single system. The specific heat capacity of the system comprising adsorbent and gaseous adsorbate c_p, and isosteric heat of adsorption were formulated.	Reference uptake was taken as zero for calculating thermodynamic surface properties. The adsorbed phase specific heat capacity (c_{ade}) was assumed independent of the adsorbed phase-specific volume.
Chakraborty et al. [104]	The chemical equilibrium between the gaseous and adsorbed phase was used to calculate the specific entropy of the adsorbed phase. The c_{ade} was formulated using a functional determinant-based mathematical tool and the temperature differential of the heat of adsorption was included to the final expression.	An equal specific volume of both the adsorbed and gaseous phase was assumed ($v_a \simeq v_g$) in deriving the c_{ade} expression. The reference uptake value was taken as zero for integral property calculation.

Table 2.2 Continued: Existing studies on adsorption thermodynamic formalism

Rahman et al. [108]	The Dubinin-Astakhov isotherm equation was applied to express thermodynamic properties using isotherm parameters. The heat of adsorption was expressed as the gaseous and adsorbed phase enthalpy difference.	The uptake-based gaseous enthalpy differential was assumed to be the same as the pressure-based differential. Both the adsorbed phase-specific volume and ideal gas assumptions were used for formulating the heat of adsorption.
Ismail et al. [100]	The adsorbed phase specific enthalpy and entropy were derived using the statistical rate theory concept. Adsorbed phase specific volume was included in the respective formulations. Respective thermodynamic property boundaries were clearly illustrated.	Knowledge of molecular particle function (q^s) of the refrigerants is required to calculate the property K included in the thermodynamic property expression.
Walton et al. [116]	Adsorbed phase specific heat capacity expression was elucidated using the path integral of the adsorbed phase specific enthalpy with respect to temperature and uptake. Final expression comprised gaseous phase $C_{p,g}$ and uptake averaged temperature differential of the heat of adsorption.	The integral path used for formulating the adsorbed phase specific heat capacity disregarded the adsorption equilibrium dependency. Reference uptake was considered zero. The ideal gas assumption was used to elucidate the heat of adsorption, used in the derivation of adsorbed phase specific heat capacity.
Schwamberger et al. [117]	The adsorbed phase specific heat capacity was elucidated as an uptake averaged temperature differential of the adsorbed phase specific enthalpy.	Reference uptake was considered zero.
Cambell and Sellers [118]	Entropy of adsorbed phase molecules was defined. The adsorbed molecule entropy values were shown to be higher than that obtained from the classical entropy models (2/3rd of the corresponding gas phase entropy values), which highlighted the contribution of the adsorbate-adsorbate interactions in the adsorbed phase entropy.	The entropy correlation is valid for adsorption in single crystal adsorbent.
Sghaier et al. [119]	Developed the thermodynamic properties of the adsorbed phase using the statistical physics-based principles. Partition function of the gaseous phase and the adsorbed phase were used to characterize the adsorbed phase enthalpy, entropy, and internal energy.	Partition function was derived by considering ideal gas assumption and monolayer formation was considered for the isotherm description.

2.1.3 Adsorption cycle development

Adsorption cooling and desalination cycles

The use of physical adsorption phenomena for generating cooling effect has been prevalent for decades. The basic processes involved in the adsorption cooling cycle are explained in the introduction section. Here, a historical perspective of the adsorption cooling cycle development is illustrated. Sakoda and Suzuki [120] demonstrated the working procedure of the adsorption cooling cycle, through development of an experimental system employing silica gel - water vapor adsorption pair. The adsorption and regeneration temperatures were considered as 293.15 K and 373.15 K, respectively. The use of solar energy in driving the regeneration of the adsorber bed in an adsorption cooling cycle was elucidated by Alsaman et al. [121] using an experimental prototype of the cycle. A specific cooling power (SCP) of 112 $\mathrm{W\,kg^{-1}}$ and coefficient of performance (COP) of 0.45 were obtained by operating the given system at the regeneration temperature of 85 °C. To achieve the usability of the adsorption cooling system in buildings, Chan et al. [122] focused on developing a compact heat exchanger for the adsorber bed. Through the experimental investigation, they showed a drastic increase in the SCP from 106 $\mathrm{W\,kg^{-1}}$ to 377 $\mathrm{W\,kg^{-1}}$ with a better adsorber design at the same working regeneration temperature of 85 °C. Xu et al. [123] developed a desiccant coated heat exchanger-based hybrid adsorption cooling system for effective utilization of the low-grade heat sources, possessing a temperature as low as 70 °C. The corresponding experimental prototype was able to generate 3 kW of cooling capacity with a moderate air-speed of 1.6 $\mathrm{m\,s^{-1}}$. Pan et al. [124] performed a parametric variation of the adsorption cooling cycle performance through experimental investigation. The SCP and COP values exhibited an increase and decrease with respect to the rise in chilled and cooling water temperatures, respectively.

Extensive numerical studies are available to characterize the adsorption cooling cycle, from both the equilibrium and dynamic perspectives. The equilibrium model of the adsorption cooling cycle is used as an effective technique for its parametric performance evaluation with respect to the selection of materials and operating temperature values. Fan et al. [125] demonstrated the use of COP formulation defined for the equilibrium model of the adsorption cooling cycle in revealing its variation with respect to use of different activated carbon adsorbents. The COP was shown to be primarily impacted by the pore size and availability of adsorptive sites in the adsorbent material. The SCP value of the relatively new MOF material called MOF-801 was determined to be $2\,\mathrm{kW\,kg^{-1}}$ in the study by Solovyeva et al. [126]. Rupam et al. [127] further compared different MOFs including MOF-801, aluminium fumarate, and MIL-100(Fe) for water adsorption in terms of SCP and COP. Accordignly, MIL-100(Fe) demonstrated the highest SCP and COP values among the three adsorbents. Loh et al. [128] carried out equilibrium cycle analysis of single-stage and single-effect double stage adsorption cooling cycles. Lower regeneration heat source temperature requirement with improved SCP of the latter was demonstrated. Miyazaki et al. [129] carried out the lumped parameter model-based analysis of a one-bed configuration of the adsorption cooling cycle. They numerically determined its optimal cycle time. Chua et al. [130] presented a transient heat and mass transfer model of the two-bed adsorption chiller and validated the performance results with the commercial adsorption chiller. The effect of the switching and cycle time on the performance parameters was observed. Askalany et al. [131] developed a granular acitvated carbon - R134a based adsorption cooling system and performed the computer simulation of the same. Two concentric tubes were used for designing the adsorber bed in which the inner and outer tubes contained heat transfer fluid and adsorbent material, respectively. Therefore, the lumped parameter model was modified to include the heat transfer occurring in the axial direction of the tubes. Miyazaki et al. [132] simulated and showed that a dual evaporator three-bed adsorption chiller was able to achieve 1.5 and 1.7 times the SCP and COP values than the corresponding two-bed system, respectively. Further details on the adsorption cooling cycles can be found in the review studies by Li et al. [133] and Sidhareddy et al. [134].

The adsorption desalination (AD) cycle follows the same thermodynamic principle as the adsorption cooling cycle. Generally, the AD cycles are known to operate in cogeneration mode, where it simultaneously produces cooling effect and potable water. Therefore, it's also termed as adsorption cooling and desalination cycle. Its theoretical and experimental investigation studies are abundant in the literature. Wu et al. [135] introduced several configurations of the adsorption desalination cycles depending upon the value of evaporator temperature relative to the cooling water temperature. A ranking among the possible AD cycles was conducted with respect to specific energy consumption and fresh water productivity. They further compared the performance parameters of the AD cycle between two modes: desalination only and cogeneration mode. In the subsequent study, Wu et al. [136] developed the experimental setup for the AD cycle and validated the theoretical models obtained in the previous study [135]. Ng et al. [137] numerically simulated an adsorption cooling and desalination system employed waste heat for regeneration. The performance parameters, viz., specific daily water production (SDWP) and specific cooling power (SCP) were validated with the corresponding experimental data. Thu et al. [138] provided estimation of the optimal driving heat source temperature and cycle times of an AD cycle to maximize its SDWP and performance ratio (PR) values. Mitra et al. [139] developed a numerical simulation model to evaluate the transient performance of two-stage four-beds/stage adsorption cooling-cum-desalination system. Later, Mitra et al. [140] implemented an air cooled heat rejection under tropical conditions to drive the adsorption cooling-cum-desalination system utilizing a low-grade heat source (85 °C). In a succeeding study, they [141] developed a experimental prototype of the two stage 4-bed/stage adsorption cooling + desalination system, which consisted of silica-gel + water as its adsorption pair. They provided a detailed description of the system configuration and investigated the performance of the identical beds. In a subsequent study, Mitra et al. [142] improved the transient model for the two-stage adsorption cooling-cum-desalination system by modeling and optimizing the interstage pressure dynamics, which was earlier assumed to be fixed during the simulation. Similar study by Chen et al. [143] presented the energetic performance evaluation and optimization of a four-bed, two-evaporator adsorption cooling-cum-desalination system. The resultant specific daily water production was shown to increase by 13.42 %. Han and Chakraborty investigated the effect of chemical modification of the MOF-based adsorbents on the performance parameters of the AD cycle. In the desorption temperature range of 60 °C to 80 °C and cycle time between 100 s and 1000 s, the simulated value of SDWP for the protonated UiO-66(Zr) MOF exhibited a significant rise to more than 50 m^3 per ton of adsorbent per day [144]. Similarly, OH-functionalized UiO-66(Zr) showed better performance in terms of SDWP of the AD system [145]. A cost analysis of the AD cycle was performed by Alsaman et al. [146], where a composite of silica gel/$CaCl_2$ was utilized as the adsorbent material. Significant water production cost reduction (as high as 60 %) was observed for the use of composite adsorbent over the corresponding raw materials. Detailed review on the adsorption desalination system are provided in the studies by Riaz et al. [147] and Asfahan et al. [148].

Thermodynamic limit of adsorption cycles

The preceding discussion indicates that the adsorption cooling/desalination cycle cooling or desalination capacity is directly proportional to the regeneration heat source temperature. However, the system can exhibit a higher thermal efficiency at lower regeneration temperatures. This improvement in the thermal efficiency is generally obtained via the adoption of multi-bed multi-stage adsorber bed configurations of the adsorption cycles. Furthermore, lowering the regeneration temperature is beneficial for increased utilization of the vastly available low-grade renewable and waste heat sources. Thu et al. [149] achieved a high SDWP value of the 4-bed adsorption desalination system at a regeneration temperature as low as 50 °C. Saha et al. [150] was able to demonstrate an improved thermal efficiency of multi-stage adsorption cooling cycle with its driving heat source temperature as 48 °C. The minimum possible regeneration or desorption temperature of the adsorption cooling/desalination cycles can be obtained from fundamental thermodynamic formalism. [151] developed a correlation for the minimum desorption temperature for the adsorption refrigeration system. This correlation was developed based on the condition of zero throughput from the adsorption process, acting as the compression in the refrigeration cycle. The derivation step included the equality between the minimum and maximum uptake values of the cooling cycle. The Dubinin-Astakhov isotherm equation was utilized for this purpose, resulting in a simple algebraic correlation for the minimum desorption temperature. The formulation is expressed as $T_{des,min} = T_{ad}^2/T_e$, where $T_{des,min}$, T_{ad}, and T_e denote the minimum desorption, adsorption and evaporator temperatures, respectively. The formalism appears to be dependent solely upon the operating temperatures of the adsorption cooling/desalination system. They further considered the effect of void volume of the adsorbent material on the minimum desorption temperature evaluation. In a subsequent study, Saha et al. [150] extended the minimum heat source temperature formulation to consider the multi-stage implementation of the adsorption cooling cycle. They further showed an alternative approach to arrive at the same correlation using the rigor of Boltzmann distribution function and condensation approximation of adsorptive molecules. Srinivasan et al. [152] delineated the adverse effect of the thermal diffusivity in the adsorber bed on the minimum desorption temperature. The new values of the minimum desorption temperature obtained using the modified correlations are found to be higher than the ones obtained by Saha et al. [150, 151] at the same operating conditions. These theoretical models based on equilibrium operation of the cycle was utilized by Mitra et al. [142] to derive the performance limit of the two-stage adsorption cooling system. Here, the entropy generation associated with the heat transfer and finite sorption cycle time were taken into consideration. An expression for the optimum interstage pressure value was determined by using the minimum desorption temperature values for each stage of the adsorption cooling system. Muttakin et al. [153] justified the universal applicability of the temperature based expression of the minimum desorption temperature. The obtained values were compared against the ones resulted from the application of different isotherm models, which were calculated using the numerical uptake balance approach between the minimum and maximum uptake values of the adsorption refrigeration cycle. A separate route for determination of the limiting temperature values associated to the adsorption cooling cycles was demonstrated by Bagheri et al. [154]. They considered a IUPAC type V isotherm equation having a distinct uptake jump at a threshold pressure value. Applying the Clausius Clapeyron equations on the requirement of the adsorption and desorption pressure values, they derived the minimum evaporation temperature and minimum regeneration temperature expressions. The latter was found to be directly proportional to the pressure step value and higher heat of adsorption of the adsorbate. In a subsequent study by Jiang et al. [155], the presence of step-like adsorption isotherm behavior was shown to be favoring the use of lower temperature low-grade heat source in regenerating the adsorption cooling cycle.

Heat and mass recovery schemes

Performance improvement schemes of the existing adsorption cooling and desalination systems encapsulate modification in the system configuration, e.g., incorporating multiple adsorber beds and stages, heat and mass recovery schemes, use of adsorbents with higher adsorption capacity, and changing operating condition of the system. Among these, heat and mass recovery schemes were recommended to be the most effective strategy for thermal performance improvement of the system whilst accounting for the economic costs and practical operability [156]. Wang et al. [157, 158] proposed a passive internal heat recovery mechanism to recover the precooling sensible heat. They experimentally implemented the given heat recovery scheme for the two-bed and four-bed adsorption cooling systems and obtained a COP increment by 38 % and 25 %, respectively [157]. In the subsequent study [158], they compared the proposed passive heat recovery scheme with the existing Nishiyodo water circulation based heat recovery scheme, and found both of these to ameliorate the thermal performance of the adsorption systems by equivalent amount. Thu et al. [159] implemented an evaporator-condenser coolant “run-around" circuit based internal heat recovery mechanism to develop an advanced AD system. They also developed an experimental prototype of the AD system with heat recovery in their succeeding study [160]. The proposed was extended to the two and four bed AD cycles and obtained the corresponding improved performance parameters through numerical simulation [161, 162]. The water production rate was shown to increase by as high as two to three times of the same produced by the conventional AD cycle. In the study by Thu et al. [162], two different types of condenser-evaporator heat recovery configurations were proposed, which included a “run-around” circuit between these components and encapsulated condenser-evaporator unit. In the succeeding study, Thu et al. [149] implemented the internal heat recovery mechanism for the master-slave configuration-based AD system. The heat source temperature was reduced to as low as 50 °C by the proposed heat recovery-based system.

Before proposal of the heat recovery schemes, Wang et al. [163] had introduced the mass recovery schemes between the adsorber beds. This performance improvement scheme was proceeded with the connection of the adsorbed beds, thereby realizing a pressure equalization between these. Akahira et al. [164, 165] introduced additional heating/cooling mechanism to enhance the mass recovery based sorption processes. They highlighted the improved cooling capacity with the mass recovery compared to the adsorption system without one. Furthermore, this recovery scheme was more effective with lower regeneration temperature. This mass recovery scheme was implemented for two-bed adsorption cycle [164] and four-bed adsorption system with cascading chilled water configuration [165]. Thu et al. [166] developed a numerical model to determine the optimum mass recovery time for the adsorption cooling and desalination system. A degradation in the positive effect of the mass recovery was highlighted if the optimum mass recovery time was exceeded in the adsorption system operation. These heat and mass recovery schemes were also integrated to ameliorate the AD cycle performance further. Muttakin et al. [167] found out the optimum heat and mass recovery times for a given operating temperature values of regeneration, evaporation, and adsorption in an adsorption cooling cycle. Amirfakhraei et al. [168] presented an advanced heat and mass recovery scheme for the adsorption desalination system, where both the condenser-evaporator and adsorber-evaporator heat exchanges were performed. The resultant water production rate and performance ratio were shown to improve by 200 % and 51 %, respectively.

Heat upgrading cycles

As highlighted in the introduction section, the heat upgrading cycles can be classified into two categories based on the type of preheating of the adsorber bed. These categories are known as (i) isosteric preheating phase and (ii) non-isosteric preheating phase. Aristov Y. [169] introduced the isosteric preheating phase-based heat upgrading cycle. This cycle was applied to generate useful heat with commercial value from a low ambient temperature. Therefore, it was termed as "Heat from Cold" (HeCol) cycle. The consideration of the inexhaustible natural thermal reservoir as the heat source for the HeCol cycle rendered its thermal efficiency meaningless. The ambient temperature ranged from 2 °C to 20 °C. For these temperatures, the condenser temperature was taken as low as −70 °C. Therefore, the applicability of this cycle was rather restricted in the countries with cold climate. In a subsequent study, a lab-scale prototype of the HeCol cycle was developed by Tokarev et al. [170]. The optimal adsorption material pair was determined based on the Dubinin adsorption potential formulation. This was followed by the operation of the prototype with CaClBr/SiO_2 and methanol as the adsorption material pair. The preheating phase was driven by the high-temperature thermal reservoir at the temperature T_H, which resulted in the isosteric nature of this phase. With the heat source temperature between 10 °C and 25 °C, and heat sink temperature as −20 °C, the heat was upgraded to 32 °C to 49 °C. In a latter study, Aristov Y. [171] summarized the state-of-the-art of the HeCol cycle in terms of its thermodynamic efficacy and practical feasibility. An S-shape isotherm was recommended for its high useful heat production. A threshold temperature lift was shown to exist, beyond which the cycle could not provide any useful heat. Furthermore, entropy generation in the HeCol cycle was demonstrated to be lower than the temperature controlled adsorption cycles. A theoretical analysis was performed for similar isosteric preheating/precooling-based adsorption heat transformer cycle by Hamamoto Y. [172]. The dependence of the preheating energy requirement on the specific heat capacity of the adsorption reactor materials was illustrated. The useful adsorption heat supply was shown to be inversely proportional to the said heat capacity. Furthermore, the author depicted an internal heat recovery mechanism to improve the cycle's heat upgrading performance. Frazzica et al. carried out a parametric investigation of the HeCol cycle with respect to the presence of heat recovery, the temperature difference between the working fluid and heat transfer fluid, and 10 different adsorption material pairs. The given temperature difference led to poorer heat upgrading performance of the HeCol cycle, which was rather improved by the use of composite adsorbents.

Unlike the HeCol cycle, the studies on the non-isosteric preheating process-based heat upgrading adsorption cycles are rather limited in the existing literature. Chandra and Patwardhan [173] first introduced the adsorption heat transformer (AHT) cycle with non-isosteric preheating and precooling phases. Zeolite-water vapor was considered as the adsorbent-adsorabte pair. Three types of configurations were proposed for the AHT cycle, which are listed as follows: (i) 2-tank system (intermittent cycle operation), (ii) 3-tank system (continuous cycle operation), (iii) 4-tank system (sensible heat recovery implementation). In first two configurations, a single adsorber bed was present, along with the hot and cold water reservoirs. In the 4-tank system, two adsorber beds were present with an internal heat exchanger between them. The gross temperature lift (GTL) from these systems was achieved as high as 50 °C. Furthermore, the GTL could be seen increasing with the rise in waste heat source temperature. where they presented three different configurations for the AHT cycle. The maximum COP values were within the span of 0.5 to 0.6. Seo et al. [174] performed a performance analysis of the equilibrium AHT cycle considering activated carbon-refrigerant pairs as the adsorption working material. They neglected the non-isosteric behavior of the preheating process from the calculation scheme of the useful adsorption heat of the AHT cycle. Similar observation as the originating study was observed for these adsorbent-adsorbate pair, where the useful heat amount increased with the increasing waste heat source temperature. Engelpracht et al. [175] developed a dynamic model of the AHT cycle for upgrading the waste heat from temperature 90 °C to 110 °C. They designed and optimized the adsorber heat exchanger to obtain high exergetic COP and specific heating power. They considered a closed-loop configuration of the AHT cycle, which is not applicable as a potable water producer.

2.2 Hybrid adsorption desalination systems

In the preceding section, a detailed description on the adsorption based cooling, desalination, and heating systems is provided. Due to limited commercialization, these techniques are regarded as the emerging technologies in their respective industries. The commercially available desalination technologies can be divided into mainly two categories viz., (i) thermal desalination technologies and (ii) membrane-based desalination technologies. In a membrane-based desalination technique, an external pressure is applied on the saline water to force it through a permeable membrane, thus leading to the separation of the salt from the water. Despite its high potable water production capacity, the membrane is expensive in nature along with its low cyclic stability. The thermal desalination technologies, as the name suggests, utilizes thermal energy to separate the salt from the saline water via its evaporation and subsequent condensation. Two major technologies hold the largest market share in this category, viz., multi-effect distillation (MED) [176] and multi-stage flash distillation (MSF) [177]. Few other emerging thermal desalination technologies include Humidification and Dehumidification (HDH) [178] and thermally driven membrane desalination (MD) [179]. An MSF system works on the principle of flashing of pressurized and heated feedwater through a series of flashing chambers, which can amount from 4 to 40 stages. Due to high operating temperature, the corrosion of the components is a crucial problem in the MSF systems. In an MED system, the feedwater is evaporated in a series of effects, where the condensation energy released in one effect is used to evaporate the resultant brine in the next effect. The MED system is advantageous than the MSF process due to its lower top brine temperature (TBT), which can be as low as 70 °C. However, in both of these systems, the thermal energy is supplied generally from the fossil fuel-based cogeneration power plant, due to their high energy consumption for driving the desalination process. Consequently, the greenhouse gas emissions and the resultant global warming are exacerbated. A hierarchical visualization of the classification of both the existing and emerging desalination technologies has been provided in the study by Youssef et al. [180].A detailed analysis and comparison of the major desalination technologies has been provided in the study by Shahzad et al. [181] from the perspective of typical size, capital cost, energy consumption, water cost, technology trend, environmental impact and water quality. Adsorption desalination (AD) technology is able to utilize low-grade waste heat and renewable energy efficiently to produce potable water from saline water. Hybridization of the conventional thermal desalination technologies with the AD systems is being adopted as an attractive solution to the global warming crisis. Few key investigations related to this hybridization methodologies are listed in Table 2.3.

Table 2.3: Existing studies on the hybridization of adsorption desalination with various thermal desalination technologies

Desalination system	Remarks	Reference
Multi-effect distillation + AD	Numerical modeling and Lab scale prototype development of the hybrid MEDAD system was performed. Gain output ratio (GOR) improvement was observed from 5.9 to 8.8 with the hybridization of these systems.	[182, 183]
Vacuum membrane distillation + AD	Water production rate and water recovery ratio were shown to enhance by 21 % and 23 % respectively for the 24-stage solar-assisted VMD + AD system compared to standalone VMD system through numerical simulation	[184]
Mechanical vapor compression (MVC) + AD	Higher SDWP, COP and SCP achieved than the AD system. SDWP and SCP values were found as $14\,\mathrm{m^3\,d^{-1}}$	[185]
Ejector + AD	Ejector was proposed to be installed before the condenser of the AD cycle. Through the theoretical investigation, an improved SDWP of $16\,\mathrm{m^3\,d^{-1}\,t^{-1}}$ and $40\,\mathrm{m^3\,d^{-1}\,t^{-1}}$ of silica gel was achieved with and without heat recovery respectively, at regeneration temperature of 95 °C.	[186]
Ejector + HDH + AD	The AD system was integrated with HDH system and two ejectors. Theoretical investigation was performed with and without evaporator-condenser heat recovery incorporation. The SDWP of this hybrid system was found to achieve $83.1\,\mathrm{m^3\,t^{-1}}$ of silica gel.	[187]

Ahmed et al. [188] and Goh et al. [189] provided extensive review on the hybridization methodologies adopted among the AD system and other conventional desalination systems.

Among the various thermal desalination technologies available, the MED system was found to exhibit the best performance in terms of energy efficiency and water production rate [190]. Further improvement in its performance parameters were attempted via the use of thermal-vapor compression (TVC) systems [191], integration with absorption heat pump [192] and heat transformer systems [193], incorporation of falling film type evaporation devices, and thermoeconomic investigation [194]. The temperature difference between the first and last effects of the MED system was identified as a key parameter for improving its energetic performance. These two temperatures are denoted as top brine temperature (TBT) and bottom brine temperature (BBT), respectively. For a fixed value of the inter-effect temperature, the temperature difference between TBT and BBT determines the required number of effects in the MED system. Both the theoretical and experimental performance evaluation of the MED system revealed the proportional relationship between the number of effects and the energetic performance parameter named performance ratio (PR). Therefore, studies on the hybridization of the adsorption desalination technology with the MED system are focused upon increasing the given temperature difference. Thu et al. [195] proposed a methodology to expand the temperature range of TBT and BBT via hybridization of the AD and MED system. The condensing temperature or BBT was lowered to 5 °C through the vapor extraction from the last effect of the MED system using the AD system. Therefore, a cascaded configuration of the MED + AD system was obtained. Consequently, a twofold elevation in the water production capacity was observed in the hybrid system compared to the standalone MED system. Notably, the number of effects was maintained constant while increasing the working temperature range of the hybrid desalination system. In a subsequent study by Thu et al. [182], the number of effects was increased to further ameliorate the water production rate and gain output ratio. These studies primarily presented a numerical simulation-based performance characterization of the proposed hybrid desalination system. Shahzad et al. [196] demonstrated a lab-scale prototype of the hybrid MEDAD system, where the improvement in the water production rate was experimentally conformed to the previously developed theoretical models. Ng et al. [197] provided a detailed documentation of the hybrid desalination system, along with its comparison with the other technologies available from energetic and exergy-economic perspectives.

Few deductions can be made from the given analysis: (i) two separate heat sources were incorporated for provide the requisite evaporation energy to the MED system and the regeneration energy in the AD system, (ii) the available configurations only accounted for the integration of the AD system to the last effect of the MED system, resulting in only reduction in the condensation temperature of the hybrid system, (iii) due to the cascading nature of the hybrid configuration, only downgrading of the heat source was performed. Incorporation of two heat sources in the hybrid system introduces an adverse effect on the net performance ratio of the system, when both the thermal and electrical energies for the parasitic pumping are taken into consideration. Therefore, to resolve this issue, Thu et al. [198] proposed an innovative hybridization between the MED and AD systems, which was termed as multi-effect adsorption desalination (MEAD). The proposed system utilized only a single low-grade heat source for the hybrid system, whose temperature was taken as low as 55 °C. Furthermore, the evaporation-condensation processes in the effects were carried out at very low temperatures (<35 °C), whilst maintaining high values of the performance parameters such as PR and WPR. The synergy between the MED and AD components was achieved via kinetic energy of the desorbed vapor for multiple evaporation and condensation process in the hybrid system. For the latter two deductions, utilization of a heat upgrading cycle is envisaged for providing the necessary heat of evaporation to the first effect of the MED system.

2.3 Summary

The presented literature survey on the adsorption phenomena can be summarized as follow:

(i) The molecular level investigation of the adsorption process of various types of adsorbent-adsorbate pairs are abundant in the literature. Yet, the studies on the activated carbon are fewer than the MOF-based adsorbents. Moreover, the parametric variation of the adsorption properties with respect to specific pore size values and type of functional groups have rarely been addressed.

(ii) Several models for the bulk thermodynamic properties of the adsorbed phase have been developed based on classical and statistical thermodynamic principles. However, there has been a lack of careful investigation on the validity of the proposed thermodynamic model with respect to the known properties of the pure adsorbate gases.

(iii) The adsorption cycle development has mainly been focused on the application of cooling and desalination. Conversely, the heat upgrading cycles have rarely been carefully investigated in the existing literature. The use of heat upgrading adsorption cycles can be extended to desalination and performance improvement of existing thermal energy consuming systems. However, no such investigation has been attempted.

The current thesis attempts to address these key research gaps. Furthermore, the present work tries to highlight the synergistic dependency among the microscopic and macroscopic aspects of the adsorption phenomena.

Chapter 3

Molecular level investigation of adsorption phenomena

The length-scale of the pores in which the adsorbed phase is generated can range from ultra-micropores (<20 Å) to mesopores (20 Å to 500 Å). These values are equivalent or lesser than the mean free path of the gaseous adsorbate. Thus, the intermolecular interaction based evaluation of the adsorption process can delineate the influence of the material properties and the pore surface chemistry on the adsorption performance. In this chapter, the principles of the GCMC simulation technique is established, which include the interaction potential, simulation conditions, and type of molecules involved in the simulation. Few examples related to the adsorption of different types of gases are provided to highlight the capability of the GCMC simulation. This section is followed by the investigation of the CO_2 adsorption in activated carbon, to elucidate the effect of pore size distribution and surface chemistry on the adsorption properties.

3.1 Grand Canonical Monte Carlo simulation of adsorption process

Grand Canonical Monte Carlo simulation is a ubiquitous probabilistic tool to obtain the equilibrium adsorption properties such as adsorption isotherm and isosteric heat of adsorption. This simulation technique evaluates the intermolecular interaction among the adsorbate and adsorbent particles and applies statistical thermodynamic principles to perform the adsorption.

3.1.1 Intermolecular interactions

The intermolecular interaction among the adsorbate and adsorbent particles can be described by two components: (i) short-range dispersive interaction, (ii) long-range electrostatic interaction. The short-range dispersive interaction is associated to the induced dipole-dipole interaction between two atoms or molecules. This type of interaction is always present for both polar and non-polar molecules. The dispersive intermolecular interaction is alternatively known as the van der Waals (vdW) interaction. The vdW potential is attractive in nature, which is inversely proportional to the intermolecular distance ($U^{vdW} \approx -C/r^6$). However, at a low separation between the molecules, the nuclear and electronic repulsions begin to dominate the attractive vdW potential [199]. Thus, net vdW potential is a culmination of repulsive and attractive interactions. This phenomenon is mathematically formulated using the empirical correlation known as the Lennard-Jones (L-J) potential. The L-J potential is represented using the following equation:

$$U_{ij}^{vdW} = 4\epsilon_{ij}\left[\left(\frac{\sigma_{ij}}{r_{ij}}\right)^{12} - \left(\frac{\sigma_{ij}}{r_{ij}}\right)^{6}\right] \tag{3.1}$$

Here, the term U_{ij}^{vdW} denotes the intermolecular van der Waals potential between two particles (atoms or molecules) i and j, whose unit is K. This quantity is a function of the intermolecular distance (r_{ij}). The coefficients ϵ_{ij} and σ_{ij} denote the potential well depth and pairwise collision diameter. The nature of the vdW interaction is attractive-repulsive depending upon the intermolecular distance. This characteristic is depicted in Fig. 3.1.

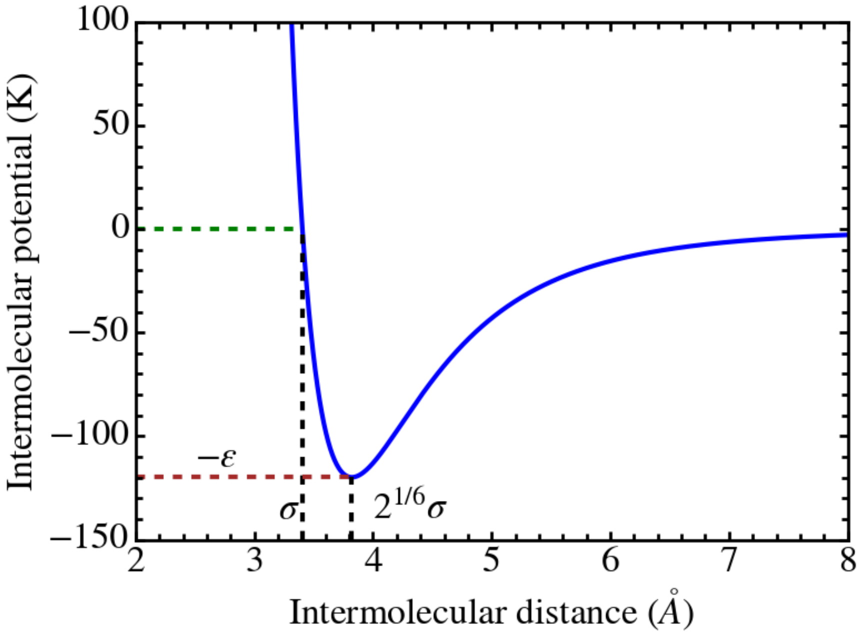

Figure 3.1: Lennard-Jones potential variation with the intermolecular distance for two Argon molecules

It can be seen that the value of U_{ij}^{vdW} is positive as the intermolecular distance is less than the value σ_{ij}. The 12th power of the ratio $\frac{\sigma_{ij}}{r_{ij}}$ governs the repulsive interaction. As the separation between the particles become greater than the collision diameter σ_{ij}, then the vdW potential possesses negative values, indicating the attractive interaction. Eventually, the potential value reaches a minimum at the intermolecular distance $r_{ij} = 2^{1/6}\sigma_{ij}$, which is equal to the ϵ_{ij}. The intermolecular potential increases with the further rise in the distance, however, only the attractive potential occurs between the molecules. In Fig. 3.1, two argon (Ar) molecules are considered, where the LJ potential parameter values are σ_{Ar-Ar} =3.405 Å and ϵ_{Ar-Ar} =119.84 K. It is to be noted that, the ϵ_{ij} value is usually calculated by dividing the potential value in J mol^{-1} by Boltzmann constant (k_B) whose unit is J K^{-1}. Thus, both the energetic parameter and the potential value are expressed in units of K. The L-J potential parameters are obtained from either *ab-initio* calculations of the interatomic interaction or by validation with the experimentally observable properties such as vapor liquid equilibrium and adsorption isotherm. Accordingly, the potential parameters for the Ar atom is obtained from the study by Perry et al. [43]. Here, the particles i and j both correspond to Ar atom. The vdW potential parameters for two hetero-atoms can be calculated by using Lorentz-Berthelot mixing rule. This rule is expressed as follows:

$$\begin{cases} \epsilon_{ij} = \sqrt{\epsilon_{ii}\epsilon_{jj}} \\ \sigma_{ij} = \dfrac{\sigma_{ii} + \sigma_{jj}}{2} \end{cases} \tag{3.2}$$

Here, the energetic L-J parameter of the hetero-atoms is calculated as the geometric mean of the self-interaction energetic parameters. Likewise, the distance parameters consider the arithmetic mean of the self-interaction distance parameters.

The electrostatic interaction is defined as the Coulombic interaction between the partial charges of the atoms or molecules. The resultant Coulombic potential between partial charges are determined as follows:

$$U_{ij}^{elec} = \frac{q_i q_j}{4\pi\varepsilon_0 r_{ij}} \tag{3.3}$$

Here, U_{ij}^{elec} stands for electrostatic potential between particles i and j, q_i denotes the partial charge value of the particle i, and ε_0 is the free space permittivity. If the charges possess opposite polarity, then the attractive interaction is generated. Likewise, two alike charges result in the repulsive potential. The total intermolecular potential is denoted by the summation of the vdW and Coulombic potential terms. Subsequently, the total potential of the molecular system containing a finite number of atoms/molecules is calculated by pairwise summation of the vdW and electrostatic potentials. This expression is given as:

$$U^{total} = \sum_{i,j \forall i<j} \left(U_{ij}^{vdW} + U_{ij}^{Elec} \right) \tag{3.4}$$

3.1.2 Adsorbent and adsorbate models

As discussed in the literature review section, the molecular simulation technique is widely used to obtain the adsorption properties for various classes of adsorbents and adsorbates. The adsorbents can be broadly classified as the (i) silica gel, (ii) zeolites, (iii) metal-organic frameworks (MOF) (iv) covalent organic frameworks (COF) (v) activated carbon (graphene, graphite, and amorphous) In this section, a brief overview on the molecular structure of the zeolites and MOFs are provided. A detailed molecular structure of the graphite-based activated carbon model is delineated in the following section. Fig. 3.2 shows the crystallographic structure of the one zeolite and two types of MOF adsorbents.

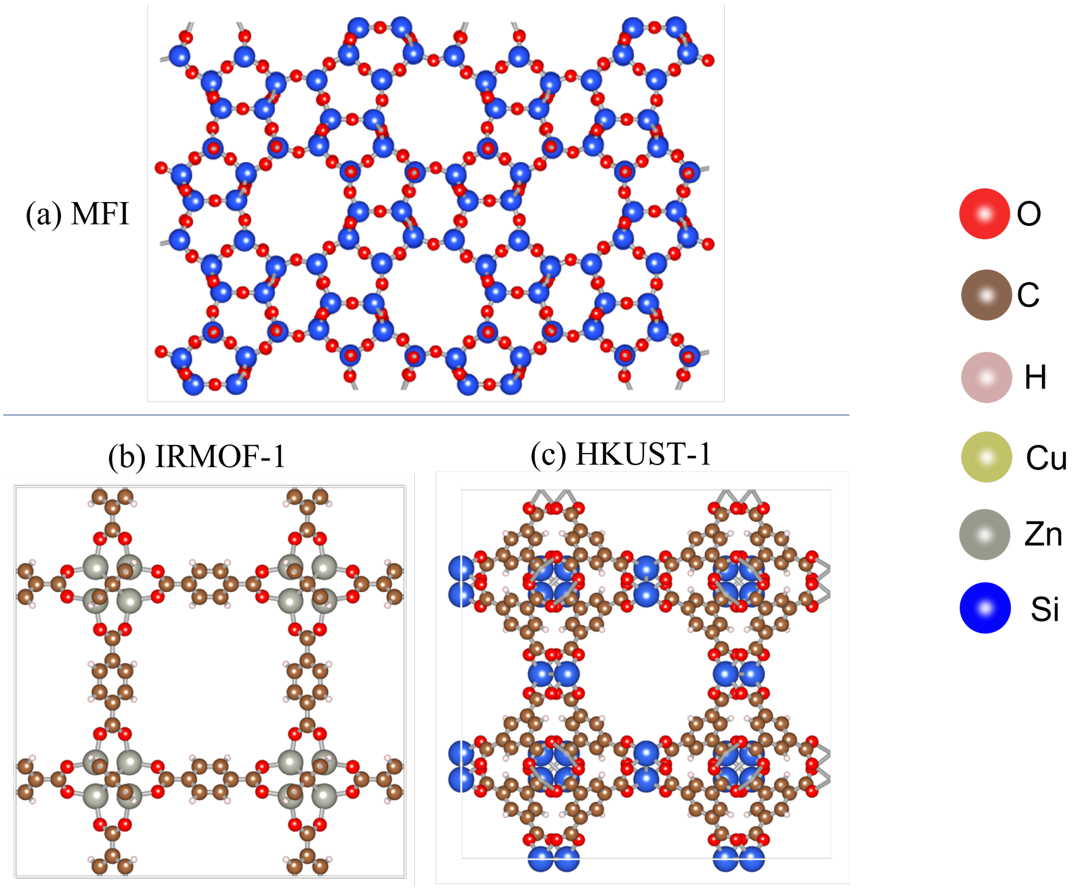

Figure 3.2: Crystallographic structure of three types of adsorbents: (a) MFI-type all-silica zeolite and two MOFs, viz., (b) IRMOF-1, and (c) HKUST-1

The crystallographic structure of the MFI-type zeolite (also known as silicalite) is provided by the following study [200]. This pure silica-type zeolite consists of Si and O atoms, whose alternate bonding structure creates the circumference of the linear and zig-zag pore channels. The unit cell lattice parameters are $20.022\,\text{Å} \times 19.899\,\text{Å} \times 13.383\,\text{Å}$ in the x, y, and z directions, respectively. The diameter of the pore channels is approximately $5.4\,\text{Å}$, which implies that the any molecule with its collision diameter as $5.4\,\text{Å}$ is able to occupy the pore channel. The number of O and Si atoms in a unit cell are 192 and 96, respectively. This densely packed crystal structure leads to low pore volume of $0.168\,\text{cm}^3\,\text{g}^{-1}$ with a low void fraction (available pore volume compared to the unit cell volume) of 0.31. The MFI structure can exist in three distinct crystal form: (i) monoclinic, (ii) Pnma, (iii) $P2_12_12_1$ orthorhombic. Here, only the orthorhombic structure is considered for the adsorption molecular simulation.

Metal-organic frameworks (MOF) are crystalline structures which are constituted by metal clusters/nodes and connecting organic linker molecules. Here, two MOFs are considered for adsorption analysis, viz., IRMOF-1 and HKUST-1. Isoreticular metal organic framework (IRMOF) materials consist of zinc (Zn) - oxygen (O) based metal clusters which are connected by the carboxylate-terminated linkers. The linker present in IRMOF-1 structure is 1,4-benzene dicarboxylate (BDC) molecule. Large cubic pore space is generated by the aforementioned configuration as shown in Fig. 3.2c. Therefore, the IRMOF-1 structure possesses a high void fraction of 0.81. This value is significantly higher than the MFI-zeolite void fraction. The molecular structure was presented in the study by Eddaoudi et al. [201]. Cu-BTC or commonly known as HKUST-1 is a copper containing MOF with benzene-1,3,5-tricarboxylate as its linker molecules. It also generates a cubic crystal structure with unit cell dimension of 26.343 Å in all three directions. The crystallographic structure is obtained from the study by Chui et al. [202]. The metal cages are formed by two Cu atoms, each bonded to four O atoms. The pore diameter of these metal cages is approximately 5 Å. The remaining porous region attains a bimodal pore size distribution of 11 Å at the center and 13 Å at the faces. Therefore, three distinct regions of adsorption sites are generated in the HKUST-1 unit cell. The void fraction is also equivalent to the IRMOF-1 structure, holding a value of 0.77 approximately. The crystal structure belongs to the 'Fm-3m' symmetry space group. A comprehensive description of the material properties of these three crystal structures are tabulated in Table 3.1. These values are calculated using the iRASPA software [203] which calculates the pore characteristics using a probe molecule such as N_2. The L-J potential parameters of the adsorbent molecules are generally obtained

Table 3.1: Structural properties of the MFI zeolite, IRMOF-1, and HKUST-1 adsorbents obtained from the respective molecular structures using the iRASPA software [203]

Property	MFI zeolite	IRMOF-1	HKUST-1
Density ($\mathrm{kg\,m^{-3}}$)	1796.34	593.31	879.09
Helium void fraction (-)	0.303	0.82	0.774
Accessible pore volume ($\mathrm{cm^3\,g^{-1}}$)	0.168	1.382	0.88
Gravimetric surface area ($\mathrm{m^2\,g^{-1}}$)	708.57	3661.9	2547.87

Table 3.2: Force field parameters of the MFI zeolite and IRMOF-1 and HKUST-1 MOFs

Adosrbent	L-J parameters (ϵ in K, σ in Å)	Partial charges (unit electron charge)	Reference
MFI	ϵ_{Si}=22, σ_{Si}=2.30 ϵ_O=53, σ_O=3.30	q_{Si}=-0.75 q_O= 1.5	TraPPE-zeo [37]
IRMOF-1	ϵ_{Zn}=62.40, σ_{Zn}=2.46 ϵ_O=48.16, σ_O=3.03 ϵ_C=47.86, σ_C=3.47 ϵ_H=7.65, σ_H=2.85	No charge used for methane gas	DREIDING [204] UFF [205]
HKUST-1	ϵ_{Cu}=2.52, σ_{Cu}=3.11 ϵ_O=48.16, σ_O=3.03 ϵ_C=47.86, σ_C=3.47 ϵ_H=7.65, σ_H=2.85	q_{Cu}=1.248 q_O=-0.624 q_C=0.494, 0.13, and -0.156 q_H=0.156	DREIDING [204] UFF [205] charge values from Perry et al. [43]

through fitting the experimental adsorption isotherm data and/or first principle DFT calculation [15]. Typically, there are two widely utilized databases for describing the L-J interaction potentials of the MOFs, which are DREIDING and UFF (Universal Force Field) models. An all-atom L-J parameter database called TraPPE-zeo is popular to model the molecular interactions of the zeolite adsorbents (including all-silica zeolites). The partial charge distribution in the adsorbent molecules is determined using either first-principle based calculation scheme (DDEC, CBAC, CHELPG, and REPEAT) or ionization energy based model such as charge equilibration (Qeq) and extended charge equilibration (EQeq) methods. The complete set of these force field parameters are given in Table 3.2.

The adsorbates are generally classified as (i) inert gas (Ar, Xe, Kr, etc.), (ii) non-polar gases (N_2, O_2,CO_2,CH_4, etc.), (iii) polar gases (H_2O,NH_3). The inert gas molecules are monoatomic and there is no net charge. Thus, inert gas molecule is modeled as a spherical particle with a single L-J interaction center. Non-polar gas molecules can contain either single atom or multiple atoms. Bi-atomic molecules such as N_2, O_2 contain the two L-J interaction centers. In case of tri-atomic molecules, e.g., CO_2 and SO_2, there are three L-J interaction centers. The net partial charge of these molecules amounts to zero. However, each individual interaction center contains a finite partial charge. The charge distribution across the different interaction centers is maintained such that there is no net dipole moment induced in any particular direction. For instance, two equal negative charges are placed on two oxygen atoms at the opposite ends of a CO_2 molecule. A positive charge with twice the magnitude of each negative charge is placed at the central carbon atom of the CO_2 molecule. In case of bi-atomic molecules, a dummy electrostatic interaction center is placed to negate the charges placed at the two atoms of the molecule present at its opposite ends. It is to be noted that this non-polar nature of the adsorbate molecule is maintained during the molecular simulation, when the molecules are considered rigid. A rigid molecule does not exhibit any intramolecular interaction such as bond stretching, bond bending, and harmonic oscillation of the bonds. In case of methane (CH_4) molecule, the molecular structure is generally considered as a single spherical particle, instead of five atoms as per its molecular formula. However, negligible differences in the adsorption isotherms between the united-atom model and the all-atom model of CH_4 gas was observed in the existing studies [206]. In this study, three adsorbates are considered for the adsorption process, viz., Ar, N_2, and CO_2. These gases represent the inert gases and the non-polar gases (both bi-atomic and tri-atomic). The structural information and the force field parameters are provided in the Table 3.3. It is to be noted that the force field values of the N_2 and CO_2 molecules are obtained from the Transferable Potentials for Phase Equilibria (TraPPE) database. These data are derived by fitting the molecular simulation results with the corresponding vapor-liquid

Table 3.3: Force field parameters and structural details of the gaseous adsorbate molecules

Adsorbates	L-J Parameters (ϵ in K, σ in Å)	Partial charges (unit electron charge)	Reference
Ar	$\epsilon_{Ar} = 119.84$, $\sigma_{Ar} = 3.405$	No charge	[207]
CH_4	$\epsilon_{CH_4} = 158.5$, $\sigma_{CH_4} = 3.72$	No charge	[208]
CO_2	$\epsilon_C = 27.00$, $\sigma_C = 2.80$ $\epsilon_O = 79.00$, $\sigma_O = 3.05$	$q_C = 0.7$ $q_O =$ -0.35 $d_{C-O} = 1.16\,$Å $\theta_{O-C-O} = 180°$	[209]

equilibrium data.

3.1.3 Simulation method

The Grand Canonical Monte Carlo (GCMC) simulation technique is used to obtain the equilibrium adsorption properties. In statistical mechanics, a Grand Canonical ensemble refers to the molecular system present at a constant chemical potential (μ), volume (V) and temperature (T), which is also known as the μVT ensemble. The system exchanges particles with an imaginary particle reservoir. The amount of the particles present in the system is determined by the given constant parameters (μ, V, and T). In an adsorption system, the particles denote the adsorbate molecules. The system or the simulation domain consists of the adsorbent crystal structure, which is assumed to be rigid during the simulation. In the GCMC simulation, the adsorbate particles are randomly inserted, removed, translated, and rotated (for CO_2 molecule) in the simulation box with equal probabilities. These actions are termed as the Monte Carlo (MC) moves. The intermolecular interaction potential is calculated among the adsorbate-adsorbate and adsorbate-adsorbent particles using the force field formulations described earlier. Based on the calculated total potential, each MC move is either accepted or rejected based on an acceptance probability. This acceptance probability is calculated using statistical mechanics principles [59]. This process is iterated until the number of adsorbate particles in the simulation box becomes constant (approximately, within an acceptable error range). The total number of attempted MC moves in each iteration is the maximum between 20 moves and the total number of adsorbate particles present in the simulation box. The simulation is begun with 25000 to 50000 number of initialization cycles. In case of CO_2 molecule adsorption, a higher value of number of initialization cycles are considered due to the presence of additional electrostatic interaction, unlike CH_4 and Ar molecules. During this initialization period, the equilibration of the adsorbed particles is achieved in the simulation box. This phase is followed by the sampling stage, where the number of adsorbed particles and the system energy are averaged over the samples obtained. This averaged quantity is also known as the ensemble average. The adsorption properties are calculated from these ensemble average values. The sampling stage is continued for 50000 cycles.

To mimic the macroscopic behavior of the adsorption process in the molecular simulation, a periodic boundary condition (PBC) is considered in the simulation domain. In this approach, replica of the simulation box is considered at the boundaries across the x, y, and z directions. Each MC move is equally performed in all the replicas of the simulation. During an MC translation move, if the particle leaves the simulation domain, the PBC ensures that the same particle is reinserted in the domain. Additionally, it can be seen that the magnitude of L-J attractive potential gradually decreases with the increase in intermolecular distance. If the number of adsorbed molecules in the simulation box is large, then the computational cost becomes expensive if all the molecules are considered for intermolecular interaction calculation. Due to the declining nature of the L-J potential, a cut-off distance is considered for calculation of L-J potential for each molecule.

Thus, the calculation of the L-J potential follows Equation (3.5)

$$U_{ij}^{vdW} = \begin{cases} U_{ij}^{vdW}(r_{ij}) & r_{ij} \leq r_c \\ 0 & r_{ij} > r_c \end{cases} \tag{3.5}$$

Only the nearest molecules present within the cut-off radius are considered to calculate the L-J potential, which includes the periodic images. Therefore, the minimum image convention (MIC) is used to assign the value of the cut-off radius as the half of the box dimension. Therefore, for accurate modeling of the molecular simulation, the box size needs to be at least twice the cut-off radius (r_c) in each direction. In the current simulation, the value of r_c is taken as 12 Å for all the adsorbates. The dimensions of the unit cell for MFI type zeolite are less than twice the r_c. Therefore, the simulation box is constructed by using two unit cells in each direction (total 8 unit cells present). Only single unit cell is necessary to satisfy the PBC and MIC for the IRMOF-1 and HKUST-1 adsorbents.

The MIC is used for the calculation of L-J potential values. However, this approach cannot be applied to the electrostatic interaction, as the rate of decrease in the coulombic potential is slower than the L-J potential (r^{-1} for coulombic as opposed to r^{-6} for L-J potential). Therefore, not only the molecules present inside the simulation box, but also the molecules present in the periodic images are necessary to be included in the electrostatic interaction. Ewald summation technique is used to achieve this purpose. An open source software called 'RASPA' is used to perform the GCMC simulation [210]. The aforementioned techniques are implemented in the program. The visualizations of the adsorbent molecular structures are obtained using the iRASPA software [203].

3.1.4 Adsorption isotherm

As mentioned in the previous section, the number of adsorbed molecules are averaged over the samples obtained during the sampling stage of the GCMC simulation. The ensemble average of the number of adsorbed adsorbate molecules denotes the absolute uptake of the adsorbent-adsorbate system at the given pressure and temperature. This quantity differs from the uptake measured in the adsorption characterization experiment, which is called as excess adsorption uptake. The absolute and excess adsorption uptakes are related as the following expression:

$$N_{abs} = N_{ex} + V_{pore}\rho_g \tag{3.6}$$

Equation (3.6) states that the absolute uptake is the summation of the excess uptake and the amount of gaseous adsorbate present in the pore volume in the absence of the adsorbent at the same thermodynamic state.

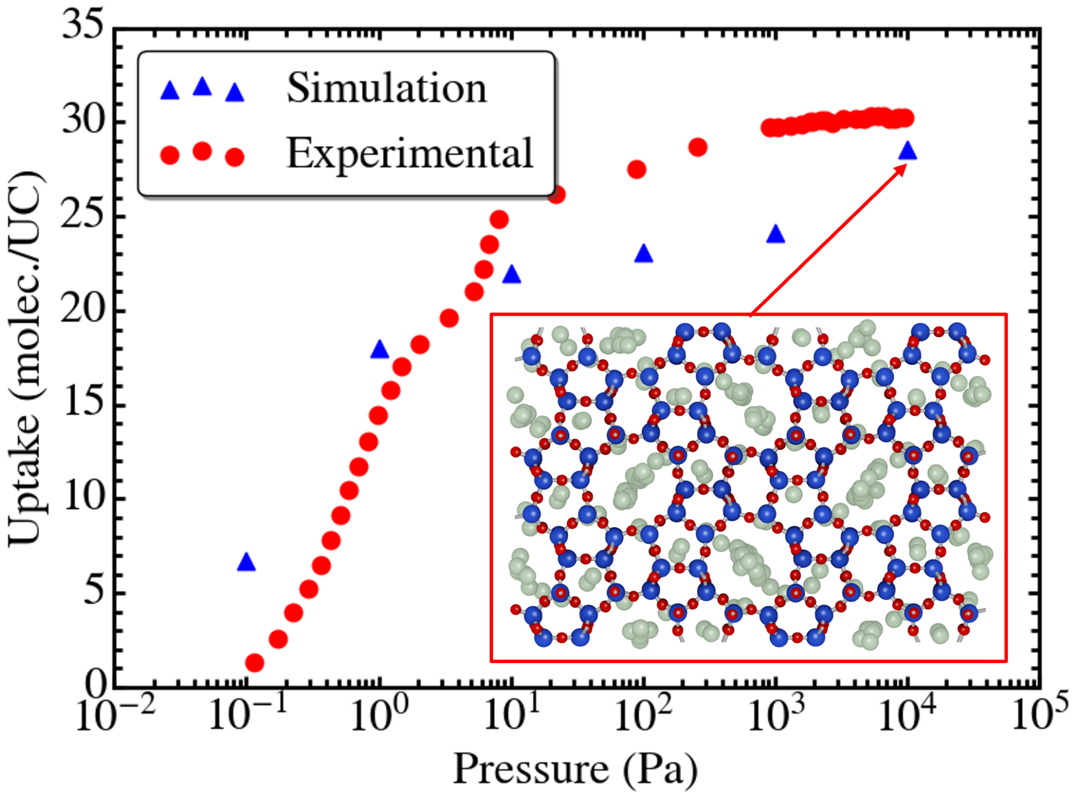

Figure 3.3: Argon adsorption isotherm in MFI type zeolite adsorbent at temperature of 87 K. The adsorbed molecules in the adsorbent pores at pressure 10 000 Pa presented in the inset figure

The adsorption isotherm of argon gas in the MFI-type zeolite is illustrated in Fig. 3.3. The temperature is considered as 87 K, at which point the adsorbent pore structure is characterized using Ar. The pressure ranges between 0.1 Pa to 10 000 Pa. The simulated adsorption isotherm is validated against the experimental data obtained from the literature [211]. It can be seen that the simulated isotherm overestimates the experimental data till 10 Pa pressure. At 10 Pa pressure, the inflection point occurs in the simulated isotherm. The subsequent simulated uptake values underestimates the experimental values beyond this pressure. The literature containing the experimental data also provided a GCMC simulation of the same adsorption system. A flexible adsorbent structure was developed to perform the simulation. Furthermore, the cross-atomic L-J interaction parameters were modified instead of following the standard Lorentz-Berthelot mixing rule. These modifications resulted in a better agreement of the simulation isotherm with the experimental data. This phenomenon was attributed to the orthorhombic to monoclinic transition of the MFI crystal structure as the number of adsorbed Ar molecules increased. However, the difference between the simulation and experimental isotherm data presented in Fig. 3.3 is ascribed to the rigid orthorhombic MFI structure with the L-J potential parameters obtained from standard mixing rules. These findings emphasize the importance of selecting appropriate simulation model parameters to accurately model physical adsorption phenomena. The inset figure in Fig. 3.3 shows the adsorbed Ar configuration in the MFI zeolite at 10 000 Pa pressure. The Ar molecules occupy the pore channels with larger diameter. Since, the van der Waals diameter of the Ar molecule is equivalent to the pore channels with smaller diameter, the probability of occupation these channels decreases.

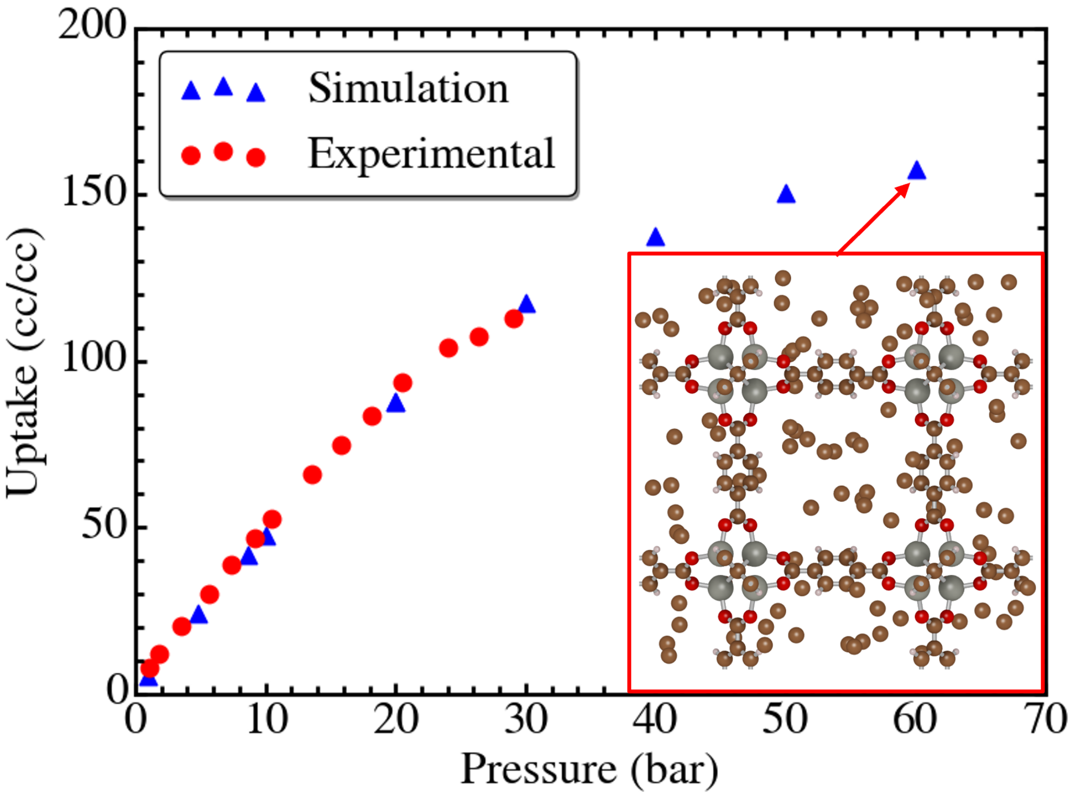

Figure 3.4: Methane adsorption isotherm in IRMOF-1 adsorbent at temperature 298.15 K. Inset figure: the adsorbed methane molecules configuration at the pressure 60 bar

. Fig. 3.4 illustrates the simulation and experimental adsorption isotherms of methane in IRMOF-1 MOF structure. The temperature is taken as 298.15 K and the pressure range is upto 60 bar. The experimental data is collected from the existing literature [212]. The simulated isotherm demonstrates a close agreement with the experimental data. The isotherm depicts a monotonic increase with the increasing pressure, which is attributed to the large accessible pore volume. As per the inset figure in Fig. 3.4, the adsorbed methane molecules are equally distributed in the porous region at 60 bar pressure. The close agreement between the simulation and experimental isotherm data further validates the single particle model of the methane molecule along with its absence of electrostatic interaction.

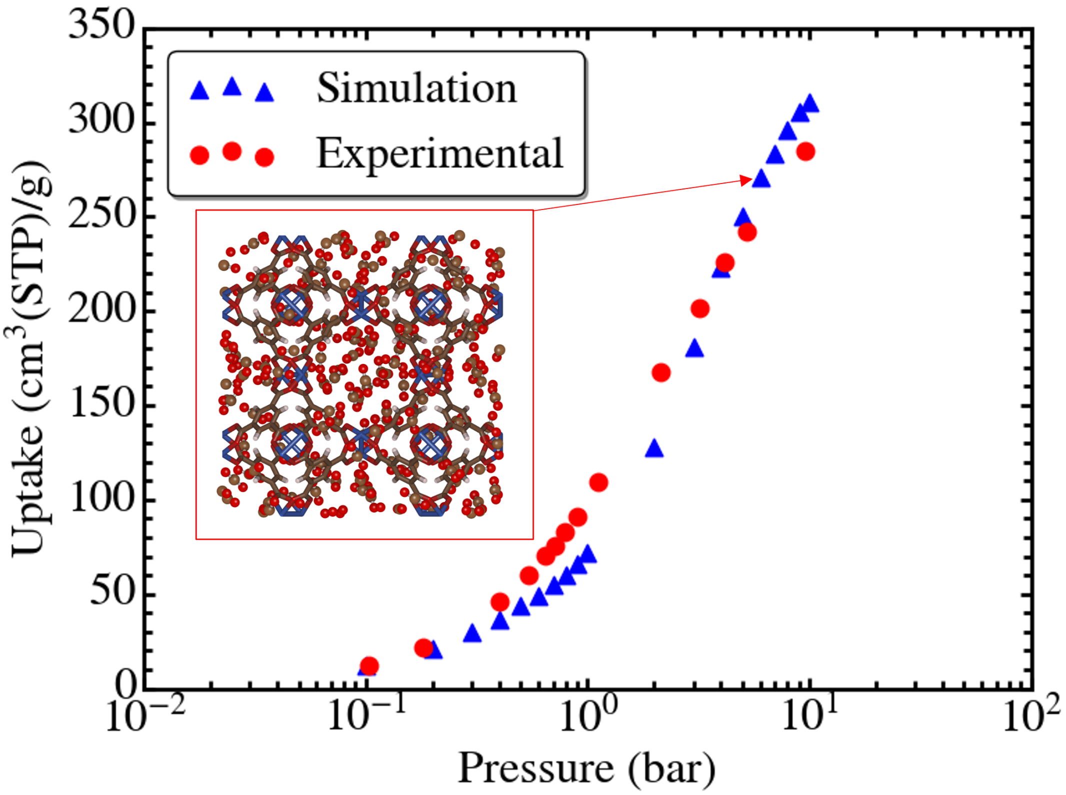

Figure 3.5: CO_2 adsorption in HKUST-1 adsorbent at temperature 298.15 K. Adsorption system at pressure 10 bar displayed in the inset figure

The CO_2-adsorbent and CO_2-CO_2 interactions involve both the vdW and electrostatic potential, unlike the Ar and CH_4 molecules. The adsorption isotherm comparison between the simulation and experimental data is illustrated in Fig. 3.5. The experimental data is collected from the study by Polat et al. [213]. It can be seen that the simulation results closely align with the experimental uptake values. However, the slight underestimation and overestimation by the simulation data can be noticed at the low and high pressure, respectively. This slight discrepancy can be attributed to the presence of defects in the adsorbent structure used for the experiment, whereas the simulation is performed in a perfect crystal. Furthermore, these defects influence the charge distribution in the MOF crystal structure. Modifications in the partial charge values used in the simulation may result in a closer values to the experimental isotherm data. The changes in the slope of the adsorption isotherm in the low pressure and high pressure regions can be explained using the energetic behavior of the adsorption system, which is described in the following section.

3.1.5 Isosteric heat of adsorption

Isosteric heat of adsorption is a characteristic property of the adsorbent-adsorabte pair. This property can be obtained from the GCMC simulation using the ensemble sampling of the total potential of the adsorption system. The fluctuation formula [214] is applied to derive the isosteric heat of adsorption from the total potential and the adsorbed number of molecules, which is defined as follows:

$$q_{st} = RT + \langle U_g \rangle_\mu - \frac{\langle U^{total} \times N \rangle_\mu - \langle U^{total} \rangle_\mu \langle N \rangle_\mu}{\langle N^2 \rangle_\mu - \langle N \rangle_\mu^2} \tag{3.7}$$

Here, R is the universal gas constant, U_g is the intramolecular potential of the gaseous molecule, and N is the number of adsorbed molecules. If the adsorbate molecules are considered rigid, then there is no bonded-interactions. Therefore, for the present simulation model, the term U_g can be neglected.

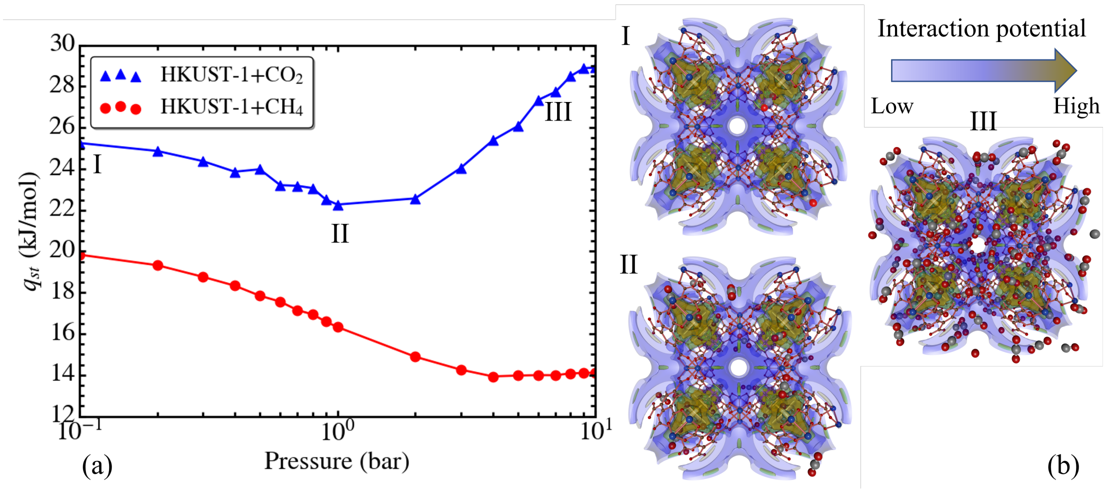

Figure 3.6: Isosteric heat of adsorption variation with pressure at temperature 298.15 K for the adsorption of CH_4 and CO_2 in HKUST-1 MOF

Fig. 3.6 depicts the isosteric heat of adsorption obtained from Equation (3.7) for the adsorption of methane and CO_2 in HKUST-1 adsorbent. The unique behavior of the q_{st} of CO_2 with respect to increasing pressure is captured through the GCMC simulation. At the low to medium pressure region, the q_{st} of CO_2 decreases continuously and attains a minimum value of 22 kJ mol^{-1} at 1 bar pressure. This trend is followed by an increasing trend of the q_{st} with the increasing pressure. This variation in the q_{st} trend can be ascribed to the pore size distribution of the HKUST-1 MOF with three primary pore sizes. At the low pressures, the CO_2 molecules occupy the tetrahedral cages formed by the Cu clusters, which corresponds to the smallest accessible pore of the MOF. As the pressure increases, the CO_2 molecules tend to interact with the linker molecules in the larger pores. Since, the linker molecules posses lower interaction potential, the rate of increase in the total potential declines, which results in the decreasing q_{st} values till 1 bar pressure. Till this stage, the adsorbent-adsorbate interactions via vdW and coulombic potential act as the major source of total potential of the adsorption system. As the number of adsorbed CO_2 molecules further increases, the adsorbate-adsorbate interactions start to dominate the adsorbent-adsorbate interactions. Thus, the adsorbate molecules begin to occupy the available large pore space, initiating a 'pore-filling' like phenomenon, resulting in the subsequent rise in the isosteric heat of adsorption. The CH_4 adsorption exhibits lower values of the q_{st} than the CO_2 adsorption. This variation is apportioned to the absence of electrostatic interaction of the CH_4 molecules as well as single-site vdW interaction. Furthermore, the continuous decrease in the CH_4's q_{st} values till the high pressure region is attributed to the dominating the adsorbate-adsorbent interactions and the smaller van der Waals size of the CH_4 molecule.

3.2 Impact of pore structural and chemical characteristics

In the previous section, the use of GCMC method to simulate the adsorption process has been introduced. The equilibrium adsorption properties such as adsorption isotherm and isosteric heat of adsorption have been determined for different classes of adsorbents and adsorbates. The effect of pore size distribution have been introduced in the energetics of the adsorption phenomena. In fact, GCMC simulation can be a powerful tool to investigate the impact of pore geometry and surface chemistry on the adsorption process. Here, the CO_2 adsorption in activated carbon is chosen to evaluate these factors.

3.2.1 Activated carbon model

Molecular models of the activated carbon used for molecular simulations of adsorption process include slit-pore graphite, wedge-pore graphite, carbon nanotubes, and amorphous carbons constructed with 3-dimensional random orientation of graphene flakes. Here, the slit-pore based graphite structure is chosen to represent the activated carbon for simplification of the analysis. The activated carbon is modeled as graphite structures, which is developed by layering of graphene sheets. A graphene sheet consists of periodic arrangement of hexagonal chains of sp^2 hybridized carbon atoms. Generally, three layers of graphene sheets are chosen to model one wall. Each unit cell consists of a single graphite wall and the slit-pore is spread in the x-y direction. Periodicity in all three directions are considered to model the slit-pore bounded by the two graphite walls. This structural information is visually depicted in Fig. 3.7.

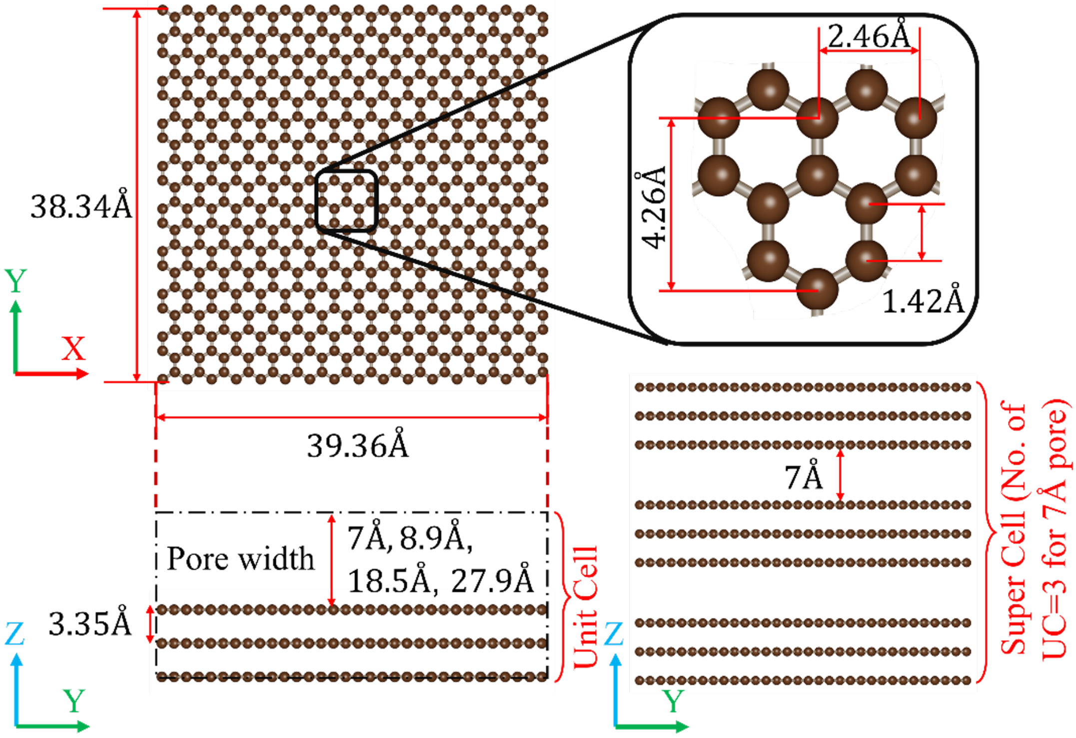

Figure 3.7: Schematic of the graphene structure used in the molecular simulation

The dimensions of the graphene sheets are chosen as 39.36 Å and 38.34 Å in the x and y directions, respectively. These values are chosen based on the existing literature for adsorption simulation. The C-C bond length is 1.42 Å. The periodic spacing between the repeating unit of the hexagonal structure in the x and y directions are 2.46 Å and 4.26 Å, respectively. Four pore widths are chosen to represent the microporous to mesoporous adsorbent structure. These pore sizes are 7 Å, 8.9 Å, 18.5 Å and 27.9 Å which are taken from an existing study on the H_2S adsorption in graphite slit-pores [61]. This study uses these four pore sizes to represent the pore size distribution of Norit RB4-type activated carbon [215]. As it has been described in the simulation method section, the minimum image convention is applied to model the graphite structure. The interlayer spacing of the graphene layers is 3.35 Å. The resultant unit cell length in the z-direction is 13.7 Å for the 7 Å pore size (calculated as $3.35\ \text{Å} \times 2 + 7\ \text{Å}$). The cut-off radius ($r_c$) is chosen as 16 Å to model the CO_2 molecule. The z-length of the unit cell is lower than the r_c. To satisfy the minimum image convention, described in the earlier section, the supercell of the slit-pore with pore-width as 7 Å is built by replicating the unit cell by three times in the z-direction. This supercell is highlighted in Fig. 3.7. Similarly, the necessary number of unit cell replicas in the z-direction for the 8.9 Å, 18.5 Å and 27.9 Å pore are fixed as 3, 2 and 2, respectively.

The functional groups play a key role in the physisorption process, as these distort the energy landscape of the adsorbent structure, impacting the resultant adsorption behavior. Here, three oxygen containing functional groups are chosen to model the activated carbon, These are carbonyl (-O), hydroxyl (-OH), and carboxyl (-COOH) groups. These functional groups are grafted onto the graphene layer. Fig. 3.8 shows the resultant structure and the associated dimensions.

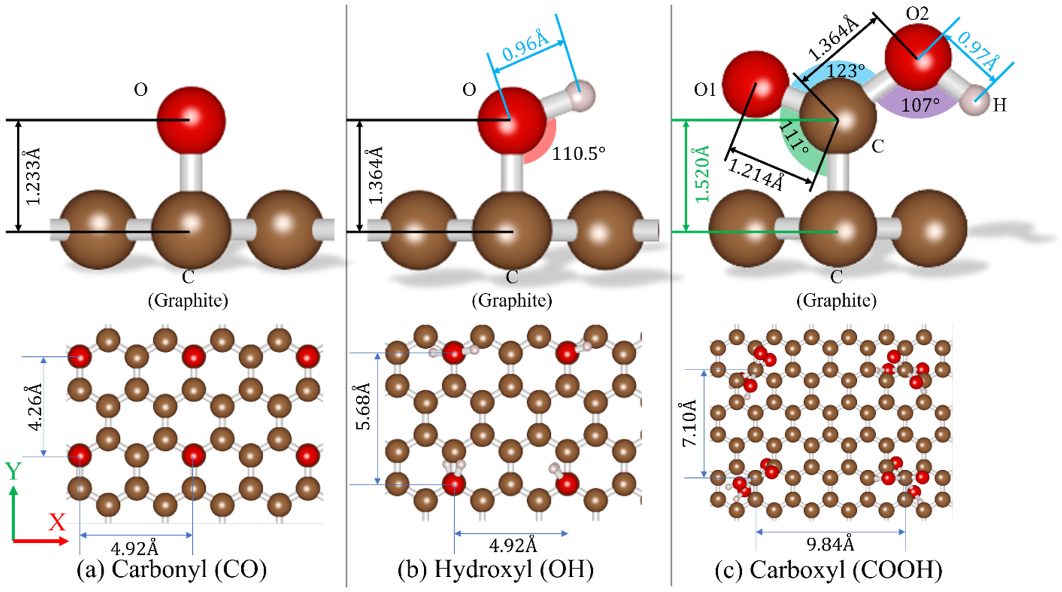

Figure 3.8: Molecular structures of the oxygen containing functional groups grafted on the graphene layer

The FGs are placed on both sides of the slit-pore. Thus, in the unit cell model of the graphite wall, both the top-most and bottom-most graphene layers are modified to place the FGs. Fig. 3.8 indicates the geometric dimensions of the FGs. The separation between two adjacent carbonyl FGs in the x and y directions are 4.92 Å and 4.26 Å, respectively. In case of the hydroxyl FG, alternate spacing between 4.26 Å to 5.68 Å in the y-direction is maintained. The total number of carbonyl and hydroxyl FGs per unit cell of graphite is taken as 96. In case of carboxyl group, this number is reduced to 48, to maintain the same number of oxygen atoms in all the FG containing unit cells. Furthermore, the spacing between the adjacent carboxyl FGs is increased to reduce the steric effect of the larger FG molecule. For the hydroxyl and carboxyl FG molecules, the orientation of the O-H and O-C-O-H bonds are randomly distributed across the x-y plane, for a closer match with the heterogeneous structure of the adsorbent.

The force field parameters for the graphene structures are obtained from the study by Liu et al. [88]. It also contains the bond length and bond angle information of the FGs.

Table 3.4: Force field parameters of the graphitic carbon and functional groups grafted

Molecule	Atom	L-J Parameters		Partial charges
		ϵ/ K	σ / Å)	(unit e^- charge)
Pristine Graphite	C	3.40	28.00	0.00
Carbonyl FG	C (graphite)	3.40	28.00	0.50
	O	2.96	105.00	-0.50
Hydroxyl FG	C (graphite)	3.40	28.00	0.20
	O	3.07	78.18	-0.64
	H	-	-	0.44
Carboxylic FG	C (graphite)	3.40	28.00	0.08
	C (FG)	3.75	52.00	0.55
	O1	2.96	105.70	-0.50
	O2	3.00	85.60	-0.58
	H	-	-	0.45

The L-J potential values for the graphitic carbon are widely used for modeling gas adsorption in carbon nanotubes and amorphous carbon-based adsorbents. It is to be noted that, the partial charge distribution is neglected in the pristine graphite structure, unless a defect is introduced to it. The vdW potential parameters of the oxygen-containing functional groups are taken from the all-atom force field model developed for characterizing the phenolic compounds [216]. This model also contains the partial charge description, which are also used to model the electrostatic interaction of the oxygen-based functional groups in the present simulation study. As the functional group act as a defect to the pristine graphite structure, a partial charge is introduced to the graphitic carbon, which is bonded to the functional group. This partial charge possesses the same magnitude and the opposite polarity to that of the atom of the functional group, which is bonded to the graphitic carbon. This atom is oxygen atom for both carbonyl and hydroxyl FG, and is carbon for the carboxyl group. The force field parameters are provided in table.

The GCMC simulation is carried out at 273.15 K temperature and in a pressure range of 1×10^{-4} bar to 1×10^{1} bar. The number of initialization and sampling cycles are taken as 25 000 and 50 000, respectively. These values are sufficient to reduce the statistical error in the ensemble averaged quantities for CO_2 adsorption. Contrarily, the adsorption of water molecules in slit-pore graphite structure require a much higher number of cycles to achieve equilibration of the number of the adsorbed molecules (typically 1×10^6 to 3×10^6 number of initialization cycles). Two new quantities are observed to delineate the effect of the pore size distribution and the functional group on the adsorption properties. These are termed as local density distribution and molecular orientation distribution.

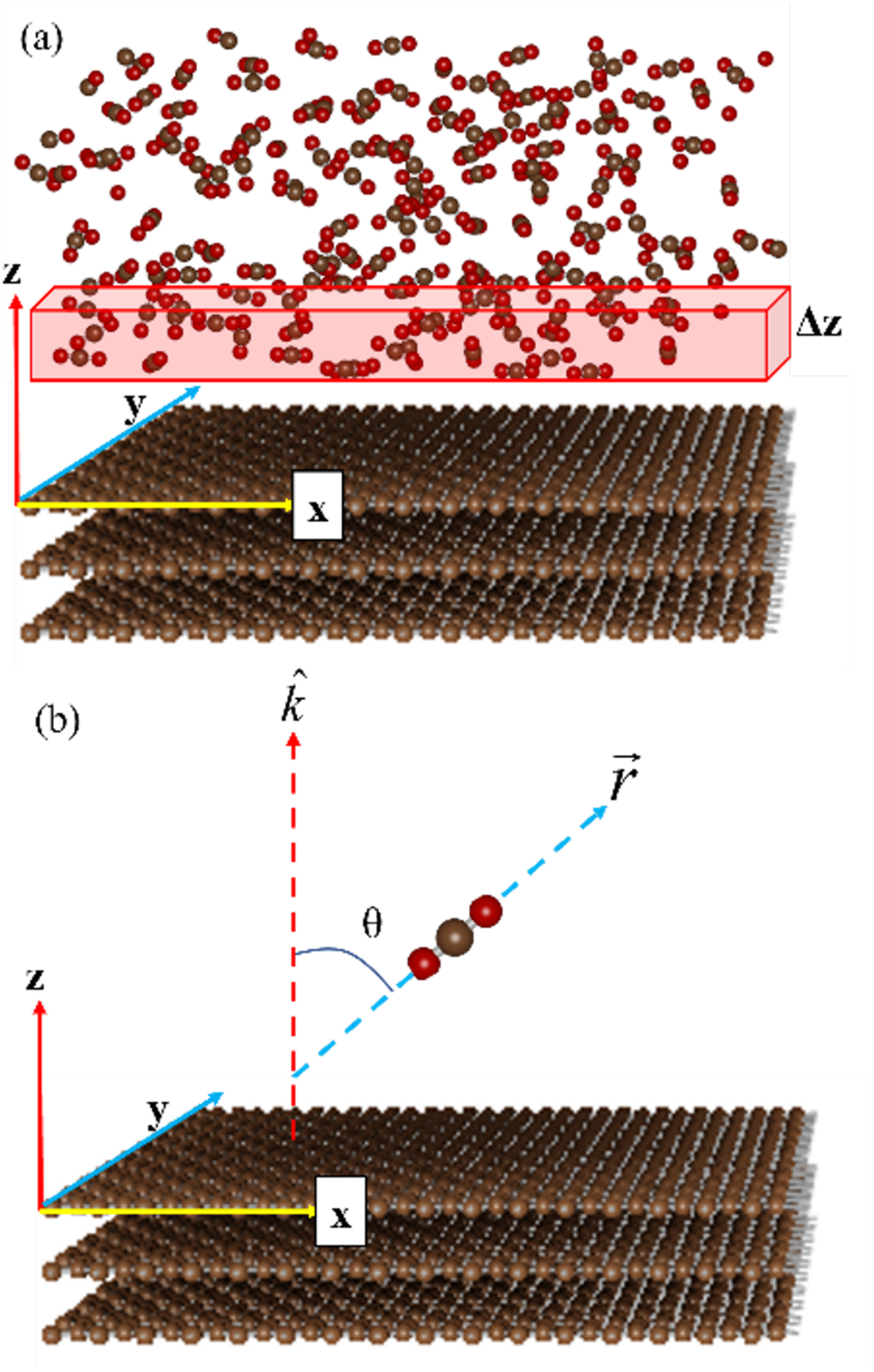

Figure 3.9: Schematic of the calculation procedure of (a) local density distribution and molecular orientation distribution

Local density distribution

Fig. 3.9a depicts the schematic to determine the adsorbed phase density at a particular location in the pore-width along the z-direction. The local density distribution is calculated by counting the number of CO_2 molecules present in the thickness $[z, z+\Delta z]$ across the pore area and dividing the number by the small volume. The number of molecules is averaged over the samples obtained during the sampling stage of the GCMC simulation. This procedure is mathematically represented as follows:

$$\rho_z = \frac{\langle N_{z+\Delta z} \rangle}{L_x L_y \Delta z} \tag{3.8}$$

Here, L_x and L_y denote the graphite lengths in the x and y directions, respectively. Here, the centroid of the CO_2 molecule, i.e., the coordinate of C atom is considered for counting the adsorbed number of molecules in the given region.

Molecular orientation distribution

The CO_2 molecular orientation refers to the angle formed between the CO_2 molecular axis and the pore-surface normal vector. This concept is visually depicted in Fig. 3.9b. The notations $\hat{k}$ and $\overrightarrow{r}$ are the pore-surface normal unit vector and vector passing through the rigid CO_2 molecule, respectively. The formulation for the angle formed is expressed as follows:

$$\theta = \cos^{-1} \frac{\hat{k} \cdot \overrightarrow{r}}{|\overrightarrow{r}|} \tag{3.9}$$

Here the $\cdot$ symbol refers to the dot product between the vectors. Histograms of the obtained angle values are averaged over the samples to obtain the average adsorbed phase molecular orientation distribution.

Model validation

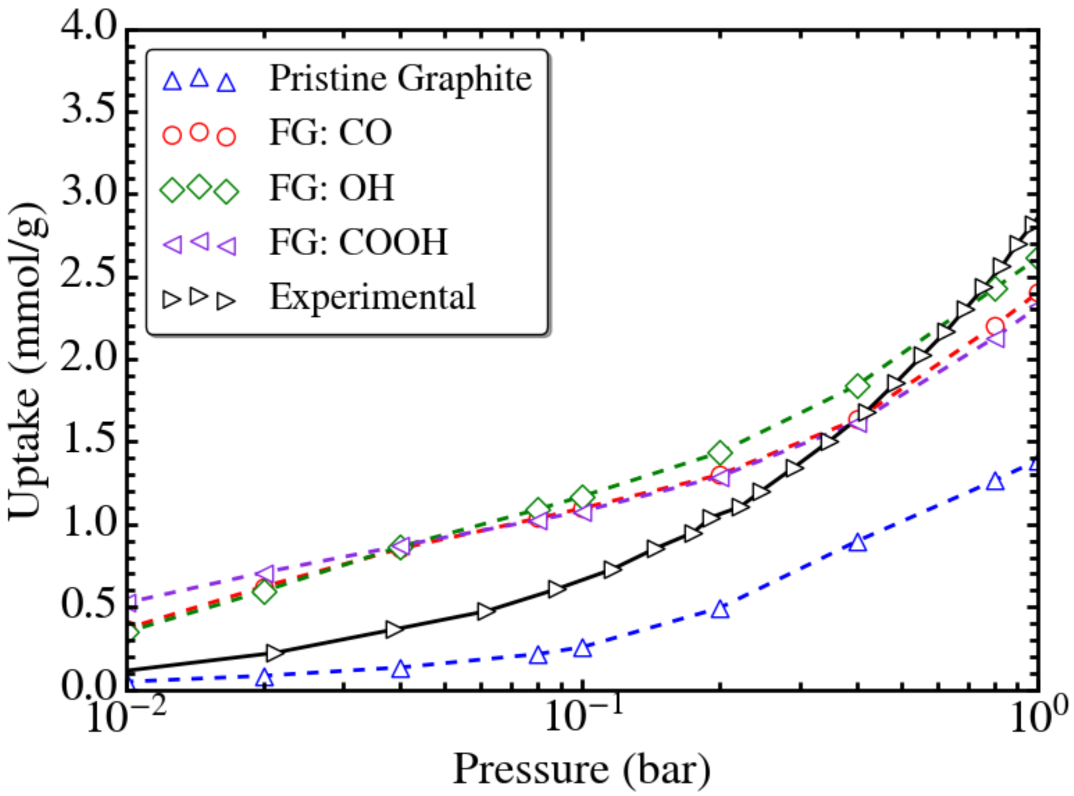

Figure 3.10: CO_2 uptake comparison among the experimental and GCMC simulation data, considering different types of functional groups and temperature 273.15 K

Fig. 3.10 compares the CO_2 adsorption uptake data obtained using the GCMC simulation with the ones obtained from the experimental study carried out the temperature 273.15 K. The GCMC simulation data is provided for four types of the graphite structures based on the functional groups. The simulated uptake data is calculated by taking the average value of the uptake values in each pore sizes, weighted by the respective pore volumes. The representative pore volume data from the pore size distribution of the Norit RB4 type activated carbon is used from the existing study [61]. It can be seen that simulated uptake values for the pristine graphite structure underestimate the experimental data in the given pressure range. The use of functional groups elevates the uptake value, with an overestimation of the experimental data in the low-pressure region. The deviation of the simulation results from the experimental observation can be attributed to the oversimplification of the adsorbent structure by using the graphite slit pore model. As a result, the given adsorbent model fails to account for the pore connectivity, missing molecules, and pore surface heterogeneity, which have a cumulative influence on the adsorption affinity toward the CO_2 molecules. The detailed investigation of the adsorption characteristics with respect to the pore size variation and type of functional groups is delineated in the following sections.

3.2.2 Effect of pore size

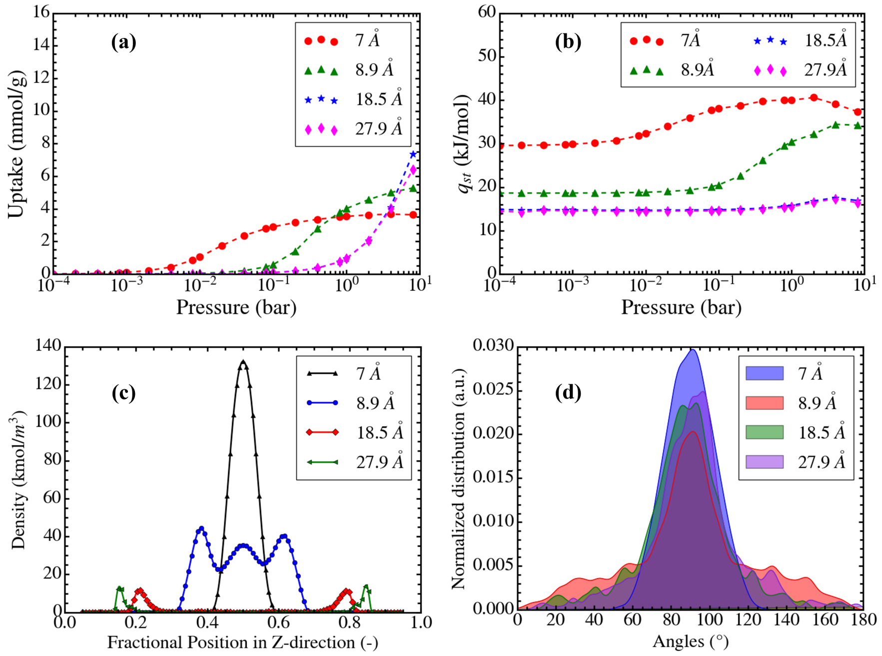

Figure 3.11: Effect of pore size distribution on the (a) adsorption isotherm, (b) isosteric heat of adsorption, (c) local adsorbed phase density distribution, (d) molecular orientation distribution

Fig. 3.11 illustrates the effect of pore size distribution on the adsorption isotherm, isosteric heat of adsorption, local adsorbed phase density distribution, and the molecular orientation distribution of the adsorbed CO_2 molecules. Four pore sizes of the pristine graphite are considered for this analysis. Variation in the pore sizes appear to impact the adsorption isotherm and isosteric heat properties significantly. The isotherms for all pore sizes in Fig. 3.11a demonstrate low uptake values in the lower pressure range. At medium to higher pressures, the adsorption uptake begins to increase. This pressure (hereby referred as the pore-filling initiation pressure) is directly proportional to the pore size. For instance, the pore-filling initiation pressure is 1×10^{-3} bar, whereas this value increases to more than 1×10^{-1} bar for the 18.5 Å and 27.9 Å pore sizes. The rapid increase in the uptake values for 7 Å pore size is attributed to the increased interaction potential between the CO_2 molecules and the graphite walls. As the distance between the adsorbate and adsorbent reduces, the magnitude of the attractive L-J potential, as depicted in Fig. 3.1. Thus, a strong energetic site is formed in the pore, enabling an increased amount of CO_2 molecules to adsorb at low-pressure. As the pore size increases to 8.9 Å, the resultant attractive potential magnitude decreases. Subsequently, this trend continues to the larger pore sizes, which requires a higher pressure to adsorbing the CO_2 molecules in the low-energy adsorption sites. This variation in the favorable energetic formation across the pore sizes is reflected in the isosteric heat of adsorption (q_{st}) variation as depicted in Fig. 3.11b. The isosteric heat of adsorption remains almost constant until the pore-filling initiation pressure of respective pore sizes. 7 Å pore size exhibits the highest value of q_{st} among all the pore sizes due to the higher interaction potential values. The number of adsorbed CO_2 molecules increases with the further increase in pressure, which results in the higher adsorbate-adsorbate interaction potential. Since, the separation among the CO_2 molecules decreases with the higher number of adsorbates, both the resultant vdW and coulombic attractive potential proportionally increases. This effect is stronger in case of 7 Å and 8.9 Å, due to relatively lower accessible pore volumes. Thus, the q_{st} trend appears to rise with increasing pressure beyond the respective pore-filling initiation pressures. The increase in the q_{st} amounts is approximately $10\,\mathrm{kJ\,mol^{-1}}$ and $16\,\mathrm{kJ\,mol^{-1}}$ for 7 Å and 8.9 Å, respectively. These q_{st} values are significantly smaller for 18.5 Å and 27.9 Å pore widths, as the available space for adsorbing the CO_2 molecules are higher than the 7 Å and 8.9 Å pore widths. Finally, the adsorbed number of molecules reaches saturation, when the accessible pore volume of the adsorbent is fully occupied by the CO_2 molecules. This saturation uptake value is directly proportional to the pore volume. Thus, the 7 Å pore width exhibits the lowest saturation uptake capacity. Consequently, the isosteric heat of adsorption also decreases as the uptake approaches the saturation capacity. This phenomenon is attributed to the increased repulsive potential among the CO_2 molecules. As the number of adsorbed molecules increases, the separation between the atoms with partial charges of same polarity reduces (e.g., C-C and O-O distances). Furthermore, if the intermolecular distance between the CO_2 molecules becomes less than the minimum L-J potential distance ($2^{1/6}\sigma$), then the magnitude of attractive L-J potential values decreases, and eventually it turns into repulsive potential. Thus, total potential of the adsorption system decreases, resulting in the decrease of q_{st} at high pressure. It is observed that the 7 Å pore width exhibits the fastest uptake saturation, whereas the pore sizes 18.5 Å and 27.9 Å do not reach the saturation capacity within the pressure of 1×10^1 bar. This phenomenon is ascribed to lower pore volume of 7 Å pore size.

Fig. 3.11c shows the local density distribution of the adsorbed phase molecules for the four pore sizes at 1 bar pressure. The density values are calculated using Equation (3.8) and is plotted against the fractional position in the z-direction of the pore width. It can be seen that the maximum local density value is inversely proportional to the pore width. This phenomenon corresponds to the adsorbed layer formation in the pore width. In case of 7 Å pore width, a single adsorbed phase layer is generated, as opposed to the multilayer formation in the higher pore sizes. The adsorbed layer is formed at the center of 7 Å pore width (fractional z-position of 0.5). The observed effect can be attributed to the fact that the pore width of 7 Å is roughly twice the collision diameter of the carbon atoms in graphene. Thus, the energetically favorable adsorption site is formed approximately at the center of the pore width due to the influence of two pore walls. As the pore size increases, this adsorption site moves away from the center of the pore width, as the favorable site associated to each graphite wall sticks close to the collision diameter of respective pore wall. Therefore, the formation of the adsorbed layers begin at these adsorption sites. As a special case for 8.9 Å pore width, an additional adsorbed layer is formed at the center of the pore width along with the two layers at the approximate fractional positions of 0.4 and 0.6. This observation is attributed to the CO_2-CO_2 interaction and the ability to reorient the CO_2 molecule for attaining a more energetically favorable configuration of the adsorbed molecules. Fig. 3.11d depicts the molecular orientation distribution of the adsorbed CO_2 molecules. The x-axis in the figure refers to the attainable range of angles of a CO_2 molecule with the pore-surface normal, as highlighted in Fig. 3.9b. This angle is calculated using Equation (3.9). An angle of 90° implies that the CO_2 molecule is oriented parallel to the pore-surface, whereas the orthogonal orientation of the same is defined by the angles 0° and 180°. The y-axis refers to the relative occurrence probability of a particular angle. It can be seen that the major orientation of the CO_2 molecules is concentrated around 90° for all the pore sizes. However, as the pore size increases, the profile of the orientation distribution widens towards the orthogonal positions. The narrowest orientation distribution for 7 Å pore size is ascribed to the inability of rotation of the adsorbed molecule. The collision diameter for the pair of graphitic carbon atom and oxygen atom of CO_2 molecule, which is calculated using Equation (3.2), is approximately the half of pore width 7 Å. Thus, a rotational move of the adsorbed CO_2 molecule results in an energetically unfavorable configuration. In case of higher pore sizes, this restriction of rotation is lifted due to the increased accessible pore volume. In case of 8.9 Å pore width, the central adsorbed layer formation is associated with the rotation of the CO_2 molecules to the near-orthogonal position. It has already been established in the literature that the 'T'-shaped orientation of the CO_2 molecules is highly stable, due to the attractive electrostatic interaction between the O and C atoms of the two CO_2 molecules [40, 71]. A similar occurrence is observed for the formation of central adsorbed layer of CO_2 molecules in 8.9 Å pore size. Thus, the probability of occurrence of near-orthogonal angles is higher in 8.9 Å pore than 18.5 Å and 27.9 Å pores. However, the near-orthogonality is caused by the inadequate pore width, which is smaller than the required distance for the 'T'-shaped configuration. Thus, the CO_2 molecules reorient in three dimensions. A similar observation related to the CO_2 molecular reorientation to achieve more energetically stable configuration in graphite adsorbed layer was demonstrated by Bhatia et al. [71].

3.2.3 Effect of functional groups

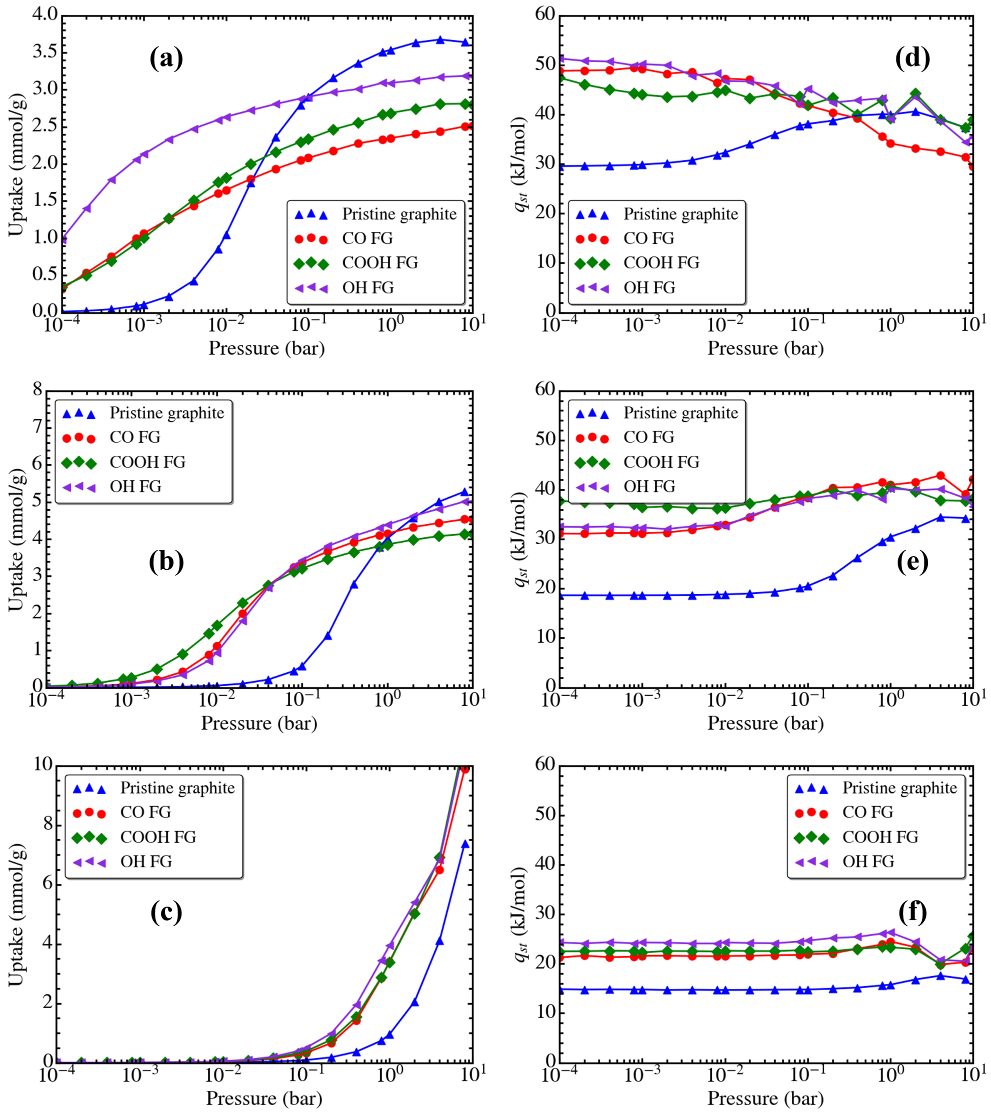

Figure 3.12: Impact of functional groups in the adsorption uptake and isosteric heat of adsorption of CO_2 adsorption in slit-pore graphite at fixed pore sizes (a) and (d) 7 Å, (b) and (e) 8.9 Å, (c) and (f) 18.5 Å

Fig. 3.12 provides a comprehensive illustration of the effect of functional groups on the adsorption uptake and isosteric heat of adsorption values at different pore sizes. The isotherms are plotted on the left column of Fig. 3.12 and the corresponding right column depicts the q_{st} profiles. It can be seen that the presence of the FGs influence both the pore-filling initiation pressure and the saturation uptake capacity. The pore-filling initiation pressure is lower for FG containing graphite structures compared to the pristine graphite for all the pore sizes. In case of 8.9 Å and 18.5 Å pore sizes, this cutoff pressure value is 10 times lesser than that of the pristine graphite. The 7 Å pore size shows significant amount of uptake at the pressure 1×10^{-4} bar pressure between $0.4\,\mathrm{mmol\,g^{-1}}$ to $1.0\,\mathrm{mmol\,g^{-1}}$, whereas the pristine graphite with same pore size shows approximately zero amount of uptake. The primary factors for the reduced cutoff pressure for pore-filling can be written as follows:

(i) higher vdW interaction parameters of the FG atoms as tabulated in Table 3.4,

(ii) presence of partial charges on the FG atoms, introducing electrostatic interactions between the adsorbent and adsorbate molecules.

While comparing among the different FGs, it can be observed that the difference between the pore-filling initiation pressure is relatively lower for hydroxyl (OH) FG than the carboxyl (COOH) and carbonyl (CO) FGs in the graphite adsorbent with 7 Å pore size. However, for the larger pore widths, this difference in cutoff pressures is negligible among the FGs. There are two factors responsible for this behavior, which are:

(i) carbonyl group contains a negative partial charge, which increases the repulsive coulombic interaction between the carbonyl group and CO_2 molecule. The net attractive potential (vdW+coulombic) is affected due to this increased repulsion,

(ii) carboxyl group contains two oxygen atoms which facilitates both increased vdW interactions and increased repulsive coulombic potential with the CO_2 molecules. Furthermore, the bulk size of the COOH group occupies significant amount of space in the small pore of 7 Å pore size. This induces a steric effect in the adsorption of CO_2 molecules.

Table 3.5: Accessible pore volumes of graphite slit pore with various pore sizes and functional groups

Pore sizes	7 Å	8.9 Å	18.5 Å	27.9 Å
Pristine graphite	0.392 $cm^3\,g^{-1}$	0.439 $cm^3\,g^{-1}$	0.829 $cm^3\,g^{-1}$	1.237 $cm^3\,g^{-1}$
Carbonyl FG	0.182 $cm^3\,g^{-1}$	0.289 $cm^3\,g^{-1}$	0.650 $cm^3\,g^{-1}$	1.017 $cm^3\,g^{-1}$
Carboxyl FG	0.283 $cm^3\,g^{-1}$	0.301 $cm^3\,g^{-1}$	0.671 $cm^3\,g^{-1}$	1.04 $cm^3\,g^{-1}$
Hydroxyl FG	0.321 $cm^3\,g^{-1}$	0.266 $cm^3\,g^{-1}$	0.628 $cm^3\,g^{-1}$	0.994 $cm^3\,g^{-1}$

Based on the abovementioned factors, the amount of energetically favorable sites reduces in the pore volume. Contrarily, the OH group has the positive partial charge containing H atom, which acts as the attractive coulombic site for the CO_2 adsorption. Furthermore, this group is smaller than the COOH group, which negates the steric hindrance in the adsorption of CO_2 molecules. Therefore, the OH group overcomes both the drawbacks mentioned above, which engenders the highest affinity for the CO_2 molecules. Thus, the pore-filling initiation pressure is the lowest for OH functional group. The effect of the functional groups on the maximum capacity varies among the different pore sizes. For 7 Å and 8.9 Å pore sizes, the maximum uptake capacity reduces with the introduction of the functional groups. The reduction in the accessible pore volume is the primary cause for this occurrence. The FGs in the decreasing order of maximum uptake capacity is OH>COOH>CO in 7 Å pore size graphite pore. This follows the trend of the accessible pore volumes obtained from the probe molecule based analysis of the iRASPA software, given in Table 3.5.

The introduction of the functional groups in the graphite pores engenders higher values of the isosteric heat of adsorption than the pristine graphite for all pore sizes. In 7 Å pore size graphite, the q_{st} exhibits a monotonic decrease with the increasing pressure for all the functional groups, unlike the q_{st} trend in pristine graphite. This occurrence is apportioned to the cumulative effect of O-O electrostatic repulsion between the CO_2-FG pair and CO_2-CO_2 pair at the increased number of adsorbed CO_2 molecules. The trend of the q_{st} with increasing pressure is similar between the functional group containing and pristine graphite structures with 8.9 Å and 18.5 Å pore sizes. Here, the adsorbent-adsorbate electrostatic repulsion is lesser than the adsorbate-adsorbate electrostatic interaction at increased number of adsorbed molecules. The difference in the q_{st} values among the functional groups is not significant as the number of oxygen atoms for all the FGs are equal, which is the primary source of vdW and electrostatic interactions.

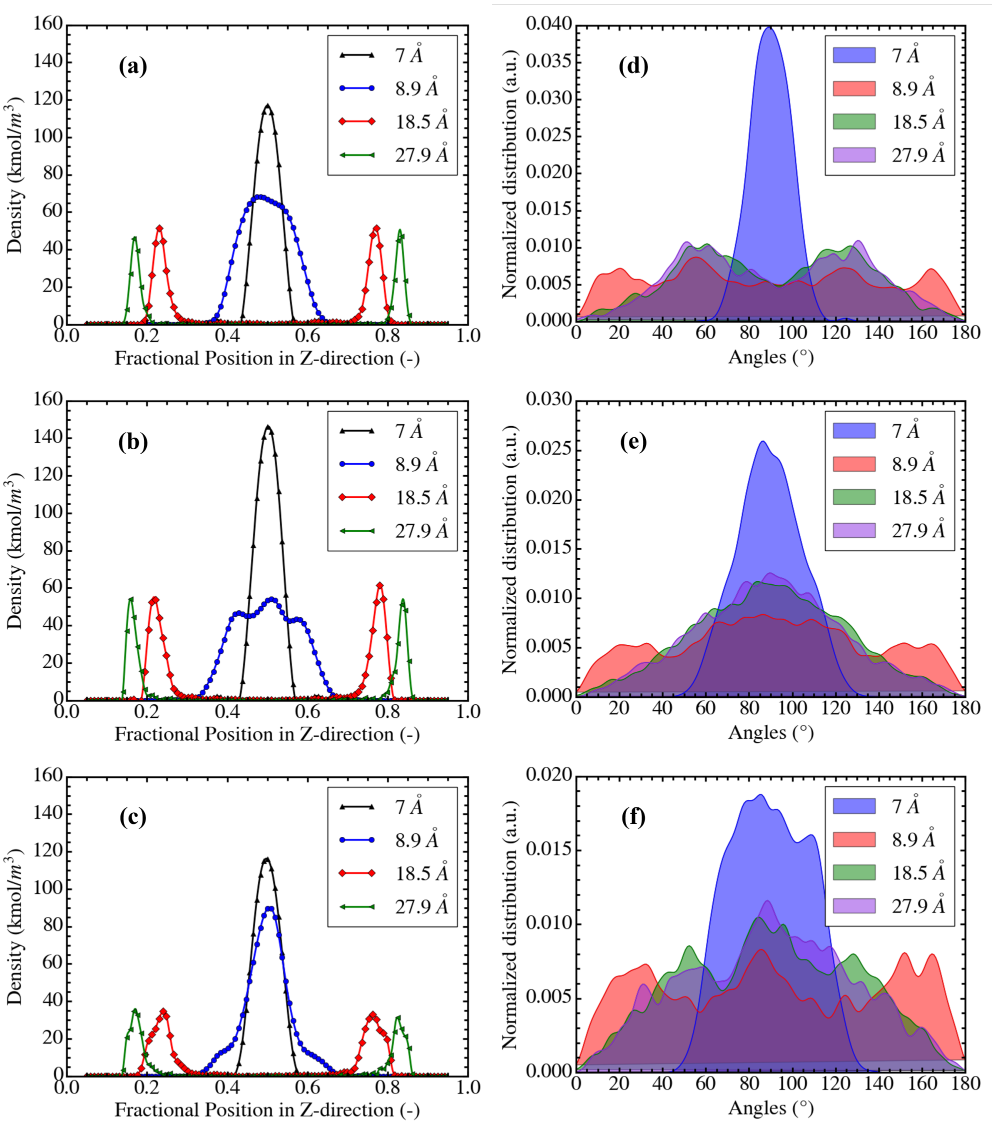

Figure 3.13: Effect of functional groups on the local density distribution and molecular orientation distribution for the CO_2 adsorption in graphite slit-pores at 0.1 bar pressure. The functional groups: (a) and (d) carbonyl (CO), (b) and (e) hydroxyl (OH), (c) and (f) carboxyl (COOH)

The change in the behavior of adsorption isotherms and isosteric heat of adsorption is accompanied by the adsorbed phase configuration change due to the presence of the functional groups. Fig. 3.13 depicts the adsorbed phase local density distribution and molecular orientation distribution variation with respect to functional groups for all pore sizes considered. The left column in the figure illustrates the local density distribution and the right one depicts the molecular orientation distributions. It can be observed that the monolayer to multilayer transition of the adsorbed phase formation is observed as the pore size increases, in the FG containing graphite slit-pores. This behavior is similar to the adsorbed phase formation in pristine graphite adsorbent, portrayed in Fig. 3.11. However, slight variations in this trend can be noticed depending upon the type of FG present in the adsorbent. For instance, in CO and OH-based graphite slit-pore with pore width of 8.9 Å, the local density distribution is spread between the fractional z-distance range between 0.35 to 0.65 (Fig. 3.13a and Fig. 3.13b), unlike the three distinct peaks observable for the pristine graphite of same pore size. This phenomenon suggests that the adsorbed phase is more distributed across the pore width, and the pore-filling is already achieved at the same pressure of 0.1 bar with the introduction of the FGs. Furthermore, in case of COOH functional group, a narrow peak in the density values is obtained at the center of the pore width for the graphite with 8.9 Å pore size (Fig. 3.13c). This occurrence is ascribed to the narrower available pore volume and increased intermolecular interaction potential due to the bulk COOH molecules. Apart from this major change in the adsorbed phase configuration, the peak adsorbed phase density for the 7 Å pore size is seen to be lesser for CO and COOH containing graphite adsorbents than that for the pristine graphite, due to the reduced energetically favorable adsorption sites as described before. However, the peak values of the multilayer adsorbed phase in the larger pore widths (18.5 Å and 27.9 Å) appear to be greater than that in the pristine graphite.

This phenomenon indicates the effect of increased intermolecular potential due to the functional groups in the mesoporous adsorbent structures.

Significant variation in the molecular orientation distribution behavior can be observed with the introduction of the functional group. Similar to the local density distribution, a drastic variation in the molecular orientation distribution can be noticed for the FG containing graphite with 8.9 Å pore size. The central peak observed around 90° orientation in the pristine graphite of 8.9 Å pore size vanishes in CO-based graphite structure, with generation of distinct peaks at 60° and 120° orientations. Due to the simultaneous effect of the attractive vdW potential and the repulsive coulombic potential between the oxygen pair of the CO group and CO_2 molecule, the CO_2 molecule tends to reorient itself in an angular configuration from the pore-surface parallel orientation. Two smaller peaks are also observed at near-orthogonal angles, which corresponds to the adsorbed layer formation in the center of the pore width. In case of OH functional group with 8.9 Å pore width, a wide orientation distribution is observed with the peak value occurring around 90° angles. This increase in the pore-surface parallel orientation is attributed to the attractive electrostatic interaction between the OH group and CO_2 molecules. This increased attractive potential leads to the formation of energetically favorable adsorption sites at the central region of the pore-width, where the most of the parallel orientation of the CO_2 molecules occur. In case of COOH functional group, the CO_2 angle values are randomly distributed for the 8.9 Å pore size. The heterogeneity in the pore surface morphology due to the bigger COOH functional group is responsible for this occurrence. The effect of the functional groups in the larger pore widths are similar to the 8.9 Å pore width. The 7 Å pore width demonstrates the usual single peak around the 90° angles. The said peak in CO containing graphite adsorbent is narrower than the pristine graphite. The increased repulsive action by the CO group on the CO_2 molecules causes this behavior. In case of OH and COOH functional groups, the peak is wider, due to the increased interaction potential by the FGs and heterogeneous orientation of the functional groups across the x-y directions. These factors result in the slightly higher probability of rotation of adsorbed CO_2 molecules even in the ultra-micropore region.

3.3 Summary

This chapter provides a broad overview of the GCMC simulation technique for investigating the molecular level adsorption phenomena. The effects of pore size distribution and the type of functional groups on the adsorption isotherm and isosteric heat of adsorption are critically evaluated. These resultant macroscopic adsorption properties are incorporated for characterizing the adsorbed phase thermodynamic properties and equilibrium cycle simulation. The fundamental theoretical models involving these aspects of the adsorption process are developed in the following chapter.

Chapter 4

Adsorption thermodynamics

The preceding chapter discusses the development of equilibrium adsorption properties from a molecular perspective using the GCMC simulation technique. This chapter consolidates these properties to characterize the bulk thermodynamic properties of the adsorbed phase and the equilibrium cycle model of the AHT cycle. The following two sections describe the performance enhancement and limitation of the AHT cycle. These two aspects consider the use of internal heat recovery scheme and the maximum temperature lift determination, respectively.

4.1 Thermodynamic properties in adsorption process

4.1.1 Adsorption isotherm

Type I isotherm can be identified by its rapidly increasing uptake value at the low pressure region. The uptake reaches a plateau nearby the saturation pressure. Dubinin-Astakhov (D-A) isotherm equation is chosen as the type I isotherm equation, which has the following form:

$$w = w_0 \exp\left[-\left(\frac{RT}{E}\ln\frac{P_{sat}}{P}\right)^n\right] \tag{4.1}$$

Here, the coefficients w_0, E, and n denote the maximum adsorption capacity, activation energy, and heterogeneity coefficient, respectively. This equation is generally applied for the low-pressure adsorption condition, where the effect of adsorbed phase specific volume is negligible. For instance, the water adsorption isotherm in the ambient temperature conditions can be represented using Equation (4.1) as adsorption occurs below the atmospheric pressure. Contrarily, the adsorption of CO_2, CH_4 etc. occurs at the high pressure region, where the effect of the adsorbed phase volume becomes significant. Therefore, a modified version of the D-A isotherm equation is used to represent their adsorption isotherms. A detailed description of the adsorbed phase volume-based D-A equation is provided in Appendix A. The water adsorption isotherm for various types of silica gel adsorbents are used in the present analysis, among which the isotherm coefficients for type RD2560 silica gel adsorbent are obtained by fitting available experimental isotherm data. This experimental data of water adsorption in type RD2560 silica gel adsorbent is obtained from the in-house Constant Volume Variable Pressure (CVVP) setup, whose details can be found in the preceding literature [174]. The D-A equation is fitted with the experimental isotherm data with an average absolute deviation of approximately 5 %. The resultant isotherm coefficients are listed in Table 4.1. The experimental data and fitted D-A isotherm lines are plotted at different temperatures, which is depicted by Fig. A.1.

The remaining isotherm models considered are of type III, IV, and V. Since different isotherm types are required to be compared based upon the uptake values, the Type II isotherm has been skipped due to its different unit of the uptake quantity than rest of the isotherms. These isotherm equations are listed below:

- **Type III:** Type III isotherm, also known as Guggenheim- Anderson-de Boer (GAB) isotherm, shows a slow rise in uptake at the low-pressure region. The uptake tends to sharply rise as the pressure approaches saturation. Moisture adsorption in the dry fruits is taken as the adsorption working material. The following equation depicts the GAB isotherm model:

$$\begin{cases} w = w_m \dfrac{ckx}{(1-kx)\{1+(c-1)kx\}} \\ c = c_0 \exp\left(\dfrac{\Delta H_1}{RT}\right) \\ k = k_0 \exp\left(\dfrac{\Delta H_2}{RT}\right) \\ \Delta H_1 = H_m - H_n \\ \Delta H_2 = H_1 - H_n \end{cases} \tag{4.2}$$

  Here, w_m represents the moisture content corresponding to an adsorbed monolayer, c and k are temperature dependent coefficients, and ΔH_1 and ΔH_2 are the functions of the heat of sorption of water. H_1 is the heat of condensation of water vapor and H_m and H_n represent the heat of sorption of monolayer and multilayer, respectively.

- **Type IV:** This type of isotherm closely resembles the Type I isotherm, in terms of the rise in uptake at the low pressures. Nevertheless, the main characteristics of this isotherm is the presence of adsorption-desorption hysteresis. The following equation formulates the isotherm:

$$w = \sum_{i=1}^{4} \frac{n_i N_{Mi} \left(\frac{P}{P_i}\right)^{n_i}}{i + \left(\frac{P}{P_i}\right)^{n_i}} \tag{4.3}$$

  Where, n_i is the number of molecules per receptor site and N_{mi} is the density of receptor sites. The pressure P_i corresponding to the half occupancy of the receptor site can be expressed as follows:

$$P_i = P_s \exp\left(\frac{E_{ai}}{RT}\right) \tag{4.4}$$

Here P_s is the saturation vapor pressure of the adsorbate and E_{ai} is the molar adsorption energy of the gas.

- **Type V:** Type V isotherm is characterized by the S-curve of the adsorption uptake with pressure as the abscissa. It also contains the adsorption-desorption hysteresis loop. This type of isotherm is typically observed for water adsorption in activated carbon. The initial small uptake values at the low-pressure region is attributed to the low intermolecular interactions among the adsorbent and adsorbate molecules. The hydrophobicity of the porous surface contributes to the low initial uptake. Depending upon the pore size distribution, the capillary condensation in the pore occurs as the pressure rises. This phenomenon gives rise to a sharp increase in the adsorption uptake in the relative pressure range of 0.4-0.6. After the pore filling is achieved, the adsorption plateau region prevails till the saturation pressure. The isotherm equation is typically expressed as follows:

$$\frac{w}{w_s} = \frac{1}{C}\left[tan^{-1}\left(\frac{x-A}{B}\right) - tan^{-1}\left(\frac{-A}{B}\right)\right] \tag{4.5}$$

where, A is dependent upon the temperature as follows:

$$A = \exp\left(A_0 + \frac{A_1}{T}\right) \tag{4.6}$$

The coefficient C is expressed as the function of the constants A and B, such that at the pressure ratio $x = 1$, the uptake w is equal to the maximum uptake capacity w_s.

$$C = \left[tan^{-1}\left(\frac{1-A}{B}\right) - tan^{-1}\left(\frac{-A}{B}\right)\right] \tag{4.7}$$

The coefficients for the Type III, Type IV, and Type V isotherms are taken from the study by Muttakin et al.[153]. Table 4.1 shows the adsorption material pair and adsorption isotherm coefficients used in the study.

Table 4.1: Adsorption isotherm data

Type	Adsorption material	Isotherm coefficients
I	Water/Type RD2560 Silica gel	w_0=0.335 kg kg^{-1} E=4729.78 kJ kg^{-1} n=1.428
III	Water/Dried fruits	w_m=12.5 % c_0=1.7×10^{-4} k_0=1.77 ΔH_1=22.7 kJ kg^{-1} ΔH_2=-1.53 kJ kg^{-1}
IV	Water/Polymer carbon (adsorption)	n_i=[2.8,0.1,0.01,0.5] N_{mi}= [0.1,0.1,3,1] (g cm^{-3}) E_{ai}= [2.407, 2.651, 2.651, -10.186] (kJ mol^{-1}) $i\epsilon[1,4]$
V	Water/BPL Carbon (Adsorption)	A_0=0.51 A_1=-313 K B=0.122

	w_s=0.41 kg kg^{-1}

4.1.2 Isosteric heat of adsorption

The isosteric heat of adsorption is generally calculated by invoking the Clausius-Clapeyron equation. Despite its accuracy in characterizing the water vapor adsorption heat values, this formulation leads to inaccuracies in the isosteric heat of adsorption values for the high pressure adsorption processes. These inaccuracies are caused by the assumption of the ideal gas behavior and negligible specific volume of the adsorbed phase. Therefore, an accurate model for the isosteric heat of adsorption applicable to a wide range of operating pressure is essential in characterizing the thermodynamic behavior of the adsorbed phase. The fundamental definition of the isosteric heat of adsorption (q_{st}) is expressed by Equation (4.8) [102].

$$q_{st} = \left.\frac{\partial Q}{\partial m_a}\right|_{P,T} \tag{4.8}$$

Equation (4.8) describes the isosteric heat of adsorption as the differential heat released (Q) with respect to the increase in the adsorbed phase mass (m_a) at constant pressure and temperature. This differential heat can be expressed as the product of temperature and differential entropy of the adsorption system, as given in Equation (4.9).

$$-\delta Q = T d\hat{S} \tag{4.9}$$

Here, $d\hat{S}$ represents the differential extensive entropy of the adsorption system. An extensive property denotes that the property is dependent upon mass of the system. The negative sign is appended to δQ to indicate the exothermal nature of the adsorption process. This equation is derived from the first law of thermodynamics for open system

($\delta Q = d\hat{U} + \delta W$) and Gibbs equation for differential internal energy ($d\hat{U} = Td\hat{S} - pd\hat{V}$). The differential entropy term $d\hat{S}$ can be expressed as the sum of the adsorbent mass, adsorbed phase, and gaseous phase differential entropy ($d\hat{S}_a + d\hat{S}_g + d\hat{S}_{ads}$). Applying this expression in Equation (4.9), the following equation is derived:

$$q_{st} = -T\left(\left.\frac{\partial \hat{S}_g}{\partial m_a}\right|_{P,T} + \left.\frac{\partial \hat{S}_a}{\partial m_a}\right|_{P,T}\right) \tag{4.10}$$

In this equation, the partial differential adsorbent entropy with respect to adsorbed phase mass ($\frac{\partial \hat{S}_{ads}}{\partial m_a}$) is ignored, as the adsorbent is assumed to be inert. The two partial differential terms on the R.H.S of Equation (4.10) are calculated at the constant pressure and temperature, since all the macroscopic properties depend upon three independent variables (m_a, P, and T). During the adsorption process, the gasoues phase adsorbate gets adsorbed onto the pore surface of the adsorbent to form the adsorbed phase. Thus, the reduction in the amount of gaseous adsorbate should be equal to the increase in the adsorbed phase mass. This is mathematically expressed as follows:

$$\begin{cases} dm_a = -dm_g \\ \dfrac{\partial}{\partial m_a} = -\dfrac{\partial}{\partial m_g} \end{cases} \tag{4.11}$$

Using the partial differential expression from Equation (4.11) in Equation (4.10), we get the following equation:

$$q_{st} = -T\left(-\left.\frac{\partial \hat{S}_g}{\partial m_g}\right|_{P,T} + \left.\frac{\partial \hat{S}_a}{\partial m_a}\right|_{P,T}\right) \tag{4.12}$$

The expression $\left.\frac{\partial \hat{S}_g}{\partial m_g}\right|_{P,T}$ can be expressed as the specific gaseous entropy s_g, since the macroscopic gaseous phase entropy $\hat{S}_g$ is independent upon the amount of the gaseous phase mass. However, $\hat{S}_a$ is dependent upon all the three independent variables. Thus, the second term on the R.H.S of Equation (4.12) is derived by applying the formulation for chemical equilibrium between the adsorbed and gaseous phase. This chemical equilibrium is represented as the chemical potential balance between these two phases, which is expressed as follows:

$$\mu_g \cong \mu_a \Rightarrow d\mu_g = d\mu_a \tag{4.13}$$

Where, μ denotes the chemical potential. The equality between the chemical potential also implies the same between the corresponding differential values, as shown in Equation (4.13). The dependence of the differential chemical potential on the differential pressure, temperature, and adsorbed phase mass can be described using the total differential formula. This relation for both the gaseous and adsorbed phase are given as follows:

$$\begin{cases} d\mu_a = \left.\dfrac{\partial \mu_a}{\partial T}\right|_{P,m_a} dT + \left.\dfrac{\partial \mu_a}{\partial P}\right|_{T,m_a} dP + \left.\dfrac{\partial \mu_a}{\partial m_a}\right|_{P,T} dm_a \\ d\mu_g = \left.\dfrac{\partial \mu_g}{\partial T}\right|_{P,m_g} dT + \left.\dfrac{\partial \mu_g}{\partial P}\right|_{T,m_g} dP + \left.\dfrac{\partial \mu_g}{\partial m_g}\right|_{P,T} dm_g \end{cases} \tag{4.14}$$

The expressions for the differential chemical potential contain the corresponding partial differentials with respect to the temperature, pressure, and adsorbed phase mass, while keeping the rest of the two properties constant in each differential term. These partial differentials are expressed as the differentials of the macroscopic properties by using the Maxwell relations. These expressions for the adsorbed phase properties are given as follows:

$$\begin{cases} \left.\dfrac{\partial \mu_a}{\partial T}\right|_{P,m_a} = -\left.\dfrac{\partial \hat{S}_a}{\partial m_a}\right|_{P,T} \\ \left.\dfrac{\partial \mu_a}{\partial P}\right|_{T,m_a} = \left.\dfrac{\partial \hat{V}_a}{\partial m_a}\right|_{P,T} = v_a \\ \left.\dfrac{\partial \mu_g}{\partial T}\right|_{P,m_g} = -\left.\dfrac{\partial \hat{S}_g}{\partial m_g}\right|_{P,T} = -s_g \\ \left.\dfrac{\partial \mu_g}{\partial P}\right|_{T,m_g} = \left.\dfrac{\partial \hat{V}_g}{\partial m_g}\right|_{P,T} = v_g \end{cases} \tag{4.15}$$

The derivation of these equations is provided in the appendix B. In Equation (4.15), the partial differential of the extensive volume of the gaseous phase and adsorbed phase with respect to corresponding masses are written as the intensive specific volumes in the respective phases (v_a and v_g). Substituting these expressions in Equation (4.14), the following expressions of the adsorbed phase and gaseous phase differential chemical potentials are found out:

$$\begin{cases} d\mu_a = -\left.\dfrac{\partial \hat{S}_a}{\partial m_a}\right|_{P,T} dT + v_a dP + \left.\dfrac{\partial \mu_a}{\partial m_a}\right|_{P,T} dm_a \\ d\mu_g = -s_g dT + v_g dP + \left.\dfrac{\partial \mu_g}{\partial m_g}\right|_{P,T} dm_g \end{cases} \tag{4.16}$$

Applying the chemical equilibrium defined by Equation (4.13) in Equation (4.16), the following correlation is expressed:

$$-\left.\frac{\partial \hat{S}_a}{\partial m_a}\right|_{P,T} dT + v_a dP + \left.\frac{\partial \mu_a}{\partial m_a}\right|_{P,T} dm_a = -s_g dT + v_g dP + \left.\frac{\partial \mu_g}{\partial m_g}\right|_{P,T} dm_g \tag{4.17}$$

The third term representing the partial differential of the chemical potential with respect to mass of the gaseous adsorbate and adsorbed phase on the L.H.S and R.H.S of Equation (4.17) can be shown to be equal by applying Equations (4.11) and (4.13) ($\left.\frac{\partial \mu_a}{\partial m_a}\right|_{P,T} dm_a = \left.\frac{\partial \mu_g}{\partial m_g}\right|_{P,T} dm_g$). Thus, the expression for the term $\left.\frac{\partial \hat{S}_a}{\partial m_a}\right|_{P,T} dT$ is found out as follows:

$$\left.\frac{\partial \hat{S}_a}{\partial m_a}\right|_{P,T} dT = s_g dT - (v_g - v_a) dP \tag{4.18}$$

Taking derivative with respect to temperature on both sides of Equation (4.18) at constant pressure and m_a, the following expression is derived:

$$\left.\frac{\partial \hat{S}_a}{\partial m_a}\right|_{P,T} = s_g - (v_g - v_a) \left.\frac{\partial P}{\partial T}\right|_{m_a} \tag{4.19}$$

The partial differential of pressure with respect to temperature at constant m_a ($\frac{\partial P}{\partial T}\big|_{m_a}$) is calculated from the adsorption isotherm equation. Replacing the expression for $\frac{\partial \hat{S}_a}{\partial m_a}\Big|_{P,T}$ from Equation (4.19) in Equation (4.10), we get the following expression for the isosteric heat of adsorption (q_{st}):

$$q_{st} = -T \left(s_g - (v_g - v_a) \left.\frac{\partial P}{\partial T}\right|_{m_a} - s_g \right) \tag{4.20}$$

Therefore, the final expression of q_{st} can be written as follows:

$$q_{st} = T \left(v_g - v_a\right) \left.\frac{\partial P}{\partial T}\right|_{w} \tag{4.21}$$

Since the adsorbent is considered inert during the adsorption, the mass of the adsorbed phase (m_a) is replaced by the equilibrium uptake w, which is expressed as $w = \frac{m_a}{M_{ads}}$. Thus, the isosteric heat of adsorption is dependent upon the temperature, specific volume of gaseous and adsorbed phase, and partial differential of pressure with respect to temperature.

The isotherm models listed in the previous section can be applied to the Equation (4.21) to develop the respective formulation for the isosteric heat of adsorption. The q_{st} expressions for the IUPAC Type-I isotherm (D-A isotherm) equation at different operating pressure range is provided in the following equation:

$$q_{st} = \begin{cases} P v_g \left[\dfrac{T}{P_{sat}} \dfrac{dP_{sat}}{dT} + \ln \dfrac{P_{sat}}{P} \right] \text{(At low pressure)} \\ P(v_g - v_a) \left[\dfrac{T}{P_{sat}} \dfrac{dP_{sat}}{dT} + \ln \dfrac{P_{sat}}{P} + \dfrac{\alpha}{n} \left(\dfrac{E}{R} \right)^n \left(T \ln \dfrac{P_{sat}}{P} \right)^{1-n} \right] \\ \text{(At high pressure)} \end{cases} \tag{4.22}$$

4.1.3 Specific entropy

The extensive entropy of the adsorbed phase ($\hat{S}_a$) is dependent upon the independent variables, viz., pressure, temperature, and mass of the adsorbed phase. Therefore, the differential entropy can be expressed using the mathematical rule of the total differential, as follows:

$$d\hat{S}_a = \left.\frac{\partial \hat{S}_a}{\partial T}\right|_{P,m_a} dT + \left.\frac{\partial \hat{S}_a}{\partial P}\right|_{T,m_a} dP + \left.\frac{\partial \hat{S}_a}{\partial m_a}\right|_{P,T} dm_a \tag{4.23}$$

Here, the partial differentials of $\hat{S}_a$ on the R.H.S. are calculated with respect to temperature, pressure and adsorbed phase mass, respectively. Gibbs equations and Maxwell relations can be applied to formulate the correlations for the pressure and temperature based partial differentials of $\hat{S}_a$. The resulting formulations are provided as follows:

$$\left.\tfrac{\partial \hat{S}_a}{\partial T}\right|_{P,m_a} = m_a \tfrac{c_{ade}}{T}, \left.\tfrac{\partial \hat{S}_a}{\partial P}\right|_{T,m_a} = -m_a \left.\tfrac{\partial v_a}{\partial T}\right|_P \tag{4.24}$$

Where, c_{ade} and v_a represent the specific heat capacity and the specific volume of the adsorbed phase. The derivation steps for these equations are provided in the appendix B. Thus, the first two terms in Equation (4.23) can be expressed using the adsorbed phase material properties. Concomitantly, the third term is already derived in the preceding section and the resulting expression is given as Equation (4.19).

Now we have the formulations for the partial derivative of extensive entropy with respect to temperature and pressure given by Equation (4.24) and that with respect to mass of the adsorbed phase given by Equation (4.19). After substituting these terms into the right-hand side of Equation (4.23), the total derivative of the adsorbed phase extensive entropy can be defined as:

$$d\hat{S}_a = m_a \frac{c_{ade}}{T} dT - m_a \left.\frac{\partial v_a}{\partial T}\right|_P dP + \left\{ s_g - (v_g - v_a) \left.\frac{\partial P}{\partial T}\right|_{m_a} \right\} dm_a \tag{4.25}$$

The absolute value of the extensive entropy of the adsorbed phase can be calculated by integrating both sides of Equation (4.25). The three terms on the R.H.S. are integrated with respect to temperature, pressure, and adsorbed phase, respectively. The integrated expression is depicted in the following equation:

$$\begin{aligned} \hat{S}_a = \hat{S}_a^{ref} + \int_{T_{ref}}^{T} m_a \frac{c_{ade}}{T} dT - \int_{P_{ref}}^{P} m_a \left.\frac{\partial v_a}{\partial T}\right|_P dP + \\ \int_{m_a^{ref}}^{m_a} \left\{ s_g - (v_g - v_a) \left.\frac{\partial P}{\partial T}\right|_{m_a} \right\} dm_a \end{aligned} \tag{4.26}$$

Where, $\hat{S}_a^{ref}$ represents the reference extensive entropy of the adsorbed phase defined by $\hat{S}_a^{ref} = m_a^{ref} \times s_g(T_{ref}, P_{ref})$. A fixed reference state is chosen as the lower limit to perform these integrations. These reference points are the reference extensive entropy ($\hat{S}_a^{ref}$), temperature (T_{ref}), pressure (P_{ref}), and adsorbed phase mass (m_a^{ref}). The choice of the reference adsorbed phase mass or the uptake needs to be defined as the equilibrium uptake corresponding to the reference pressure and temperature ($m_a^{ref}(P_{ref}, T_{ref})$). However, the choice of the reference uptake is generally vague in the existing literature. For instance, Chakraborty et al. [104] assumed the reference uptake as zero, even though the reference temperature and pressure were finite non-zero values. This inconsistent assumption of the reference states contributes to the anomalous behavior of the thermodynamic property surfaces. Dividing Equation (4.26) by the mass of the adsorbent (M_{ads}), the formulation of extensive entropy per mass of the adsorbent can be expressed in terms of equilibrium uptake (w).

$$\frac{\hat{S}_a}{M_{ads}} = w^{ref} s_g(T_{ref}, P_{ref}) + \int_{T_{ref}}^{T} w \frac{c_{ade}}{T}\, dT - \int_{P_{ref}}^{P} w \left.\frac{\partial v_a}{\partial T}\right|_P dP + \int_{w^{ref}}^{w} \left\{ s_g - (v_g - v_a) \left.\frac{\partial P}{\partial T}\right|_w \right\} dw \quad (4.27)$$

The left-hand side of Equation (4.27) can be written as $w \times s_a$, where s_a is the adsorbed phase specific entropy. The final expression of the specific entropy of the adsorbed phase is obtained as follows:

$$s_a = \frac{w^{ref}}{w} s_g(T_{ref}, P_{ref}) + \frac{1}{w}\int_{T_{ref}}^{T} w \frac{c_{ade}}{T}\, dT - \frac{1}{w}\int_{P_{ref}}^{P} w \left.\frac{\partial v_a}{\partial T}\right|_P dP + \frac{1}{w}\int_{w^{ref}}^{w} \left\{ s_g - (v_g - v_a) \left.\frac{\partial P}{\partial T}\right|_w \right\} dw \quad (4.28)$$

4.1.4 Specific enthalpy

The specific enthalpy of the adsorbed phase can be formulated by considering the energy balance during the adsorption process. The adsorption system can be considered as an open thermodynamic system, where the formation of the adsorbed phase is associated with the release of the adsorption heat out of the system. The initial specific enthalpy of the adsorbate corresponds to that of the gaseous phase. Likewise, the final state of the adsorbate is the adsorbed phase, generated at the end of the adsorption process. The adsorbed phase in the adsorbent pores (micropore/mesopore) is generated by the interaction of the adsorbate molecules with the adsorbent molecules by the virtue of the van der Waals and electrostatic interactions. As the adsorbate molecules occupy the energetically favorable positions in the porous structure, the molecular movement (translation and rotation) gets restricted. Thus, the kinetic energy associated to this molecular movement is released in the form of the heat of adsorption. This heat release results in the decrease in the enthalpy of the adsorbed phase than the gaseous phase. Therefore, the enthalpy balance of the adsorbate can be written as follows:

$$h_a(P,T,w) = h_g(P,T) - q_{st}(P,T,w) \tag{4.29}$$

Where, h_a and h_g denote the specific enthalpy of the adsorbed phase and gaseous phase, respectively.

4.1.5 Specific heat capacity

The fundamental definition of the specific heat capacity is given as the differential enthalpy with respect to temperature. In case of adsorbed phase, this definition can be formulated as the following equation:

$$c_{ade} = \left.\frac{\partial h_a}{\partial T}\right|_w \tag{4.30}$$

Here, the derivate of the enthalpy is taken keeping the uptake constant. Using the adsorbed phase enthalpy formulation derived in Equation (4.29), the following formulation for the adsorbed phase specific heat capacity (c_{ade}) is obtained:

$$c_{ade} = \left.\frac{\partial h_g}{\partial T}\right|_w - \left.\frac{\partial q_{st}}{\partial T}\right|_w \tag{4.31}$$

Here, the partial derivative of the quantities h_g and q_{st} are taken at a constant uptake value. The gaseous phase specific heat capacity ($c_{p,g}$) is defined as the partial differential of the specific enthalpy with respect to temperature at constant pressure ($c_{p,g} = \left.\frac{\partial h_g}{\partial T}\right|_P$). In the existing literature [105], the differential in the first term on the R.H.S. of Equation (4.31) was calculated at the constant pressure, instead of the constant uptake. This led to the inconsistency in the derivation of the adsorbed phase specific heat capacity formulation. Chakraborty et al. [103] derived the c_{ade} formulation using the Jacobian based mathematical technique, whose resulting expression was different than the ones found by Rahman et al. [105]. For accurate derivation of the c_{ade} values, a chain rule based mathematical technique is used in calculating the partial differentials in Equation (4.31). The total differential of h_g can be expressed as follows:

$$dh_g = \left.\frac{\partial h_g}{\partial T}\right|_P dT + \left.\frac{\partial h_g}{\partial P}\right|_T dP \tag{4.32}$$

Since, the equilibrium adsorption isotherm equation is a homogeneous equation of pressure, temperature, and uptake, the chain rule can be applied to any of these variables. Therefore, the total differential pressure can be expressed as follows:

$$dP = \left.\frac{\partial P}{\partial T}\right|_w dT + \left.\frac{\partial P}{\partial w}\right|_T dw \tag{4.33}$$

Replacing the expression for dP from Equation (4.33) in Equation (4.32) and taking derivative on both sides of the resulting equation, the following relationship is obtained:

$$\left.\frac{\partial h_g}{\partial T}\right|_w = \left.\frac{\partial h_g}{\partial T}\right|_P + \left.\frac{\partial h_g}{\partial P}\right|_T \left.\frac{\partial P}{\partial T}\right|_w \tag{4.34}$$

Now, the first term on the R.H.S of Equation (4.34) is the specific heat capacity of the gaseous phase ($c_{p,g}$). The partial differential of h_g with respect to pressure at constant temperature is obtained using the Gibbs equations and Maxwell relations. Therefore, this quantity can be written as follows:

$$\left.\frac{\partial h_g}{\partial P}\right|_T = v_g - T\left.\frac{\partial v_g}{\partial T}\right|_P \tag{4.35}$$

The detailed derivation of Equation (4.35) is illustrated in the Appendix B.3. The expression for the partial differential of pressure with respect to temperature at constant uptake ($\left.\frac{\partial P}{\partial T}\right|_w$) can be expressed in terms of the isosteric heat of adsorption (q_{st}) from Equation (4.21). This expression is given as follows:

$$\left.\frac{\partial P}{\partial T}\right|_w = \frac{q_{st}}{T\left(v_g - v_a\right)} \tag{4.36}$$

Hence, the expressions obtained from Equations (4.35) and (4.36) can be applied in Equation (4.34) to form the following equation:

$$\left.\frac{\partial h_g}{\partial T}\right|_w = c_{p,g} + \left(v_g - T\left.\frac{\partial v_g}{\partial T}\right|_P\right)\frac{q_{st}}{T\left(v_g - v_a\right)} \tag{4.37}$$

Finally, substituting the formalism for $\left.\frac{\partial h_g}{\partial T}\right|_w$ in Equation (4.31), the adsorbed phase specific heat capacity can be expressed as a function of gaseous phase specific heat capacity, specific volume, isosteric heat of adsorption and its partial differential with respect to temperature.

$$c_{ade} = c_{p,g} + \left(v_g - T\left.\frac{\partial v_g}{\partial T}\right|_P\right)\frac{q_{st}}{T\left(v_g - v_a\right)} - \left.\frac{\partial q_{st}}{\partial T}\right|_w \tag{4.38}$$

The resulting expression slightly deviates from the Jacobian based approach delineated by Chakraborty et al. [103, 104]. In the literature, the denominator of the second term of the c_{ade} expression contains only the specific volume of the gaseous phase. Whereas, the present expression includes the difference between the gaseous and adsorbed phase specific volume. The current model is able to consider both the low-pressure and high-pressure adsorption conditions, since at high pressure the value of v_a is not negligible. Furthermore, the third term in the c_{ade} expression is calculated at constant pressure in the literature instead of constant uptake derived in the present correlation. This difference may result in significant variation in the obtained c_{ade} values, due to the non-linear dependence of q_{st} on the pressure, temperature, and uptake.

4.2 Adsorption Heat Transformer cycle

4.2.1 Working principle of adsorption heat transformer cycle

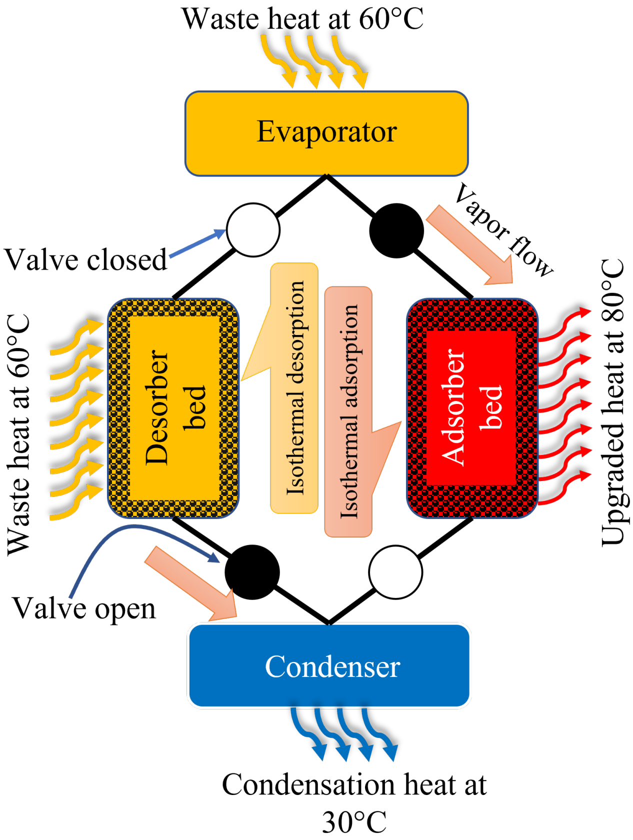

Figure 4.1: Process flow schematic of the adsorption heat transformer cycle

Fig. 4.1 depicts the process flow schematic of the AHT cycle. The corresponding equilibrium cycle is depicted on the pressure-temperature-uptake plane as shown in Fig. 4.1b. The AHT cycle consists of three major components, viz., evaporator, sorption bed, and condenser. These components are connected via the gas valves, which control the working fluid flow among the components. Two sorption beds are connected to both the evaporator and condensers, where the gas valve's opening/closing status is highlighted in Fig. 4.1. Here, the sorption bed which is connected to the evaporator and the gas valve is kept open, is referred as the adsorber bed. Likewise, the sorption bed connected to the condenser with the open gas valve is denoted as the desorber bed. As the names suggest, the adsorber and desorber beds are responsible for the adsorption and desorption phenomena in the AHT cycle. The adsorber bed can act as the desorber bed when the gas valve is opened to the condenser and closed to the evaporator and vice versa. Thus, the periodic continuous operation of the AHT cycle is ensured via the repetitive opening/closing of the valves. The adsorber (desorber) bed is further equipped as a heat exchanger for supplying (receiving) the upgraded heat (waste heat). Water vapor is chosen as the working fluid which gets adsorbed/desorbed in the adsorber/desorber bed. This water vapor can be generated by supplying either pure water or seawater (in case the AHT cycle is used for desalination along with the heat upgrading). Silica gel is ubiquitous as the solid adsorbent material for adsorption cooling and desalination applications. Here, the silica gel of type RD-2560 is used to depict the working principle of the AHT cycle.

The AHT cycle upgrades the low-grade waste heat using the principle of pressure swing adsorption phenomenon. This process is different from the adsorption cooling cycle, where the pressurization/depressurization is carried out via thermal swing adsorption phenomena. It can be seen that this cycle operates among three temperature levels. These are identified as heat source temperature of the waste heat source (T_M), heat sink temperature (T_L), and the upgraded heat supply temperature (T_H). These temperature values are depicted as T_L=30 °C, T_M=60 °C, and T_H=80 °C. The waste heat is applied to evaporate the incoming water/seawater in the evaporator to generate the gaseous vapor. Due to the evaporation of the water, the evaporator pressure remains at the saturation pressure corresponding to the temperature T_M ($P_{evap} = P_{sat}(T_M)$). The condenser remains at the saturation pressure at temperature T_L ($P_{cond} = P_{sat}(T_L)$). Since, $T_L < T_M$, the evaporator is at a higher pressure than the condenser ($P_{cond} < P_{evap}$). Initially, the adsorber bed is at the temperature T_M and pressure P_{cond}. When the gas valve is opened between the evaporator and the adsorber bed, the water vapor with higher pressure (P_{evap}) flows from the former to the latter. Since, the adsorption uptake is directly proportional to the pressure, the adsorption phenomenon initiates in the adsorber bed. The heat of adsorption is released due to the formation of the adsorbed phase in the pores of the silica gel adsorbent. If there is no heat exchange between the adsorber bed and the application requiring the upgraded heat, then this adsorption heat is transformed into the sensible heat. This sensible heat increases the temperature of the adsorbed phase, the adsorbent material, and the heat exchanger thermal mass. This temperature lifting phase is termed as the ‘preheating’ phase of the AHT cycle. More specifically, this can be referred as the ‘non-isosteric preheating’ phase, due to the uptake consumption requirement for increasing the temperature of the bed. During the ‘preheating’ phase, the temperature and pressure in the bed increase simultaneously. The pressure reaches an intermediate value between the P_{evap} and P_{cond}, which is determined by the heat supply temperature T_H. After reaching the desired T_H, the heat exchanger between the adsorber bed to the required application is connected. Thus, the heat of adsorption generated during the pressurization of the bed is extracted via this heat exchanger. Since, the heat of adsorption is no longer used for the temperature increase in the bed, the adsorption process continues at the constant temperature T_H. Thus, this phase is denoted as the ‘isothermal adsorption’ phase. This phase stops when the pressure of the adsorber bed reaches the evaporator pressure. In Fig. 4.1, only the ‘isothermal adsorption’ phase in the adsorber bed is depicted.

The regeneration process of the adsorber bed is carried out via opening the valve between the adsorber bed and the condenser. Furthermore, the valve between the adsorber bed and evaporator is closed. Henceforth, the adsorber bed is identified as the desorber bed. The initial pressure and temperature of the desorber bed are P_{evap} and T_H, respectively. Due to the influence of the low-pressure condenser (P_{cond}), the adsorbed vapor starts to flow from the desorber bed to the condenser. Thus, the uptake in the desorber bed continuously decreases. This desorption process is endothermic in nature, which requires a heat of desorption. Initially, the heat exchanger between the desorber bed and the waste heat source is kept disconnected. This action results in the conversion of the sensible heat provided by the desorber bed thermal mass to the requisite heat of desorption. Therefore, the temperature of the desorber bed starts to decrease. This phase is termed as the 'non-isosteric precooling' phase, due to the decrease in the uptake. After reaching the waste heat temperature T_M, the 'precooling' phase is stopped by connecting the heat exchanger between the desorber bed and waste heat source. An intermediate pressure is reached within the bed, which is still higher than the P_{cond}. The subsequent desorption process is carried out isothermally, since the requisite heat of desorption is provided by the waste heat source at the temperature T_M. This 'isothermal desorption' phase concludes once the pressure in the desorber bed becomes equal to the condenser pressure. Fig. 4.1 highlights the 'isothermal desorption' phase in the desorber bed only.

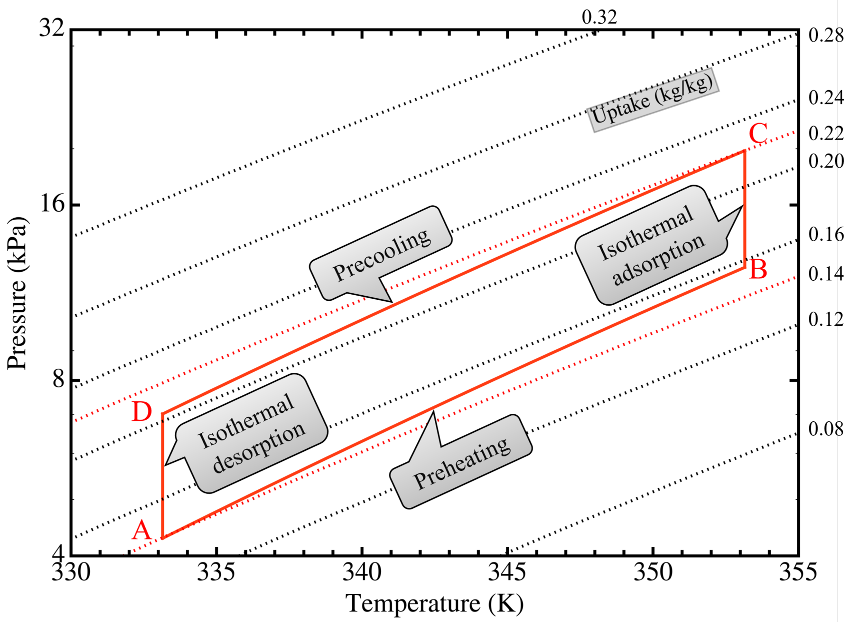

Figure 4.2: Cycle diagram on pressure-temperature-uptake plane of the adsorption heat transformer cycle

Fig. 4.2 illustrates the AHT cycle in the pressure-temperature-uptake plane. The operating temperature values are the same as given in the Fig. 4.1. The individual phases of the AHT cycle are pointed out in the figure. The paths 'A-B', 'B-C', 'C-D', and 'D-A' denote the 'preheating', 'isothermal adsorption', 'precooling', and 'isothermal desorption' phases, respectively. Points 'B' and 'D' refer to the end of 'preheating' and 'precooling' phases, respectively. As mentioned earlier, these points lie between the two pressure levels (P_{evap} and P_{cond}). Hereby, these are denoted as preheating (P_{ph}) and precooling (P_{pc}) intermediate pressure, respectively. An uptake consumption of approximately $0.02\,\mathrm{kg\,kg^{-1}}$ is required to increase the temperature from T_M=60 °C to T_H=80 °C. This uptake consumption is calculated by taking the difference between the uptake at point 'B' ($w(P_{ph}, T_H)$) and point 'A' ($w(P_{cond}, T_M)$). Likewise, the precooling uptake difference is calculated by taking the difference of uptakes at point 'C' ($w(P_{evap}, T_H)$) and point 'D' ($w(P_{pc}, T_M)$). A detailed mathematical description of the energy balance in the AHT cycle is provided in the following section.

4.2.2 Energy balance in adsorption heat transformer cycle

Preheating phase

During the 'non-isosteric preheating' phase of the AHT cycle, the increase in the temperature and pressure of the adsorber bed is owed to the heat of adsorption provided by the finite adsorption amount. Thus, the energy balance is considered between the sensible heat gain by the adsorber bed and the latent heat of adsorption. The latent heat is determined by taking the cumulative heat of adsorption during the preheating uptake consumption. The corresponding expression is given as follows:

$$e_{ph}^{lat} = \int_{w_1}^{w_2} q_{st}\, dw \tag{4.39}$$

Here, e denotes the specific heat per unit mass of adsorbent, w refers to the uptake value in $\mathrm{kg\,kg^{-1}}$, and q_{st} is the isosteric heat of adsorption. The integral of q_{st} is taken in the uptake range from $w_1(P_{cond}, T_M)$ to $w_2(P_{ph}, T_H)$. These uptake values refer to the points 'A' and 'B' in Fig. 4.2, respectively. The sensible heat is gained by three components of the adsorber beds: (i) adsorbent material, (ii) adsorbed phase water, (iii) heat exchanger material. The sensible heat gain by the adsorbent material is given by the following equation:

$$e_{ph,ads}^{sen} = \int_{T_M}^{T_H} c_{p,ads}\, dT \tag{4.40}$$

Where, the subscript *sen,ads* denotes the sensible heat gain in the adsorbent and $c_{p,ads}$ is the specific heat capacity of the adsorbent. The formulation of $c_{p,ads}$ as a function of temperature is determined by the following empirical correlation:

$$c_{p,ads} = a + bT + cT^2 + dT^3 \tag{4.41}$$

The coefficients in Equation (4.41) for silica gel adsorbent is listed in Table 4.2. These values determine the $c_{p,ads}$ value in $\mathrm{J\,kg^{-1}\,K^{-1}}$.

Table 4.2: Coefficients of Equation (4.41) for specific heat capacity of silica gel adsorbent [217]

Coefficient	**Value**
a	-9344.51
b	87.8609
c	-0.253036
d	0.000247696

The adsorbed phase water can be assumed equivalent to the liquid phase water. Thus, the liquid phase properties can be used to calculate the adsorbed phase heat gain. The formulation is given as follows:

$$e^{sen}_{ph,ade} = \int_{T_M}^{T_H} w(P,T) c_{p,l} \, dT \tag{4.42}$$

Here, the subscript *ade* is the adsorbed phase. The integral includes the liquid phase specific heat capacity $c_{p,l}$ and the adsorption uptake as a function of pressure and temperature. The sensible heat gain by the heat exchanger mass is characterized similarly as the adsorbent mass as follows:

$$e^{sen}_{ph,HX} = \frac{m_{HX}}{m_{ads}} \int_{T_M}^{T_H} c_{p,HX} \, dT \tag{4.43}$$

The additional mass ratio of the heat exchanger mass and adsorbent mass is multiplied with the integral to maintain the unit consistency of the specific heat obtained. $c_{p,HX}$ denotes the specific heat capacity of the heat exchanger mass. For the present analysis, the Aluminium is chosen as the heat exchanger mass. The $c_{p,HX}$ of Aluminium is determined as a function of temperature by the following empirical formulation:

$$c_{p,HX}(T) = (4.94 + 0.00296T) \times \frac{4184}{26.9815} \tag{4.44}$$

Here, the unit of $c_{p,HX}$ is $\mathrm{J\,kg^{-1}\,K^{-1}}$. Therefore, the total sensible heat is expressed as follows:

$$e_{ph}^{sen} = e_{ph,ads}^{sen} + e_{ph,ade}^{sen} + e_{ph,HX}^{sen} \tag{4.45}$$

The energy balance between the sensible heat gain and latent adsorption heat supply is achieved by equating Equations (4.39) and (4.45). This equality is expressed as follows:

$$e_{ph}^{lat}(P_{ph}; T_M, T_H, P_{cond}) = e_{ph}^{sen}(T_M, T_H) \tag{4.46}$$

Here, the independent variables are shown for the sensible and latent heat. From this energy balance, the value of the preheating intermediate pressure P_{ph} is obtained. This value is dependent upon the working temperature range, isotherm characteristics, and thermo-physical properties of the adsorbent and adsorbate. Once the P_{ph} is obtained, the value of the net preheating uptake consumption can be obtained as $w_2(P_{ph}, T_H) - w_1(P_{cond}, T_M)$.

Isothermal adsorption phase

The preheating phase in the AHT cycle is followed by the isothermal adsorption phase. During this phase, the upgraded heat at the higher temperature T_H is supplied to the application. This heat of adsorption is expressed as the following equation:

$$e_{ad}^{lat} = \int_{w_2}^{w_3} q_{st}\, dw \tag{4.47}$$

Here, the subscript *ad* denotes the isothermal adsorption phase in the AHT cycle and w_3 is the equilibrium uptake at pressure P_{evap} and temperature T_H. This latent heat of adsorption is accompanied by the sensible heat generation due to the enthalpy addition by the increasing pressure of the adsorbed phase. The sensible enthalpy addition is formulated as follows:

$$e_{ad}^{sen} = \int_{w_2}^{w_3} h_l(w)\, dw \tag{4.48}$$

Where, $h_l(w)$ refers to the saturated liquid enthalpy of the adsorbed phase as a function of the uptake. These latent and sensible heat components constitute the upgraded heat supply, expressed as:

$$e_{ad} = e_{ad}^{lat} + e_{ad}^{sen} \tag{4.49}$$

Precooling and isothermal desorption phase

During the ‘non-isosteric precooling’ phase of the AHT cycle, the governing heat balance equations are equivalent to that obtained for the preheating phase. Thus, the heat balance equation similar to Equation (4.46) can be written as follows:

$$e_{pc}^{lat}(P_{pc}; T_M, T_H, P_{evap}) = e_{pc}^{sen}(T_M, T_H) \tag{4.50}$$

Here, the subscript *pc* denotes the precooling phase. The left-hand side in Equation (4.50) is the latent specific heat of desorption and the right-hand side is the sensible heat supplied by the desorber bed. Ideally, the uptake desorbed during the precooling phase should be equal to the uptake consumed during the preheating phase. Equation (4.50) can be further expressed by expanding the respective terms in both sides as follows:

$$\int_{w_3(P_{evap},T_H)}^{w_4(P_{pc},T_M)} q_{st}\, dw = \int_{T_H}^{T_M} \left(c_{p,ads}(T) + w(T,P)c_{p,l}(T) + \frac{m_{HX}}{m_{ads}} c_{p,HX}(T) \right) dT \quad (4.51)$$

From Equation (4.51), the precooling intermediate pressure P_{pc} and subsequently the precooling net desorbed uptake amount (w_3) is determined.

The regeneration process of the AHT cycle is concluded with the isothermal desorption phase after the precooling phase. Similar to the formulation for upgraded adsorption heat supply (Equation (4.49)), the net desorption heat input is calculated as follows:

$$e_{des} = \int_{w_4(P_{pc},T_H)}^{w_1(P_{cond},T_M)} \left(q_{st}(w) + h_l(w) \right) dw \quad (4.52)$$

The total amount of uptake consumption during the preheating and isothermal adsorption phase is given as $w_3 - w_1$. This amount of gaseous adsorbate is generated in the evaporator. The net evaporation heat required for this requisite uptake amount is calculated as follows:

$$e_{evap} = (w_3 - w_1) \times h_{fg}(T_M) \quad (4.53)$$

Where, $h_{fg}(T_M)$ denotes the specific enthalpy of vaporization of the adsorbate at the waste heat source temperature T_M. The desorbed adsorbate vapor gets condensed in the condenser during the precooling and isothermal desorption phases. The net desorbed vapor amount is same as the net uptake consumption. Therefore, the condensation heat released to the condenser is expressed as the following equation:

$$e_{cond} = (w_3 - w_1) \times h_{fg}(T_L) \quad (4.54)$$

Here, the specific enthalpy of vaporization is obtained at the ambient/heat sink temperature (T_L). The total energy balance of the AHT cycle is expressed as follows:

$$e_{evap} + e_{des} = e_{cond} + e_{ad} \tag{4.55}$$

Here, the evaporation and desorption heat are the input energy to the system. The condensation heat and adsorption heat are the output of the AHT cycle.

Performance parameters

The performance of the AHT cycle can be characterized using two parameters, viz., (i) useful heat ratio (UHR), (ii) condensation heat ratio (CHR). The formulation for these two parameters are provided in the following equations:

$$\begin{cases} UHR = \dfrac{e_{ad}}{e_{des} + e_{evap}} \\ CHR = \dfrac{e_{cond}}{e_{des} + e_{evap}} \end{cases} \tag{4.56}$$

It can be seen that the numerators of UHR and CHR contain net upgraded adsorption heat and condensation heat, respectively. The input heat consists of evaporation heat and desorption heat. UHR represents the heat upgrading performance of the AHT cycle. Likewise, CHR determines the desalination performance of the AHT cycle, when the potable water generation is considered from the saline water.

4.3 Thermodynamic framework of adsorption heat transformer cycle

In the previous section, the equilibrium cycle modeling of the AHT cycle is delineated. The intermediate pressures determination and the performance parameters of the AHT cycle are derived for a given temperature lift. However, designing an energy-efficient AHT cycle requires the knowledge of its maximum capability. This information helps in choosing optimum design parameters and operating condition for the optimum performance of the AHT cycle. Furthermore, possible modifications to the AHT cycle's working mechanism need to be explored for improving its performance. Therefore, in this section, the maximum thermodynamic potential determination and the incorporation of the internal heat recovery in the AHT cycle are discussed.

4.3.1 Heat upgrading potential

The primary objective of the AHT cycle is to upgrade the low-grade waste heat temperature to a higher temperature. The maximum value of the temperature lift produced by the AHT cycle can be the characteristic performance limiting parameter of the AHT cycle. Here, three thermodynamic models are proposed to evaluate the said maximum temperature lift. These are listed as (i) Heat engine-heat pump representation, (ii) Entropy balance, (iii) Complete preheating. These methods are described in the following sections.

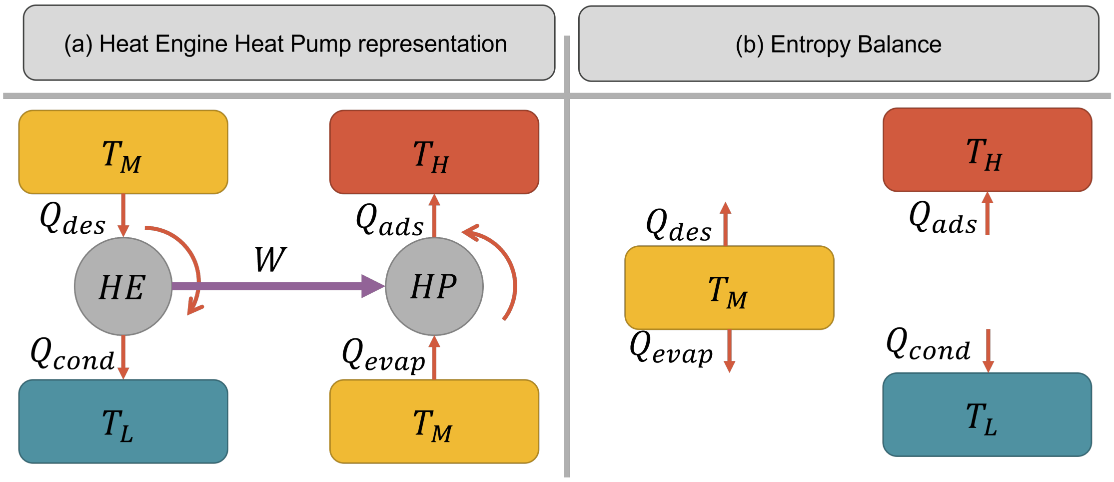

Figure 4.3: Theoretical maximum temperature lift models assuming reversible thermodynamic processes (a) Heat engine heat pump representation, (b) Entropy balance approach

Heat engine-heat pump representation

As already established in cycle description of the AHT cycle in the previous section, the heat exchange occurs among three temperature reservoirs in an AHT cycle. A thermodynamic way to represent these heat interactions is to assume the complete cyclic process as a combination of a heat engine and a heat pump. This representation eradicates the dependence of the process mechanism on the adsorption properties. Fig. 4.3a depicts the schematic of the heat engine-heat pump representation. It can be seen that the heat engine receives the desorption heat Q_{des} from the reservoir with low-grade waste heat temperature T_M. The heat engine then produces a certain amount of work (W) and rejects the condensation heat (Q_{cond}) to the ambient temperature reservoir (T_L). The produced work W is provided to the heat pump working between the temperatures T_M and upgraded heat supply temperature T_H. The heat input and output to and from heat pump are evaporation heat (Q_{evap}) and adsorption heat (Q_{ad}), respectively. Thus, the work produced by the heat engine drives the heat pump to produce the upgraded heat at the temperature T_H. The working mechanism of the heat pump is equivalent to the heat interaction between adsorber bed and the evaporator during the preheating and isothermal adsorption phases. Likewise, the heat engine represents the regeneration of the desorber bed during the precooling and isothermal desorption phase through the interaction with the condenser. Since, the heat engine and heat pump considered are reversible cycles, the net efficiency of the system is equivalent to the Carnot efficiency. This ensures the operation of the system in its maximum potential.

Following equations represent the thermodynamic characterization of the combined heat engine-heat pump system. The energy balance in the heat engine is expressed as follows:

$$Q_{des} = W + Q_{cond} \tag{4.57}$$

The Carnot efficiency of the heat engine system is expressed as Equation (4.58).

$$\eta_{HE} = \frac{W}{Q_{des}} = 1 - \frac{T_L}{T_M} \tag{4.58}$$

Similarly, the expressions for the energy balance and the Carnot coefficient of performance (COP) for the heat pump system are given by Equations (4.59) and (4.60), respectively.

$$Q_{ad} = W + Q_{evap} \tag{4.59}$$

$$COP_{HP} = \frac{Q_{ad}}{W} = \frac{T_H}{T_H - T_M} \tag{4.60}$$

From Equations (4.58) and (4.60), the ratio of adsorption heat to the desorption heat is obtained as follows:

$$\frac{Q_{ad}}{Q_{des}} = \left(1 - \frac{T_L}{T_M}\right)\left(\frac{T_H}{T_H - T_M}\right) \tag{4.61}$$

The ratio of the adsorption and desorption heats can be denoted as the coefficient of performance of the combined HE-HP system. This quantity can further be expressed using the ratio of the isosteric heat of adsorption (q_{st}) values calculated at the respective pressure and temperature states. Therefore, the following equation can be written:

$$COP_{net} = \frac{Q_{ad}}{Q_{des}} = \frac{q_{st}(T_H, P_{sat}(T_M))}{q_{st}(T_M, P_{sat}(T_L))} \tag{4.62}$$

Here, the q_{st} is calculated at the temperature T_H and pressure $P_{sat}(T_M)$ for the adsorption phase, whereas for the desorption phase these states are T_H and $P_{sat}(T_M)$, respectively. Rearranging Equation (4.62), the maximum upgraded temperature obtainable by the HE-HP system is expressed as follows:

$$T_H^{max} = T_M \left[1 - \frac{1}{COP_{net}} \left(1 - \frac{T_L}{T_M}\right)\right]^{-1} \tag{4.63}$$

The net COP considered in this equation is equivalent to the adsorption cooling cycle's COP. Typically, as the cooling cycle approaches cyclic equilibrium, this COP value approaches unity. Similar approximation can be applied to Equation (4.63). Substituting the value of $COP_{net} = 1$ in Equation (4.63), the following equation is obtained:

$$T_H^{max} = \frac{T_M^2}{T_L} \tag{4.64}$$

The expression of T_H^{max} in Equation (4.64) resembles the minimum desorption temperature expression obtained for the adsorption cooling cycle [153]. The resultant expression for T_H^{max} is independent of the adsorption material properties. Hence, this formulation can be used as a benchmark for assessing the AHT cycle's heat upgrading potential.

Entropy balance

The second approach ignores the working mechanism of the heat interaction between the heat engine and the heat pump systems. Here, only the thermal reservoirs and the corresponding heat interaction values are considered to evaluate the maximum heat upgrading potential. The entropy balance approach considers the entropy associated to the heat interactions in the overall AHT cycle. The entropy generation in the system can be considered zero if the AHT cycle is assumed to be reversible. Fig. 4.3b depicts the thermal reservoir temperatures and the associated heat interactions. Using the notations provided in the Fig. 4.3, the following entropy balance equation can be derived:

$$\frac{Q_{des} + Q_{evap}}{T_M} = \frac{Q_{ad}}{T_H} + \frac{Q_{cond}}{T_L} \tag{4.65}$$

The left-hand side of the Equation (4.65) refers to the total input entropy, and the corresponding R.H.S is the total output entropy. Now, the energy balance equation can be written as follows:

$$Q_{des} + Q_{evap} = Q_{ad} + Q_{cond} \tag{4.66}$$

An expression for the maximum upgraded temperature T_H^{max} can be derived by combining Equations (4.65) and (4.66). The resulting equation for the T_H^{max} is given as:

$$T_H^{max} = \left[\frac{1}{T_M} - \frac{Q_{cond}}{Q_{ad}}\left(\frac{1}{T_L} - \frac{1}{T_M}\right)\right]^{-1} \tag{4.67}$$

A heat ratio of condensation heat and adsorption heat is included in Equation (4.67). Using the previous assumption of the equality between the adsorption and desorption heat ($COP_{net} = 1$) in Equation (4.66), the following equality between the heat ratios can be derived:

$$\frac{Q_{cond}}{Q_{ad}} = \frac{Q_{evap}}{Q_{des}} \tag{4.68}$$

Furthermore, the ratio of the evaporation and desorption heat can be expressed in terms of the associated specific heat values (similar to Equation (4.62)), which is depicted as follows:

$$\frac{Q_{evap}}{Q_{des}} = \frac{h_{fg}(T_M)}{q_{st}(T_M, P_{cond})} \tag{4.69}$$

Complete preheating process

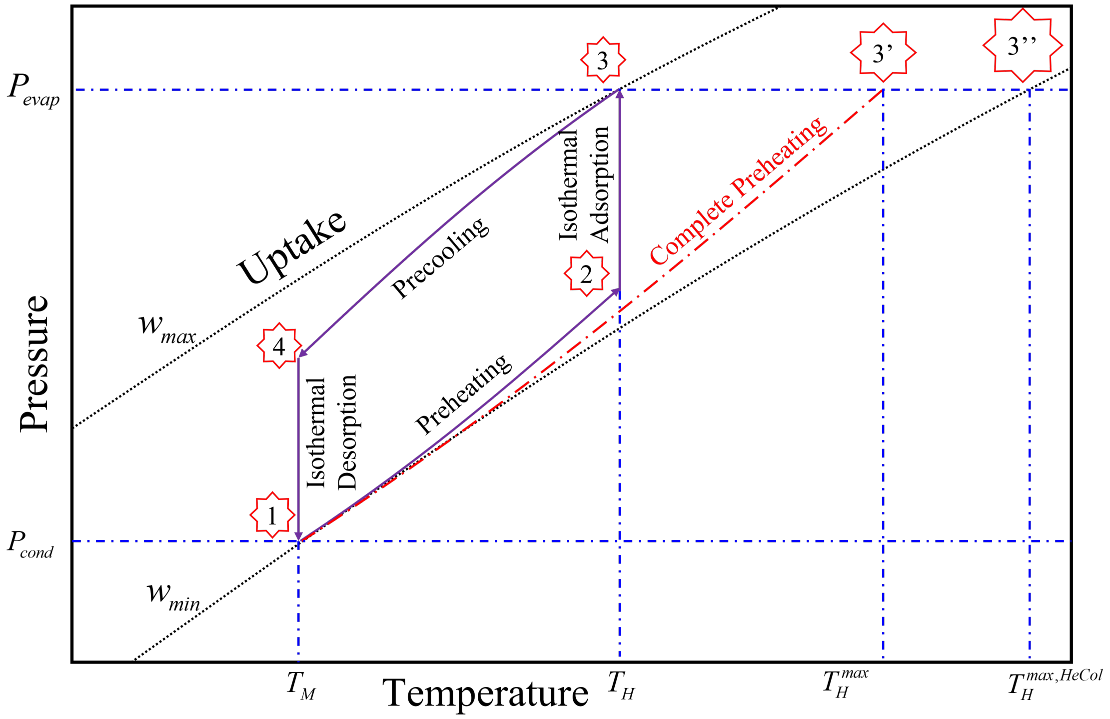

Figure 4.4: Maximum temperature lift from the complete preheating phase approach for both the non-isosteric adsorption heat transformer cycle and isosteric 'HeCol' cycle

The previous approaches to calculate the maximum temperature lift in the AHT cycle assume the cycle to be operating in a reversible manner. However, irreversibilities are present in the practical thermodynamic cycles. These irreversibilities are caused die to the finite heat transfer between the thermal reservoirs, which is further impacted by the thermophysical properties of the associated material in the process. In case of AHT cycle, the ‘adsorbent-adsorbate’ pair’s thermophysical properties and their adsorption isotherm give rise to the deviation of the maximum temperature lift potential from that obtained by the reversible cycle assumption. As highlighted in the sensible heat quantity expression for preheating phase given by Equation (4.45), the thermophysical properties include the specific heat capacity of the adsorbent, adsorbed phase (liquid adsorbate), and the thermal mass of the heat exchanger. This correlation also involves the initial and final uptake values and the isosteric heat of adsorption as a function of the uptake. Therefore, in this approach, these parameters are considered to evaluate the maximum temperature lift of the AHT cycle. Equation (4.45) can be modified by neglecting the thermal mass effect on the preheating sensible heat as follows:

$$\int_{w_1(T_M,P_{cond})}^{w_2(T_H,P_{ph})} q_{st}\, dw = \int_{T_M}^{T_H} \left(c_{p,ads} + w c_{p,ade}\right) dT \tag{4.70}$$

Theoretically, the maximum temperature lift can be obtained when there is no upgraded isothermal adsorption heat supply. In the previous section concerning the mathematical modeling of the AHT cycle, the extent of the preheating phase is determined by defining a fixed temperature lift. Thus, removing this constraint will allow the preheating phase to progress towards higher temperature. This phenomenon is equivalent to the AHT cycle being depicted by a single process line, which can be identified as the complete preheating process. This process is illustrated in Fig. 4.4. Path ‘1-3” denotes the complete preheating path leading to the maximum temperature T_H^{max}, as opposed to the line ‘1-2’ which is limited by the chosen T_H value for the isothermal adsorption heat supply. Mathematically this complete preheating process can be expressed as the following equation:

$$\int_{w(T_M,P_{cond})}^{w\left(T_H^{max},P_{evap}\right)} q_{st}\, dw = \int_{T_M}^{T_H^{max}} \left(c_{p,ads} + wc_{p,l}\right) dT \tag{4.71}$$

The upper limit of the integral in the R.H.S of Equation (4.71) is different from that in Equation (4.70). Instead of an intermediate pressure P_{ph}, the evaporator pressure is considered to calculate the uptake at the end of the complete preheating phase. This integral equation can be simplified to an algebraic formulation as the following equation:

$$q_{st}\Delta w = \left(c_{p,ads} + w_1 c_{p,l}\right) \Delta T^{max} \tag{4.72}$$

Here, Δw refers to the difference between initial uptake $(w(T_M, P_{cond}))$ and final uptake $(w(T_H^{max}, P_{evap}))$. The term ΔT^{max} denotes the difference between the temperatures T_H^{max} and T_M. Since, the L.H.S of Equation (4.72) contains the T_H^{max} term, therefore a non-linear solution methodology needs to be applied to obtain the value of the T_H^{max}. The adsorbent $(c_{p,ads})$ and the liquid adsorbate $(c_{p,l})$ specific heat capacity and the isosteric heat of adsorption are included in Equation (4.72), which constitutes the impact of material characteristics on the maximum heat upgrading potential.

4.3.2 Internal heat recovery scheme

In the theoretical development of maximum temperature lift formulation, the maximum heat upgrading potential of the ATH cycle is investigated. However, for fixed operating conditions and material properties, the cycle can be modified to improve its heat upgrading and desalination performance parameters. Hence, an internal heat recovery mechanism is introduced to the AHT cycle to reduce its requisite energy consumption for the temperature lift. Similar heat and mass recovery techniques are heavily implemented in the adsorption cooling and desalination cycles, which are delineated in the literature review chapter.

Description of the AHT cycle with heat recovery

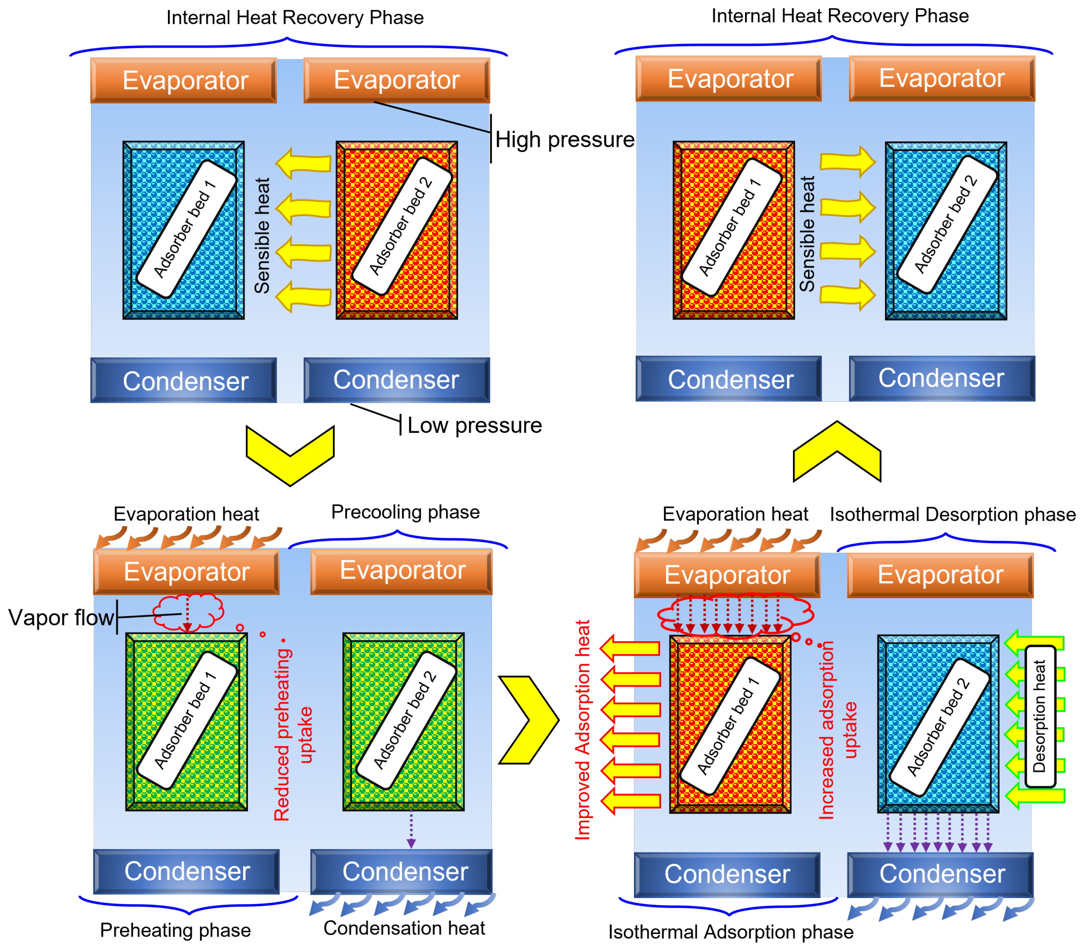

Figure 4.5: AHT cycle process schematic with the internal heat recovery between the adsorber beds

Fig. 4.5 depicts the implementation of the internal heat recovery process in the AHT cycle. The 'Adsorber bed 1' and 'Adsorber bed 2' denote the adsorber and desorber beds, respectively. The desorber bed is at the higher temperature at the end of the isothermal adsorption phase (T_H). The adsorber bed is at the initial low-grade waste heat temperature T_M at the end of the isothermal desorption phase. As explained in the AHT cycle process section, the preheating phase requires the sensible heat to increase the temperature of the bed from the waste heat temperature T_M to higher temperature T_H. This sensible heat is supplied by the adsorption heat generated by the pressure swing adsorption. The resultant uptake consumption reduces the available uptake amount for the isothermal adsorption phase. Therefore, the reduction in the uptake consumption will lead to higher uptake amount for the upgraded heat supply. The internal heat recovery process is implemented to supply the requisite preheating heat from the high temperature desorber bed to the low-temperature adsorber bed. The same is illustrated in Fig. 4.5 as the first phase of the process. After the heat recovery phase, both the adsorber and desorber beds attain intermediate temperatures between T_M and T_H. The subsequent non-isosteric preheating and precooling phases are initiated in the 'adsorber bed 1' and 'adsorber bed 2' by connecting these to the high pressure evaporator and low pressure condenser, respectively. Since, the initial temperature for the preheating phase is higher than T_M, the net uptake consumption is reduced for achieving the same value of T_H. Thus, the internal heat recovery reduces the preheating uptake consumption. These phases are followed by the isothermal adsorption and desorption phases in the 'adsorber bed 1' and 'adsorber bed 2', respectively. After reaching the final temperatures T_H and T_M in the 'adsorber bed 1' and 'adsorber bed 2', these sorption beds are again connected to initiate the internal heat recovery process.

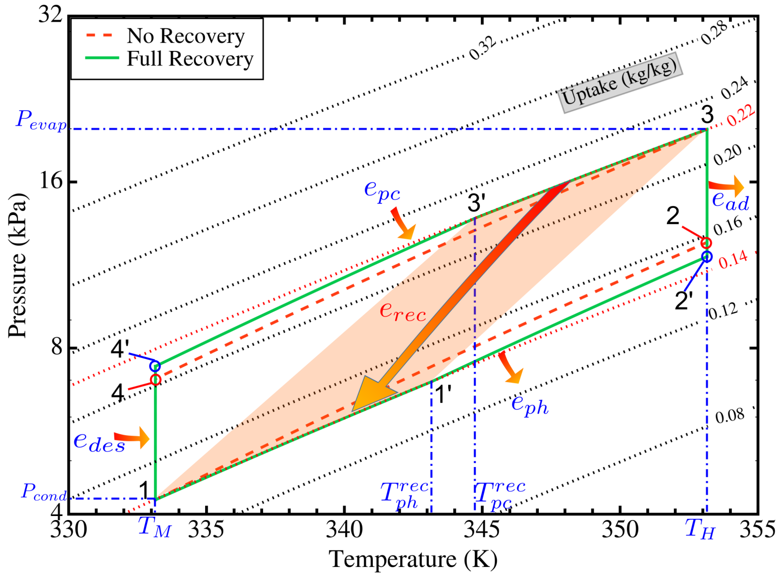

Figure 4.6: AHT cycle diagram considering no heat recovery and maximum possible heat recovery

Fig. 4.6 illustrates the AHT cycle in the pressure-temperature-uptake plane. Both the cycles with and without the internal heat recovery scheme are presented in the figure. The AHT cycle without heat recovery is represented by the path 1-2-3-4-1, whereas, the cycle with the heat recovery is depicted by the path 1-1'-2'-3-3'-4'-1. The internal heat recovery introduces two intermediate state points (1' and 3'). The state points 2 and 4 are changed to 2' and 4' due to the heat recovery. The cycle is drawn for the temperature range between T_M=60 °C and T_H=80 °C. It can be seen that the path 1-1' and 3-3' are isosteric in nature. Since, the sensible heat exchange between the adsorber and desorber beds is responsible for the temperature change during the heat recovery phase, there's no change in the uptake value in both the beds. The heat transfer is indicated from the path 3-3' to the path 1-1', denoted by the specific heat value e_{rec}. The resultant intermediate temperature levels in the adsorber and desorber beds are denoted by T_{ph}^{rec} and T_{pc}^{rec}. The equality between these values are dependent upon the material properties and its variation with the operating temperature and the type of the adsorption isotherm considered. Here, it can be observed that these temperature values are slightly different. The final uptake value at the end of the non-isosteric preheating phase is lower for the cycle with heat recovery than the one without ($w_{2'} < w_2$). This results in an increased uptake difference during the isothermal adsorption phase ($w_3 - w_{2'} > w_3 - w_2$). Contrarily, the precooling final uptake value is higher for the cycle with heat recovery ($w_{4'} > w_4$). This internal heat recovery depicted in Fig. 4.6 corresponds to the maximum possible heat recovery for the AHT cycle. A lesser degree of heat exchange results in the partial heat recovery in the AHT cycle. Fig. 4.7 depicts the state points during the internal heat recovery, preheating, and precooling phases in the 'adsorber bed 1' and 'adsorber bed 2'.

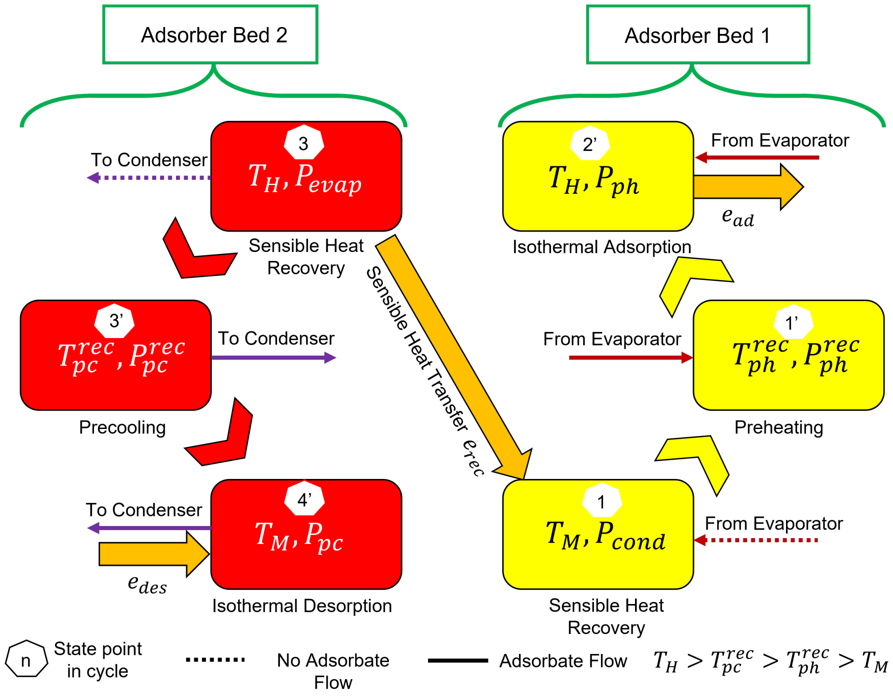

Figure 4.7: Schematic diagram of the AHT cycle with the internal heat recovery and the corresponding state points highlighted as Fig. 4.6

Mathematical formulation of the heat recovery process

The introduction of the internal heat recovery in the AHT cycle leads to the modification in the heat exchange values in each phase. The amount of sensible heat received by the adsorber bed during the heat recovery phase is calculated using the following formulation:

$$e_{ph}^{rec,max} = \int_{T_M}^{T_{ph}^{rec,max}} c_{p,ads}(T)\,dT + w(P_{cond}, T_M) \int_{T_M}^{T_{ph}^{rec,max}} c_{p,ade}(P,T)\,dT + \frac{m_{HX}}{m_{ads}} \int_{T_M}^{T_{ph}^{rec,max}} c_{p,HX}(T)\,dT \quad (4.73)$$

Here, the superscript *rec,max* represents the maximum possible heat recovery condition. Equation (4.73) resembles the non-isosteric preheating sensible heat formulation derived in Equation (4.45). The sensible heat provided to the adsorber bed simultaneously increases the temperatures of the adsorbent, adsorbed phase, and the heat exchanger thermal mass. The maximum temperature limit in the integral terms are $T_{ph}^{rec,max}$ instead of the temperature T_H. Moreover, the second term in Equation (4.73) takes the uptake term ($w(P_{cond}, T_M)$) outside the integral, since the uptake remains constant. Similarly, the sensible heat provided by the desorber bed during the internal heat recovery phase is mathematically expressed by the following equation:

$$e_{pc}^{rec,max} = \int_{T_H}^{T_{pc}^{rec,max}} c_{p,ads}(T)\,dT + w(P_{evap}, T_H) \int_{T_H}^{T_{pc}^{rec,max}} c_{p,ade}(P,T)\,dT + \frac{m_{HX}}{m_{ads}} \int_{T_H}^{T_{pc}^{rec,max}} c_{p,HX}(T)\,dT \quad (4.74)$$

Where, $T_{pc}^{rec,max}$ represents the intermediate temperature of the adsorber bed at end of maximum possible heat recovery at the precooling side.

The energy balance equation for the internal heat recovery is represented by the equality between the specific heats $e_{ph}^{rec,max}$ and $e_{pc}^{rec,max}$. Due to the non-linear behavior of the governing equations, this equality is represented in the following form:

$$\underset{T_{ph}^{rec,max},T_{pc}^{rec,max}}{\text{minimize}} \left(|e_{pc}^{rec,max} - e_{ph}^{rec,max}|\right) \forall \left(T_{pc}^{rec,max} > T_{ph}^{rec,max}\right) \tag{4.75}$$

Thus, solving Equation (4.75) leads to the simultaneous determination of the preheating and precooling intermediate temperatures ($T_{ph}^{rec,max}$ and $T_{pc}^{rec,max}$ respectively). It is noted that the precooling intermediate temperature must be higher than the preheating intermediate temperature, so that the second law of thermodynamics isn't violated. Once the intermediate temperatures are determined, the corresponding intermediate pressures can be determined using the following equations:

$$\begin{cases} P_{ph}^{rec,max} = P(T_{ph}^{rec,max}, w_1(T_M, P_{cond})) \\ P_{pc}^{rec,max} = P(T_{pc}^{rec,max}, w_3(T_H, P_{evap})) \end{cases} \tag{4.76}$$

The abovementioned formulations are derived for the maximum possible heat recovery in the AHT cycle. However, due to the variation in the heat exchanger effectiveness, the amount of heat recovery may not reach its maximum value. Thus, the intermediate state points need to be determined for the partial heat recovery process in the AHT cycle. A fraction *'r'* is multiplied to the heat exchange values $e_{ph}^{rec,max}$ and $e_{pc}^{rec,max}$. Therefore, the new intermediate temperature values are obtained by the following equation:

$$\underset{T_{ph}^{rec},T_{pc}^{rec}}{\text{minimize}}\, r \times \left(|e_{pc}^{rec,max} - e_{ph}^{rec,max}|\right)\ r\epsilon[0,1] \tag{4.77}$$

Here, T_{ph}^{rec} and T_{pc}^{rec} denote the preheating and precooling intermediate temperatures for partial heat recovery.

The internal heat recovery phase is followed by the non-isosteric preheating and precooling phases in the adsorber and desorber beds, respectively. The modified correlations for the sensible preheating and precooling heats are provided in the following equations:

$$e_{ph}^{sen} = \int_{T_{ph}^{rec}}^{T_H} c_{p,ads}(T)\,dT + \int_{T_{ph}^{rec}}^{T_H} w(P,T)c_{p,ade}(P,T)\,dT + \frac{m_{HX}}{m_{ads}} \int_{T_{ph}^{rec}}^{T_H} c_{p,HX}(T)\,dT \quad (4.78)$$

$$e_{pc}^{sen} = \int_{T_{pc}^{rec}}^{T_M} c_{p,ads}(T)\,dT + \int_{T_{pc}^{rec}}^{T_M} w(P,T)c_{p,ade}(P,T)\,dT + \frac{m_{HX}}{m_{ads}} \int_{T_{pc}^{rec}}^{T_M} c_{p,HX}(T)\,dT \quad (4.79)$$

The latent heat formulation during the preheating and precooling phases are expressed similar to the formulation in Equation (4.39), as the initial uptake values remain unchanged for these phases. The modified final preheating and precooling uptake values are calculated by the following equations:

$$\begin{cases} \underset{w_2^{rec}}{\text{minimize}} \left(|e_{ph}^{sen} - e_{ph}^{lat}| \right) & \text{Preheating} \\ \underset{w_4^{rec}}{\text{minimize}} \left(|e_{pc}^{sen} - e_{pc}^{lat}| \right) & \text{Precooling} \end{cases} \quad (4.80)$$

The resultant uptake values for the preheating and precooling phases are w_2^{rec} and w_4^{rec}, respectively. These modified uptake values are used to determine the new heat values in the isothermal adsorption and desorption phases. These formulations are expressed in Equation (4.81).

$$\begin{cases} e_{ad}^{rec} = \int_{w_2^{rec}}^{w_3} q_{st}(w)\,dw & \text{Adsorption heat supply} \\ e_{des}^{rec} = \int_{w_4^{rec}}^{w_1} q_{st}(w)\,dw & \text{Desorption heat input} \end{cases} \quad (4.81)$$

The modified heat exchange values in the AHT cycle with the introduction to the internal heat recovery modifies the expression for the performance parameters. The following equations display the modified expressions for UHR and CHR, hereby denoted as UHR^{rec} and CHR^{rec}, respectively.

$$\begin{cases} UHR^{rec} = \dfrac{e_{ad}^{rec}}{e_{des}^{rec} + e_{evap}} & \text{Useful heat ratio} \\ CHR^{rec} = \dfrac{e_{cond}}{e_{des}^{rec} + e_{evap}} & \text{Condensation heat ratio} \end{cases} \tag{4.82}$$

Exergy analysis

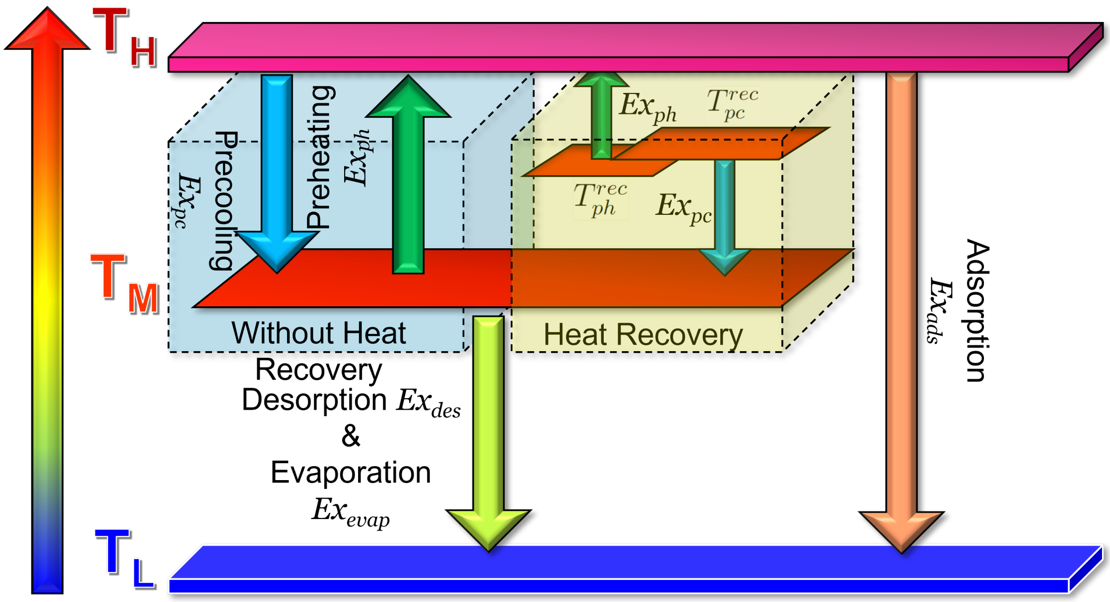

Figure 4.8: Exergy Interaction between the different temperature levels for different phases of the AHT cycle

Exergy analysis of a thermodynamic system characterizes its combined energetic and entropic performance. Exergy is defined as the maximum amount of reversible work obtainable from an energy source. Thus, the exergy corresponding to a heat quantity can be expressed by the Carnot efficiency, which includes the heat associated temperature values. For instance, the exergy of the heat amount Q can be expressed as $Q\left(1 - \frac{T_0}{T_{source}}\right)$, when the associated temperature is T_{source} and the dead state temperature is T_0. The

AHT cycle can be analyzed using the exergy formulations for the heat exchange among the evaporator, condenser, and sorption beds. Fig. 4.8 depicts the temperature levels in an AHT cycle. The exergy flows among the temperature levels are also highlighted. In case of an AHT cycle without heat recovery, the precooling and preheating exergy are considered between the temperatures T_M and T_H. The exergy flow for the desorption nad evaporator heat occur between the temperatures T_M and T_L (T_L is considered as the ambient temperature). The adsorption exergy flow corresponds to the temperatures T_H and T_L. Thus formulations for the exergy flows are expressed in the following set of equations:

$$\begin{cases} Ex_{ad} = e_{ad} \times \left(1 - \dfrac{T_L}{T_H}\right) \\ Ex_{des} = e_{des} \times \left(1 - \dfrac{T_L}{T_M}\right) \\ Ex_{evap} = e_{evap} \times \left(1 - \dfrac{T_L}{T_M}\right) \\ Ex_{ph} = e_{ph} \times \left(\dfrac{T_L}{T_M} - \dfrac{T_L}{T_H}\right) \\ Ex_{pc} = e_{pc} \times \left(\dfrac{T_L}{T_M} - \dfrac{T_L}{T_H}\right) \end{cases} \tag{4.83}$$

The exergy value corresponding to the condensation heat is not considered since the associated heat interacting temperature is same as the dead state temperature T_L.

Using the given exergy formulations, the exergy efficiency of the AHT cycle without heat recovery is given as follows:

$$\eta_{ex} = \frac{Ex_{ad}}{Ex_{evap} + Ex_{des} + Ex_{ph}} = \frac{e_{ad}\left(1 - \frac{T_L}{T_H}\right)}{e_{evap}\left(1 - \frac{T_L}{T_M}\right) + e_{des}\left(1 - \frac{T_L}{T_M}\right) + e_{ph}\left(\frac{T_L}{T_M} - \frac{T_L}{T_H}\right)} \tag{4.84}$$

This equation is the modified version of the formulation provided in the study by Hamamoto Y. [172]. The additional input exergy component is included in the denominator of Equation (4.84). Thus, the effect of change in preheating input heat and the corresponding temperature levels can be observed.

The incorporation of the internal heat recovery in the AHT cycle impacts the exergetic performance of the cycle due to the change in the preheating and precooling temperatures. As it can be seen in Fig. 4.8, in case of internal heat recovery, two intermediate temperature levels appear during the preheating and precooling phase. The preheating exergy interacts between the temperature levels T_{ph}^{rec} and T_H. Likewise, the precooling exergy is calculated using the temperatures T_{pc}^{rec} and T_M. Thus, the modified exergy efficiency due to the internal heat recovery can be written as follows:

$$\eta_{ex}^{rec} = \frac{e_{ad}\left(1 - \frac{T_L}{T_H}\right)}{e_{evap}\left(1 - \frac{T_L}{T_M}\right) + e_{des}\left(1 - \frac{T_L}{T_M}\right) + e_{ph}^{sen}\left(\frac{T_L}{T_{ph}^{rec}} - \frac{T_L}{T_H}\right)} \tag{4.85}$$

The third term denotes the modified preheating exergy value due to the internal heat recovery. The value of the preheating specific heat e_{ph}^{sen} is obtained from Equation (4.78).

4.4 Hybrid adsorption heat transformer cycle + multi-effect distillation system (AHT-MED)

As discussed in the preceding sections, the AHT cycle generates an upgraded heat supply via increasing the low-grade waste heat temperature. Therefore, the AHT system can be integrated with an application system to utilize the upgraded heat supply and improve its thermodynamic performance. In the present work, the multi-effect distillation system is chosen to develop a hybrid adsorption heat transformer + multi-effect distillation (AHT-MED) system. A process schematic of the proposed AHT-MED system is illustrated in Fig. 4.9. MED systems are considered to be the most efficient thermal desalination technology. This system works on the principle of evaporation of the saline water or seawater in an evaporator to separate the salt content and produce distillate water vapor. Sequential arrangement of such evaporators (which is termed as effect) leads to the formation of the multiple effect distillation system. In MED system, the condensation heat rejected by an effect is supplied to the subsequent effect for maximum utilization of the input heat energy. The seawater is first evaporated in the brine heater or the first effect of the MED system, where an input heat energy is provided. This heat is generally supplied by the use of hot water vapor at constant temperature. The evaporation of the seawater occurs due to the condensation of the given water vapor. The resultant distillate vapor from the evaporation of the seawater is present at a superheated state, which is caused by decrease in the saturation temperature of the vapor by the boiling point elevation (BPE) of the saline water. Therefore, the temperature of each subsequent effects decreases till the ambient seawater temperature. Depending upon the value of BPE and the total temperature difference between the first and last effects, the number of effects of the MED system is determined. The amount of potable water generated from the whole MED system is directly proportional to the number of effects keeping other system parameters unchanged. Therefore, for a fixed temperature difference between two adjacent effects, the number of effects increases with the increase in the heat source temperature in the first effect. Therefore, a heat supply at an elevated temperature to the first effect of the MED system while transforming the primarily obtained heat from the low-temperature waste heat source, would benefit the net desalination performance of the MED system. A detailed heat and mass transfer balance of an MED system is provided in the appendix (Fig. C.1 and Table C.1).

In Fig. 4.9, it is shown that the AHT cycle produces the upgraded heat (Q_{ad}) by increasing the low-grade waste-heat from temperature T_M to T_H. This upgraded Q_{ad} is supplied to the first effect of the given MED system, which produces the distillate vapor and concentrated brine solution. These two products are supplied to the next effect, where the concentrated brine solution is evaporated using the distillate water vapor to further split it into brine and distillate vapor. The condensed distillate is collected as potable water from each effect in the MED system. The condensed desorbed water vapor from the AHT system is also collected as potable water supply. The condensation process in the AHT cycle is carried out using seawater at the ambient temperature (T_L). The waste heat source is providing the input energy to the evaporator (Q_{evap}) and desorber beds (Q_{des}) of the AHT cycle at the temperature T_M. Thus, the effective heat source temperature of the whole system is the low-grade waste heat temperature T_M.

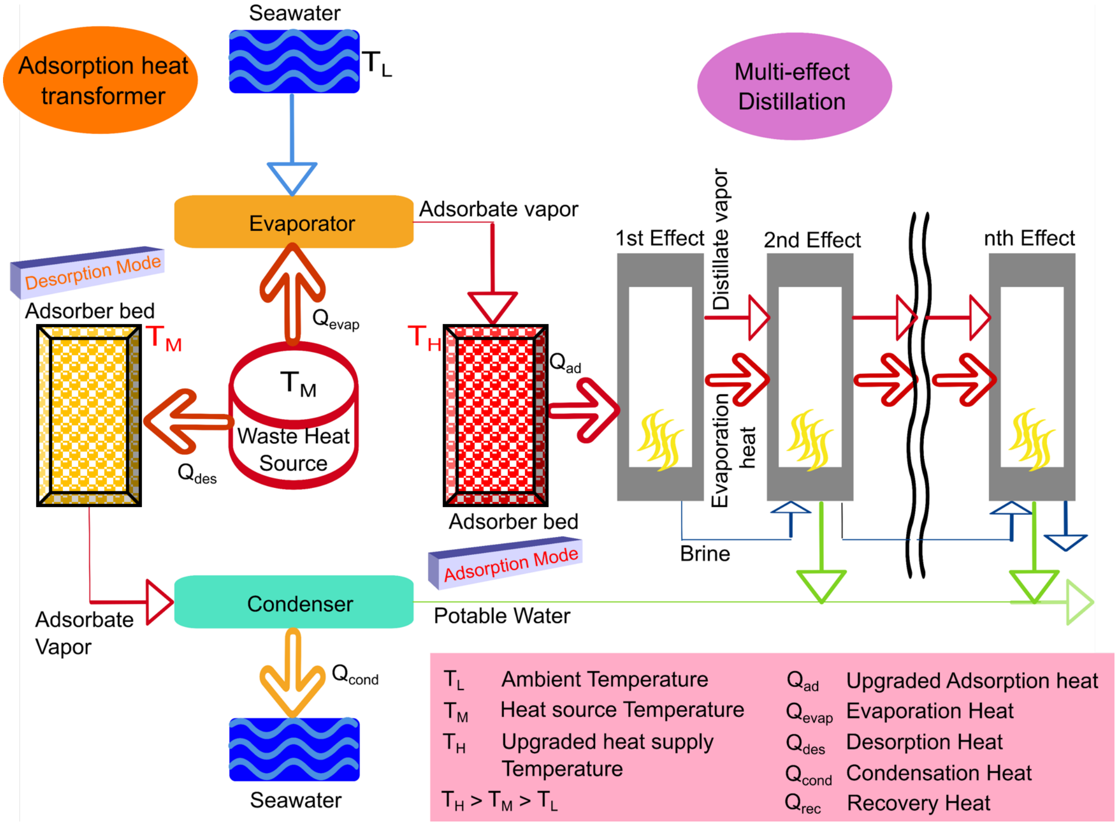

Figure 4.9: Schematic of the working principle of the hybridized adsorption heat transformer cycle and multi-effect distillation system

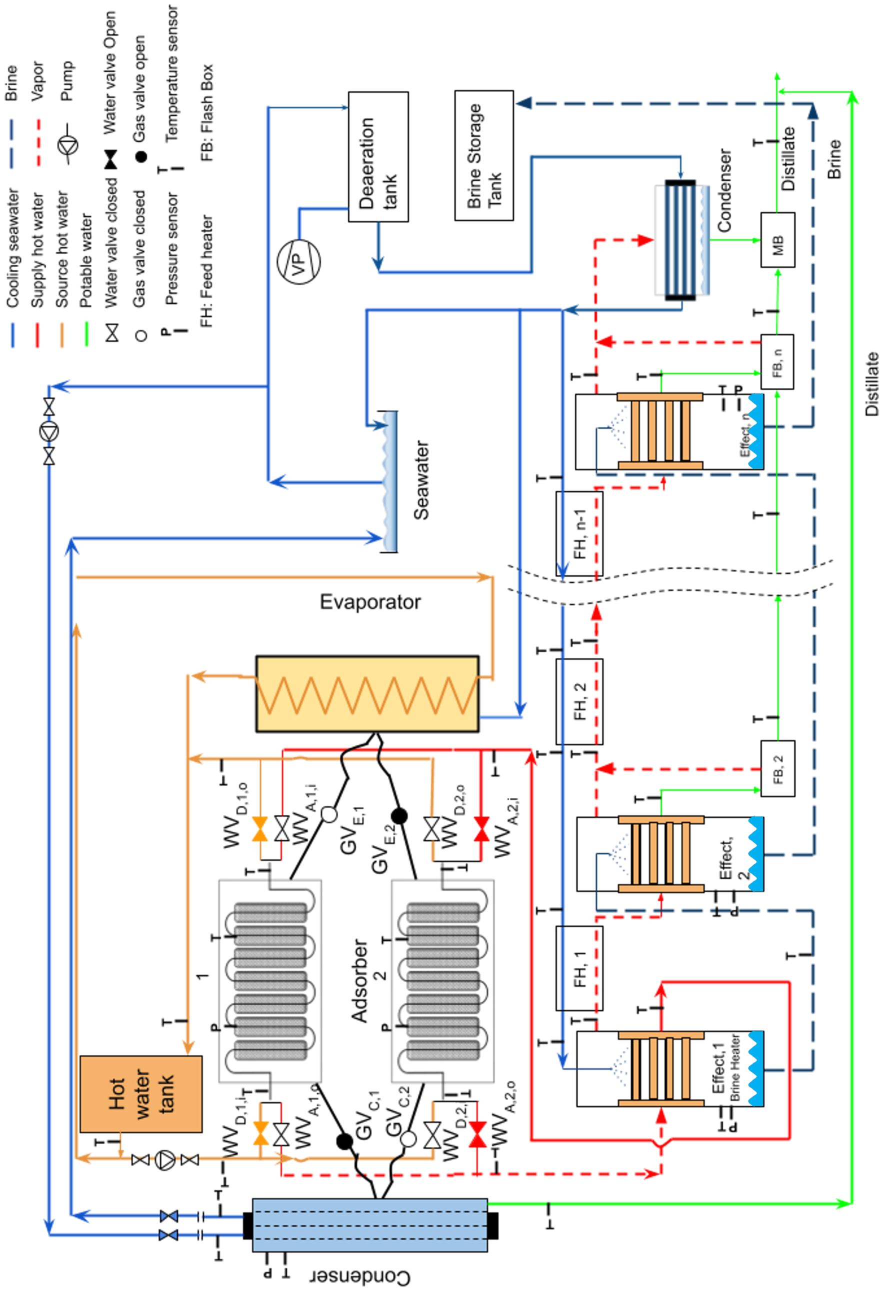

Figure 4.10: Proposed system operation design of a hybrid adsorption heat transformer cycle and multi-effect distillation system

Fig. 4.10 illustrates a detailed operating procedure of the proposed AHT-MED hybrid system. A detailed flow structure of each of the heat transfer fluids, seawater/brine, hot water and cooling water supply, and the vapor flow in both the AHT and MED systems are clearly highlighted. As already introduced in Fig. 4.1, the AHT cycle requires the presence of the at least two adsorber beds for periodic continuous operation of the AHT cycle. The state of the internal gas valves between the evaporator, adsorber beds, and the condenser are provided in Fig. 4.1. Here, a further detailed operation is depicted by using naming convention for the associated gas valves. The gas valves (GV) connected to the evaporator and condenser are denoted using the subscript ‘E’ and ‘C’, respectively. Therefore, the gas valve $\mathrm{GV}_{\mathrm{E},1}$ and $\mathrm{GV}_{\mathrm{C},1}$ denote the gas valve connecting the evaporator and condenser to the adsorber bed 1, respectively. An adsorber bed can be represented as a packed bed heat exchanger which contains the adsorbent material (such as silica gel) directly subjected to the adsorbate gas. The corresponding tube side contains the heat transfer fluids (HTF) which provide the necessary desorption heat or extract the upgraded adsorption heat. Each of the inlet and outlet HTF lines of the adsorber bed are divided into two components for the hot water supply to provide the low-grade desorption heat and the upgraded adsorption heat extraction. Each of these lines are associated with a water valve (WV). The input and output lines are denoted using the subscripts ‘i’ and ‘o’, respectively. The desorption heat input and upgraded heat extraction HTF lines are represented with the subscripts ‘D’ and ‘A’, respectively. Thus, $\mathrm{WV}_{\mathrm{A},1,\mathrm{i}}$ and $\mathrm{WV}_{\mathrm{D},2,\mathrm{o}}$ represent the inlet water valve of the adsorber bed 1 to extract adsorption heat and the outlet water valve of the adsorber bed 2 to supply desorption heat, respectively. The outlet HTF lines for the adsorption heat extraction extends to the first effect of the MED system, where it supplies the saturated water vapor generated using the upgraded adsorption heat from the adsorber beds. A filled valve symbol means that the valve is open, whereas a white symbol is used for the closed status of the valve. When the adsorber bed executing the adsorption process, water valves for the desorption heat supply remain closed. Likewise, the water valves for the adsorption heat extraction remain closed during the desorption or regeneration of the adsorber bed. The waste heat is supplied from a hot water tank which is connected to both the adsorber beds and the evaporator. The evaporator generates the adsorbate water vapor by boiling the incoming seawater using the hot water supply through a heat exchanger. The condenser contains a cooling water loop, which is constructed to extract the condensation heat released by the desorbed adsorbate vapor. Seawater at the ambient temperature is used as the cooling water.

A brief description of the valve opening/closing sequence during each phase of the AHT cycle is provided here. During the preheating phase in the adsorber bed 1, $\mathrm{GV}_{\mathrm{E},1}$ is kept open for inflow of the pressurized water vapor from the evaporator. Meanwhile, $\mathrm{WV}_{\mathrm{A},1,\mathrm{i}}$ and $\mathrm{WV}_{\mathrm{A},1,\mathrm{o}}$ valves are closed to maintain the adiabatic preheating process. When the adsorber bed reaches the desired high temperature due to the pressure swing adsorption, these valves are opened to extract the adsorption heat isothermally. The resultant two-phase or vapor phase water is supplied to the first effect of the MED system via $\mathrm{WV}_{\mathrm{A},1,\mathrm{o}}$. After supplying the upgraded heat to the MED system, the condensed water is returned to the adsorber bed 1 through $\mathrm{WV}_{\mathrm{A},1,\mathrm{i}}$. At the end of the isothermal adsorption phase, $\mathrm{GV}_{\mathrm{E},1}$ is closed and $\mathrm{GV}_{\mathrm{C},1}$ is opened to begin the precooling phase in the adsorber bed 1. At the same time, $\mathrm{WV}_{\mathrm{A},1,\mathrm{i}}$ and $\mathrm{WV}_{\mathrm{A},1,\mathrm{o}}$ are also closed. During the precooling phase, the valves $\mathrm{WV}_{\mathrm{D},1,\mathrm{i}}$ and $\mathrm{WV}_{\mathrm{D},1,\mathrm{o}}$ remain closed to prevent the hot water circulation. As the pressure swing desorption takes place due to the low pressure in the condenser, the adsorber bed temperature reduces to the initial waste heat temperature. Now, the valves $\mathrm{WV}_{\mathrm{D},1,\mathrm{i}}$ and $\mathrm{WV}_{\mathrm{D},1,\mathrm{o}}$ are opened to initiate the flow of the hot water at the waste heat temperature. Thus, the isothermal desorption phase is performed by the supply of requisite desorption heat using the HTF. The desorbed vapor is condensed in the condenser. The condensed distillate is collected as the potable water.

On the MED side, the seawater is sprayed onto the heat exchanger of the first effect after its pre-treatment (e.g., using deaeration tank). The distillate vapor generated by the evaporation of the seawater is supplied to the next effect. The concentrated brine emanating from the first effect is sprayed onto the next effect for further evaporation. The temperature of the incoming distillate vapor on the condensing side of the second effect is lower than the heat supply temperature in the first effect. This reduction is caused by the decrease in the saturation temperature due to the BPE of the saline water. Therefore, the condensation process of the distillate vapor in each effect occurs at a lower temperature than its preceding effect. The condensed distillate emanating from each effect (starting from the second effect) goes to the flash box, where an excess amount of distillate vapor is generated, which is added to the distillate vapor produced in each effect. The distillate condensate from each flash box is considered as potable water, which flows to the subsequent flash boxes. After the n^{th} effect, the distillate vapor is condensed in a condenser, where the condensation heat is extracted by the seawater at the ambient temperature. The condensed distillate is mixed with the blowdown from the last flash box. The brine from the last effect is collected in a brine storage tank. Furthermore, since the seawater is supplied to the first effect after preheating in the condenser, it goes through a feed heater situated between two effects. The temperature of the seawater is increased in these feed heaters by the high temperature distillate vapor emanating from the effect. Increasing the feed seawater temperature in the first effect leads to lower energy requirement for its evaporation. If the two adsorber beds are run in the pairwise sequence of “adsorption-desorption” and “preheating-precooling” phases, then the resultant water production would be intermittent in nature. Therefore, the use of a suitable valve sequence and/or more number of adsorber beds is required for continuous operation of the hybrid AHT-MED system.

Performance parameters

The performance of the thermal desalination system can be characterized using two major parameters, viz., performance ratio (PR) and water production rate (WPR). The PR value is calculated as the ratio of the total condensation heat output for the distillate water production upon the input driving thermal energy. Denoting the condensation rate of heat transfer in the i$^{\text{th}}$ effect as $\dot{Q}_e^i$ and for the condenser as $\dot{Q}_{cond,MED}$, the PR can be formulated as follows:

$$PR_{MED} = \frac{\sum_{i=2}^{n} \dot{Q}_e^{(i)} + \dot{Q}_{cond,MED}}{\dot{Q}_e^{(1)}} \tag{4.86}$$

The first summation in the numerator is carried out for the 2$^{\text{nd}}$ to n$^{\text{th}}$ effect. The denominator denotes the input rate of heat transfer in the brine heater or the first effect. The water production rate of the MED system can be expressed as the summation of condensed distillate production from the last flash box and the condenser as follows:

$$WPR_{MED} = \dot{m}_{D_{bd}|out}^{(n)} + \dot{m}_{D_{cond}|out} \tag{4.87}$$

Here, the subscript $D_{bd}|out$ denotes the distillate blowdown from the flash box and $D_{cond}|out$ is the condensed distillate from the condenser of the MED system.

In the hybrid AHT-MED system, the energy in the brine heater/first effect is provided by the adsorber bed during the isothermal adsorption phase. Therefore, an energy balance can be derived between these two components. However, since the MED system is modeled in steady state and the AHT cycle operates in cyclic steady state, the output energy from the AHT cycle and the input energy to the MED system need to be synchronized using the cycle time of the AHT cycle. If the cycle time is denoted as t_{cycle}, then the heat balance is written as follows:

$$e_{ad}m_{ads} = \dot{m}_s h_{fg,s}(T_H)t_{cycle} \tag{4.88}$$

Here, e_{ad} denotes the specific heat exchange during the isothermal adsorption phase, m_{ads} is the mass of the adsorbent, $\dot{m}_s$ is the steam mass flow rate in the first effect and $h_{fg,s}$ denotes latent heat of vaporization taken at the upgraded waste heat temperature T_H. From this expression, the mass of the adsorbent can be determined for the given steam mass flow rate, cycle time, and the specific adsorption heat. This value is used in the modified correlation for the PR of the AHT-MED system, which is defined as follows:

$$PR_{hybrid} = \frac{\left(\sum_{i=2}^{n} \dot{Q}_e^{(i)} + \dot{Q}_{cond}^{MED}\right) \times t_{cycle} + \left(|e_{ad}^{AHT}| + |e_{cond}^{AHT}|\right) \times m_{ads}}{\left(|e_{des}^{AHT}| + |e_{evap}^{AHT}|\right) \times m_{ads}} \tag{4.89}$$

Here, the total output heat transfer rate is multiplied by the cycle time to obtain the total output heat. The total heat generated by the MED system and the AHT cycle (containing the isothermal adsorption heat and condensation heat) are added to represent the total output energy of the hybrid AHT-MED system. The input energy in the denominator of Equation (4.89) is considered the same as the input energy for the AHT cycle (evaporation and desorption heat at the waste heat source temperature). The modified water production rate is defined by the following expression:

$$WPR_{hybrid} = \dot{m}_{D_{bd}|out}^{(n)} + \dot{m}_{D_{cond}|out} + \frac{(w_3 - w_1) \times m_{ads}}{t_{cycle}} \tag{4.90}$$

The additional term on the R.H.S refers to the potable water mass flow rate from the condenser of the AHT cycle.

The implementation of the internal heat recovery scheme in the AHT cycle also influences the desalination performance of the hybrid AHT-MED system. The necessary modification to the performance ratio and water production rate formulation due to the internal heat recovery is provided in the following equations:

$$PR^{rec}_{Hybrid} = \frac{\left(\sum_{i=2}^{n} \dot{Q}_e(i) + \dot{Q}^{MED}_{cond}\right) \times t_{cycle} + \left(|e^{AHT,rec}_{ad}| + |e^{AHT}_{cond}|\right) \times m^{rec}_{ads}}{\left(|e^{AHT,rec}_{des}| + |e^{AHT}_{evap}|\right) \times m^{rec}_{ads}} \tag{4.91}$$

$$WPR^{rec}_{hybrid} = \frac{(w_3 - w_1) \times m^{rec}_{ads}}{t_{cycle}} + \dot{m}_{MED} \tag{4.92}$$

Here, the subscript 'rec' of each heat exchange terms denotes the heat exchange values for the heat recovery-based AHT cycle. It can be seen that both the output adsorption heat and input desorption heat are impacted by the heat recovery. Furthermore, the modified requisite mass of the adsorbent is represented by m^{rec}_{ads}, which is calculated using the following equation:

$$|e^{AHT,rec}_{ad}| \times m^{rec}_{ads} = \dot{Q}_e(1) \times t_{cycle} \tag{4.93}$$

The formulation of the WPR with the heat recovery-based AHT cycle (Equation (4.92)) can be converted into the specific daily water production (SDWP) rate per unit mass of the adsorbent as follows:

$$SDWP^{rec}_{hybrid} = \frac{WPR^{rec}_{hybrid} \times 3600 \times 24}{m^{rec}_{ads}} \tag{4.94}$$

The SDWP provides the measure of the improvement in the potable water generation performance considering the modified mass of the adsorbent.

4.5 Summary

In this chapter, detailed mathematical frameworks are developed for the bulk thermodynamic properties of the adsorbed phase and energy balance in the AHT cycle. The energy balance model is extended and modified to obtain the equations for the internal heat recovery mechanism and the formulations for the maximum temperature lift of the AHT cycle. In the subsequent chapter, these models are utilized to obtain the adsorbed phase behavior of different adsorbent-adsorbate pairs. Furthermore, the performance evaluation of the AHT cycle and the corresponding hybridization with the AHT-MED system are also illustrated.

Chapter 5

Results and discussion

In the current chapter, several observations are made for the adsorption phenomena, based on the theoretical development carried out in the previous two chapters. The first section provides an insight on the use of the molecular simulation technique to characterize the water adsorption phenomena in the activated carbon. The conceptual understanding of the GCMC simulation technique provided in chapter 3 is utilized to translate the molecular activity during the adsorption process into the corresponding macroscopic adsorption isotherm and isosteric heat properties. The following section extends these macroscopic properties obtained through the molecular simulation to characterize the adsorbed phase thermodynamic properties, such as specific heat capacity, specific entropy, and specific enthalpy. Finally, the system level perspective is provided using the equilibrium analysis of the adsorption heat transformer cycle. Furthermore, this section is complemented with the desalination performance improvement of the MED system by proposing the development of a hybrid AHT-MED system. The theoretical basis for the latter two sections has been developed in chapter 4.

5.1 GCMC simulation of water adsorption in activated carbon

Chapter 3 has elucidated the molecular simulation for the adsorption of noble and non-polar gases in the zeolites, MOFs, and graphite structures. The effect of pore size distribution and surface chemistry has been delineated using the CO_2 adsorption simulation in graphite slit-pore. Here, the adsorption of a polar adsorbate in the graphite structure is demonstrated. Water is ubiquitous as an adsorbate used for adsorption cooling and desalination applications, due to its high heat of adsorption values. Grand Canonical Monte Carlo (GCMC) simulation of the water adsorption process can explain its unique adsorption characteristics such as its ‘S’-shaped isotherm, which generally appears for activated carbon and MOF adsorbents. In this study, a detailed GCMC simulation of the water adsorption in activated carbon is carried out, which aims to unravel the corresponding molecular level adsorption phenomena.

5.1.1 Simulation model

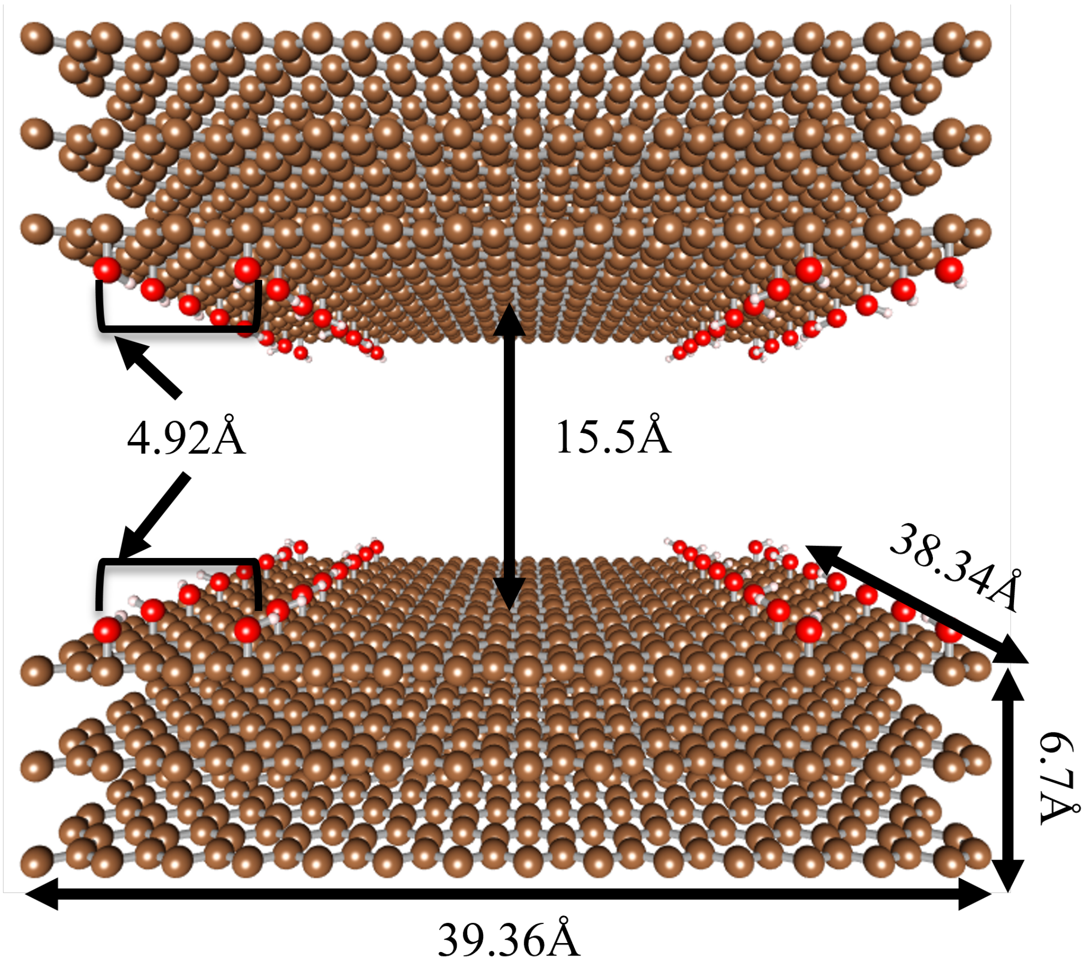

Figure 5.1: Molecular structure of the graphite slit-pore containing hydroxyl functional group and its dimensions

Fig. 5.1 illustrates the graphite slit-pore used in the GCMC simulation. This graphite model contains the hydroxyl (OH) functional group. However, unlike the model described for the CO_2 adsorption in Fig. 3.8, a non-uniform distribution of the OH functional group is considered along the x-direction. There are two rows at each end of the graphite slit-pore on both the inner walls of the slit-pore. The separation between the adjacent rows in the x-direction is taken as 4.92 Å. The FGs are distributed along the y-direction with uniform spacing, and there are 8 FGs in this direction. The OH molecule is grafted

Table 5.1: SPC/E force field parameters of the water molecule

L-J parameters (ϵ in K, σ in Å)	Partial charges (unit electron charge)	Reference
ϵ_O=78.23, σ_O=3.166	q_O=-0.8476	[89]
ϵ_H=-, σ_H=-	q_H= 0.4238	

with random angular orientation of the O-H bond in the x-y plane. The pore width is considered as 15.5 Å, which represents the micropores of the heterogeneous activated carbon. The force field description of the graphite slit-pore with OH functional group is provided in Table 3.4.

The water molecule and its force field are described using the 'SPC/E' model. As per this model, the water molecule consists of two hydrogen and one oxygen atoms, among which the O atom is chosen as the L-J interaction center. The O atom contains a negative partial charge and the H atoms contain positive partial charges with half the magnitude of that of the O atom. These force field values are provided in Table 5.1. The O-H bond length is 1 Å and the H-O-H angle is 109.4°. Due to this configuration, a strong dipole moment exists in the water molecule. This phenomenon results in the formation of hydrogen bonds in the adsorbed phase. Therefore, the acceptance probability of adsorbing the water molecule is very low during the GCMC simulation. As a result, the water adsorption simulation requires much higher number of MC cycles for equilibration of the adsorbed number of molecules. For reduction in the computational cost, a finite simulation box is considered, which denotes the absence of periodic boundary condition across all the directions. Therefore, every adsorbent and adsorbate atom present in the simulation box is considered for calculating the total interaction potential.

5.1.2 Equilibrium adsorption properties

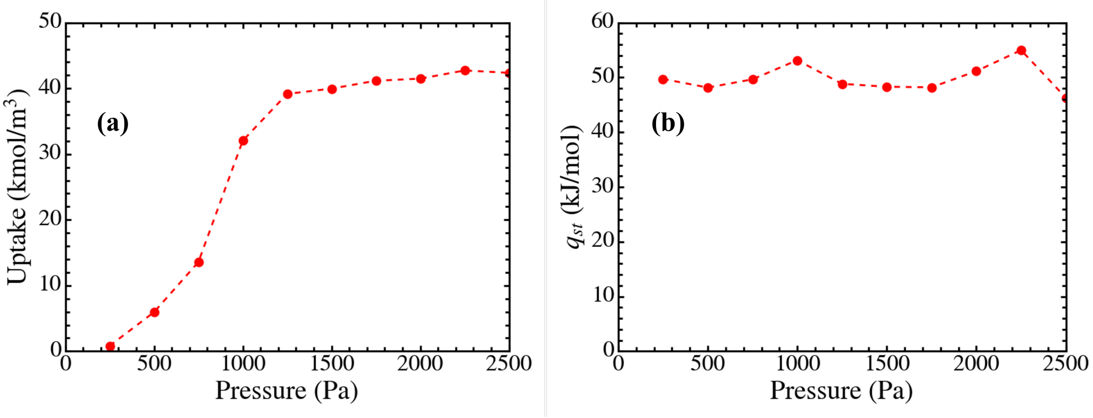

Figure 5.2: Water adsorption isotherm and isosteric heat of adsorption obtained from the GCMC simulation at the temperature 25 °C

The adsorption isotherm and the isosteric heat of adsorption of the water adsorption in the graphite structure is depicted in Fig. 5.2. The characteristic S-shaped adsorption curve resembles the IUPAC type V isotherm. The water adsorption uptake values remain low at the low-pressure region. This low uptake value prevails till a threshold pressure, after which a sudden rise in the uptake can be observed. In Fig. 5.2a, this threshold pressure is approximately 250 Pa. The sharp increasing trend of the uptake values occurs in the pressure range from 500 Pa to 1000 Pa. The slope of the isotherm starts to reduce beyond 1000 Pa pressure. As a result, the adsorption isotherm reaches its saturation uptake value towards the saturation pressure of water. A uniform and high value of the isosteric heat of adsorption is obtained for the water adsorption in OH-containing graphite slit-pore, as depicted in Fig. 5.2b. This trend is attributed to the strong interaction potential between the water molecules and the OH functional groups. With the increasing amount of adsorbed water molecules, the water-water interactions starts to dominate the water-graphite interaction potential. The competing effect of these two interactions gives rise to the uniform heat of adsorption value in the given pressure range.

5.1.3 Adsorbed phase formation characteristics

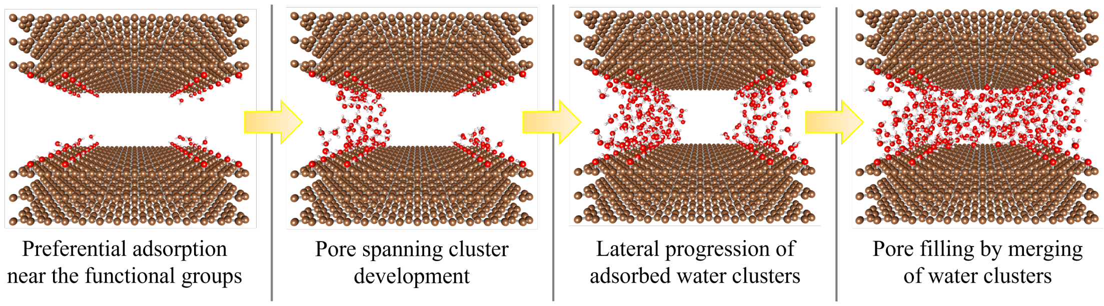

Figure 5.3: Molecular description of the water adsorption process in the OH group containing graphite slit-pore with the distinct adsorption steps at 25 °C temperature and four different pressure levels

Fig. 5.3 delineates the molecular level adsorbed phase generation during the water adsorption in graphite pore containing OH functional groups. The snapshots of the molecular configuration are taken at the pressures 250 Pa, 750 Pa, 1000 Pa and 1250 Pa. The water molecules are seen to be adsorbed close to the functional groups at 250 Pa pressure. The interaction potential is higher between the water molecules and the OH functional groups, compared to that between the water and graphitic carbon atoms. This phenomenon is attributed to the presence of positive partial charge on the H atom of the OH group, which elevates the value of net Coulombic potential. Moreover, the van der Waals potential between the O atoms of both the water and OH molecules is greater than that between the graphitic carbon and water molecule. The large FG-H_2O interaction potential leads to the high values of isosteric heat of adsorption at the low pressure. Continuous occupation of the energetically favorable regions with the increasing pressure leads to slight decrease in the isosteric heat of adsorption. At this low-pressure region, the adsorbed amount of water is directly proportional to the density of the hydrophilic functional groups. As the pressure increases, more number of gaseous water molecules are available to be adsorbed in the graphite structure. At 750 Pa pressure, it can be seen that the water molecules stack onto the existing adsorbed water layer nearby the functional groups. Therefore, a clustering phenomenon occurs for the adsorption of water molecules across the pore width. The highly stable hydrogen bonds are formed between the H atom of one H_2O molecule and O atom of another H_2O molecule. The criterion for hydrogen bond formation are (i) the distance between the O and H atoms of two water molecules is shorter than 2.45 Å, (ii) the O-H. . . O angle exceeds 150°. Due to the formation of the hydrogen bonds with the increasing number of water molecules, these clusters propagate towards the center of the pore width from opposite pore walls. After coalescence of these clusters, a bridged cluster formation of the adsorbed phase occurs in the pore width. This bridged cluster is termed as 'pore spanning cluster' (PSC). The formation of the PSC is spatially heterogeneous. It can be seen that at 750 Pa, the only one PSC is formed concentrated around the functional groups on the left side of the graphite pore. This heterogeneity is caused by the dominating effect of energy over entropy. The entropic effect denotes the thermal fluctuations of the adsorbed molecules. From statistical mechanics principle, a uniform distribution of the energy level occupation by the particle can be obtained at high temperatures. Therefore, the formation of the PSCs would have occurred on both functional group-based energetically favorable sites at the higher temperature. This dominating water-water interactions lead to a slight increase in the isosteric heat of adsorption values. At 1000 Pa pressure, PSCs on both sides of the pore are fully generated. With further increase in the available water molecules, these PSCs propagate in the lateral direction of the pore. Continuous propagation of these adsorbed water molecules lead to a slight decrease in the isosteric heat of adsorption with the increasing pressure values. At 1250 Pa pressure, the adsorbed phase occupies the bulk of the available pore space after merging of two PSCs. The total water-water interaction potential begins to rise again due to the increased amount of the hydrogen bonds.

Therefore, at approximately 2250 Pa pressure, the isosteric heat reaches its peak value in the operating pressure range. Further increase in the pressure leads to the saturation of the pore, and the consequent decrease in the isosteric heat of adsorption towards the latent heat of vaporization.

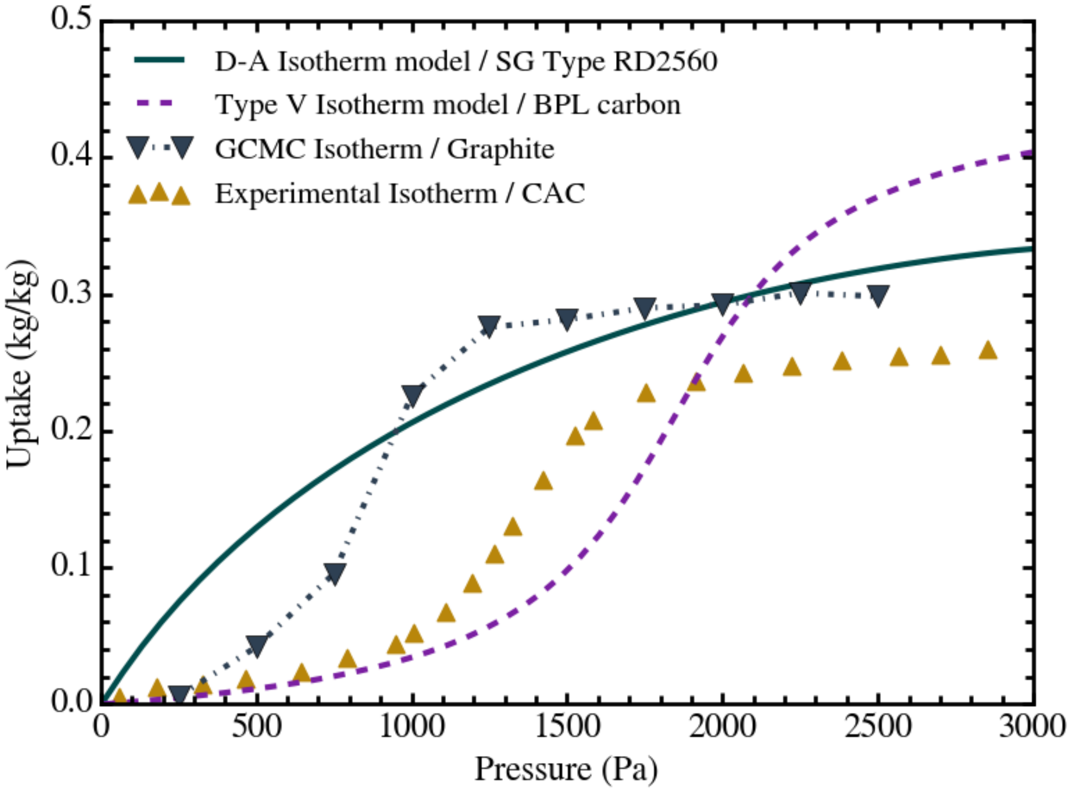

Figure 5.4: Water adsorption isotherms on four adsorbent materials obtained from experimental data, D-A and Type V isotherm models, and GCMC-based molecular simulation

Fig. 5.4 illustrates a comparison among the water adsorption uptake values obtained for various adsorbents. These adsorbents include CAC activated carbon, BPL carbon, type RD2560 silica gel, and graphite slit pore. The experimental uptake data for water adsorption in CAC activated carbon is taken from the study by Jin et al. [218]. It demonstrates an S-shaped isotherm trend with the maximum uptake capacity of approximately 0.26 kg kg^{-1}. The water adsorption isotherms for the adsorbents BPL carbon and type RD2560 silica gel exhibit type V and type I isotherm trends, respectively. These uptake values depicted in Fig. 5.4 are obtained via the corresponding isotherm equations, whose fitting coefficients are tabulated in Table 4.1. The maximum uptake capacity values of these two adsorbents are $0.4\,\mathrm{kg\,kg^{-1}}$ and $0.33\,\mathrm{kg\,kg^{-1}}$, respectively. The isotherm data from these three adsorbents are compared against the ones obtained from the GCMC simulation for the graphite slit pore. Since, the graphite slit pore model is developed to represent the activated carbon structure, a resemblance can be observed between the isotherms of this graphite model with the other two CAC and BPL carbon adsorbents. Despite the close uptake capacities between the graphite model and the silica gel adsorbent, the shape of the isotherms differ significantly. This occurrence highlights the difference in the mechanics of water adsorption process between these two adsorbents. Furthermore, the uptake data obtained from the GCMC simulation can be used to analyze the activated carbon-based adsorption thermal systems, as the simulation data reasonably approximates the experimentally observed uptake trend. This exercise accentuates the bridge between the microscopic and macroscopic aspects of the adsorption phenomena.

5.2 Thermodynamic properties of adsorbed phase

5.2.1 Measurable properties

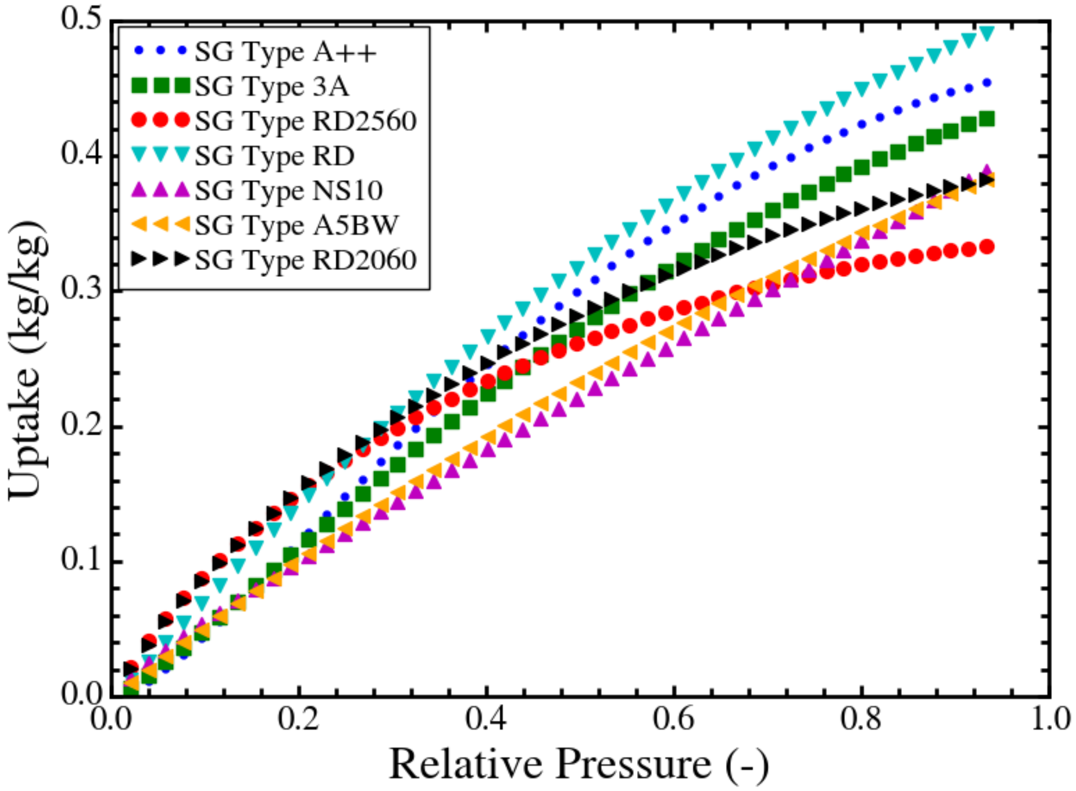

Figure 5.5: Adsorption isotherm of water adsorption in various silica gel adsorbents at the temperature 30 °C, calculated using Dubinin-Astakhov isotherm equation

Fig. 5.5 depicts the adsorption isotherm profile for water adsorption in different types of silica gel adsorbents. The isotherm trends are almost equivalent across the different silica gel materials. The maximum values of the uptake remain between the $0.3\,\mathrm{kg\,kg^{-1}}$ to $0.5\,\mathrm{kg\,kg^{-1}}$. Type RD silica gel and type RD2560 silica gel demonstrate the highest and lowest uptake capacity values, respectively. The uptake values are calculated using the D-A isotherm equation, denoted by Equation (4.1). In this equation, the uptake is directly proportional to the coefficients representing the maximum uptake capacity (w_0)

and the activation energy (E). On the contrary, an inverse proportionality is present between the surface heterogeneity coefficient (n) and the adsorption uptake. As shown in Table A.1, the value of w_0 is higher for type RD silica gel than type RD2560 silica gel, which results in the higher maximum uptake value in the isotherm trend. Furthermore, the uptake values of the type RD silica gel are enhanced by the slightly lower value of n as compared to type RD2560 silica gel. However, at the lower relative pressures (up to 0.28), the uptake values of type RD2560 silica gel slightly dominates type RD silica gel, due to the higher values of activation energy coefficient (E) of the former adsorbent than the latter. Additionally, the lower values of the term E for the types NS10 and A5BW silica gel adsorbents lead to lower uptake values in the low-pressure region. Therefore, the low-pressure adsorption is favored by the higher values of activation energy coefficient in the D-A isotherm model.

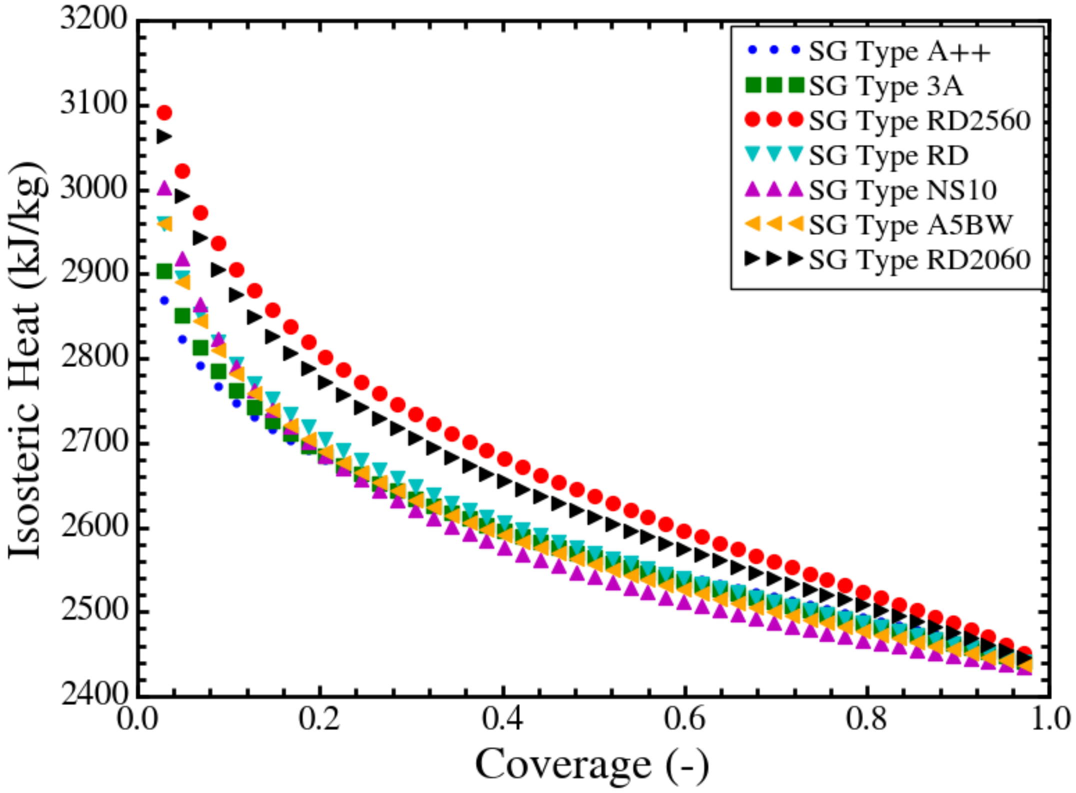

Figure 5.6: Isosteric heat of adsorption of water in various silica gel adsorbents at the temperature 30 °C, calculated using the q_{st} fundamental equation with the no adsorbed phase volume correction assumption

The variation in the isosteric heat of adsorption (q_{st}) for water adsorption in various types of silica gel adsorbents is portrayed in Fig. 5.6. The x-axis denotes the surface coverage value, which is expressed as the ratio of uptake and the maximum uptake capacity (w/w_0). Since, the water adsorption at the temperature 30 °C is at the sub-atmospheric condition, the q_{st} correlation for the low-pressure condition (Equation (4.22)) is applied for generating the q_{st} profile. This q_{st} correlation is independent of the isotherm coefficients. Thus, the variation of q_{st} with respect to the relative pressure values is absent between the different water-based adsorption pairs in the given temperature condition. However, since the adsorption isotherms show a distinction among the chosen adsorbents, the variation of q_{st} according to the surface coverage is observed. Consequently, an almost reversed trend of q_{st} values among the different types of silica gel adsorbents can be noticed. The type RD2560 silica gel appears to possess the highest values of q_{st}, whereas, type RD silica gel seems to exhibit low values of q_{st}. Generally, the q_{st} values appear to decrease with the increasing surface coverage for all the water-based adsorption pairs. The intermolecular interactions between the adsorbent and adsorbate molecules tend to reduce with the increasing surface coverage. The formation of monolayer or multilayer adsorbed phase onto the adsorbent surface leads to increased separation between the gaseous phase molecules and the adsorbent molecules. Since, the intermolecular interaction potential is inversely proportional to the intermolecular distance, the said reducing q_{st} profile with the increasing surface coverage becomes apparent. It is noted that, all the q_{st} profiles converge to a single value at the saturation surface coverage, which is almost equal to the latent heat of vaporization of water at the temperature $30\,^{\circ}\mathrm{C}$. Therefore, the occurrence of capillary condensation with the increased surface coverage can be concluded from this observation. The slope of the q_{st} values at the higher surface coverage is lower than the ones at the low surface coverage values. As described in the previous section, the onset of capillary condensation is initiated by the lateral interactions among the adsorbed water molecules. This interaction is stronger for water than the other adsorbates due to the highly stable cluster configuration of the adsorbed phase, generated by the strong hydrogen bond formation. At the low surface coverage, the q_{st} value is directly proportional to the strength of the interaction potential between the water and adsorbent molecules, since the lateral interactions remain absent due to the fewer adsorbed water molecules.

5.2.2 Derived properties

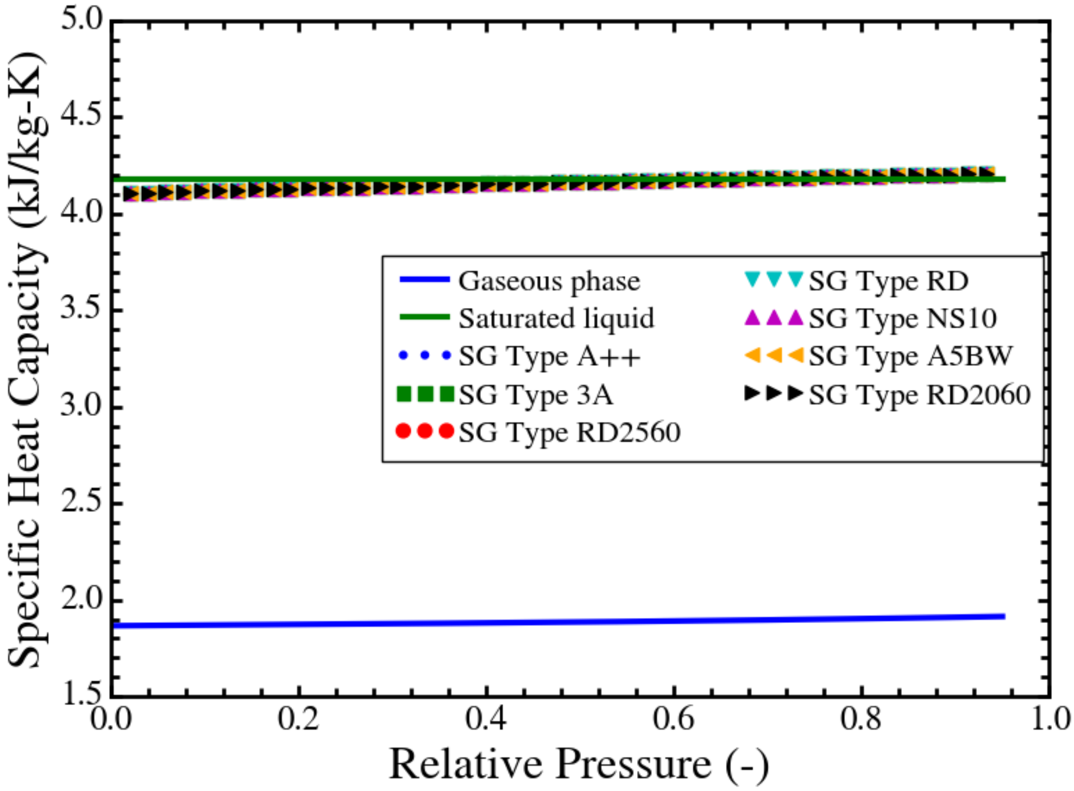

Figure 5.7: Specific heat capacity of the adsorbed phase water in various silica gel adsorbents at the temperature 30 °C, calculated invoking no adsorbed phase volume correction assumption

The specific heat capacity (c_{ade}) values of the water adsorption in various types of silica gel are depicted in Fig. 5.7. The c_{ade} values are plotted against the relative pressure of water vapor at the temperature 30 °C and compared with the corresponding gaseous ($c_{p,g}$) and saturated liquid phase ($c_{p,l}$) specific heat capacity values. It can be observed that the c_{ade} values remain close to the corresponding saturated liquid phase $c_{p,l}$ values. This behavior can be ascribed to the reduced intermolecular distance among the adsorbed phase water molecules, similar to the corresponding condensed phase's molecular configuration. A slight deviation of c_{ade} from the $c_{p,l}$ values can be attributed to the effect of the adsorbent-adsorbate intermolecular interactions. An increasing trend of

c_{ade} values can be observed with respect to the increasing relative pressure. This phenomenon is attributed to the increased intermolecular interaction among the adsorbed phase water molecules at the higher uptake values. Therefore, a higher amount of energy is required to increase the temperature of the adsorbed phase by a unit amount at the higher relative pressure values. A contrary trend in the c_{ade} values can also be observed for adsorption of a different adsorbate gas. Based on the mathematical formulation, the c_{ade} values of water vapor adsorption is independent of the isotherm coefficients, since the similar behavior is exhibited by the q_{st} property. Therefore, the profiles of c_{ade} with respect to different adsorbent material appear to overlap upon each other in Fig. 5.7.

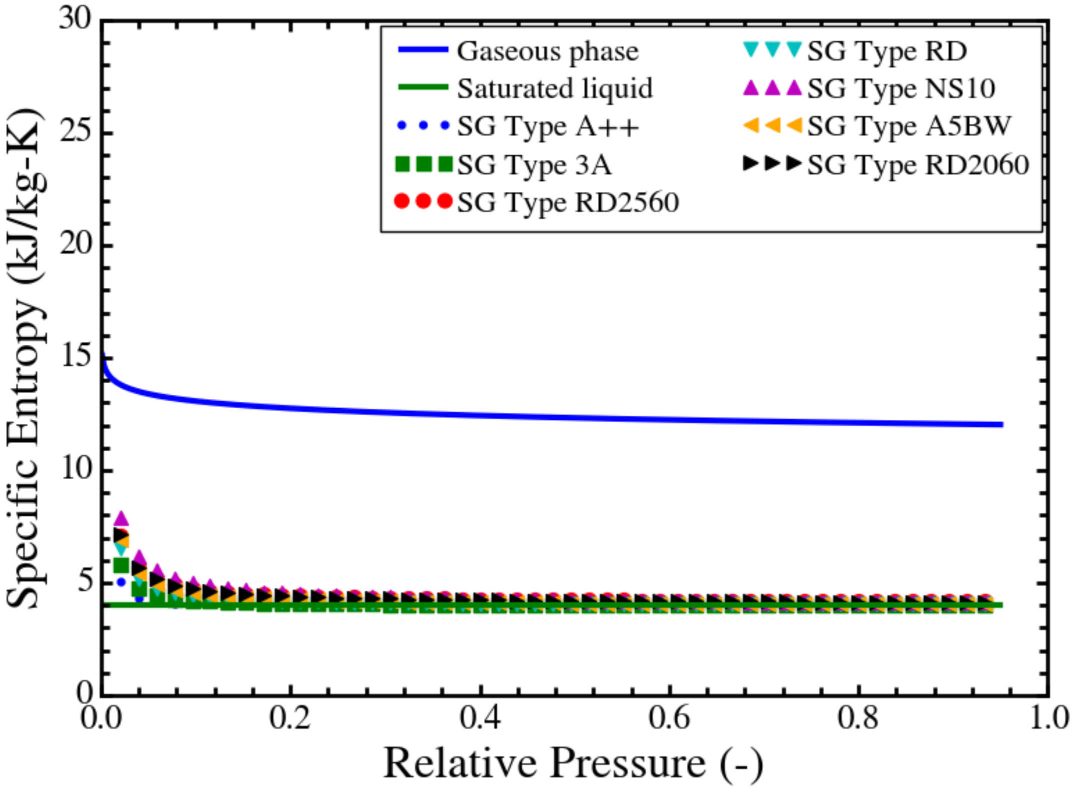

Figure 5.8: Adsorbed phase mass specific entropy of the adsorbed phase water in various silica gel adsorbents at the temperature 30 °C, calculated invoking no adsorbed phase volume correction

The specific entropy (s_a) values of the adsorbed phase water developed on various types of silica gel adsorbents are depicted in Fig. 5.8. The comparison between the s_a

values with the corresponding gaseous (s_g) and saturated liquid phase (s_l) entropy values resembles the said comparison for c_{ade}. The s_a values get closer to s_l values at the higher relative pressure values. However, at the low relative pressure values (approximately $<$ 0.1), s_a values are significantly higher than the s_l values. This trend in the adsorbed phase specific entropy values can be explained by the molecular level entropic behavior of the adsorbed phase. The entropy can be described as the measure of possible distribution of a molecular configuration consistent with the given macroscopic state. This definition is mathematically expressed in the form of Boltzmann equation for entropy ($S = k_B \ln W$, W is the possible number of microstates). This distribution of molecular configurations is associated with the molecular motions such as translation, rotation, vibration, etc. With the increase in these molecular motions, the corresponding entropy value increases accordingly. Therefore, the gaseous phase adsorbate possesses higher specific entropy values than that of the saturated liquid phase, due to the higher molecular motion in the gaseous phase. The adsorbed phase is generated with the influence of the adsorbent induced attractive potential field. The transition of the adsorbate molecules from the gaseous phase to the adsorbed phase with the influence of the said potential field is associated with the loss in the degrees of freedom in the molecular motion. This behavior is consistent with the molecular orientation distribution of the adsorbed phase, as shown in Fig. 3.11d and Fig. 3.13. In these figures, the adsorbed CO_2 molecules exhibit a narrow distribution around the angle 90° with the effect of the strong potential field generated by the narrow pore size of the graphite. Therefore, the loss of rotational degree of freedom is realized. Similar conclusion can be drawn for the adsorption of water in various silica gel adsorbents. Hence, the adsorbed phase specific entropy values remain closer to the corresponding saturated liquid phase values. At the low relative pressures, the density of the adsorbed phase is lower than at the higher relative pressures. As a result, the degrees of freedom of the adsorbed water molecules increase with the reduction in the pressure. The variation of s_a among the different silica gel adsorbents is significant at the lower relative pressures. Types NS10 and A++ silica gel exhibit a maximum difference of approximately $5\,\mathrm{kJ\,kg^{-1}\,K^{-1}}$ in the s_a values. This difference is caused by the inclusion of the uptake quantity in the s_a formulation, given by Equation (4.28).

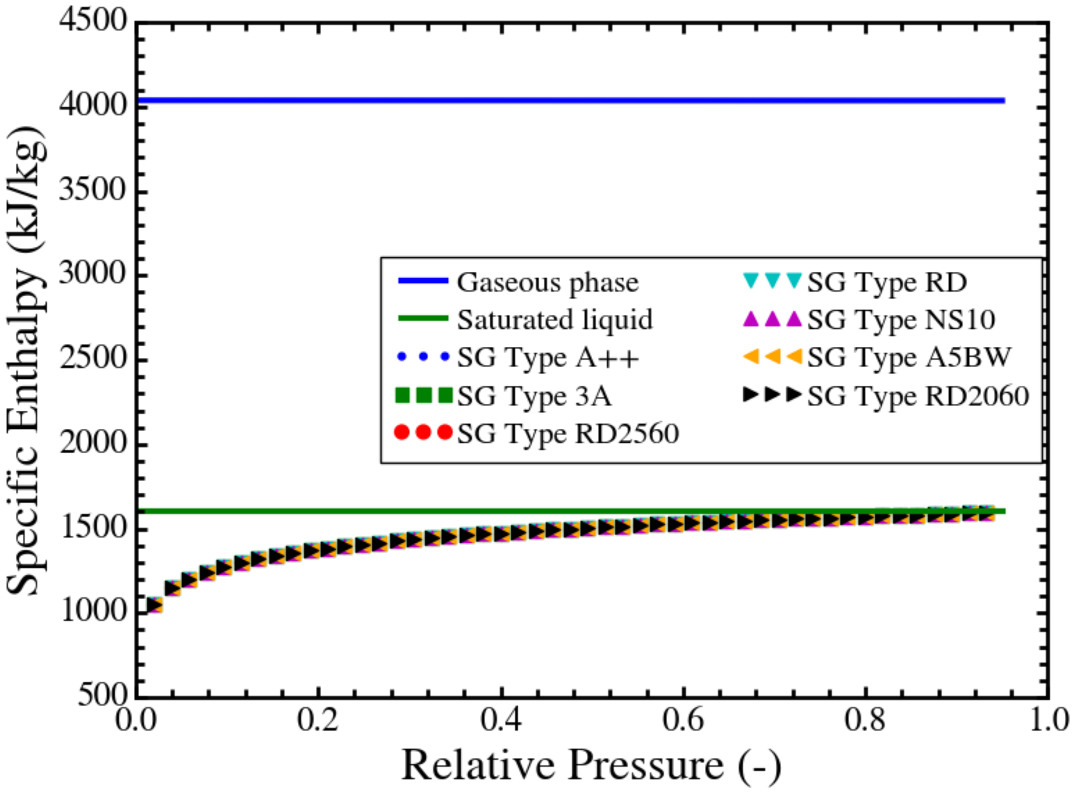

Figure 5.9: Adsorbed phase mass specific enthalpy of the adsorbed phase water in various silica gel adsorbents at the temperature 30 °C, calculated invoking no adsorbed phase volume correction

The adsorbed phase specific enthalpy (h_a) variation of the water adsorption in various silica gel is illustrated in Fig. 5.9. The h_a values also exhibit a closer values with the corresponding saturated liquid phase enthalpy (h_l) than the gaseous phase specific enthalpy (h_g) values at the given temperature of 30 °C. The simple correlation for h_a provided in Equation (4.29) dictates that the h_a value is obtained by reduction of the h_g by the amount of isosteric heat of adsorption (q_{st}). Since, the q_{st} values are greater than the latent heat of vaporization (h_{fg}) of water, the resultant h_a values go below the h_l values. The increasing trend of h_a with the increasing relative pressure is caused by the reduction in the q_{st} values. Likewise, the variation in h_a among the different adsorbents is absent due to the indifference in the corresponding q_{st} values.

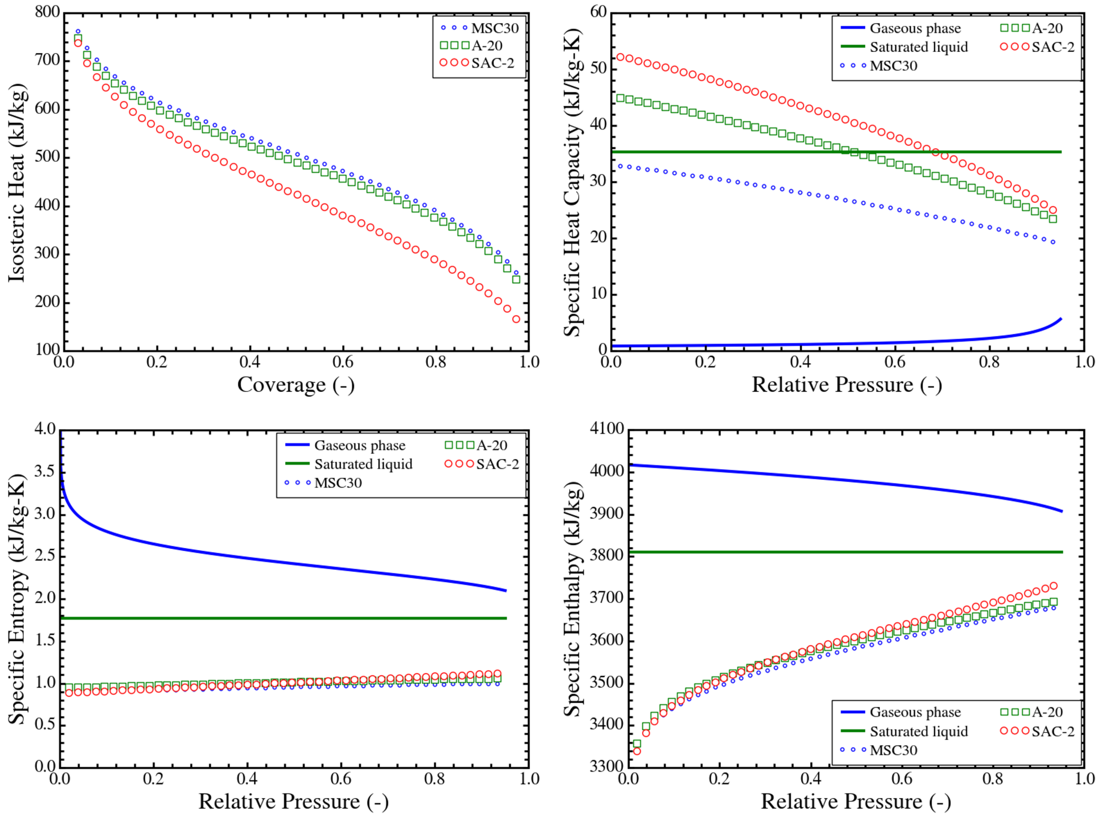

Figure 5.10: Thermodynamic properties of the CO_2 adsorbed phase developed on different types of activated carbon adsorbents at the temperature 30 °C, calculated using adsorbed phase volume correction in the isotherm model

The thermodynamic properties of water adsorption are associated with the assumption of negligible adsorbed phase specific volume (v_a) due to the sub-atmospheric operating pressure condition. The correlations obtained for these properties can be applied for adsorbent-adsorbate pair where the value of v_a is not negligible. Therefore, the thermodynamic properties of the CO_2 adsorbed phase formed on different types of activated carbon adsorbents are depicted in Fig. 5.10. These activated carbons included are MSC30, A-20, and SAC-2. The isosteric heat of adsorption trend for the three adsorbent-adsorbate pair are similar to that of the water adsorption. It can be seen that MSC30 and A-20 activated carbon adsorbents give higher values of q_{st} than the SAC-2 activated carbon. This behavior is attributed to the proportional relationship between the activation energy term (E) in the D-A isotherm equation and q_{st}. The c_{ade} values remain close to the $c_{p,l}$ values. Since, the temperature 30 °C is very close to the critical temperature of CO_2 (31 °C), the $c_{p,l}$ values are much higher than the $c_{p,g}$ values. A decreasing trend in the c_{ade} with the increasing relative pressure can be noticed for CO_2 adsorption in activated carbon adsorbents. This behavior is caused by the effect of finite adsorbed phase specific volume (v_a). The intermediate term of the c_{ade} formulation expressed by Equation (4.38) containing the v_a quantity manifests a dominating negative effect over the temperature differential of q_{st}, resulting in the overall decrease in the value of c_{ade} with increasing relative pressure. Similarly, the presence of v_a in the formulation for adsorbed phase specific entropy (s_a) engenders its lower value than the corresponding saturated liquid phase specific entropy values (s_l). Furthermore, the adsorbed phase specific enthalpy (h_a) values demonstrate a difference among the activated carbon adsorbents with respect to the relative pressure. The consideration of v_a in the isotherm formulation leads to the presence of isotherm coefficients in the q_{st} formulation. Therefore, the q_{st} values vary among the different adsorbents considered for its variation with respect to the relative pressure. The same is reflected on the variation in the values of h_a.

5.3 Thermodynamic characterization of the adsorption heat transformer cycle

The present section delves into the thermodynamic characterization of the adsorption heat transformer (AHT) cycle. Initially the effect of the operating conditions and the adsorbent properties on the performance parameters of the AHT cycle is delineated. This analysis is followed by the estimation of the performance improvement of the AHT cycle by introduction of the internal heat recovery scheme. Finally, the theoretically obtainable maximum temperature lift of the AHT cycle and its dependence on the adsorption isotherm models are observed.

5.3.1 Effect of operating condition and adsorbent properties

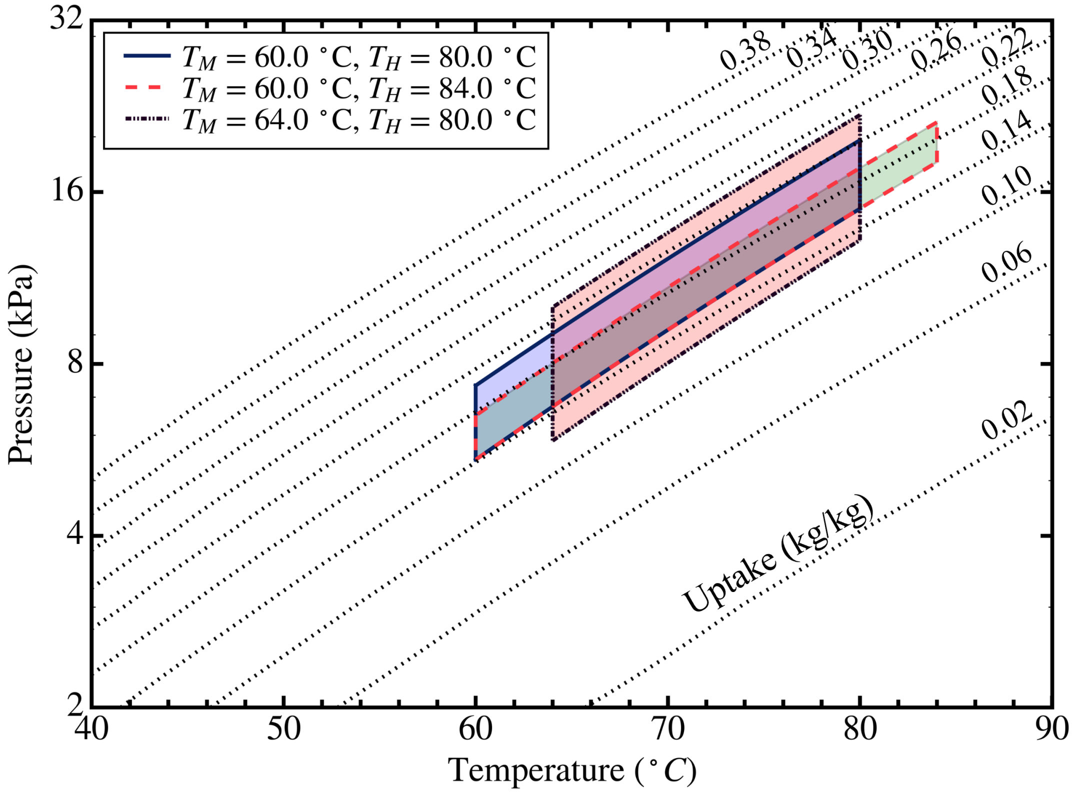

Figure 5.11: Adsorption heat transformer cycle in pressure - temperature - uptake plane at different operating heat source (T_M) and heat supply (T_H) temperature values, fixed heat sink temperature (T_L) at 30 °C for the type A++ silica gel adsorbent and water vapor adsorbate

Fig. 5.11 depicts the AHT cycle diagram on the pressure-temperature-uptake plane for three different combinations of heat source and heat supply temperatures. For this analysis, the Type A++ silica gel is used as the adsorbent material and the water is chosen as the adsorbate fluid. The parameters of the D-A isotherm equation of this adsorption material pair are provided in the Table A.1. The heat upgrading performance can be characterized by the upgraded useful heat generated during the isothermal adsorption phase and the useful heat ratio (UHR). The mathematical expressions for these two quantities are given by Equations (4.49) and (4.56), respectively. The potable water generation potential of the AHT cycle is characterized by its condensation heat ratio, which is determined by using the CHR correlation given in Equation (4.56). These quantities are dependent upon the operating temperature conditions (e.g., heat source temperature, heat supply temperature, and heat sink temperature) as well as the adsorber heat exchanger properties (heat exchanger thermal mass ratio). The effect of these parameters on the AHT cycle performance are depicted in the following figures.

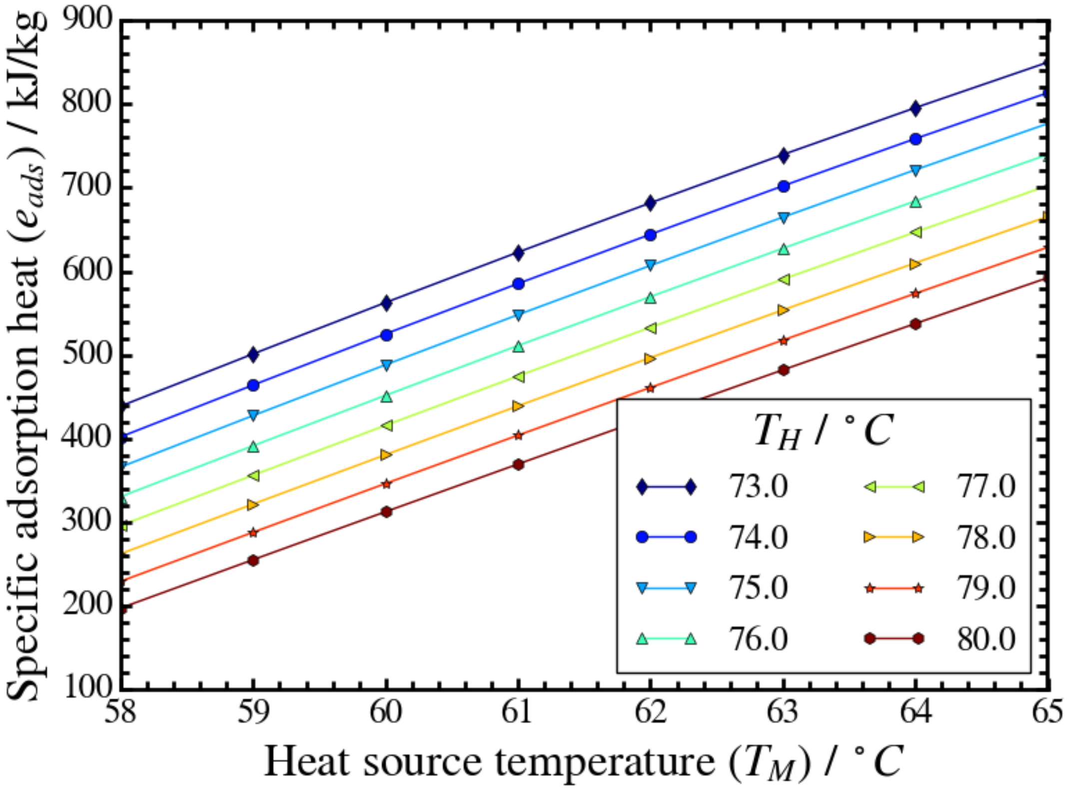

Figure 5.12: Isothermal adsorption heat supply variation with respect to heat source temperature (T_M) and heat supply temperature (T_H) at the heat sink temperature (T_L) 30 °C

Fig. 5.12 portrays the variation in the useful adsorption heat generated with the change in heat source temperature (T_M) and heat supply temperature (T_H). The heat sink temperature (T_L) is fixed at 30 °C and the heat exchanger thermal mass ratio (m_{HX}/m_{ads}) is kept at 0.25. The upgraded heat is denoted as the adsorption heat released per mass of the adsorbent (e_{ad}). A linearly rising trend of e_{ad} can be observed with the increase in the temperature T_M for all T_H values. This trend can be explained using the net uptake difference with the variation in T_M. The initial uptake value before the preheating phase when the temperature T_M increases at constant condenser pressure (P_{cond}). Likewise, the final uptake value at the end of the isothermal adsorption phase increases with the increase in T_M, as the evaporator pressure corresponds to the saturation pressure of the adsorbate at temperature T_M. Thus, the net uptake $(w_3 - w_1)$ increases with the temperature T_M. For a fixed value of T_H, the net sensible heat requirement for preheating the adsorber bed decreases as the integral on the L.H.S of Equation (4.46) correspond to the temperature difference. Therefore, the requisite adsorption heat in the preheating phases decreases as per the preheating energy balance Equation (4.46). Thus, if the value of w_1 decreases, the final uptake value of the preheating phase (w_2) also reduces. Therefore, the net uptake in the isothermal adsorption phase $(w_3 - w_2)$ increases, which determines the integral limits of the adsorption heat supply in Equation (4.49). The variation of temperature T_H at constant T_M exhibits a contrary behavior, where the increase in T_H leads to the decline in the useful adsorption heat. The value of w_3 decreases with the increase in T_H at the constant evaporator pressure $(P_{sat}(T_M))$. Consequently, the net uptake difference decreases, affecting the amount of the adsorption heat released during the isothermal adsorption phase. Therefore, the plot indicates an inverse relationship between the useful adsorption heat generated and the net temperature difference between the heat source and heat supply temperatures in the AHT cycle.

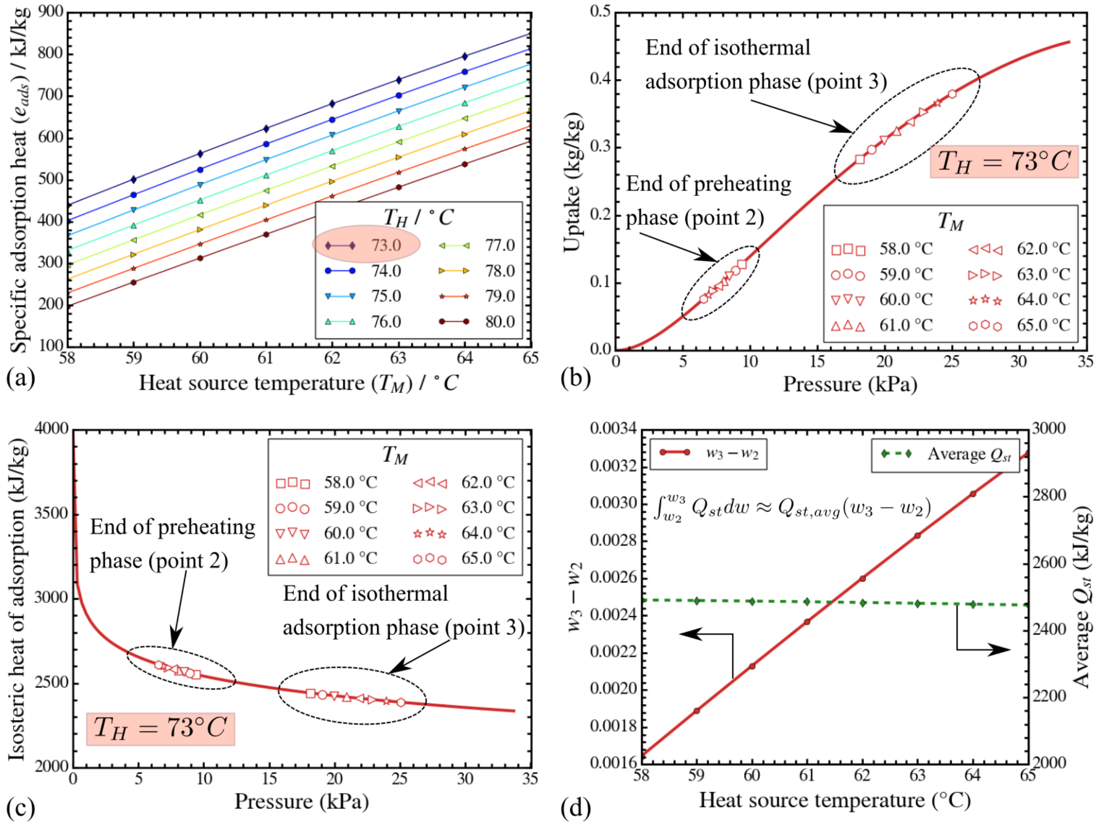

Figure 5.13: (a) Adsorption heat supply variation with respect to heat source temperature, (b) adsorption isotherm for type A++ silica gel at temperature 73 °C, (c) isosteric heat of adsorption for type A++ silica gel at temperature 73 °C, (d) net uptake difference and average isosteric heat of adsorption during the isothermal adsorption phase

The linear nature of the adsorption heat supply with the variation in the heat source temperature can be attributed to the shape of the isotherm and isosteric heat of adsorption in the given pressure range. Fig. 5.13a depicts the adsorption heat supply variation with respect heat source and heat supply temperatures. The heat supply temperature T_H is taken as 73 °C for demonstrating the isotherm and isosteric heat profile in figures 1b and 1c, respectively. In these figures, the points corresponding to the end of the preheating phase (point 2 in AHT cycle) and the end of isothermal adsorption phase (point 3) are highlighted. As shown in Fig. 5.13b, as T_M increases, the point 2 moves to lower uptake values. Contrarily, the point 3 attains higher uptake values with increase in T_M. This behavior is ascribed to the increase in evaporator pressure with the increase in T_M.

It is observed that the isotherm profile exhibits near linear profile between the points 2 and 3. The same can be noticed in the isosteric heat profile, as shown in Fig. 5.13c. Fig. 5.13d shows the uptake difference and average isosteric heat value over the different heat source temperature. The product of these two quantities is the approximated formulation of the isosteric heat integral, as highlighted in Fig. 5.13d. The net uptake difference during the isothermal adsorption phase is exhibiting a linear profile because of the near-linear profile of the isotherm. Moreover, the change in average q_{st} during the isothermal adsorption phase with respect to temperature T_M is negligible. Therefore, the resultant upgraded adsorption heat supply variation demonstrates a linear behavior with respect to the heat source temperature. A non-linear profile for the same is expected when the isotherm exhibits an S-shaped profile, which is generally observed for water adsorption in activated carbon and MOF adsorbents.

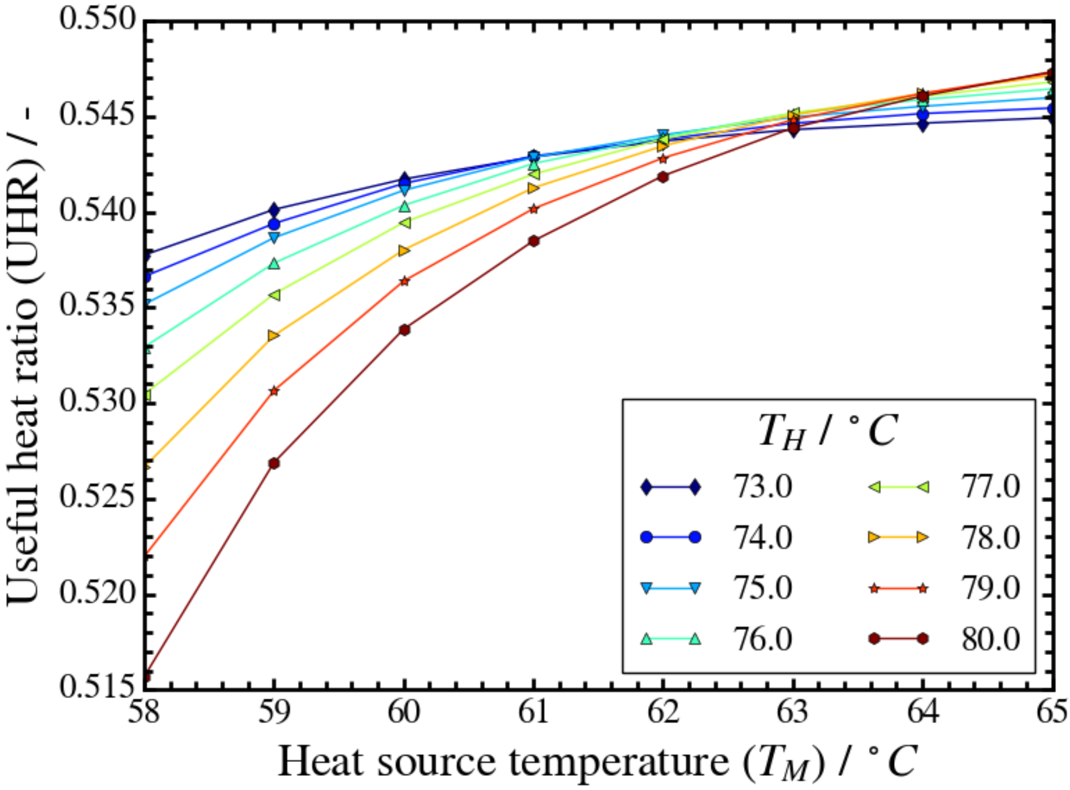

Figure 5.14: Useful heat ratio variation with respect to heat source temperature (T_M) and heat supply temperature (T_H) at condenser temperature 30 °C

The variation in the useful heat ratio (UHR) across the operating temperature range of the AHT cycle is illustrated in Fig. 5.14 at the same fixed conditions mentioned for Fig. 5.12. The UHR values do not appear to significantly vary with the change in the operating temperature, which mainly stays between the values 0.515 to 0.547. This limited variation is attributed to the simultaneous change in the input and output heats present in the denominator and numerator of the UHR formulation in Equation (4.56), respectively. As the temperature T_M increases at constant T_H, the output upgraded adsorption heat increases, as depicted in Fig. 5.12. At the same time, the net sensible heat supplied by the desorber bed during the precooling phase decreases, which results in the reduced requisite desorption heat. Thus, the net uptake difference during the precooling phase $(w_3 - w_4)$ decreases, along with the reduction in the value of w_3 as described above. Consequently, the uptake difference $w_4 - w_1$ increases with the simultaneous decrease in w_1 and increase in w_4. As a result, the input desorption heat increases with the increase in T_M. Furthermore, the input evaporation heat also increases, as it is directly proportional to the net uptake difference of the AHT cycle $(w_3 - w_1)$ as per Equation (4.53). Thus, the simultaneous increase in the numerator and denominator inhibits any significant change in the UHR value. However, the slight increasing trend is attributed to the difference in rate of increase in the input and output heats. The input heats are dependent upon the isosteric heat of adsorption and latent heat of vaporization at the temperature T_M. These quantities are inversely proportional to temperature. This behavior inhibits the increasing rate of the input desorption and evaporation heat values. Thus, the rate of increase in the adsorption heat is higher than the input desorption and evaporation heat. The values of UHR is higher for lower values of temperature T_H, which is caused by the higher output adsorption heat as portrayed in Fig. 5.12.

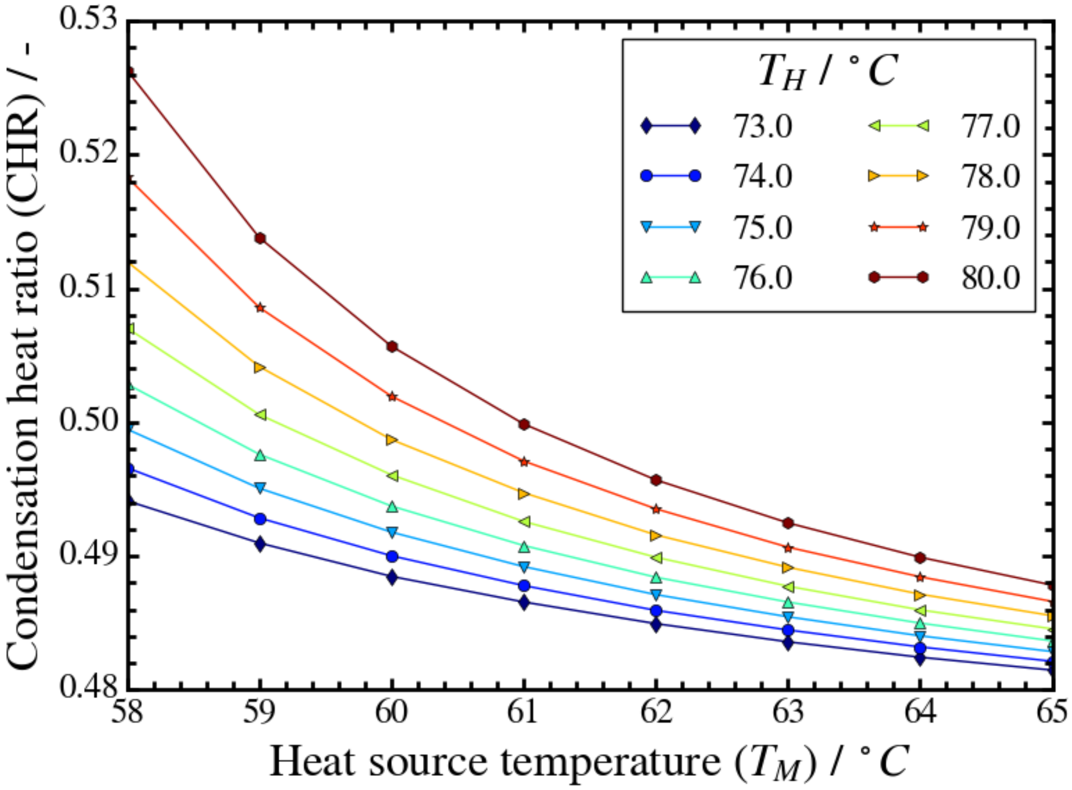

Figure 5.15: Condensation heat ratio variation with respect to heat source temperature (T_M) and heat supply temperature (T_H) at condenser temperature 30 °C

The condensation heat ratio (CHR) of an AHT cycle exhibits an opposite behavior to the UHR variation. As depicted in Fig. 5.15, the value of CHR decreases with the increase in temperature T_M and the decrease in temperature T_H. This behavior can be attributed to the higher rate of increase in the output condensation heat than the input desorption heat and evaporation heat. As the temperature T_H increases, the net uptake value of the AHT cycle decreases, causing the output condensation heat and input evaporation heat to fall. Concomitantly, the value of the input desorption heat decreases, as the requisite precooling desorption heat increases with the increasing temperature difference. Thus, the decrease in the maximum uptake value w_3 with the increasing T_H causes the precooling final uptake to decrease, resulting in the lower value of input desorption heat. Hence, the CHR value is directly proportional to the temperature T_H. Thus, a trade-off relation between the useful heat ratio and the condensation heat ratio can be observed with respect to the operating temperature range.

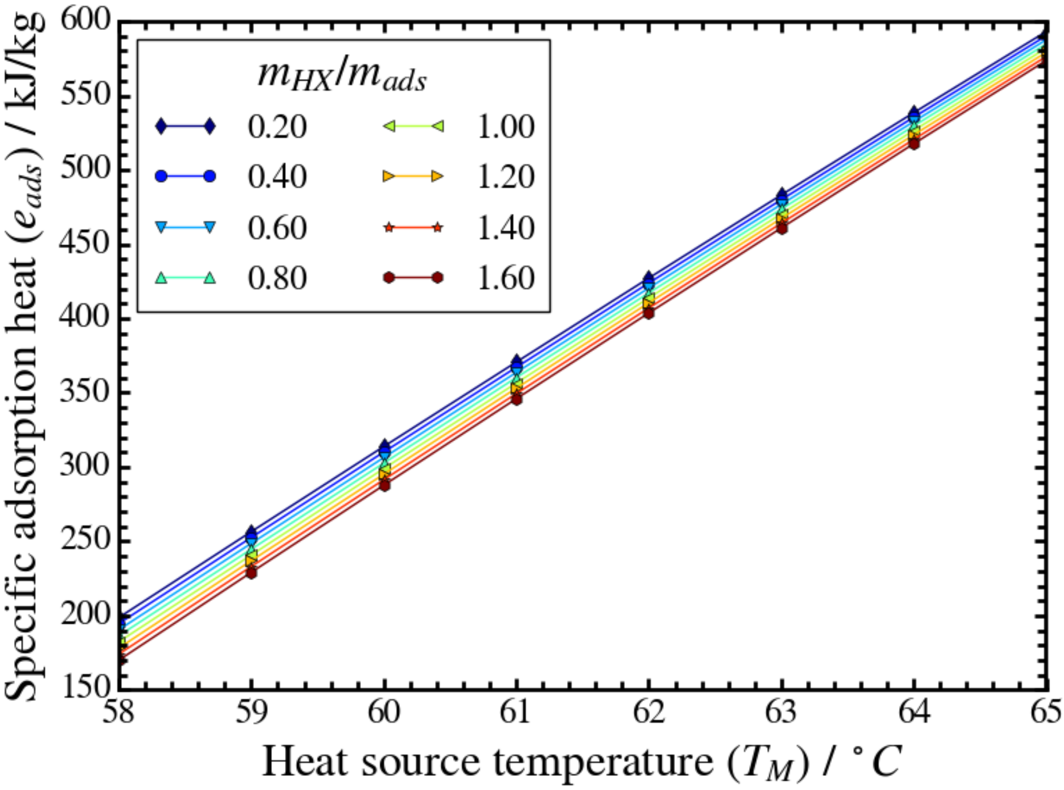

Figure 5.16: Isothermal adsorption heat supply variation with respect to heat source temperature (T_M) and adsorber bed thermal mass ratio (m_{HX}/m_{ads}) at the heat sink temperature (T_L) 30 °C

Fig. 5.16 demonstrates the effect of the heat exchanger thermal mass ratio (m_{HX}/m_{ads}) on the useful adsorption heat generation. It can be seen that there is a small decrease in the adsorption heat produced during the isothermal adsorption phase with the increase in the given thermal mass ratio. This occurrence is caused by the increase in the requisite sensible heat for increasing the temperature of the bed during the preheating phase. Mathematically, the sensible heat required by the thermal mass is directly proportional to the given mass ratio, as expressed in Equation (4.43). Thus, the net adsorption heat to be supplied during the preheating phase increases. Since, the operating temperatures are fixed, the difference in uptake increases during the preheating phase. Therefore, the amount of uptake change in the isothermal adsorption phase decreases, engendering a decrease in the upgraded adsorption heat supply. However, this change is small as only a part of the total sensible heat is impacted by the change in the thermal mass ratio.

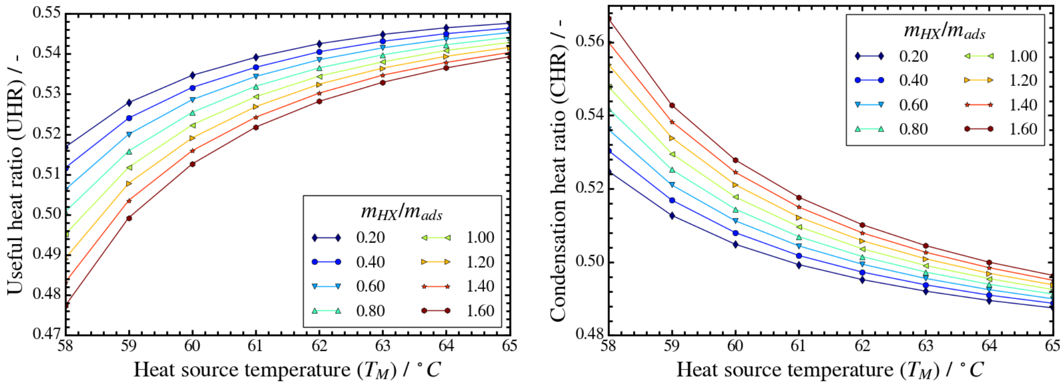

(a) Useful heat ratio variation

(b) Condensation heat ratio

Figure 5.17: Heat ratio variation with respect to heat source temperature (T_M) and adsorber bed thermal mass ratio (m_{HX}/m_{ads}) at condenser temperature 30 °C

The variation in the UHR and CHR values with respect to the change in thermal mass ratio is relatively significant than the effect on solely the upgraded adsorption heat supply. As the thermal mass ratio increases, the UHR and CHR values exhibit opposite trends. The decrease in the UHR values with the increase in the thermal mass ratio, as depicted in Fig. 5.17a is attributed to the higher rate of decline in the output adsorption heat compared to the input desorption heat. The slopes of the preheating and precooling paths in the cycle diagram (Fig. 5.11) appears to be different, which is dependent upon the adsorption isotherm nature. Therefore, the rate of the change in the sensible heat of preheating and precooling phases are different, which results in the given UHR behavior. This decreasing tendency of UHR with increasing thermal mass ratio reduces at the higher values of temperature T_M. Since, the specific heat capacity of the HX material depicts a linear relationship with temperature (Equation (4.44)), the rate of decrease in the input desorption heat increases. Consequently, the reduction in the UHR quantity with the increase in thermal mass ratio decelerates. Contrarily, the CHR value increases with the increasing thermal mass ratio. This phenomenon is ascribed to the independence of the condensation heat upon the thermal mass ratio. Therefore, only the denominator tends to decrease, engendering the increase in the CHR value with an increase in the thermal mass ratio.

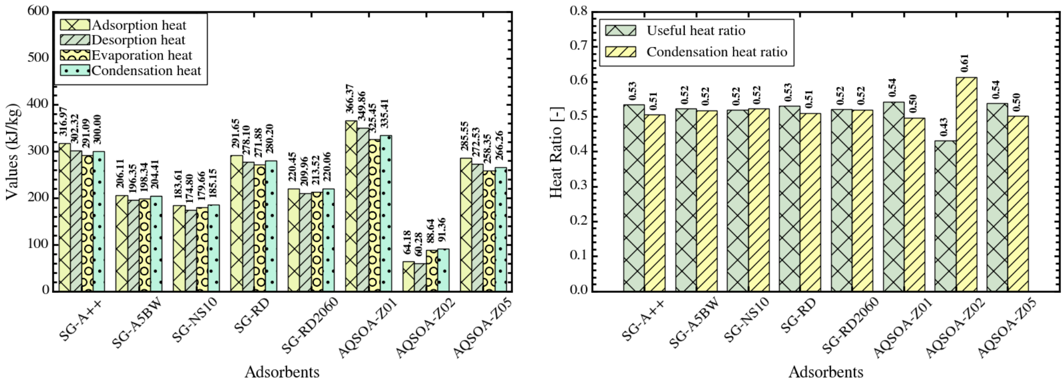

(a) Heat exchange values (b) Useful and condensation heat ratio values

Figure 5.18: Comparison of performance parameters of adsorption heat transformer cycle among different adsorbent materials at the heat source temperature of 60 °C, heat supply temperature 80 °C, and condenser temperature 30 °C

From the preceding discussion on the effect of temperature and thermal mass ratio of the adsorber bed on the performance parameters of the AHT cycle, it is evident that the type of the adsorption isotherm influences the net uptake value and the corresponding heat exchange values. The type of adsorption isotherm varies among the adsorbent-adsorbate pair chosen for the cycle. Hereby, a comparison of the performance parameters among different adsorption material pairs are evaluated. Fig. 5.18 compares the AHT cycle performance parameters among five types of silica gel and three types of AQSOA zeolite adsorbents. The structural characteristics of these adsorbents are provided in Table A.2. Water vapor is considered as the adsorbate fluid. For all the adsorbent-adsorbate pairs, D-A isotherm equation is used to calculate the uptake values. The coefficients of the D-A equation are tabulated in Table A.1. In Fig. 5.18a it can be seen that type-A++ silica gel exhibits the highest heat exchange values. These values are slightly lower for the type RD silica gel. A reduction of approximately $80\,\mathrm{kJ\,kg^{-1}}$ to $100\,\mathrm{kJ\,kg^{-1}}$ is observed in the given heat exchange values for the rest of the silica gel adsorbents considered. This observation can be explained by the trends of the adsorption isotherm and isosteric heat of adsorption, as illustrated in Fig. 5.19. The operating regions of the preheating and precooling phases are highlighted, whose values are tabulated in Table 5.2. The isotherms of type A++ silica gel shows higher values of the uptake in the operating preheating and precooling pressure range. Likewise, the gradient of the isosteric heat of adsorption is lower for this adsorbent. These two factors contribute to the highest values of the specific heat exchange values. Type RD silica gel follows the similar isotherm and isosteric heat behavior, resulting in its high heat exchange values. Contrarily, type NS10 silica gel exhibits the lowest uptake values as well as a slightly higher slope of the isosteric heat of adsorption in the operating range of preheating and precooling. Therefore, the heat exchange values are the lowest for this type of silica gel. Despite the significant variations in the heat exchange values, the useful and condensation heat ratio parameters remain relatively unaffected by the type of the silica gel materials. This phenomenon is attributed to the near-equal values of the different heat exchange values (output adsorption and condensation heats and input desorption and evaporation heats) for each silica gel adsorbent.

Among the zeolite adsorbents, AQSOA-Z01 zeolite exhibits the highest heat exchange values, which are even higher than the corresponding values of type-A++ silica gel. Contrarily, AQSOA-Z02 depicts the lowest heat exchange values. This occurrence can be delineated by the isotherm and isosteric heat behavior of the zeolites, portrayed by Fig. 5.20. Unlike the silica gel adsorbents, the AQSOA type zeolites exhibit an S-shaped adsorption isotherm, which represents the very-low uptake at the lower relative pressures, which is followed by the sudden uptake rise and the subsequent saturation. Therefore, the operating region of the preheating and precooling phases are critical. Within the current operating pressure range, as documented in Table 5.2, AQSOA-Z01 type zeolite exhibits the highest uptake difference. This zeolite also possess a low gradient of the isosteric heat of adsorption in the operating conditions. Therefore, the highest heat exchange values are observed for this adsorbent. Contrarily, the initial relative pressure of the preheating phase results in a high value of initial uptake for the AQSOA-Z02 type zeolite. Therefore, the net uptake difference is less than the same for AQSOA-Z01 and AQSOA-Z03 type zeolites. This behavior is accompanied by the highest slope in the isosteric heat of adsorption among the zeolites. Thus, the AQSOA-Z02 gives the poorest performance in terms of heat exchange values. A distinct variation in the UHR and CHR values can be observed among the zeolite adsorbents, as opposed to the same for silica gel adsorbents. Especially for the AQSOA-Z02 type zeolite, the difference between the CHR and UHR values is 0.18, which is more than the other adsorption material pair considered in the analysis. This behavior is ascribed to the higher condensation heat than the adsorption heat value of this adsorbent.

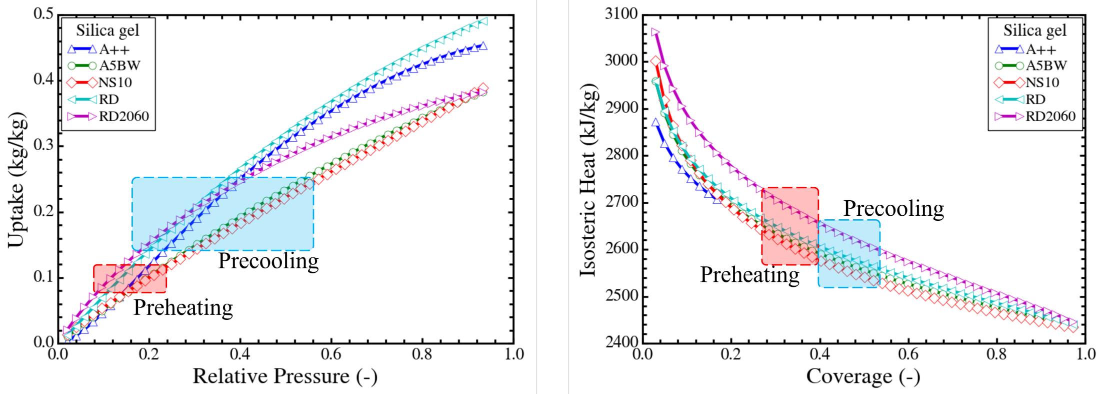

Figure 5.19: Adsorption isotherms and isosteric heat of adsorption for five types of silica gel adsorbents + water vapor adsorption at temperature 60 °C with the preheating and precooling domains highlighted

Table 5.2: Uptake and pressure state points of the adsorption heat transformer cycle for different adsorbent materials at the heat sink temperature 30 °C, heat source temperature 60 °C, and heat supply temperature 80 °C

Adsorbent	Uptake(kg kg^{-1})				Pressure(Pa)			
	w_1	w_2	w_3	w_4	P_1	P_2	P_3	P_4
SG A++	0.105	0.119	0.229	0.211	4246.97	11979.74	19946.43	7415.96
SG A5BW	0.093	0.106	0.177	0.162	4246.97	12391.37	19946.43	7257.19
SG NS10	0.092	0.105	0.169	0.153	4246.97	12547.71	19946.43	7209.20
SG RD	0.130	0.144	0.246	0.228	4246.97	12090.94	19946.43	7358.01
SG RD2060	0.142	0.157	0.233	0.215	4246.97	12313.55	19946.43	7159.04
AQSOA-Z01	0.051	0.062	0.189	0.174	4246.97	11491.09	19946.43	7093.07
AQSOA-Z02	0.236	0.253	0.273	0.255	4246.97	13624.24	19946.43	5543.96
AQSOA-Z05	0.000	0.009	0.110	0.097	4246.97	15555.68	19946.43	7767.29

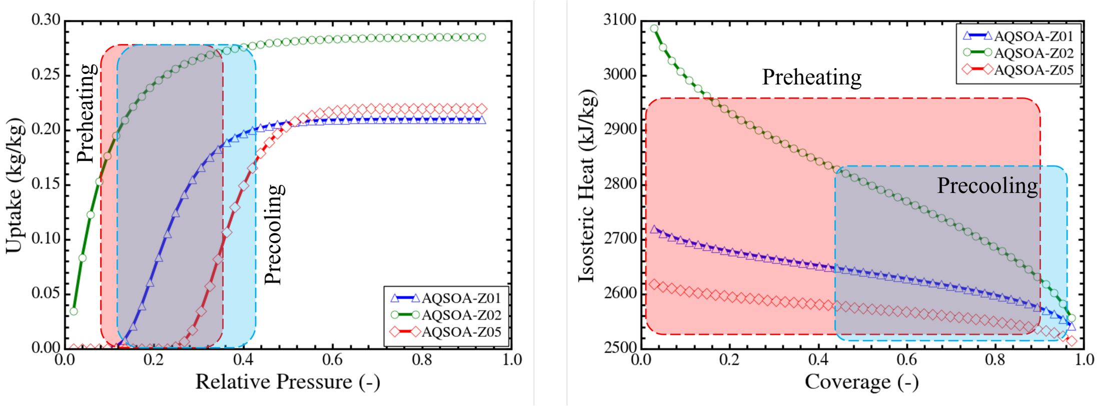

Figure 5.20: Adsorption isotherms and isosteric heat of adsorption for AQSOA type zeolite adsorbents at temperature 60 °C with the preheating and precooling domains highlighted

5.3.2 Effect of internal heat recovery

In the previous section, an overview of the impact of operating conditions on the performance parameters of the AHT cycle has been delineated. The non-isosteric preheating and precooling phases appear to be the bottleneck to the performance improvement of the AHT cycle. Therefore, the internal heat recovery methodology is introduced in Section 4.3.2 to reduce the preheating energy requirement. Here, the resultant improvement in the performance parameters are described as the heat recovery is applied between the adsorber and desorber beds. The respective property variations are plotted against a range of fractions of maximum possible heat recovery amount (0 % to 100 %).

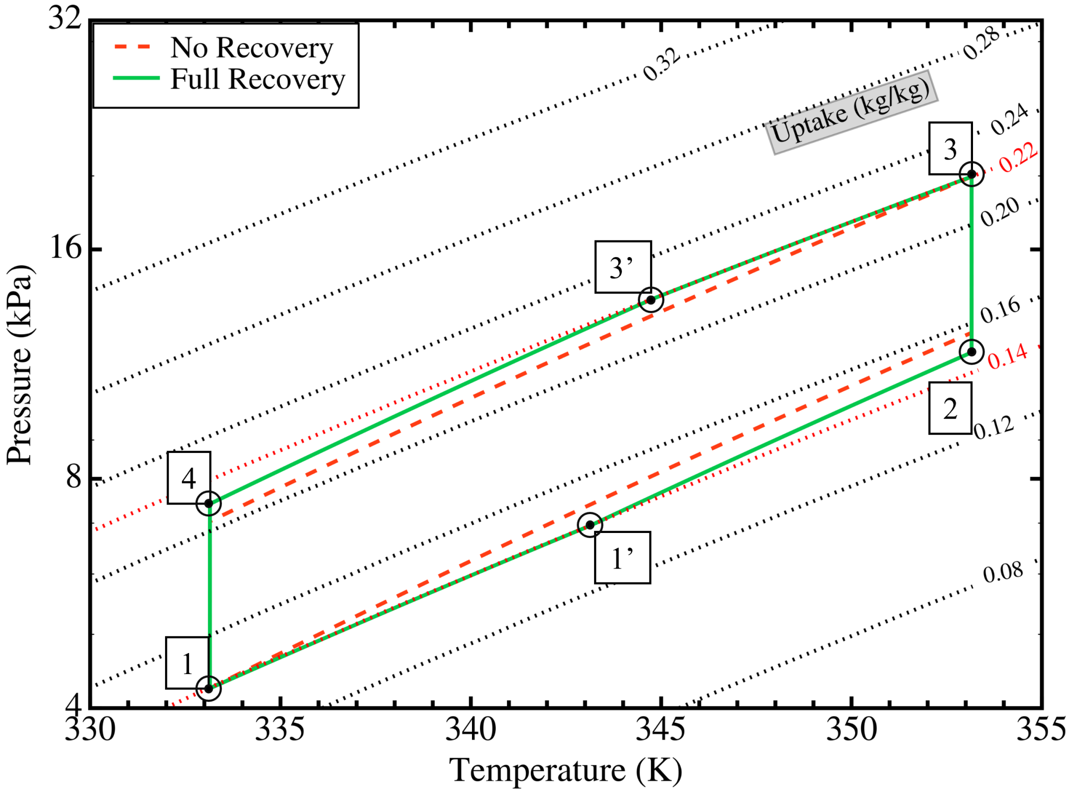

Figure 5.21: Adsorption heat transformer cycle with no heat recovery and maximum possible heat recovery for the heat source temperature of 60 °C and heat supply temperature of 80 °C

Table 5.3: State points in an adsorption heat transformer cycle with no heat recovery, 50 % of maximum possible heat recovery, and maximum possible heat recovery. P = Pressure in Pa, w = Uptake in kg kg^{-1}

Recovery	Quantity	State points					
		1	1'	2	3	3'	4
No HR	P	4246.97		12440.32	19946.43		7034.91
	w	0.142		0.156	0.221		0.204
50 % HR	P	4246.97	5458.64	12078.99	19946.43	16625.73	7224.81
	w	0.142	0.142	0.152	0.221	0.221	0.208
Full HR	P	4246.97	6949.56	11722.79	19946.43	13778.09	7416.43
	w	0.142	0.142	0.149	0.221	0.221	0.211

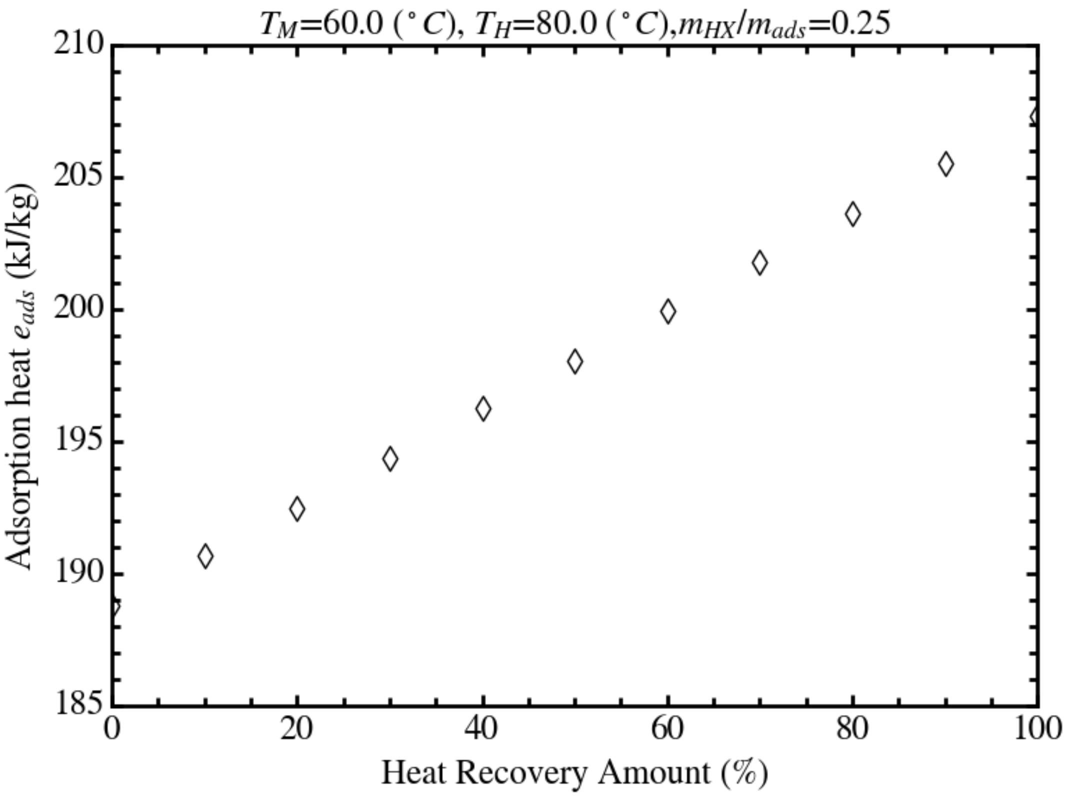

Figure 5.22: Adsorption heat variation with respect to fraction of maximum heat recovery possible at the constant heat source temperature 60 °C, heat supply temperature 80 °C, and thermal mass ratio of 0.25

Fig. 5.22 depicts the upgraded adsorption heat variation with respect to the fraction of maximum possible heat recovery amount at a constant temperature lift and thermal mass ratio of the AHT cycle. It can be seen that the adsorption heat amount monotonically increases with the increase in the heat recovery amount. This variation can be explained by the change in the net uptake amount during the isothermal adsorption phase due to the introduction of the heat recovery. Fig. 5.21 shows the AHT cycle diagram in pressure-temperature-uptake plane. Three cases of the AHT cycle are plotted in the diagram based on the conditions of (i) no heat recovery, (ii) 50 % of maximum possible heat recovery, (iii) maximum possible heat recovery The corresponding state points are tabulated in Table 5.3. It can be seen that at 50 % amount of heat recovery, the preheating phase begins at an intermediate uptake value of 0.152 kg kg^{-1} obtained at the end of the isosteric heat recovery phase. Thus, the resultant preheating uptake value obtains a value lower than the case where no heat recovery is present. Therefore, the net uptake difference increases during the isothermal adsorption phase, indicated by the increase in the value of $w_3 - w_2$ by 0.004 kg kg^{-1}. Therefore, the integration limit increases in Equation (4.47), engendering the increase in the upgraded adsorption heat amount released. The resultant uptake difference during the isothermal adsorption phase further increases when the heat recovery fraction is increased from 50 % to 100 %. This elevation is caused by the shift of the intermediate point at the end of isosteric heat recovery phase towards a higher uptake value.

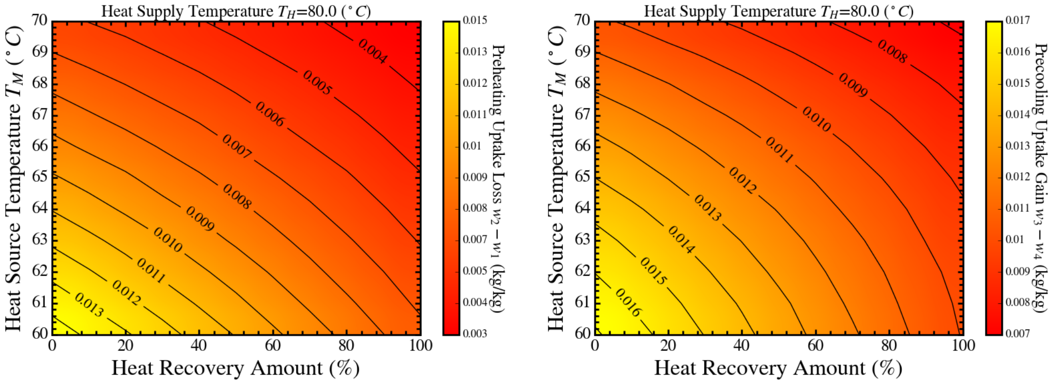

(a) Uptake loss

(b) Uptake gain

Figure 5.23: Variation in the uptake loss during the preheating phase and uptake release during the precooling phase with respect to fraction of the maximum heat recovery possible at constant heat supply temperature 80 °C and thermal mass ratio of 0.25 [219]

As highlighted in the previous figure, the change in the uptake change in the preheating phase is responsible for the change in the upgraded heat supply amount. Therefore, a detailed variations in the preheating uptake loss and precooling uptake release are illustrated in Fig. 5.24 with respect to the partial heat recovery amounts and heat source temperature at the fixed heat supply temperature and thermal mass ratio. As evident from the Fig. 5.21, the uptake loss during the preheating phase decreases with the increase in the heat recovery amount. When the heat recovery scheme is implemented, the temperature and pressure of the adsorber bed increases isosterically during the heat recovery phase. Thus, when the preheating phase is initiated, the pressure swing adsorption is carried out from the intermediate pressure and temperature value. Therefore, a reduced amount of preheating uptake consumption is required to achieve the desired net temperature lift of the AHT cycle. It is to be noted that the requisite uptake for the preheating phase will further reduce if the inverse relationship between the isosteric heat of adsorption and relative pressure is absent. The reduction in the uptake loss also varies with respect to the heat source temperature (T_M). As the value of T_M increases, the sensible heat exchange amount reduces due to the reduction in the initial uptake value. Therefore, the slightly increased amount of preheating uptake becomes necessary to achieve the same value of the heat supply temperature (T_H).

A similar occurrence for the precooling uptake gain can be observed. As the heat recovery is implemented, the precooling phase begins at an intermediate pressure and temperature. Therefore, the net uptake release during the precooling phases reduces with the increase in the heat recovery amount. This simultaneous change in the preheating and precooling uptake change with the change in heat recovery amount impacts the useful heat ratio and exergy efficiency values, which is discussed in the following figures.

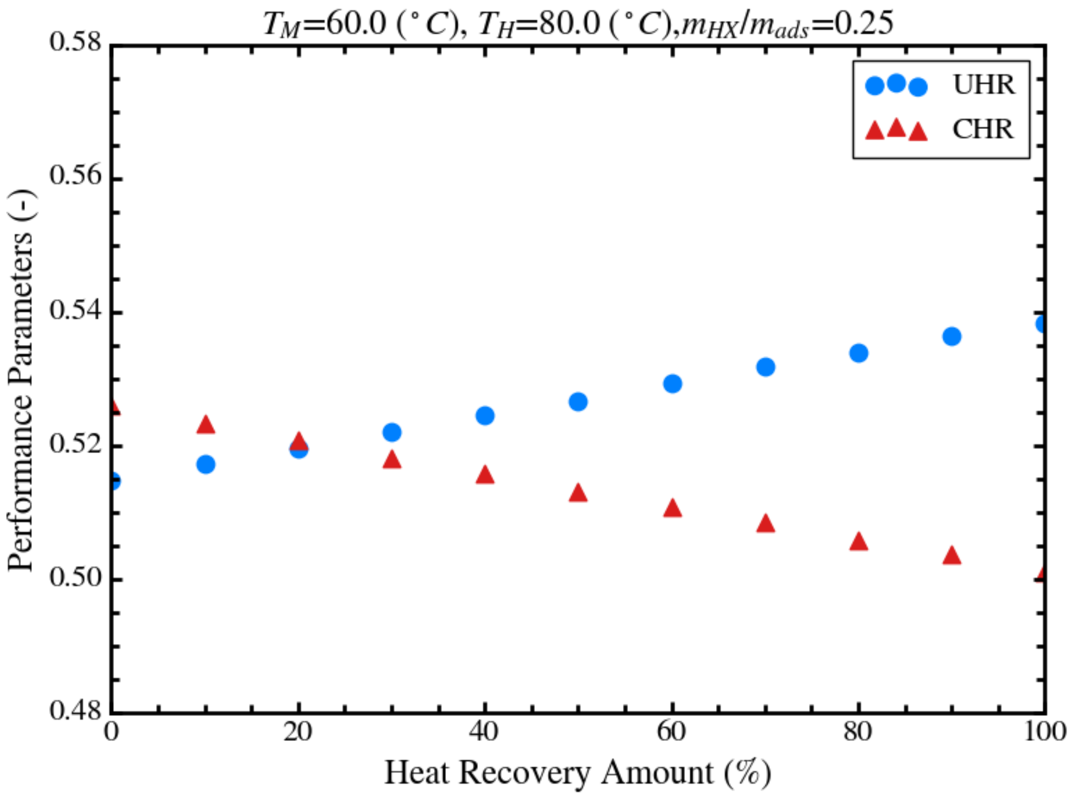

Figure 5.24: Useful heat ratio and condensation heat ratio variation with respect to fraction of maximum heat recovery possible at the fixed heat source temperature of 60 °C and heat supply temperature of 80 °C and thermal mass ratio of 0.25 [219]

Fig. 5.24 illustrates the variation in the useful heat ratio (UHR) and condensation heat ratio (CHR) with respect to fraction of maximum possible heat recovery amount at constant temperature lift of the AHT cycle. An increasing trend of the UHR values is observed with respect to the heat recovery amount. However, the amount of increase is negligibly small (0.52 to 0.55 approximately). This miniscule increase in the UHR values can be ascribed to the simultaneous decrease in the preheating uptake loss and precooling uptake gain with the increasing heat recovery amount. Consequently, both the numerator output adsorption heat and denominator input desorption heat increase simultaneously, which inhibits the rise in the UHR values. The slightly increasing trend is observed due to difference in rate of increase in these values. The difference in slopes of the preheating and precooling phases in the p-T-q plane, as depicted in Fig. 5.21, is responsible for this difference. Contrarily, the value of the CHR decreases with the increase in the heat recovery fraction, since the value of the condensation heat remains unaffected due to the introduction of the heat recovery scheme.

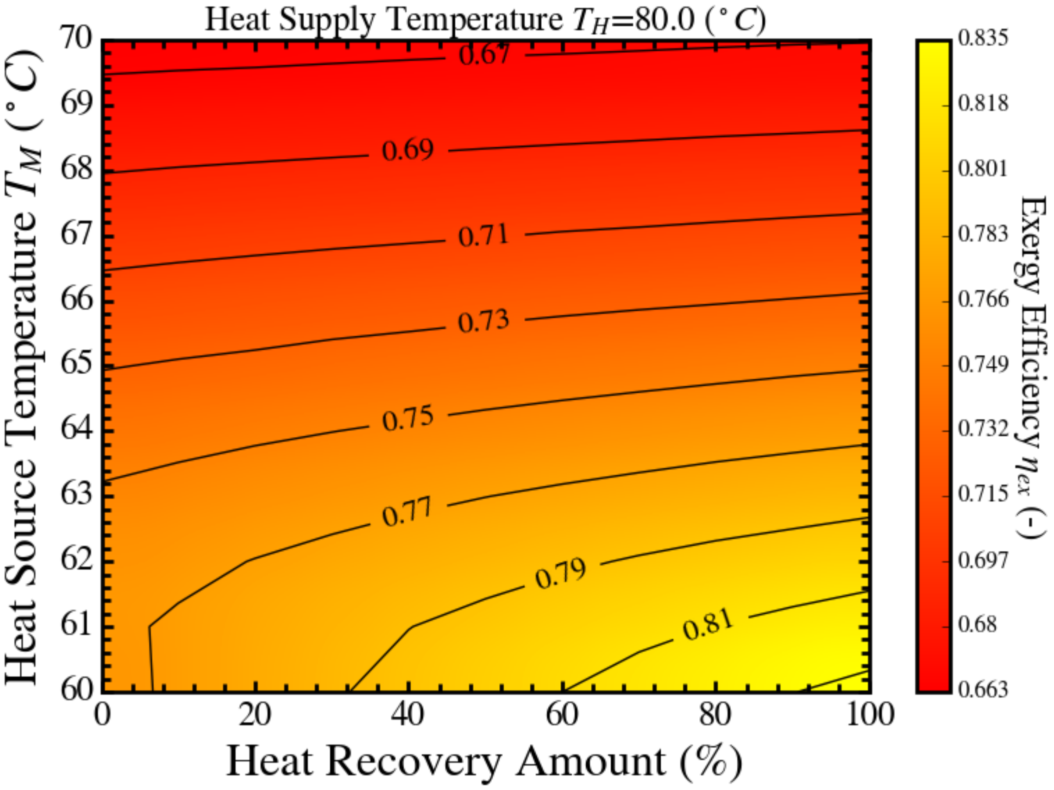

Figure 5.25: Exergy efficiency variation with respect to fraction of maximum heat recovery possible and heat source temperature at the fixed heat supply temperature of 80 °C and thermal mass ratio of 0.25 [219]

The exergy efficiency formulation associates the heat exchange value with the corresponding interacting temperature. Therefore, the heat recovery implementation strongly impacts the exergetic performance of the AHT cycle. Fig. 5.25 displays the exergy efficiency variation with the fraction of the maximum heat recovery possible and the heat source temperature values. An increasing trend of the exergy efficiency can be observed, where it increases from 0.77 to 0.83 as the heat recovery fraction increases from 0 % to 100 % at the heat source temperature of 60 °C. This large increse in the exergy efficiency values, as opposed to the UHR value, can be explained using the corresponding correlation given in Equation (4.85). As the heat recovery amount increases, the preheating uptake loss decreases, resulting in the reduced preheating heat exchange value (e_{ph}^{sen}), which is considered in the denominator of Equation (4.85). Therefore, the ratio of the input and output exergies increases despite the simultaneous increase in the output adsorption and input desorption exergy amounts. The said increase in the exergy efficiency value decelerates at the higher value of heat source temperature. This phenomenon is attributed to the increase in the evaporation and desorption exergy values, as per Equation (4.85).

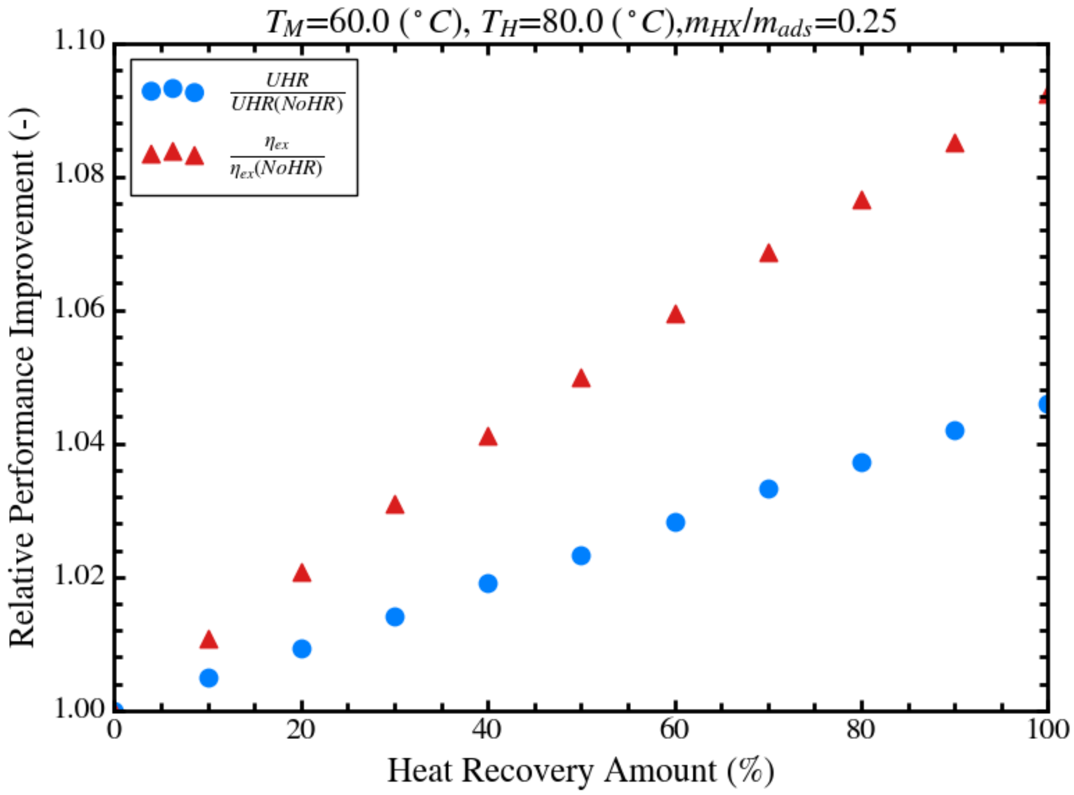

Figure 5.26: Releative performance improvement of the useful heat ratio and exergy efficiency with the heat recovery scheme implemented in the AHT cycle at the constant heat source temperature of 60 °C and heat supply temperature of 80 °C [219]

The comparison between the performance improvement in terms of the useful heat ratio and exergy efficiency are clearly highlighted in Fig. 5.26. Here, the ratio of the performance parameter upon the corresponding value for the AHT cycle without heat recovery is plotted against the fraction of the maximum possible heat recovery. Thus, both the ratios corresponding to the UHR and exergy efficiency starts at the value of unity. As highlighted in the previous figures, the effect of heat recovery scheme is stronger for the exergetic performance of the AHT cycle than its UHR values due to the association of the temperature values with the heat exchange amounts. Therefore, the reduction in the preheating exergy value becomes the dominating factor for the increase in the exergy efficiency.

5.3.3 Maximum temperature lift of adsorption heat transformer cycle

A possible performance improvement in the AHT cycle using the internal heat recovery scheme has been analyzed in the previous section using the energetic performance metrics such as upgraded adsorption heat, useful heat ratio, condensation heat ratio, and exergy efficiency. However, the key characteristics of the heat upgrading AHT cycle is its ability to elevate the temperature of the low-grade waste heat. Therefore, a theoretical analysis on the maximum temperature lift of the AHT cycle is discussed in this section. Water vapor is chosen as the adsorbate fluid, whereas four types of adsorbents are considered for different adsorption isotherm models. The details of the isotherm equation parameters are already provided in Table 4.1.

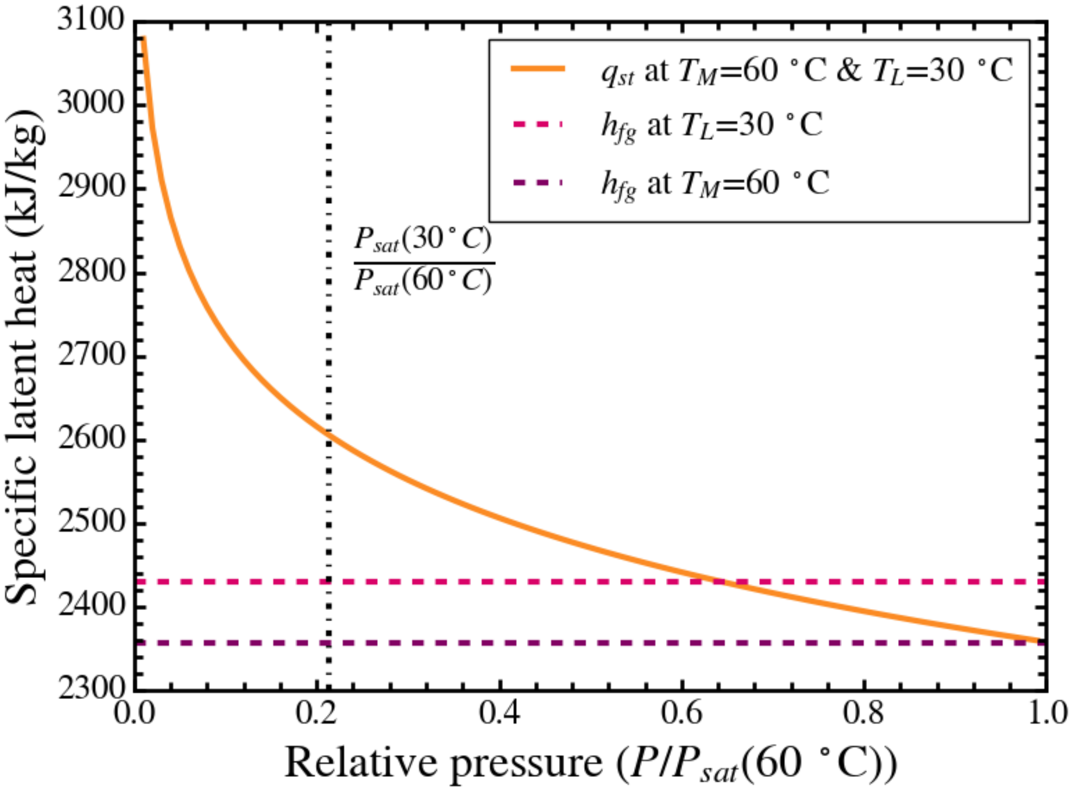

Figure 5.27: Isosteric heat of adsorption and latent heat of vaporization of water variation with respect to relative pressure and temperature

Fig. 5.27 demonstrates the isosteric heat of adsorption of water vapor with respect to relative pressure at the temperature 60 °C. Furthermore, the latent heat of vaporization values at the temperatures 30 °C and 60 °C are indicated. The theoretical model of the maximum temperature lift includes the ratio of h_{fg}/q_{st} as per Equation (4.69) in the "entropy balance" approach. For the relative pressure of the condenser, which denotes the initiating pressure of the preheating phase, the value of q_{st} is greater than h_{fg} at the same temperature of 60 °C. Therefore the ratio h_{fg}/q_{st} remains less than unity in the range of operating condition of the AHT cycle. This behavior is later highlighted to describe the maximum temperature lift potential variation.

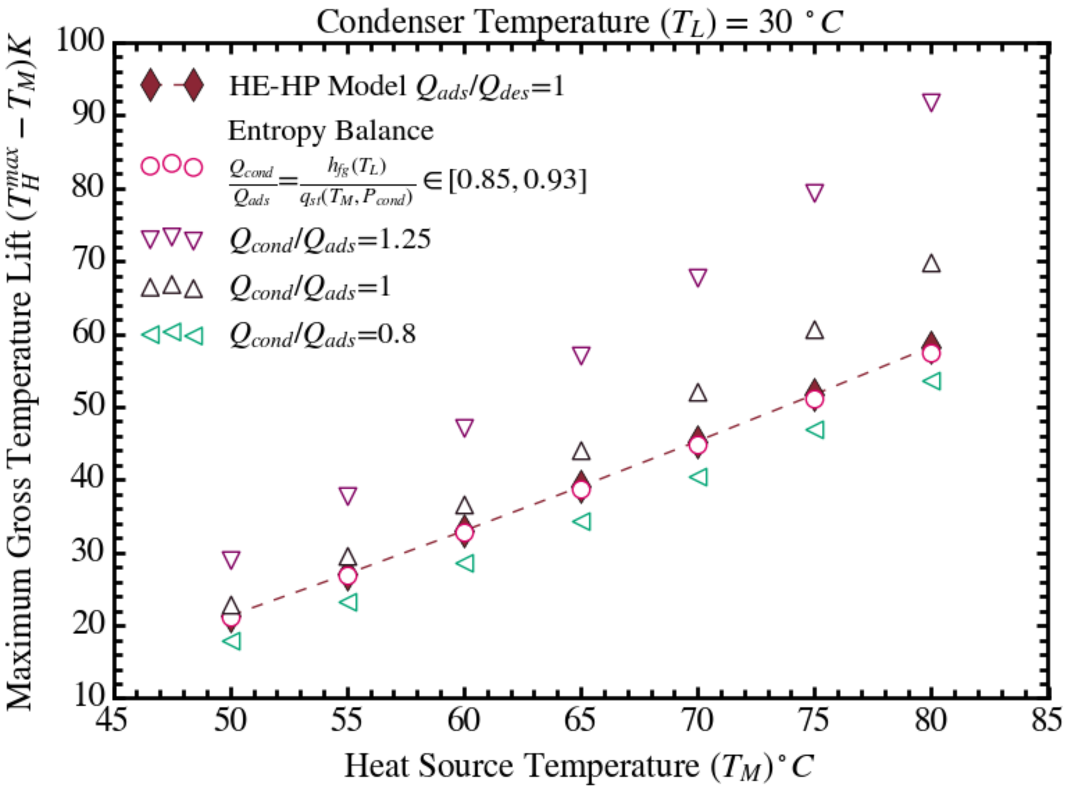

Figure 5.28: Comparison among the reversible models to determine the maximum temperature lift along with its variation with respect to heat source temperature

Fig. 5.28 illustrates the variation in the maximum temperature lift obtained from the reversible thermodynamic models with respect to the heat source temperature (T_M) at a constant condenser temperature of 30 °C. A further comparison between the two reversible models is carried out to determine the maximum temperature lift of the AHT cycle. These two models are "heat engine - heat pump" (HE-HP) and "entropy balance" approaches. The HE-HP model derived by assuming unity ratio of the adsorption and desorption heats is considered in the analysis, which is expressed by Equation (4.64). Equation (4.67) expresses the maximum temperature lift formulation using the "entropy balance" approach, which includes the ratio of condensation and adsorption heat values (Q_{cond}/Q_{ads}). Four values of this ratio are considered to evaluate the deviation of the resultant maximum temperature lift values of the "entropy balance" approach from the

HE-HP model. One of these values chosen is approximated by the ratio q_{st}/h_{fg} at the temperatures 60 °C and 30 °C for the numerator and denominator, respectively. It can be noticed that the temperature lift values increase monotonically with the increase in the value of T_M for all the theoretical models. Physically, an increase in the temperature of the heat source reservoir in the hypothetical "heat engine" section of the HE-HP model enhances the work provided to the "heat pump" component. Therefore, the temperature lift potential by the "heat pump" elevates with the enhanced hypothetical work input. Furthermore, the maximum temperature lift obtained by the "entropy balance" model results in equal values with that obtained from the HE-HP model when the given heat ratio is considered as the specific heat ratio of q_{st} and h_{fg} values. Since, both the HE-HP and "entropy balance" models evaluate the AHT cycle from a reversible cycle perspective, the assumption of the heat ratio involved in the correlation is reasonable. A miniscule deviation of the "entropy balance" approach from the HE-HP model can be observed at the higher heat source temperature. This phenomenon can be ascribed to the effect of the adsorbate properties, i.e., isosteric heat of adsorption and latent heat of vaporization, that are considered in the "entropy balance" correlation. A value of unity for the ratio Q_{cond}/Q_{ads} apparently leads to a higher value of the maximum temperature lift than the HE-HP model. However, this unity value can be achieved when the specific heat ratio approaches unity. From Fig. 5.27 it can be observed that this required condition is satisfied at the unit relative pressure. This unit relative pressure suggests that the condensation pressure is equal to the evaporator pressure, which is physically impossible for operating the AHT cycle. Hence, the "entropy balance" approach should be used considering the condensation heat to adsorption heat ratio values as less than one. From this analysis, the HE-HP model is suggested as the benchmark of the theoretically maximum temperature lift potential of the AHT cycle. Subsequently, this model is used to compare the maximum temperature values obtained from "complete preheating" approach for different adsorption isotherm models.

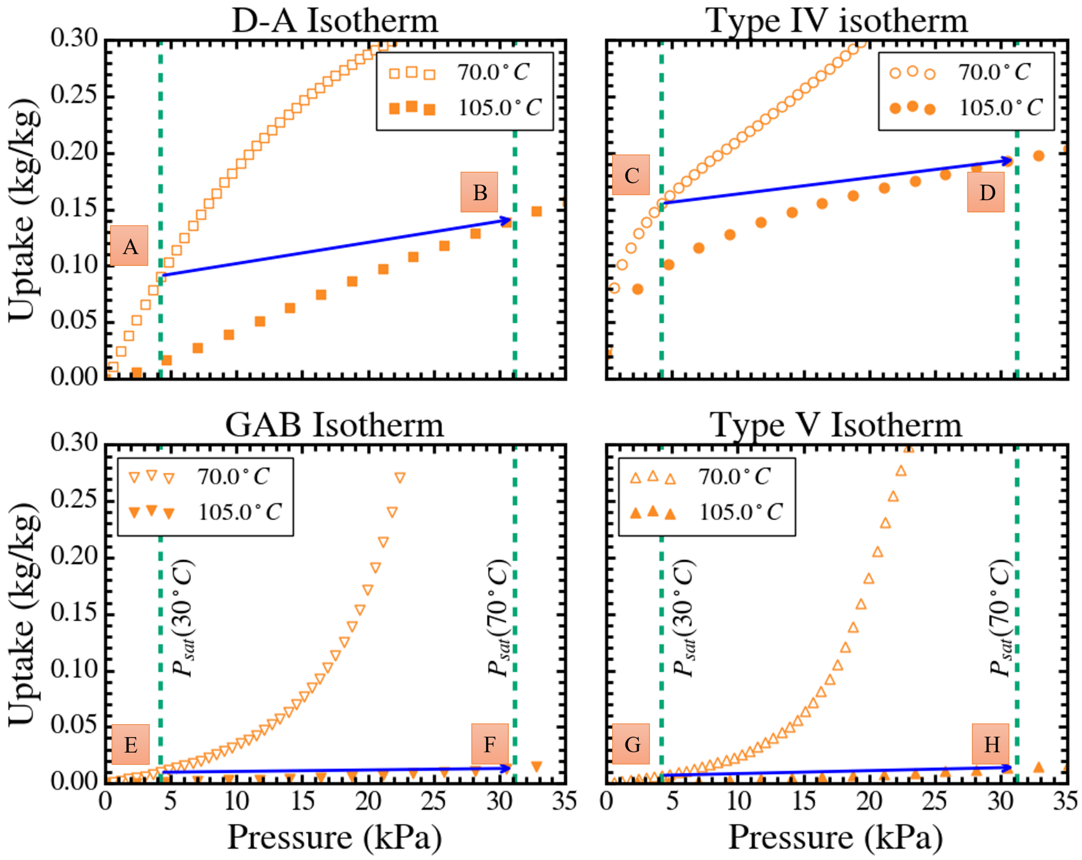

Figure 5.29: Four types of adsorption isotherms at the heat source temperature of 60 °C, heat supply temperature of 105 °C, and heat sink temperature of 30 °C

Four kinds of isotherm models are used to delineate the corresponding effect on the maximum temperature lift potential of the AHT cycle. Fig. 5.29 depicts the respective isotherm trends with respect to pressure and two temperature levels at 70 °C and 105 °C. The condenser and evaporator pressures are denoted by the vertical lines in each subplot, which are calculated as the saturation pressure at 30 °C and 70 °C, respectively. The lines 'AB', 'CD', 'EF', and 'GH' represent the preheating process from 70 °C to 105 °C for the D-A, Type IV, GAB, and Type V isotherms, respectively. Based on the similarity of the isotherm shapes, these four isotherms can be grouped as (D-A and Type IV) and

(GAB and Type V) isotherms. The first group refers to the isotherm shape of continuous increase in the uptake with the increasing pressure with gradual reduction in the slope. The second group denotes the S-shaped isotherm shape, which includes the initial low-uptake region and its sudden elevation with the pressure. As the temperature increases, the low-uptake region expands to higher pressures for this second group of isotherms. The preheating process lines indicated in the figure is used for comparing the different isotherm models in the maximum temperature lift determination.

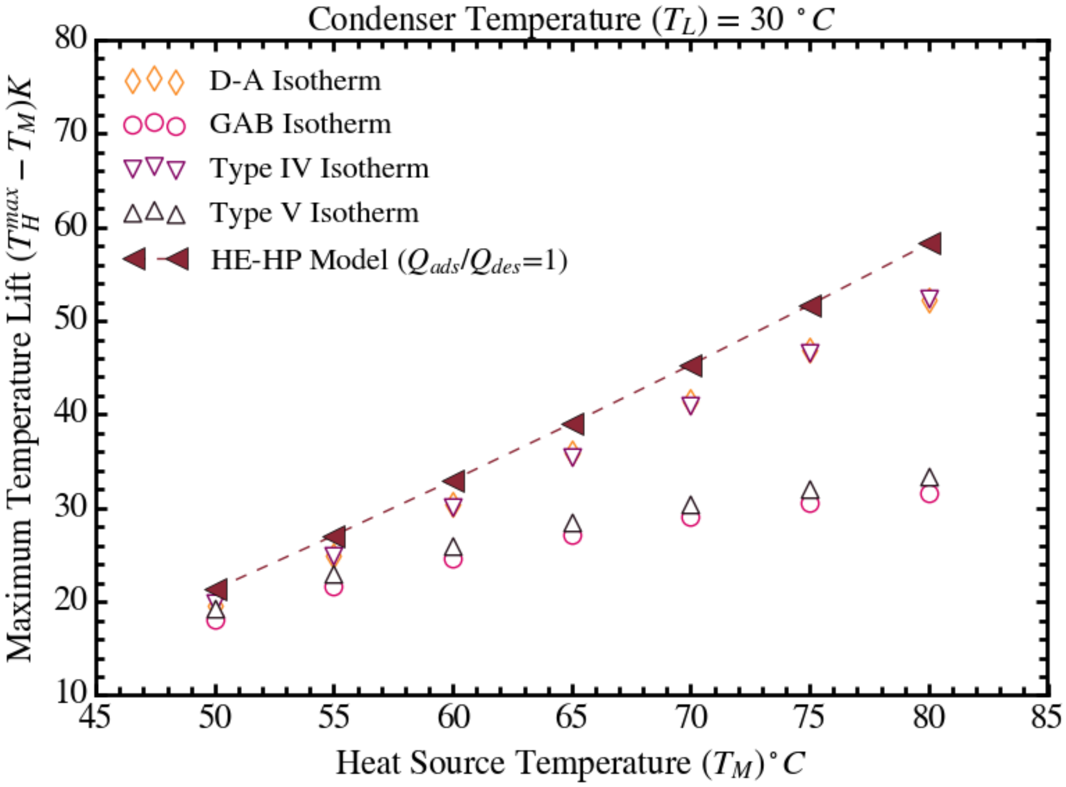

Figure 5.30: Maximum temperature lift variation with respect to heat source temperature and different adsorption isotherm models and its comparison with the ones obtained from reversible heat engine-heat pump model

Fig. 5.30 illustrates the maximum temperature lift variation with the heat source temperature and its comparison among the different isotherm models and reversible HE-HP model. Here, the maximum temperature lift values for the different isotherm models are evaluated using the 'complete preheating' approach discussed in Section 4.3. As the name suggests, this model considers the finite heat and mass transfer in the adsorption system during the preheating phase. The correlation for the maximum temperature lift for this approach includes the specific heat capacity of the adsorbent material and adsorbed phase water, the uptake and isosteric heat of adsorption values. It can be observed that the maximum temperature lift values obtained from the 'complete preheating' approach are less than the ones obtained from the reversible HE-HP model. This phenomenon is apportioned to the presence of the irreversibilities due to the finite heat and mass transfer process occurring during the actual preheating phase. Despite this occurrence, the increasing tendency of the maximum temperature lift with the heat source temperature is preserved for all the isotherm models. This trend is attributed to the higher uptake difference of the preheating process, leading to the increased heat of adsorption generation necessary. However, a distinct difference among the temperature lifts obtained for the different isotherm models can be observed.

As already mentioned, the isotherms can be grouped together based on its shapes. Similar categorization of the isotherms can be performed with respect to the maximum temperature lift values. It can be seen that the D-A and Type IV isotherms exhibit higher values of temperature lift than the ones obtained for the GAB (Type III) and Type V isotherms using the 'complete preheating' approach. The respective similarities in the maximum temperature lift values are caused by the similarities between the shapes of the corresponding isotherms. Equation (4.72) depicts that the operating uptake difference is the key driving force for the temperature lift. Therefore, for a fixed pressure range, the uptake difference will be similar between the isotherms with the similar shapes. However, a significant difference between the maximum temperature lift values obtained for the groups (D-A and Type IV) and (GAB and Type V) can be noticed in Fig. 5.30. An example temperature range between 70 °C to 105 °C can be considered for explaining the mentioned behavior. The condenser pressure is fixed at 30 °C and the heat source temperature is considered as the 70 °C. The initial uptake value of the preheating process (points A, C, E, and G in Fig. 5.29) are calculated as a function of the heat source temperature and condenser pressure ($w_1(T_M = 70°C, P_{sat}(30°C))$). Similarly, the final uptake values (points B, D, F, and H in Fig. 5.29) are calculated at the upgraded temperature and evaporator pressure corresponding to the saturation pressure at 70 °C ($w_1(T_H = 105°C, P_{sat}(70°C))$). Thus, for the D-A and Type IV isotherm models in Fig. 5.29, the preheating process leads to approximate uptake differences of 0.05 kg kg^{-1} and 0.04 kg kg^{-1}, respectively. Contrarily, the values of the uptake difference obtained for GAB and Type V isotherms are negligibly small for the same operating temperature range. These differences in the uptake values between the two groups lead to the large difference in their maximum temperature lift. Furthermore, as per Fig. 5.30, the maximum temperature lift values of the GAB and Type V isotherms are lower than the temperature lift of 35 °C considered in the example. This event can be explained using the maximum temperature lift formulation given by Equation (4.72). Since, the uptake and temperature quantities are inversely proportional to each other, the correlation in the given equation leads to the minimum threshold uptake difference required for obtaining the maximum temperature lift. A comparison between the final uptake values obtained for the four adsorption isotherm models and the corresponding minimum threshold final uptake values is depicted in Fig. 5.31 for the operating condition in the example. It can be observed that the final uptake values for the first group (D-A and Type IV isotherms) are higher than the corresponding threshold uptake values, which indicates that the temperature 70 °C can be upgraded to the temperature 105 °C. However, for the second group (GAB and Type V isotherms), the final uptake values are lower than the threshold uptake values. Therefore, these isotherms can not upgrade the waste heat from 70 °C to 105 °C. Based on this analysis, D-A (Type I) and Type IV isotherms are concluded to be suitable for the AHT cycle heat upgrading performance.

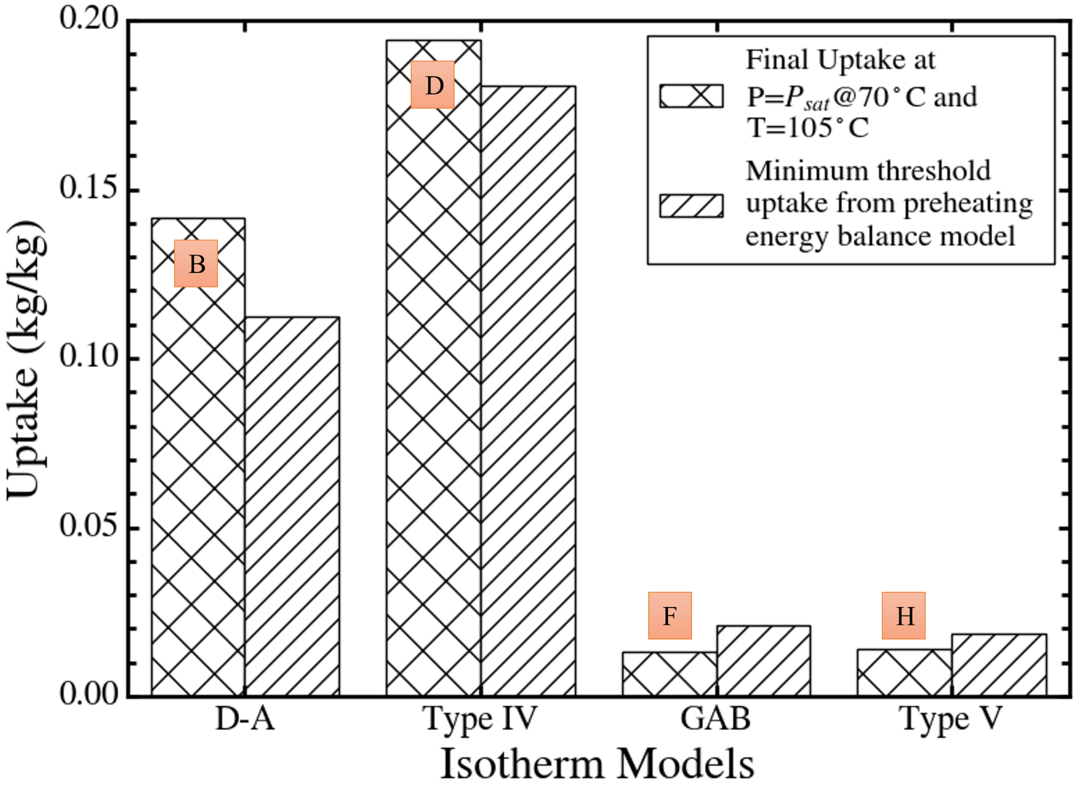

Figure 5.31: Uptake comparison between the final uptake determined by the adsorption isotherm and minimum threshold uptake obtained from the maximum temperature lift model

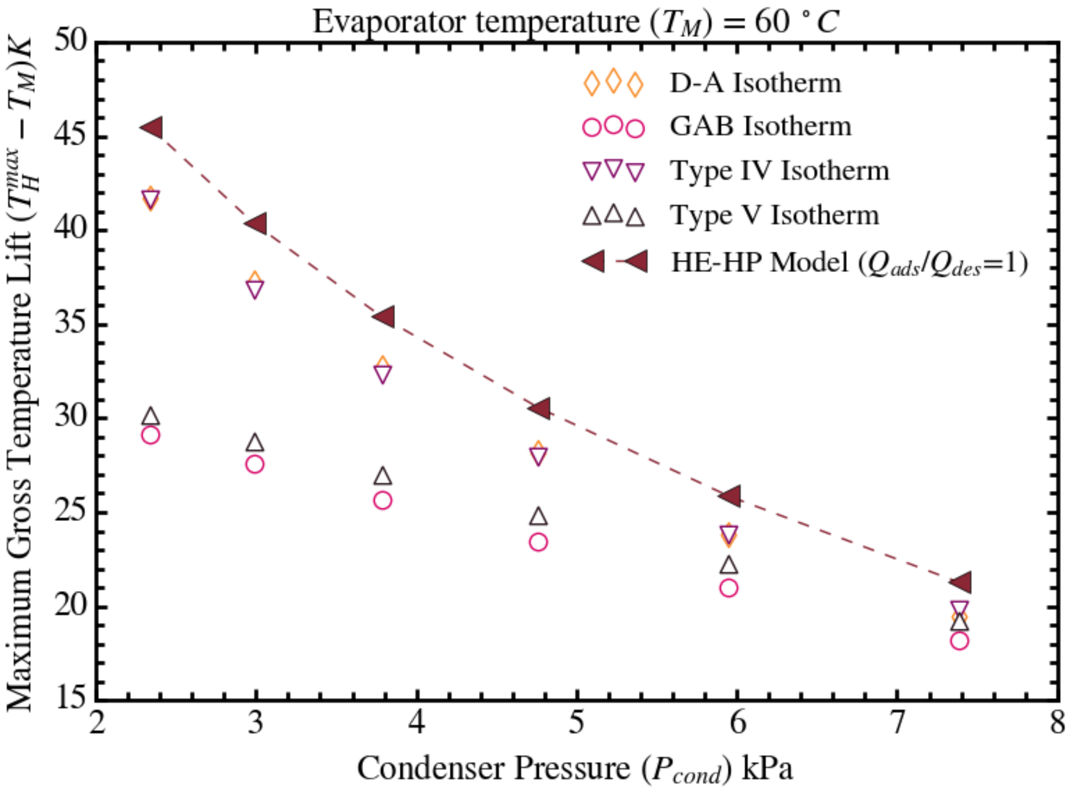

Figure 5.32: Maximum temperature lift variation with respect to condenser pressure and different adsorption types and its comparison with the same obtained from reversible heat engine - heat pump model

Fig. 5.32 shows the variation in the maximum temperature lift with respect to the condenser pressure calculated using the 'complete preheating' model for the four isotherms considered and reversible HE-HP approach. An increase in the condenser pressure implies the increase in the heat sink temperature (T_L) of the AHT cycle. As the condenser pressure increases, the net adsorption uptake during the preheating phase reduces due to the increase in the initial uptake value. Similar trend can be observed for the values obtained from the reversible HE-HP model as the increase in the temperature T_L leads to reduced work generated by the 'heat engine' component of the HE-HP model. The variation among the different isotherm models is analogous to the one delineated in Fig. 5.30. The D-A and Type IV isotherm models portray closer values of the maximum temperature lift to the ones obtained from the HE-HP model. Whereas, the same values obtained for the GAB and Type V isotherms are farther from the HE-HP model.

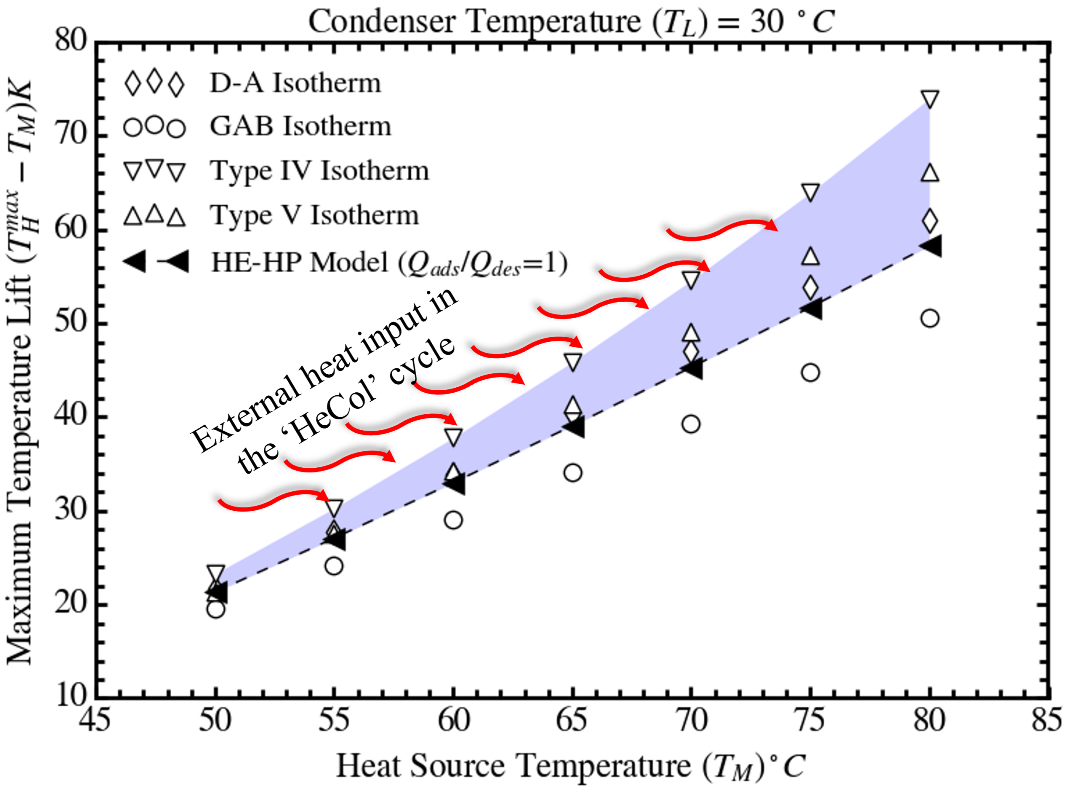

Figure 5.33: Maximum temperature lift values obtained using the "uptake balance approach" for the "Heat from Cold" cycle and its comparison with the reversible heat engine - heat pump model

The current thermodynamic models to obtain the maximum temperature lift are developed for the heat upgrading cycle which comprises the non-isosteric preheating phase to generate the required temperature lift. The same principles can be further utilized to the heat upgrading cycle with the isosteric preheating process such as the 'HeCol' cycle. A detailed description of the 'HeCol' cycle and the corresponding maximum temperature lift formulation is provided in the appendix. The 'complete preheating' approach developed for the AHT cycle is equivalent to the 'uptake balance' approach in the 'HeCol' cycle. This 'uptake balance' approach considers the equality between the minimum and maximum uptake values of the 'HeCol' cycle when the cycle is assumed to be consisting of a single complete preheating phase. The detailed mathematical formulation is provided in the appendix. Fig. 5.33 depicts the maximum temperature lift values obtained from the 'uptake balance' approach for the 'HeCol' cycle with four different isotherm models. These values are compared with the HE-HP model developed for the AHT cycle. It is observed that the 'uptake balance' approach generally overestimates the HE-HP model. However, as the HE-HP model is developed from the reversible cycle perspective, any higher value of maximum temperature lift than the one obtained using this model is considered thermodynamically inconsistent. As highlighted in Fig. 5.33, the excess temperature lift obtained for the 'HeCol' cycle is attributed to the external heat input during its isosteric preheating phase. Therefore, this reversible HE-HP model may not be applicable to the heat upgrading cycle with the isosteric preheating phase.

5.4 Hybrid adsorption heat transformer - multi-effect distillation system

The proposed hybrid AHT-MED system is compared with the standalone MED system with respect to the performance ratio and water production rate. The heat source temperature (T_M) in the AHT cycle of the hybrid AHT-MED system is kept equal to the first effect condensing temperature in the standalone MED system. Therefore, the net temperature difference between the heat source and the last effect of the MED are the same between the standalone MED and hybrid AHT-MED systems. The parametric variation of the performance parameters are carried out via changing the value of heat source temperature. For fair comparison, the interstage/inter-effect temperature difference in both the systems is kept equivalent. The minimum value of this temperature difference is defined by the summation of the boiling point elevation temperature and non-equilibrium allowance temperature values. For seawater, this net value is 1.2 °C, approximately. The interstage temperature difference has been considered greater than this minimum value in the study by Mistry et al. [220]. The same behavior is maintained for the modeling of the MED system in the present study.

5.4.1 Desalination performance evaluation

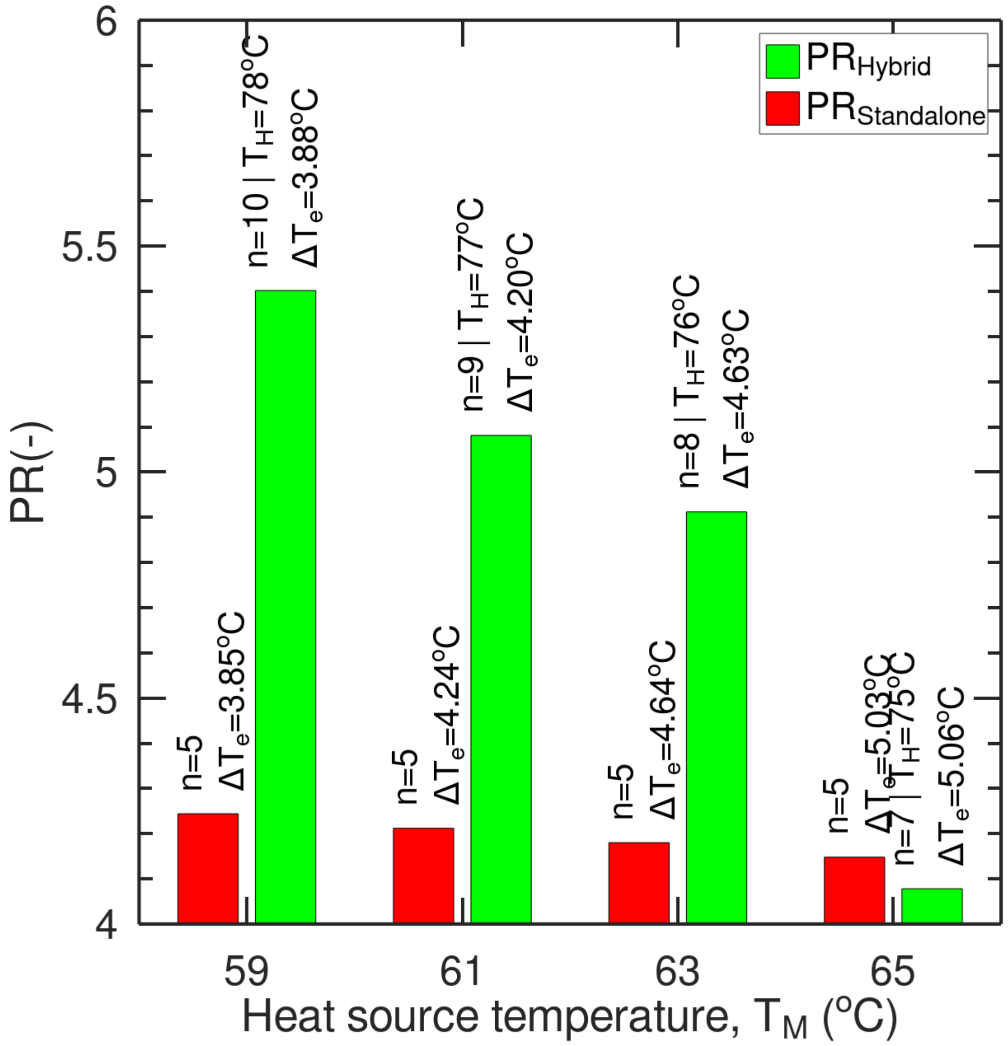

Figure 5.34: Performance ratio variation of the standalone MED and hybrid AHT-MED systems with respect to heat source temperature (T_M) at constant number of effects (n) in the standalone MED system

Fig. 5.34 depicts the parametric variation of the performance ratio (PR) of the standalone MED and hybrid AHT-MED systems with respect to the heat source temperature (T_M) between 59 °C to 65 °C. It can be observed that the hybrid AHT-MED system results in higher PR values than the standalone MED system till the T_M of 63 °C. The number of effects of the standalone MED system is kept fixed at 5 in the given T_M range, to maintain a fixed configuration of the standalone MED system. Therefore, the interstage temperature difference (ΔT_e) is directly proportional to the temperature T_M ($\Delta T_e = \left(T_e^{(1)} - T_e^{(n)}\right)/(n-1)$). The upgraded temperature of the AHT cycle (T_H) is chosen such that the value of ΔT_e is equivalent between the standalone and hybrid systems at each temperature T_M. This choice accordingly influences the number of effects utilized in the MED component of the hybrid AHT-MED system. As the upgraded adsorption heat of the AHT cycle is supplied to the first effect of the MED system, an increased number of effects can be employed in the hybrid system at the same ΔT_e value of the standalone MED system. For instance, at 59 °C T_M, the value of n is 10 in the hybrid system with the T_H value of 78 °C. Due to the increase in the value of n, the total condensation energy released in the MED system increases, as per the numerator of the PR formulation given by Equation (4.86). Thus, the value of PR increases by an approximate value of 1 in the hybrid system compared to the standalone MED. However, this increase in the PR value gradually declines as the T_M increases. This phenomenon is attributed to the decrease in n with the increase in T_M, since the value of ΔT_e increases accordingly. The decrease in the value of n results in the reduction in the total condensation energy in the MED system. Consequently, at 65 °C heat source temperature, the output condensation energy is not sufficient to engender a higher PR value of the hybrid system than the standalone MED system.

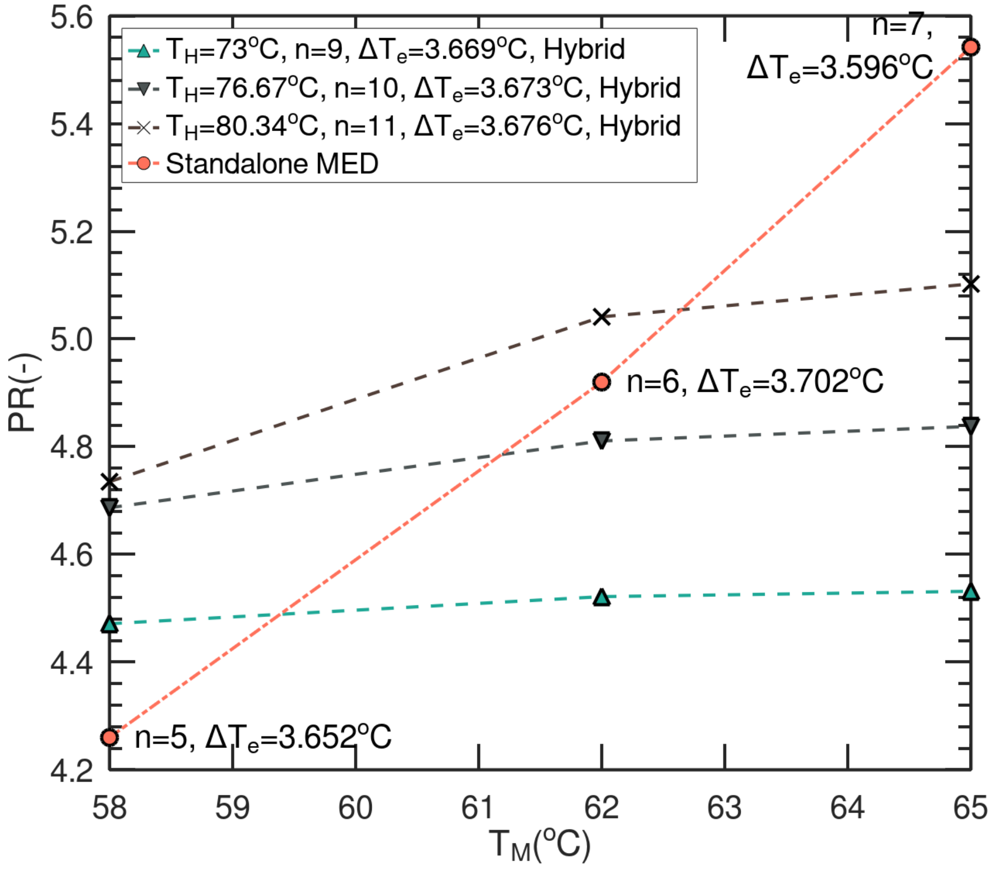

Figure 5.35: Performance ratio variation of the standalone MED and hybrid AHT-MED systems with respect to heat source temperature (T_M) at equal interstage temperature difference for every T_M value

Fig. 5.35 depicts the PR variation of the hybrid AHT-MED and standalone MED systems with varying configuration of the latter across the heat source temperature (T_M) range. The value of ΔT_e is kept equal, which results in varying number of effects for the standalone MED system as the value of T_M changes. Therefore, as the T_M increases, the PR value of the standalone MED system increases due to the higher number of effects employed. The hybrid systems are configured for three different upgraded heat supply temperatures (T_H). The number of effects in the hybrid system and the T_H value of the corresponding AHT cycle simultaneously increase. This rise in the number of effects also engenders an elevation in the value of PR of the hybrid system. However, the hybrid system exhibits a poorer performance than the standalone MED system at the higher values of T_M. The reduced rate of increase in the hybrid system's PR value with increasing T_M is attributed to the given phenomena. This decreasing slope in the PR trend is ascribed to two simultaneous contributions: (i) monotonically increasing trend of the standalone MED system's PR with the increasing value of T_M, (ii) the increase in the output adsorption and input desorption heats of the AHT cycle with increasing T_M (as shown in Fig. 5.12), which results in the simultaneous rise in the numerator and denominator of the PR formulation given by Equation (4.89). Therefore, from both the Figs. 5.34 and 5.35 it can be concluded that the hybrid system demonstrates a better energetic performance than the standalone MED system at an increased temperature lift produced by the AHT cycle and a reduced waste heat source temperature.

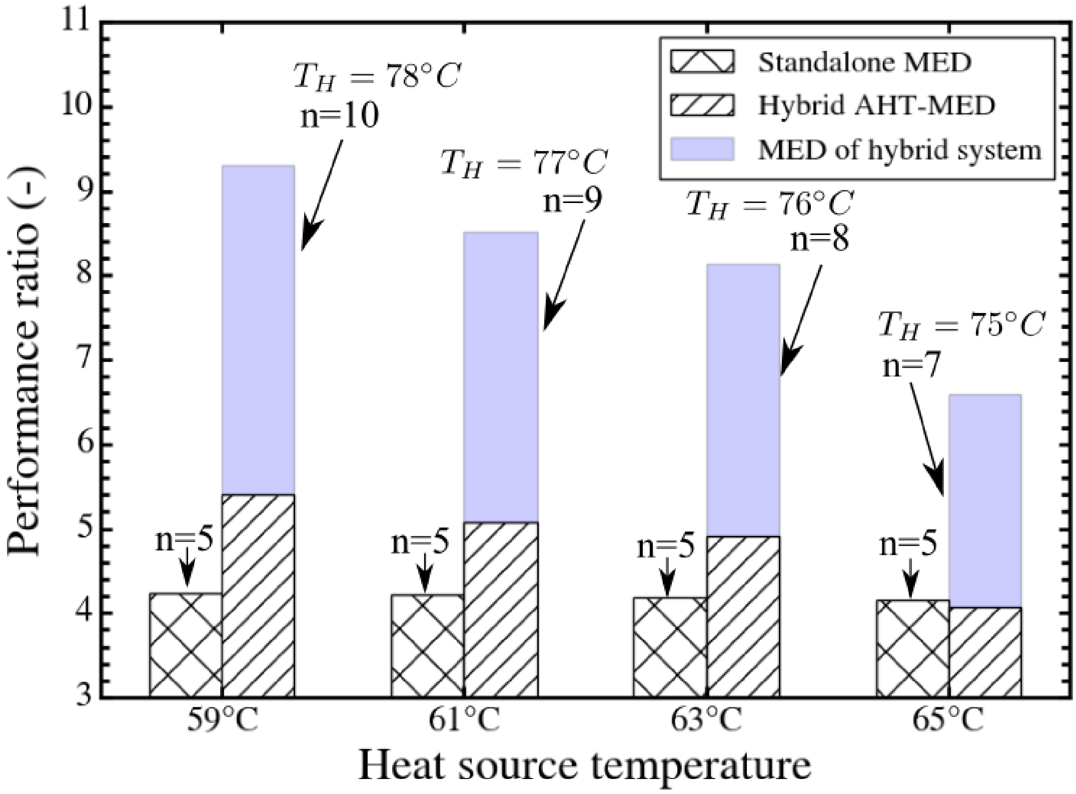

Figure 5.36: Performance ratio variation of the standalone MED and hybrid AHT-MED systems with respect to heat source temperature (T_M) and its comparison with the MED component of the hybrid system

Fig. 5.36 compares the net performance ratio of the hybrid AHT-MED system with that of the MED component in the hybrid system. The upgraded heat supply to the first effect of the hybrid AHT-MED system leads to the increase in the number of effects in the MED component. Therefore, the PR for the MED section of the hybrid AHT-MED system increases substantially. However, the efficiency of the AHT cycle (denoted as the useful heat ratio or UHR) is included in the net PR calculation of the AHT-MED system. As depicted in Fig. 5.14a, the UHR value is approximately 0.5 across different waste heat temperature values. Therefore, the net PR value of the hybrid AHT-MED system becomes considerably lower than the PR calculated for only the MED system.

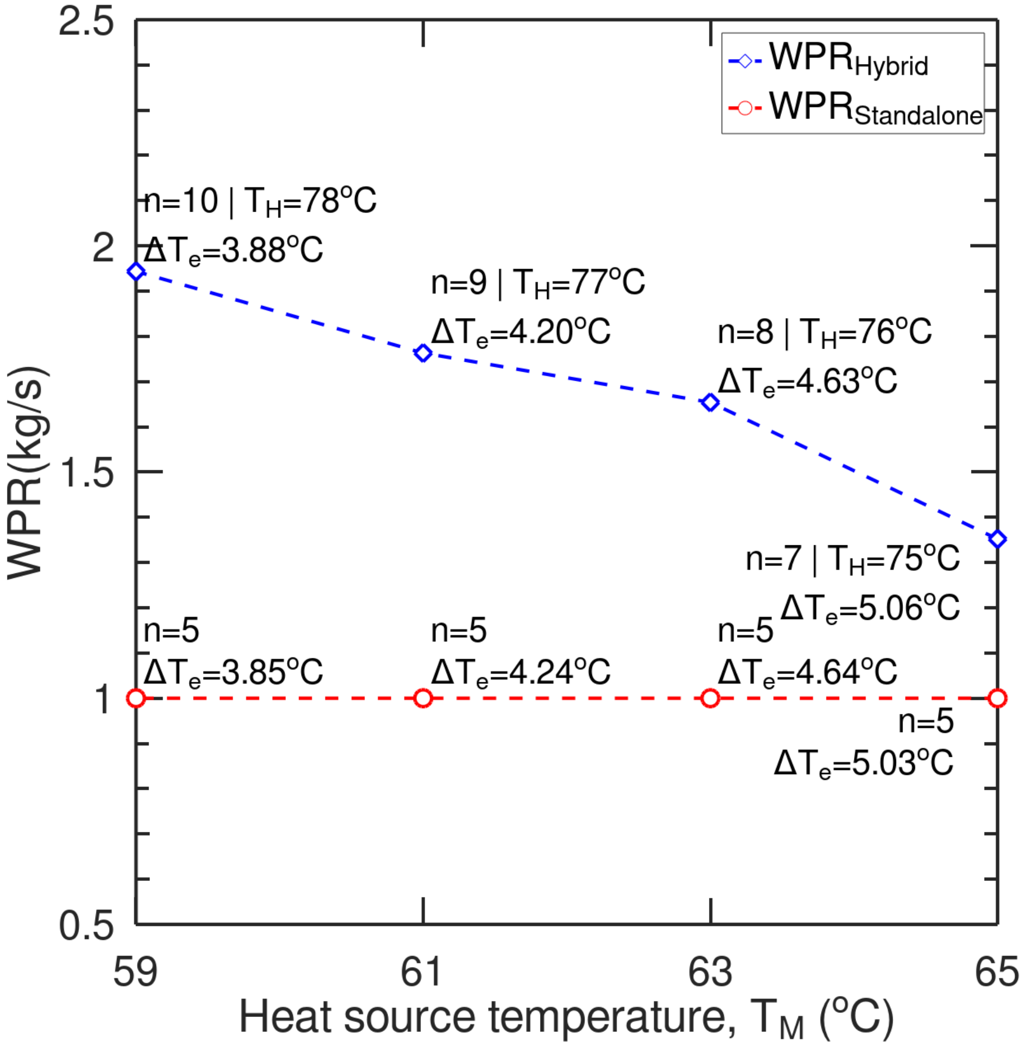

Figure 5.37: Water production rate variation of the standalone MED and hybrid AHT-MED systems with respect to heat source temperature (T_M) at constant number of effects (n) in the standalone MED system

The water production rates variation in the hybrid AHT-MED system and standalone MED system are depicted in Fig. 5.37 for the fixed configuration of the standalone MED system across the temperature range of T_M. The standalone MED system produces $1\,\mathrm{kg\,s^{-1}}$ at all the values of T_M considered. Despite the possibility of reduction in the PR value of the hybrid system than the standalone MED system with increasing T_M, the consistent higher value of WPR is maintained for the former than the latter. This occurrence is caused by the combined impact of the increased number of effects in the

AHT-MED system and the addition of potable water generated from the AHT cycle, which is run in an open cycle mode. Therefore, a WPR value, as high as twice the magnitude for the standalone MED system, is generated for the hybrid system. This value decreases with the increasing T_M, which is attributed to the decreasing number of effects, to maintain the same ΔT_e as the standalone MED system, operating at the corresponding T_M.

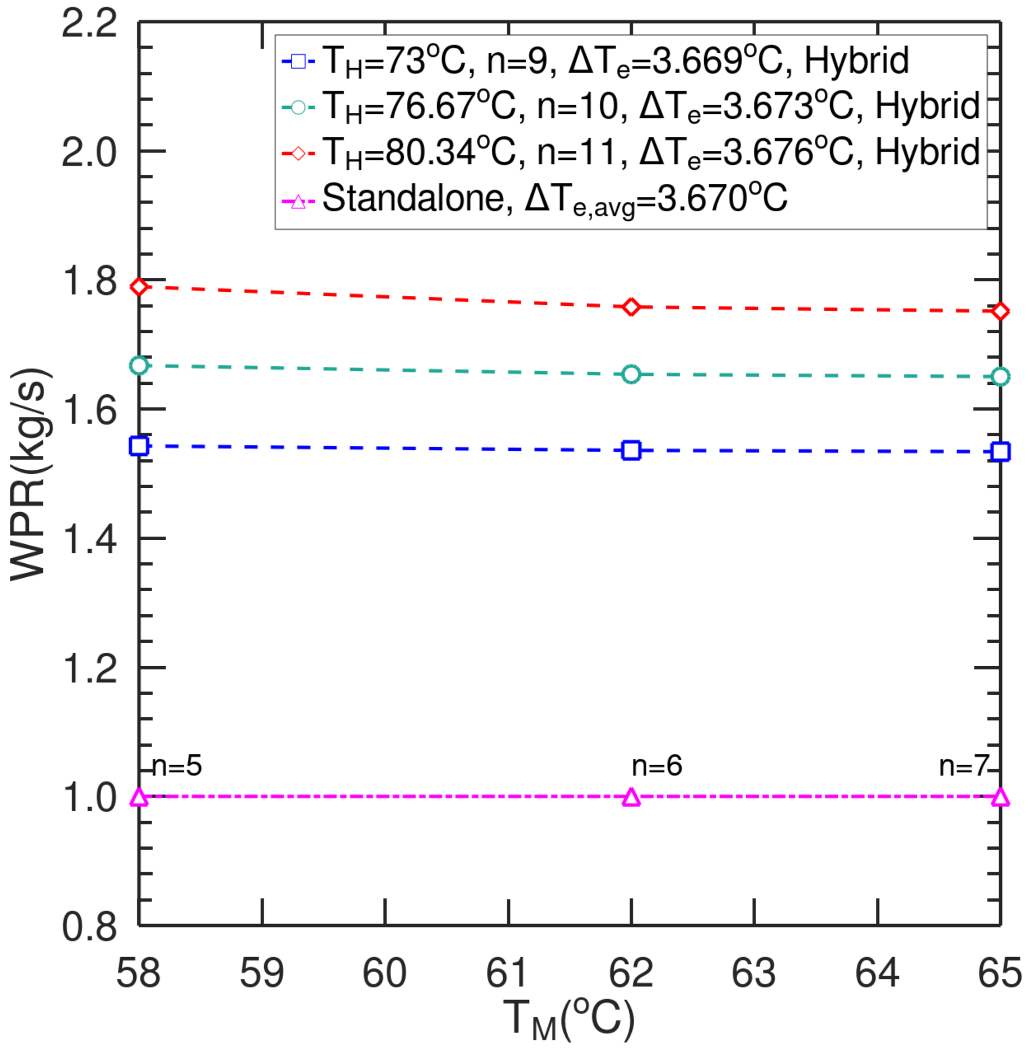

Figure 5.38: Water production rate variation of the standalone MED and hybrid AHT-MED systems with respect to heat source temperature (T_M) at equivalent interstage temperature difference in both the system

Fig. 5.38 portrays the behavior of WPR when the standalone MED configuration is varied across different values of T_M. As the value of T_H increases, the resultant increasing trend of the number of effects engenders an increasing WPR value of the hybrid AHT-MED system. The increasing value of T_M results in a slight reduction in the requisite mass of the adsorbent at the constant cycle time, as per Equation (4.88). Therefore, the value of WPR slightly decreases with the rise in T_M at a constant T_H value of the hybrid system. Nevertheless, the WPR is improved for the AHT-MED system compared to the standalone MED system, which can go as high as 1.79 times the WPR of the latter at the upgraded heat supply temperature T_H of 80.34 °C.

5.4.2 Effect of adsorption heat transformer cycle heat recovery

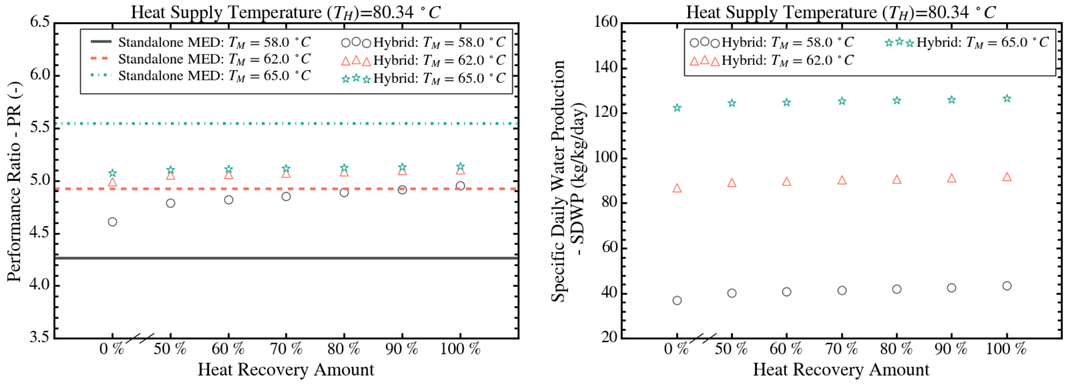

(a) Performance ratio (b) Specific daily water production rate

Figure 5.39: Effect of internal heat recovery in the AHT cycle on the performance parameters of the hybrid AHT-MED systems with the MED interstage temperature value of approximately 3.67 °C

Fig. 5.39 illustrates the effect of internal heat recovery implemented in the AHT cycle on the performance parameters of the hybrid AHT-MED system. The correlations developed for the modified PR (Equation (4.91)) and SDWP (Equation (4.94)) are used to analyze the effect of internal heat recovery. Three heat source temperature levels (T_M) are considered to obtain the PR values of the hybrid AHT-MED and the standalone MED systems in Fig. 5.39a. Here the standalone MED systems are considered with variable configuration (increasing number of effects with the increasing T_M). The variation in the PR of the AHT-MED system is plotted against the fraction of the maximum possible heat recovery possible in the AHT cycle. A slightly increasing trend in the PR values is observed as the heat recovery amount increases. The rate of increase in the PR is decelerated by the simultaneous increase in the output adsorption and input desorption heats, as highlighted in Fig. 5.22. The same behavior causes the slight improvement in the UHR values of the AHT cycle. Since, the PR correlation of the hybrid cycle includes the UHR component of the AHT cycle, the modified PR values are also impacted similar to the variation in the UHR values (Fig. 5.26) with the change in heat recovery amount.

A slight improvement in the values of the SDWP with the increase in the heat recovery amount can be seen in Fig. 5.39b. The specific adsorption heat released during the isothermal adsorption phase of the AHT cycle (e_{ad}^{rec}) is directly proportional to the heat recovery amount (Fig. 5.22). This trend results in the decrease in the requisite mass of the adsorbent for the AHT cycle, as per the modified correlation of the AHT-MED systems heat balance (Equation (4.71)). Therefore, the denominator slightly increases in the SDWP correlation (Equation (4.94)).

5.5 Summary

In this chapter, the results of the multiscale investigation of the adsorption phenomena are synthesized. These results include the GCMC simulation-based adsorbed phase generation of the water in graphite slit pore, bulk thermodynamic property evaluation of the adsorbed phase, and system-level analysis of the AHT cycle. The dependence of the latter two observations on the fundamental equilibrium adsorption properties, i.e., isotherm and isosteric heat of adsorption, are clearly established. The molecular interaction-based determination of these properties is able to constitute a co-dependency between the adsorbent material characteristics and the adsorption system's energetic performance.

Chapter 6

Conclusion and future recommendations

6.1 Conclusion

The research work presented in the thesis encompasses a holistic evaluation of the equilibrium adsorption phenomena. The theoretical characterization of the adsorption phenomena includes its molecular level description, macroscopic thermodynamic property evaluation, and its system-level application. Firstly, a GCMC simulation is carried out for CO_2 adsorption in activated carbon. The activated carbon is represented using a graphitic slit-pore with varying widths and chemical functionalization. The dependence of macroscopic adsorption properties, such as isotherm and isosteric heat of adsorption, on the pore size distribution and type of oxygen-containing functional groups is delineated through this simulation study. The same technique is applied for simulating the water adsorption phenomena in graphite slit-pore with hydroxyl functional group to present an augmented view of the adsorbed phase generation. These analyses are followed by the thermodynamic property determination of the adsorbed phase. This exercise is focused on accurately describing the thermodynamic state of the adsorbed phase with respect to the corresponding gaseous and liquid phases of the adsorbate. Finally, the heat upgrading AHT cycle is chosen for the study on system-level application of adsorption phenomena. The heat upgrading and desalination performance characterization of the AHT cycle is carried out with respect to operating temperature conditions, adsorber bed properties, and type of adsorbent-adsorbate pair dictating the isotherm nature. This investigation is followed by the exploration of the limiting performance characteristics and performance improvement tactics of the AHT cycle. Finally, the performance improvement of the existing desalination technique is explored using the heat upgrading capability of the AHT cycle through hybridization of the AHT and MED systems. The key contributions made by the present thesis are listed as follows:

(i) The important findings from the GCMC simulation of CO_2 adsorption in graphite slit-pore based activated carbon are listed as follows:

  - A directly proportional relationship between the pore size and maximum adsorption uptake capacity is found out. A reduced pore size facilitates the pore-filling of the adsorbed phase at lower pressure values due to the higher adsorbent-adsorbate interaction potential. Accordingly, the local density distribution profile of the adsorbed phase displays higher peak density value for the smaller pore sizes.
  - The oxygen containing functional groups act as attractive sites for adsorbing the CO_2 molecules via its enhanced van der Waals interaction potential. The presence of H atom in the functional groups such as hydroxyl and carboxyl groups leads to the generation of additional electrostatic attractive potential.

  Therefore, these two groups demonstrate significantly greater adsorption uptake capacity and lower pore-filling initiation pressure values.

  - The presence of functional groups in the ultra-micropores (pore size of 7 Å) appears to affect the adsorption capacity due to the increased electrostatic repulsion between the adsorbent and adsorbate molecules. The reduced pore volume also contributes to the reduction of the adsorption capacity.
  - The reduced pore size and presence of functional groups have favorable effect on the isosteric heat of adsorption values. Furthermore, the appearance of 'T'-shaped molecular configuration of the CO_2 adsorbed phase leads to a substantial leap in the isosteric heat of adsorption value for the 8.9 Å pore size at the higher pressures.

(ii) The specific heat capacity, specific entropy and specific enthalpy values of the adsorbed phase is found to be closer to the liquid phase or subcooled region than the gaseous phase. This phenomenon is attributed to the reduced degrees of freedom of the adsorbed phase molecules compared to the gaseous phase. Furthermore, consideration of the adsorbed phase specific volume in the adsorption isotherm significantly influences the nature of the thermodynamic property trend, as depicted by the CO_2 adsorbed phase properties.

(iii) The difference between the waste heat source and upgraded heat supply temperatures is found to be inversely proportional to the heat exchange values of the AHT cycle. The reduced net uptake difference of the cycle is the direct cause for this phenomenon. Simultaneous increase in the input and output heat exchange values lead to negligible change in the values of useful heat ratio, representing the heat upgrading efficiency of the AHT cycle. Moreover, increased thermal mass of the adsorber bed has a deteriorating effect on AHT cycle's performance due to the increased demand for preheating sensible heat.

(iv) Isotherm and isosteric heat of adsorption profiles of the adsorbent-adsorbate pair substantially influence the AHT cycle's performance. The S-shaped isotherm of AQSOA-Z02 type zeolite and water vapor pair leads to higher uptake consumption in a given operating temperature range, which results in higher UHR values of the AHT cycle compared to the silica gel adsorbents.

(v) Incorporation of an internal heat recovery scheme improves the energetic and exergetic performance of the AHT cycle. These improvements are facilitated by the reduction in the preheating uptake consumption, which is directly proportional to the requisite adsorption heat to elevate the adsorber bed temperature. Therefore, an enhanced isothermal adsorption heat supply is obtained, engendering approximately 5 % increase in the UHR. However, the rate of increase in the UHR value is thwarted by the simultaneous increase in the output adsorption and input desorption heat values. The exergetic performance improvement is more sound than the energetic one due to the presence of temperature values associated to the respective heat exchange in the AHT cycle. The reduction in the preheating exergy with the increase in the heat recovery amount results in the exergy efficiency improvement of approximately 10 %.

(vi) From the assessment of the limiting performance parameters of the AHT cycle, its theoretical maximum temperature lift is obtained. Three theoretical models are developed to evaluate this property, which include two reversible thermodynamic process-based approaches and the other one that takes into account the existence of irreversibilities. The former processes ('heat engine heat pump representation' and 'entropy balance') result in the maximum temperature lift formulation containing only the heat source and heat sink temperature values. The latter approach, viz., ‘complete preheating process’ approach considers the isotherm, isosteric heat of adsorption, and adsorbent specific heat capacity. The maximum temperature lift value obtained from the reversible methods are found to be greater than the ones obtained from the irreversible method. For instance, at 80 °C heat source temperature, the maximum temperature lift is determined as 58 °C by the ‘HE-HP’ approach, whereas the same obtained from ‘complete preheating’ approach is 52 °C when IUPAC classified type I and type IV isotherms are considered. The corresponding values further reduce to 32 °C for type III and 34 °C for type V isotherms. The difference in isotherm shapes lead to this behavior.

(vii) The heat upgrading potential of the AHT cycle is utilized to augment the desalination performance of the multi-effect distillation (MED) system through the hybridization of these two technologies. The performance ratio improves from 4.25 to 5.4 at the same heat source temperature of 59 °C in the hybrid AHT-MED system. Likewise, the water production rate exhibits a twofold improvement in the hybrid AHT-MED system compared to the standalone MED system. These performance amplifications are caused by the increase in the first effect temperature of the MED system with the upgraded heat supply from the AHT cycle. While maintaining the same interstage temperature difference (ΔT_e=3.85 °C) between the standalone and hybrid MED systems, the increase in the number of effects in the hybrid system results in the given desalination performance enhancement. However, the diminution of performance ratio is observed in the hybrid AHT-MED system at the higher heat source temperature values.

Based on these key insights, a hierarchical interrelation between the performance of adsorption-based thermal systems and the material characteristics of the adsorbent and adsorbate can be clearly established. The influence of the isotherm and isosteric heat of adsorption shape varies among different energetic performance parameters of the AHT cycle. For instance, type V isotherm is found to be beneficial to the adsorption heat supply amount due to the large uptake difference. However, the same isotherm presents a deteriorating effect on the maximum temperature lift attainable by the AHT cycle. Therefore, customization of the macroscopic adsorption properties is necessary for optimizing the energetic performance of the AHT cycle. One of the key method to incorporate such customization is development of tailored adsorbent material. The modification of these adsorption properties is illustrated by the GCMC simulation of various pore size distribution and surface chemistry. Moreover, the bulk thermodynamic properties obtained for the adsorbed phase will facilitate the 2^{nd} law based performance optimization of the adsorption cycles. Therefore, this multiscale study on the adsorption phenomena is envisaged to propel the development of energy-efficient adsorption-based systems.

6.2 Recommendations for future work

Based on the present study, the following incremental research can be undertaken:

(i) Realistic graphite slit-pore structure can be considered in the GCMC simulation of the adsorption process for mimicking the activated carbon material. For example, the spatial distortion in the graphene layer due to the presence of functional group can be considered. The electronegativity difference between the graphene carbon atoms and oxygen functional group will lead to bond stretching and/or bending in the graphene layer, causing the generation of pore surface heterogeneity.

(ii) Additional bulk thermodynamic properties such as internal energy and Gibbs free energy of the adsorbed phase can be evaluated. Gibbs free energy is used to explain the vapor-liquid phase change phenomena. The same is expected to be applied for elucidating the adsorbed phase formation from the gaseous phase.

(iii) Dynamic performance characterization of the AHT cycle can be performed by considering adsorption kinetics. The intermediate states after the preheating and precooling phases found from the equilibrium cycle analysis can be applied for this dynamic adsorption simulation.

(iv) The experimental system of the AHT cycle needs to be developed for validation of the given dynamic simulation model.

(v) The upgraded adsorption heat from the AHT cycle can be used for low-grade waste heat recovery-based power generation cycle, e.g., Organic Rankine Cycle.

(vi) Different adsorbent-adsorbate pairs can be evaluated for improved performance of the AHT cycle, when it is used only for heat upgrading application.

Appendix A

Adsorption isotherm

The following formulations correspond to the D-A isotherm equation incorporating adsorbed phase volume correction, i.e. specific volume of the adsorbed phase is non-negligible.

$$w = \frac{c_0}{v_a} \exp\left\{ - \left[\left(\frac{RT}{E} \right) \ln \left(\frac{P_{sat}}{P} \right) \right]^n \right\} \tag{A.1}$$

In the above equation, c_0 is the maximum volumetric uptake in $\mathrm{m^3\,kg^{-1}}$, with adsorbed phase volume as v_a in $\mathrm{m^3\,kg^{-1}}$. v_a is formulated as [221],

$$v_a = \begin{cases} v_b \exp(\alpha[T - T_b]), & \text{if } P_{Trip} < P_{Amb} \\ v_{Trip} \exp(\alpha[T - T_{Trip}]), & \text{otherwise} \end{cases} \tag{A.2}$$

There are three approaches to calculate the thermal expansion coefficient α, which are (i) 0.0025 $\mathrm{K^{-1}}$ (ii) $1/T$ $\mathrm{K^{-1}}$ (iii) Nikolayev and Dubinin [222] model (Equation (A.3)).

$$\alpha = \begin{cases} \frac{\ln(b/v_b)}{(T_{Crit} - T_b)}, & \text{if } P_{Trip} < P_{Amb} \\ \frac{\ln(b/v_b)}{(T_{Crit} - T_{Trip})}, & \text{otherwise} \end{cases} \tag{A.3}$$

Here, b is van der Waals volume in $\mathrm{m^3\,mol^{-1}}$, v_b is specific volume at normal boiling point in $\mathrm{m^3\,mol^{-1}}$.

Table A.1: D-A Isotherm parameters for many pairs based on the volume correction (VC) used

Working Pairs	Models	E($\mathrm{J\,mol^{-1}}$)	n	c_0 in $\mathrm{m^3\,kg^{-1}}$ (for VC) w_0 in $\mathrm{m^3\,kg^{-1}}$ (No VC)	k	Error in %	Reference
A++/Water	No VC	3266.7	1.43	0.4604	-	1.86	[223]
A5BW/Water	No VC	3067.4	1.12	0.3986	-	1.57	[223]
NS10/Water	No VC	2826.8	0.98	0.415	-	1.31	[223]
RD/Water	No VC	3335	1.21	0.5046	-	1.16	[224]
RD2060/Water	No VC	4266.2	1.29	0.3888	-	1.28	[224]
MSC30/CO_2	No VC	5417	1.28	1.5302	6.01	2.06	[125]
MSC30/CO_2	α=0.0025	5321.1	1.31	0.0016	4.63	1.39	[125]
MSC30/CO_2	α=1/T	5355.3	1.3	0.0017	4.99	1.39	[125]
MSC30/CO_2	α=ND	5334.6	1.31	0.0015	4.76	1.45	[125]
A-20/CO_2	No VC	5270.7	1.26	0.9726	5.13	2.12	[225]
A-20/CO_2	α=0.0025	5375.7	1.32	0.0009	3.68	1.87	[225]
A-20/CO_2	α=1/T	5397.8	1.33	0.0010	4	2.03	[225]
A-20/CO_2	α=ND	5369.1	1.32	0.0009	3.82	1.76	[225]
SAC-2/CO_2	No VC	3668.3	1.01	2.1928	4.41	5.18	[226]
SAC-2/CO_2	α=0.0025	3714.6	1.03	0.0022	3.33	4.38	[226]
SAC-2/CO_2	α=1/T	3711.9	1.02	0.0024	3.51	4.38	[226]
SAC-2/CO_2	α=ND	3710.2	1.02	0.0022	3.42	4.45	[226]

Table A.2: Structural characteristics of different types of silica gel [223, 224] and zeolites [227]

Adsorbent	BET surface area ($m^2\,g^{-1}$)	Pore volume ($cm^3\,g^{-1}$)	Pore size (nm)
SG A++	864	0.476	2.44
SG A5BW	769	0.446	2.58
SG NS10	586	0.375	2.33
SG RD	780	0.44	2.24
SG RD2060	707	0.34	1.92
SG RD2560	636	0.314	2.24
AQSOA-Z01	189.6	0.071	1.178
AQSOA-Z02	717.8	0.27	1.184
AQSOA-Z05	187.1	0.07	1.176

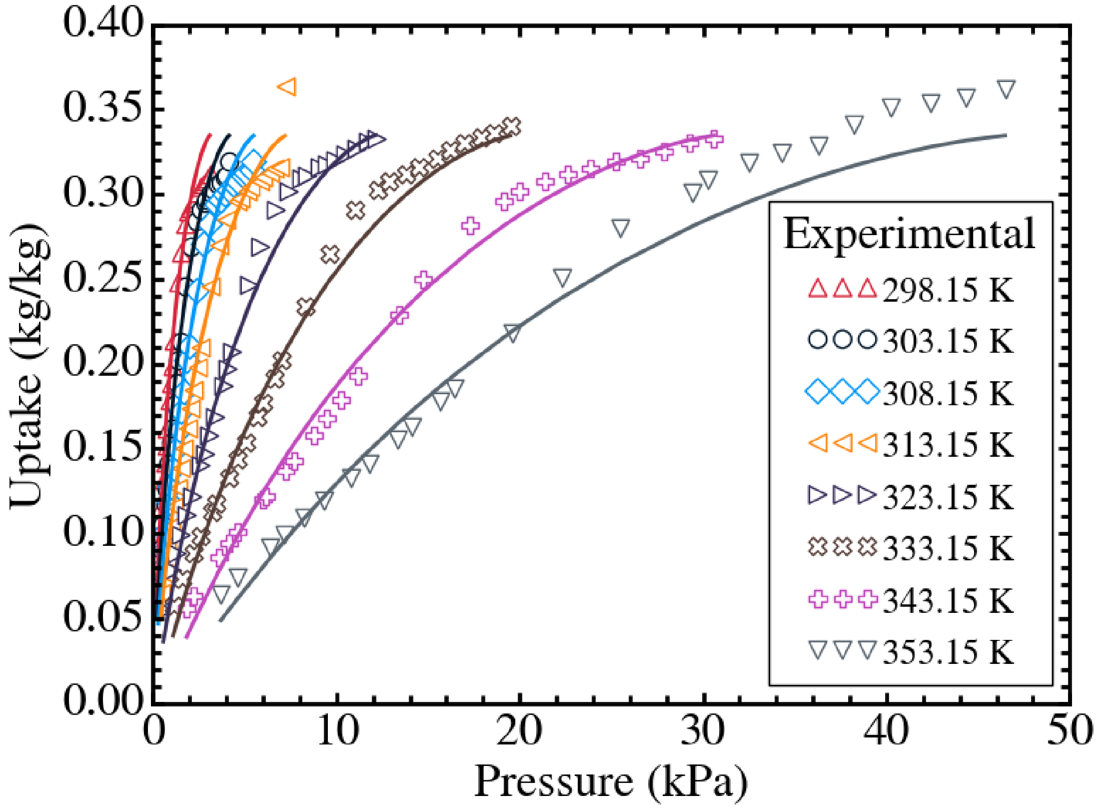

Figure A.1: Adsorption isotherm fitting of the silica gel type RD2560 + water adsorption pair using the D-A isotherm equation without volume correction

Appendix B

Adsorption thermodynamics mathematical formulations

B.1 Differential chemical potential expressions

The differential Gibbs free energy of the adsorbed phase can be expressed as follows:

$$d\hat{G}_a = -\hat{S}_a dT + \hat{V}_a dP + \mu_a dm_a \tag{B.1}$$

Taking the partial derivatives of the Gibbs free energy with respect to temperature (T), pressure (P), and mass of the adsorbate (m_a), the following expressions can be written:

$$\begin{cases} \left.\dfrac{\partial \hat{G}_a}{\partial T}\right|_{P,m_a} = -\hat{S}_a \\ \left.\dfrac{\partial \hat{G}_a}{\partial P}\right|_{T,m_a} = \hat{V}_a \\ \left.\dfrac{\partial \hat{G}_a}{\partial m_a}\right|_{T,P} = \mu_a \end{cases} \tag{B.2}$$

Using the above equations, the partial derivative of the adsorbate mass differential of the Gibbs free energy with respect to temperature and vice versa can be formulated as the following two equations:

$$\left.\frac{\partial}{\partial T}\left.\frac{\partial \hat{G}_a}{\partial m_a}\right|_{P,T}\right|_{P,m_a} = \left.\frac{\partial \mu_a}{\partial T}\right|_{P,m_a} \tag{B.3}$$

$$\left.\frac{\partial}{\partial m_a}\left.\frac{\partial \hat{G}_a}{\partial T}\right|_{P,m_a}\right|_{P,T} = -\left.\frac{\partial \hat{S}_a}{\partial m_a}\right|_{P,T} \tag{B.4}$$

Equating the terms on the left hand side of Equations (B.3) and (B.4), the following relationship between the temperature differential of the chemical potential and the adsorbate mass differential of the entropy can be derived as follows:

$$\begin{cases} \left.\frac{\partial}{\partial T}\left.\frac{\partial \hat{G}_a}{\partial m_a}\right|_{P,T}\right|_{P,m_a} = \left.\frac{\partial}{\partial m_a}\left.\frac{\partial \hat{G}_a}{\partial T}\right|_{P,m_a}\right|_{P,T} \\ \Longrightarrow \left.\frac{\partial \mu_a}{\partial T}\right|_{P,m_a} = -\left.\frac{\partial \hat{S}_a}{\partial m_a}\right|_{P,T} \end{cases} \tag{B.5}$$

Similar differentiation of the differential Gibbs free energy terms as shown in Equations (B.3) and (B.4) can be performed with respect to pressure instead of temperature, which results in the following two equations:

$$\left.\frac{\partial}{\partial P}\left.\frac{\partial \hat{G}_a}{\partial m_a}\right|_{P,T}\right|_{T,m_a} = \left.\frac{\partial \mu_a}{\partial P}\right|_{T,m_a} \tag{B.6}$$

$$\left.\frac{\partial}{\partial m_a}\left.\frac{\partial \hat{G}_a}{\partial P}\right|_{T,m_a}\right|_{P,T} = \left.\frac{\partial \hat{V}_a}{\partial m_a}\right|_{P,T} \tag{B.7}$$

Holding the equality between the terms on the left hand side of Equations (B.6) and (B.7), the following expression for the differential chemical potential in terms of the adsorbed phase volume is derived:

$$\begin{cases} \dfrac{\partial}{\partial P} \left.\dfrac{\partial \hat{G}_a}{\partial m_a}\right|_{P,T}\Bigg|_{T,m_a} = \dfrac{\partial}{\partial m_a} \left.\dfrac{\partial \hat{G}_a}{\partial P}\right|_{T,m_a}\Bigg|_{P,T} \\ \implies \left.\dfrac{\partial \mu_a}{\partial P}\right|_{T,m_a} = \left.\dfrac{\partial \hat{V}_a}{\partial m_a}\right|_{P,T} \end{cases} \tag{B.8}$$

B.2 Entropy differential formulations

The fundamental expression for the enthalpy differential can be expressed in terms of entropy, volume, and adsorbate mass as the control variables. The temperature differential of this fundamental formulation leads to the formulation of the temperature differential of entropy in terms of the specific heat capacity. These derivation steps are provided in Equation (B.9).

$$\begin{cases} d\hat{H}_a = Td\hat{S}_a + \hat{V}_a dP + \mu_a dm_a \\ \implies \left.\dfrac{\partial \hat{H}_a}{\partial T}\right|_{P,m_a} = T\left.\dfrac{\partial \hat{S}_a}{\partial T}\right|_{P,m_a} \\ \implies m_a c_{ade} = T\left.\dfrac{\partial \hat{S}_a}{\partial T}\right|_{P,m_a} \\ \implies \left.\dfrac{\partial \hat{S}_a}{\partial T}\right|_{P,m_a} = m_a \dfrac{c_{ade}}{T} \end{cases} \tag{B.9}$$

To derive the expression for the pressure differential of the adsorbed phase entropy, the partial differentiation of the enthalpy fundamental equation is carried out with respect to pressure, which leads to the following equation:

$$\implies \left.\frac{\partial \hat{H}_a}{\partial P}\right|_{T,m_a} = T\left.\frac{\partial \hat{S}_a}{\partial P}\right|_{T,m_a} + \hat{V}_a \tag{B.10}$$

Taking the temperature and pressure based differentials of the above expression, the following two equations are obtained respectively:

$$\Longrightarrow \frac{\partial}{\partial T}\left.\left.\frac{\partial \hat{H}_a}{\partial P}\right|_{T,m_a}\right|_{P,m_a} = \left.\frac{\partial \hat{S}_a}{\partial P}\right|_{T,m_a} + T\,\frac{\partial}{\partial T}\left.\left.\frac{\partial \hat{S}_a}{\partial P}\right|_{T,m_a}\right|_{P,m_a} + \left.\frac{\partial \hat{V}_a}{\partial T}\right|_{P,m_a} \tag{B.11}$$

$$\Longrightarrow \frac{\partial}{\partial P}\left.\left.\frac{\partial \hat{H}_a}{\partial T}\right|_{P,m_a}\right|_{T,m_a} = T\,\frac{\partial}{\partial P}\left.\left.\frac{\partial \hat{S}_a}{\partial T}\right|_{P,m_a}\right|_{T,m_a} = T\,\frac{\partial}{\partial T}\left.\left.\frac{\partial \hat{S}_a}{\partial P}\right|_{T,m_a}\right|_{P,m_a} \tag{B.12}$$

Equating the terms on the left hand side of the above two equations, the expression for the pressure differential of the adsorbed phase entropy can be obtained as follows:

$$\frac{\partial}{\partial T}\left.\left.\frac{\partial \hat{H}_a}{\partial P}\right|_{T,m_a}\right|_{P,m_a} = \frac{\partial}{\partial P}\left.\left.\frac{\partial \hat{H}_a}{\partial T}\right|_{P,m_a}\right|_{T,m_a} \tag{B.13}$$

$$\Longrightarrow \left.\frac{\partial \hat{S}_a}{\partial P}\right|_{T,m_a} = -\left.\frac{\partial \hat{V}_a}{\partial T}\right|_{P,m_a} \tag{B.14}$$

B.3 Gaseous enthalpy differential

$$dh_g = T ds_g + v_g dP \tag{B.15}$$

$$\left.\frac{\partial h_g}{\partial P}\right|_T = T\left.\frac{\partial s_g}{\partial P}\right|_T + v_g \tag{B.16}$$

$$\text{Maxwell relations} - \left.\frac{\partial s_g}{\partial P}\right|_T = \left.\frac{\partial v_g}{\partial T}\right|_P \tag{B.17}$$

$$\Longrightarrow \left.\frac{\partial h_g}{\partial P}\right|_T = v_g - T\left.\frac{\partial v_g}{\partial T}\right|_P \tag{B.18}$$

Appendix C

Mathematical modelling of multi-effect distillation system

C.1 Governing equations

Effect

Mass balance in the effect:

$$\dot{m}_F = \dot{m}_D + \dot{m}_B \tag{C.1}$$

Salinity balance of the feed and brine streams:

$$\dot{m}_F X_F = \dot{m}_B X_B \tag{C.2}$$

$$\dot{m}_F X_F = \dot{m}_{B_e} X_{B_e} \tag{C.3}$$

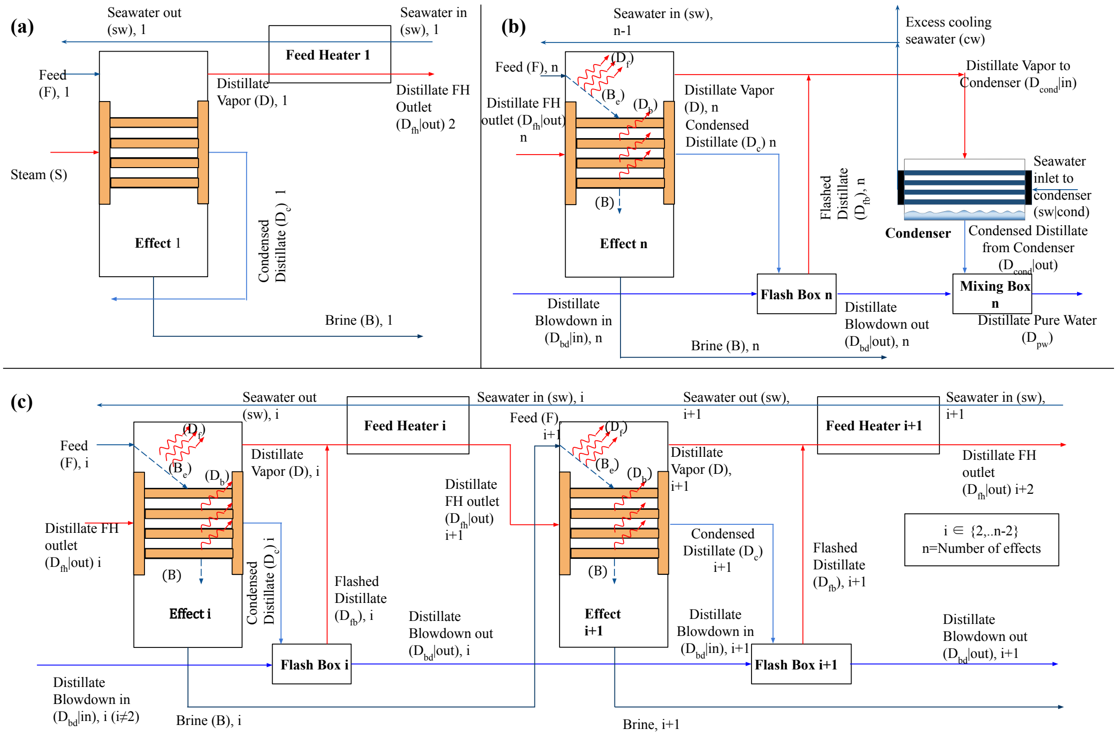

Figure C.1: Schematic of control volume of (a) first stage, (b) last or nth stage and (c) intermediate stages of an MED system

Energy balance inside the effect:

$$\dot{m}_{D_c}\Delta h_{D_c} = \dot{m}_D h_D + \dot{m}_B h_B - \dot{m}_F h_F \tag{C.4}$$

The decrease in the saturation temperature of the vapor due to superheating by the amount of boiling point elevation (BPE):

$$T_{D_{sat}} = T_D - BPE_D \tag{C.5}$$

Heat transfer area of the heat exchanger of the Effect:

$$\dot{m}_{D_c} h_{D_c}\Delta h_{D_c} = A_e U_e \left(T_{D_{sat}}^{prev} - T_e\right) \tag{C.6}$$

$$U_e = 10^{-3} \times \begin{bmatrix} 1939.1 + 1.40562 \left(T_{D_{sat}}^{prev} - 273.15\right) \\ -0.02075255 \left(T_{D_{sat}}^{prev} - 273.15\right)^2 \\ +0.0023186 \left(T_{D_{sat}}^{prev} - 273.15\right)^3 \end{bmatrix} \tag{C.7}$$

Following two equations are applicable for the first effect:

$$\dot{m}_{D_f}^{(1)} = 0 \tag{C.8}$$

$$\dot{m}_{D_c} h_{D_c} = \dot{m}_s h_{fg,s} \tag{C.9}$$

The following equations are valid for the rest of the effects:

$$\dot{m}_F = \dot{m}_{B_e} + \dot{m}_{D_f} \tag{C.10}$$

Equation (C.10) expresses the separation of the incoming feed into the distillate vapor and brine due to flashing occurred by the lower-pressure before the boiling evaporation process.

$$\dot{m}_D = \dot{m}_{D_f} + \dot{m}_{D_b} \tag{C.11}$$

The total distillate vapor generated in the effect consists of the flash evaporated vapor ($\dot{m}_{D_f}$) and the boiling evaporated vapor ($\dot{m}_{D_b}$), expressed by Equation (C.11).

$$\dot{m}_F h_F = \dot{m}_{B_e} h_{B_e} + \dot{m}_{D_f} h_{D_f} \tag{C.12}$$

$$\Delta h_{D_c} = h_{D_{fh}|out} - h_{D_c} \tag{C.13}$$

Flash box

$$\dot{m}_{D_{bd}|out} + \dot{m}_{D_{fb}} = \dot{m}_{D_{bd}|in} + \dot{m}_{D_c} \tag{C.14}$$

$$\dot{m}_{D_{bd}|out} h_{D_{bd}|out} + \dot{m}_{D_{fb}} h_{D_{fb}} = \dot{m}_{D_{bd}|in} h_{D_{bd}|in} + \dot{m}_{D_c} h_{D_c} \tag{C.15}$$

Feed heater

$$\dot{m}_D + \dot{m}_{D_{fb}} = \dot{m}_{D_{fh}|in} \tag{C.16}$$

$$\dot{m}_D h_D + \dot{m}_{D_{fb}} h_{D_{fb}} = \dot{m}_{D_{fh}|in} h_{D_{fh}|in} \tag{C.17}$$

$$\dot{m}_{D_{fh}|in} \left(h_{D_{fh}|in} - h_{D_{fh}|out} \right) = \dot{m}_{sw} \left(h_{sw}^{out} - h_{sw}^{in} \right) \tag{C.18}$$

$$\dot{m}_{D_{fh}|in} \left(h_{D_{fh}|in} - h_{D_{fh}|out} \right) = A_{fh} U_{fh} \left[\frac{\left(T_{D_{fh}|out} - T_{sw}^{in} \right) - \left(T_{D_{fh}|in} - T_{sw}^{out} \right)}{\ln \left(\frac{T_{D_{fh}|out} - T_{sw}^{in}}{T_{D_{fh}|in} - T_{sw}^{out}} \right)} \right] \tag{C.19}$$

$$T_{D_{fh}|avg} = \frac{T_{D_{fh}|in} + T_{D_{fh}|out}}{2} \tag{C.20}$$

$$U_{fh} = 10^{-3} \times \begin{bmatrix} 1617.5 + 0.1537 \left(T_{D_{fh}|avg} - 273.15 \right) \\ +0.1825 \left(T_{D_{fh}|avg} - 273.15 \right)^2 \\ -0.00008026 \left(T_{D_{fh}|avg} - 273.15 \right)^3 \end{bmatrix} \tag{C.21}$$

$$T_{D_{fh}|in} - T_{sw}^{out} = TTD_{fh} \tag{C.22}$$

Condenser

$$\dot{m}_D + \dot{m}_{D_{fh}|in} = \dot{m}_{D_{cond}|in} \tag{C.23}$$

$$\dot{m}_{D_{cond}} \left(h_{D_{cond}|in} - h_{D_{cond}|out} \right) = \dot{m}_{sw|cond} \left(h_{sw}^{out} - h_{sw}^{in} \right) \tag{C.24}$$

$$\dot{m}_{sw|cond}\left(h_{sw}^{out}-h_{sw}^{in}\right)=A_{cond}U_{cond}\frac{T_{sw}^{out}-T_{sw}^{in}}{\ln\left(\frac{T_{D_{cond}|sat}-T_{sw}^{in}}{T_{D_{cond}|sat}-T_{sw}^{out}}\right)} \tag{C.25}$$

$$U_{cond}=10^{-3}\times\begin{bmatrix}1617.5+0.1537\left(T_{cond|sat}-273.15\right)\\ +0.1825\left(T_{cond|sat}-273.15\right)^{2}\\ -0.00008026\left(T_{cond|sat}-273.15\right)^{3}\end{bmatrix} \tag{C.26}$$

$$\dot{m}_{sw|cond}=\dot{m}_{sw}+\dot{m}_{cw} \tag{C.27}$$

Mixing box

$$\dot{m}_{D_{fb}}^{(mb)}=0 \tag{C.28}$$

$$\dot{m}_{D_{cond}|out}+\dot{m}_{D_{bd}|out}^{(n)}=\dot{m}_{D_{pw}} \tag{C.29}$$

Table C.1: Thermodynamic properties of the various streams of an MED system with heat source temperature of 80 °C in the 1st effect

Stream	Effect No.	Pressure (Pa)	Temperature (°C)	Salinity (g kg^{-1})	Mass flow rate (kg s^{-1})	Specific enthalpy (J kg^{-1})
Feed (F)	1	26527	66.81	42	2.000	264988
	2	35795	73.81	45.93	1.829	291509
	3	27845	68.04	50.53	1.662	266978
	4	21100	61.92	56.01	1.500	241052
	5	15463	55.37	62.75	1.339	213364
	6	10807	48.19	71.51	1.175	183122
Steam (S)	1	35795	80	0	0.197	2643030
Distillate Feed Heater Outlet ($D_{fh}\|out$)	2	27845	73.81	0	0.171	2335664
	3	21100	68.04	0	0.168	2319457
	4	15463	61.92	0	0.166	2318919
	5	10807	55.37	0	0.167	2347220
	6	7003	48.19	0	0.172	2422027
Condensed Distillate (D_c)	1	35795	80	0	0.197	335015
	2	27845	73.81	0	0.171	306557
	3	21100	68.04	0	0.168	282182

Stream	Effect No.	Pressure (Pa)	Temperature (°C)	Salinity ($\mathrm{g\,kg^{-1}}$)	Mass flow rate ($\mathrm{kg\,s^{-1}}$)	Specific enthalpy ($\mathrm{J\,kg^{-1}}$)
	4	15463	61.92	0	0.166	256351
	5	10807	55.37	0	0.167	228671
	6	7003	48.19	0	0.172	198310
Distillate vapor (D)	1	35795	73.81	0	0.171	2632768
	2	27845	68.04	0	0.166	2622908
	3	21100	61.92	0	0.163	2612340
	4	15463	55.37	0	0.161	2600899
	5	10807	48.19	0	0.164	2588238
	6	7003	40	0	0.175	2573649
Brine (B)	1	35795	73.81	45.93	1.829	291509
	2	27845	68.04	50.53	1.662	266978
	3	21100	61.92	56.01	1.500	241052
	4	15463	55.37	62.75	1.339	213364
	5	10807	48.19	71.51	1.175	183122
	6	7003	40	84	1.000	148708
Distillate Blowdown in ($D_{bd}\|in$)	3	27845	67.4	0	0.169	282134
	4	21100	61.23	0	0.334	256286

Stream	Effect No.	Pressure (Pa)	Temperature (°C)	Salinity ($\mathrm{g\,kg^{-1}}$)	Mass flow rate ($\mathrm{kg\,s^{-1}}$)	Specific enthalpy ($\mathrm{J\,kg^{-1}}$)
	5	15463	54.62	0	0.494	228582
	6	10807	47.36	0	0.653	198187
Distillate Blowdown out ($D_{bd}\|out$)	2	27845	67.4	0	0.169	282134
	3	21100	61.23	0	0.334	256286
	4	15463	54.62	0	0.494	228582
	5	10807	47.36	0	0.653	198187
	6	7003	39.05	0	0.813	163384
Flashed distillate in Flash Box (D_{fb})	2	27845	67.4	0	0.002	2621630
	3	21100	61.23	0	0.004	2610959
	4	15463	54.62	0	0.006	2599392
	5	10807	47.36	0	0.008	2586565
	6	7003	39.05	0	0.012	2571733
Seawater in (sw)	1	26527	60.45	42	2.000	239569
	2	26527	54.05	42	2.000	214050
	3	26527	47.92	42	2.000	189640
	4	26527	42.6	42	2.000	168464
	5	26527	39	42	2.000	154148

Stream	Effect No.	Pressure (Pa)	Temperature (°C)	Salinity ($\mathrm{g\,kg^{-1}}$)	Mass flow rate ($\mathrm{kg\,s^{-1}}$)	Specific enthalpy ($\mathrm{J\,kg^{-1}}$)
Seawater out (sw)	1	26527	66.81	42	2.000	264988
	2	26527	60.45	42	2.000	239569
	3	26527	54.05	42	2.000	214050
	4	26527	47.92	42	2.000	189640
	5	26527	42.6	42	2.000	168464

Publications

1 Journal Articles

1. Saren, S., Mitra, S., Miyazaki, T., Ng, K. C. & Thu, K. A novel hybrid adsorption heat transformer – multi-effect distillation (AHT-MED) system for improved performance and waste heat upgrade. *Applied Energy* **305,** 117744. ISSN: 03062619. doi:10.1016/j.apenergy.2021.117744 (Jan. 2022).
2. Saren, S., Mitra, S., Miyazaki, T., Ng, K. C. & Thu, K. Adsorption heat transformer cycle using multiple adsorbent + water pairs for waste heat upgrade. *Journal of Thermal Analysis and Calorimetry 2022,* 1–13. ISSN: 1588-2926. doi:10.1007/S10973-022-11350-3 (Apr. 2022).
3. Saren, S., Mitra, S., Miksik, F., Miyazaki, T., Ng, K. C. & Thu, K. Impacts of the internal heat recovery scheme on the performance of an adsorption heat transformer cycle for temperature upgrade. *International Communications in Heat and Mass Transfer* **144,** 106774. ISSN: 0735-1933. doi:10.1016/J.ICHEATMASSTRANSFER.2023.106774 (May 2023).

2 Conference Proceedings

1. Saren, S., Mitra, S., Miyazaki, T., Ng, K. C. & Thu, K. *Equilibrium analysis of Adsorption Heat Transformer cycle with silica gel - water vapor pairs for waste heat upgrade* in *7th International Conference on Saving Energy for Refrigeration and Air-Conditioning (ICSERA) (virtual)* (2021).
2. Saren, S., Mitra, S., Miyazaki, T., Ng, K. C. & Thu, K. *Performance Characteristics of hybrid Adsorption heat transformer-Multi effect distillation (AHT+MED) system using different Silica gel adsorbent* in *13th International Conference on Applied Energy (virtual)* (2021).
3. Saren, S., Mitra, S., Miksik, F., Miyazaki, T., Ng, K. C. & Thu, K. *Theoretical Framework to Evaluate Maximum Temperature Lift in Adsorption Heat Transformer Cycle* in *14th International Conference on Applied Energy (virtual)* (2022).
4. Saren, S., Chen, H., Miksik, F., Miyazaki, T. & Thu, K. *Towards the precision adsorbents via understanding molecular-level surface phenomena of noble gases and non-polar gases on common adsorbents: Part 1 - Monte Carlo Approach* in *JSRAE Annual Conference, Okayama University, Japan* (2022).

5. Saren, S., Miyazaki, T. & Thu, K. *Effect of Hydroxylic (OH) Functional Group on CO2 Adsorption in Activated Carbon: A Molecular Simulation Study* in *24th Cross Straits Symposium on Energy and Environmental Science and Technology (virtual)* (2022).
6. Saren, S., Miyazaki, T. & Thu, K. *Effect of Pore Size Distribution on Carbon Dioxide Adsorption in Activated Carbon: A Grand Canonical Monte Carlo Simulation Study* in *13th ISAJ Annual Symposium, Embassy of India Tokyo, Japan* (2022).

References

1. Wennersten, R., Sun, Q. & Li, H. The future potential for Carbon Capture and Storage in climate change mitigation – an overview from perspectives of technology, economy and risk. *Journal of Cleaner Production* **103,** 724–736. ISSN: 0959-6526. doi:10.1016/J.JCLEPRO.2014.09.023 (Sept. 2015).
2. *Key aspects of the Paris Agreement | UNFCCC* https://unfccc.int/most-requested/key-aspects-of-the-paris-agreement. [Accessed 10-April-2023].
3. Fawzy, S., Osman, A. I., Doran, J. & Rooney, D. W. Strategies for mitigation of climate change: a review. *Environmental Chemistry Letters 2020 18:6* **18,** 2069–2094. ISSN: 1610-3661. doi:10.1007/S10311-020-01059-W (July 2020).
4. Bian, Q. Waste heat: the dominating root cause of current global warming. *Environmental Systems Research 2020 9:1* **9,** 1–11. ISSN: 2193-2697. doi:10.1186/S40068-020-00169-2 (May 2020).
5. Jouhara, H., Khordehgah, N., Almahmoud, S., Delpech, B., Chauhan, A. & Tassou, S. A. Waste heat recovery technologies and applications. *Thermal Science and Engineering Progress* **6,** 268–289. ISSN: 2451-9049. doi:10.1016/J.TSEP.2018.04.017 (June 2018).
6. Little, A. B. & Garimella, S. Comparative assessment of alternative cycles for waste heat recovery and upgrade. *Energy* **36,** 4492–4504. ISSN: 0360-5442. doi:10.1016/J.ENERGY.2011.03.069 (July 2011).
7. Bong, P. X., Malek, M. A., Mardi, N. H. & Hanafiah, M. M. Cradle-to-gate water-related impacts on production of traditional food products in Malaysia. *Sustainability (Switzerland)* **12,** 5274. ISSN: 20711050. doi:10.3390/su12135274 (2020).
8. Chen, Z., Ngo, H. H. & Guo, W. A Critical Review on the End Uses of Recycled Water. *Critical Reviews in Environmental Science and Technology* **43,** 1446–1516. ISSN: 1064-3389. doi:10.1080/10643389.2011.647788 (Jan. 2013).
9. Abdelkareem, M. A., El Haj Assad, M., Sayed, E. T. & Soudan, B. Recent progress in the use of renewable energy sources to power water desalination plants. *Desalination* **435,** 97–113. ISSN: 00119164. doi:10.1016/j.desal.2017.11.018 (June 2018).
10. Eke, J., Yusuf, A., Giwa, A. & Sodiq, A. The global status of desalination: An assessment of current desalination technologies, plants and capacity. *Desalination* **495,** 114633. ISSN: 00119164. doi:10.1016/j.desal.2020.114633 (2020).
11. Ng, K. C., Thu, K., Kim, Y.-D., Chakraborty, A. & Amy, G. Adsorption desalination: An emerging low-cost thermal desalination method. *Desalination* **308,** 161–179. ISSN: 00119164. doi:10.1016/j.desal.2012.07.030 (Jan. 2013).

12. Wu, X., Cao, Z., Lu, X. & Cai, W. Prediction of methane adsorption isotherms in metal–organic frameworks by neural network synergistic with classical density functional theory. *Chemical Engineering Journal* **459,** 141612. ISSN: 1385-8947. doi:10.1016/J.CEJ.2023.141612 (Mar. 2023).
13. Zhang, G., Liang, Y., Cui, G., Dou, B., Lu, W., Yang, Q. & Yan, X. Grand canonical Monte Carlo simulation of the adsorption and separation of carbon dioxide and methane using functionalized Mg-MOF-74. *Energy Reports* **9,** 2852–2860. ISSN: 2352-4847. doi:10.1016/J.EGYR.2023.01.121 (Dec. 2023).
14. Fei, S., Hsu, W. L., Delaunay, J. J. & Daiguji, H. Molecular dynamics study of water confined in MIL-101 metal–organic frameworks. *The Journal of Chemical Physics* **154,** 144503. ISSN: 0021-9606. doi:10.1063/5.0040909 (Apr. 2021).
15. Dubbeldam, D., Walton, K. S., Vlugt, T. J. & Calero, S. Design, Parameterization, and Implementation of Atomic Force Fields for Adsorption in Nanoporous Materials. *Advanced Theory and Simulations* **2.** ISSN: 25130390. doi:10.1002/adts.201900135 (2019).
16. Kessler, C., Eller, J., Gross, J. & Hansen, N. Adsorption of light gases in covalent organic frameworks: comparison of classical density functional theory and grand canonical Monte Carlo simulations. *Microporous and Mesoporous Materials* **324,** 111263. ISSN: 13871811. doi:10.1016/j.micromeso.2021.111263. arXiv: 2103.12455 (Sept. 2021).
17. Alonso, G., Bahamon, D., Keshavarz, F., Giménez, X., Gamallo, P. & Sayós, R. Density functional theory-based adsorption isotherms for pure and flue gas mixtures on Mg-MOF-74. Application in CO2 capture swing adsorption processes. *Journal of Physical Chemistry C* **122,** 3945–3957. ISSN: 19327455. doi:10.1021/acs.jpcc.8b00938 (Feb. 2018).
18. Grinev, I. V., Zubkov, V. V. & Samsonov, V. M. Calculation of isosteric heats of molecular gas and vapor adsorption on graphite using density functional theory. *Colloid Journal* **78,** 37–46. ISSN: 1061933X. doi:10.1134/S1061933X15060101 (Jan. 2016).
19. Paudel, H. P., Shi, W., Hopkinson, D., Steckel, J. A. & Duan, Y. Computational modelling of adsorption and diffusion properties of CO2and CH4in ZIF-8 for gas separation applications: A density functional theory approach. *Reaction Chemistry and Engineering* **6,** 990–1001. ISSN: 20589883. doi:10.1039/d0re00416b (June 2021).
20. Boulfelfel, S. E., Findley, J. M., Fang, H., Daou, A. S., Ravikovitch, P. I. & Sholl, D. S. A Transferable Force Field for Predicting Adsorption and Diffusion of Small Molecules in Alkali Metal Exchanged Zeolites with Coupled Cluster Accuracy. *Journal of Physical Chemistry C* **125,** 26832–26846. ISSN: 19327455. doi:10.1021/ACS.JPCC.1C07790/SUPPL_FILE/JP1C07790_SI_002.ZIP (Dec. 2021).
21. Findley, J. M., Boulfelfel, S. E., Fang, H., Muraro, G., Ravikovitch, P. I. & Sholl, D. S. A Transferable Force Field for Predicting Adsorption and Diffusion of Hydrocarbons and Small Molecules in Silica Zeolites with Coupled-Cluster Accuracy. *Journal of Physical Chemistry C* **125,** 8418–8429. ISSN: 19327455. doi:10.1021/ACS.JPCC.1C00943/SUPPL_FILE/JP1C00943_SI_002.ZIP (Apr. 2021).
22. Kulkarni, A. R. & Sholl, D. S. DFT-Derived Force Fields for Modeling Hydrocarbon Adsorption in MIL-47(V). *Langmuir* **31,** 8453–8468. ISSN: 15205827. doi:10.1021/ACS.LANGMUIR.5B01193/SUPPL_FILE/LA5B01193_SI_001.PDF (Aug. 2015).

23. Gee, J. A. & Sholl, D. S. Prediction of Adsorption Properties of Cyclic Hydrocarbons in MOFs Using DFT-Derived Force Fields. *Journal of Physical Chemistry C* **119,** 16920–16926. ISSN: 19327455. doi:10.1021/ACS.JPCC.5B03147/SUPPL_FILE/JP5B03147_SI_001.PDF (July 2015).

24. Breneman, C. M. & Wiberg, K. B. Determining atom-centered monopoles from molecular electrostatic potentials. The need for high sampling density in formamide conformational analysis. *Journal of Computational Chemistry* **11,** 361–373. ISSN: 1096-987X. doi:10.1002/JCC.540110311 (Apr. 1990).

25. Bultinck, P., Van Alsenoy, C., Ayers, P. W. & Carbó-Dorca, R. Critical analysis and extension of the Hirshfeld atoms in molecules. *The Journal of Chemical Physics* **126,** 144111. ISSN: 0021-9606. doi:10.1063/1.2715563 (Apr. 2007).

26. Hirshfeld, F. L. Bonded-atom fragments for describing molecular charge densities. *Theoretica Chimica Acta* **44,** 129–138. ISSN: 00405744. doi:10.1007/BF00549096/METRICS (June 1977).

27. Bader, R. F., MacDougall, P. J. & Lau, C. D. Bonded and Nonbonded Charge Concentrations and Their Relation to Molecular Geometry and Reactivity. *Journal of the American Chemical Society* **106,** 1594–1605. ISSN: 15205126. doi:10.1021/JA00318A009/ASSET/JA00318A009.FP.PNG_V03 (Mar. 1984).

28. Bader, R. F. & Matta, C. F. Atomic Charges Are Measurable Quantum Expectation Values: A Rebuttal of Criticisms of QTAIM Charges. *Journal of Physical Chemistry A* **108,** 8385–8394. ISSN: 10895639. doi:10.1021/JP0482666 (Oct. 2004).

29. Campañá, C., Mussard, B. & Woo, T. K. Electrostatic Potential Derived Atomic Charges for Periodic Systems Using a Modified Error Functional. *Journal of Chemical Theory and Computation* **5,** 2866–2878. ISSN: 15499618. doi:10.1021/CT9003405 (Oct. 2009).

30. Manz, T. A. & Sholl, D. S. Chemically meaningful atomic charges that reproduce the electrostatic potential in periodic and nonperiodic materials. *Journal of Chemical Theory and Computation* **6,** 2455–2468. ISSN: 15499618. doi:10.1021/CT100125X/SUPPL_FILE/CT100125X_SI_001.PDF (Aug. 2010).

31. Ravikovitch, P. I., Haller, G. L. & Neimark, A. V. Density functional theory model for calculating pore size distributions: pore structure of nanoporous catalysts. *Advances in Colloid and Interface Science* **76-77,** 203–226. ISSN: 0001-8686. doi:10.1016/S0001-8686(98)00047-5 (July 1998).

32. Kupgan, G., Liyana-Arachchi, T. P. & Colina, C. M. NLDFT Pore Size Distribution in Amorphous Microporous Materials. *Langmuir* **33,** 11138–11145. ISSN: 15205827. doi:10.1021/ACS.LANGMUIR.7B01961/ASSET/IMAGES/LARGE/LA-2017-019618_0007.JPEG (Oct. 2017).

33. Jagiello, J., Kenvin, J., Celzard, A. & Fierro, V. Enhanced resolution of ultra micropore size determination of biochars and activated carbons by dual gas analysis using N2 and CO2 with 2D-NLDFT adsorption models. *Carbon* **144,** 206–215. ISSN: 0008-6223. doi:10.1016/J.CARBON.2018.12.028 (Apr. 2019).

34. Hu, X., Radosz, M., Cychosz, K. A. & Thommes, M. CO 2-filling capacity and selectivity of carbon nanopores: Synthesis, texture, and pore-size distribution from quenched-solid density functional theory (QSDFT). *Environmental Science and Technology* **45,** 7068–7074. ISSN: 0013936X. doi:10.1021/ES200782S/SUPPL_FILE/ES200782S_SI_001.PDF (Aug. 2011).

35. Ravikovitch, P. I. & Neimark, A. V. Density functional theory model of adsorption on amorphous and microporous silica materials. *Langmuir* **22,** 11171–11179. ISSN: 07437463. doi:10.1021/LA0616146/ASSET/IMAGES/MEDIUM/LA0616146N00001.GIF (Dec. 2006).

36. Keskin, S., Liu, J., Rankin, R. B., Johnson, J. K. & Sholl, D. S. Progress, Opportunities, and Challenges for Applying Atomically Detailed Modeling to Molecular Adsorption and Transport in Metal-Organic Framework Materials. *Industrial and Engineering Chemistry Research* **48,** 2355–2371. ISSN: 08885885. doi:10.1021/IE800666S (Mar. 2008).

37. Bai, P., Tsapatsis, M. & Siepmann, J. I. TraPPE-zeo: Transferable potentials for phase equilibria force field for all-silica zeolites. *Journal of Physical Chemistry C* **117,** 24375–24387. ISSN: 19327447. doi:10.1021/JP4074224/SUPPL_FILE/JP4074224_SI_001.TXT (Nov. 2013).

38. Oktavian, R., Schireman, R., Glasby, L. T., Huang, G., Zanca, F., Fairen-Jimenez, D., Ruggiero, M. T. & Moghadam, P. Z. Computational Characterization of Zr-Oxide MOFs for Adsorption Applications. *ACS Applied Materials and Interfaces* **14,** 56947. ISSN: 19448252. doi:10.1021/ACSAMI.2C13391/SUPPL_FILE/AM2C13391_SI_005.XLSX (2022).

39. Dantas, S., Struckhoff, K. C., Thommes, M. & Neimark, A. V. Pore size characterization of micro-mesoporous carbons using CO2 adsorption. *Carbon* **173,** 842–848. ISSN: 0008-6223. doi:10.1016/J.CARBON.2020.11.059 (Mar. 2021).

40. Xu, H., Zeng, Y., Do, D. D. & Nicholson, D. On the Nonwetting/Wetting Behavior of Carbon Dioxide on Graphite. *Journal of Physical Chemistry C* **123,** 9112–9120. ISSN: 19327455. doi:10.1021/acs.jpcc.9b00635 (Apr. 2019).

41. Zhang, H., Tan, S. J., Liu, L., Do, D. D. & Nicholson, D. Comparison of the Adsorption Transitions of Methane and Krypton on Graphite at Sub-Monolayer Coverage. *Journal of Physical Chemistry C* **122,** 7737–7748. ISSN: 19327455. doi:10.1021/ACS.JPCC.8B00535/ASSET/IMAGES/LARGE/JP-2018-005352_0013.JPEG (Apr. 2018).

42. Pham, T., Forrest, K. A., Banerjee, R., Orcajo, G., Eckert, J. & Space, B. Understanding the H2 sorption trends in the M-MOF-74 series (M = Mg, Ni, Co, Zn). *Journal of Physical Chemistry C* **119,** 1078–1090. ISSN: 19327455. doi:10.1021/JP510253M (Jan. 2015).

43. Perry, J. J., Teich-Mcgoldrick, S. L., Meek, S. T., Greathouse, J. A., Haranczyk, M. & Allendorf, M. D. Noble gas adsorption in metal-organic frameworks containing open metal sites. *Journal of Physical Chemistry C* **118,** 11685–11698. ISSN: 19327455. doi:10.1021/jp501495f (June 2014).

44. Hackett, C. & Hammond, K. D. Simulating the effect of the quadrupole moment on the adsorption of nitrogen in siliceous zeolites. *Microporous and Mesoporous Materials* **263,** 231–235. ISSN: 1387-1811. doi:10.1016/J.MICROMESO.2017.12.018 (June 2018).

45. Martin, R. L., Simon, C. M., Smit, B. & Haranczyk, M. In silico design of porous polymer networks: High-throughput screening for methane storage materials. *Journal of the American Chemical Society* **136,** 5006–5022. ISSN: 15205126. doi:10.1021/JA4123939 (Apr. 2014).

46. Liu, L., Zhang, H., Do, D. D., Nicholson, D. & Liu, J. On the microscopic origin of the temperature evolution of isosteric heat for methane adsorption on graphite. *Physical Chemistry Chemical Physics* **19,** 27105–27115. ISSN: 1463-9084. doi:10.1039/C7CP04497F (Oct. 2017).

47. Teo, H. W. B., Chakraborty, A. & Kayal, S. Evaluation of CH4 and CO2 adsorption on HKUST-1 and MIL-101(Cr) MOFs employing Monte Carlo simulation and comparison with experimental data. *Applied Thermal Engineering* **110,** 891–900. ISSN: 1359-4311. doi:10.1016/J.APPLTHERMALENG.2016.08.126 (Jan. 2017).

48. Rahmati, M. & Modarress, H. Selectivity of new siliceous zeolites for separation of methane and carbon dioxide by Monte Carlo simulation. *Microporous and Mesoporous Materials* **176,** 168–177. ISSN: 1387-1811. doi:10.1016/J.MICROMESO.2013.03.054 (Aug. 2013).

49. Lim, J. R., Yang, C. T., Kim, J. & Lin, L. C. Transferability of CO2 Force Fields for Prediction of Adsorption Properties in All-Silica Zeolites. *Journal of Physical Chemistry C* **122,** 10892–10903. ISSN: 19327455. doi:10.1021/ACS.JPCC.8B02208 (May 2018).

50. Zhao, H., Bahamon, D., Khaleel, M. & Vega, L. F. Insights into the performance of hybrid graphene oxide/MOFs for CO2 capture at process conditions by molecular simulations. *Chemical Engineering Journal* **449,** 137884. ISSN: 1385-8947. doi:10.1016/J.CEJ.2022.137884 (Dec. 2022).

51. Wang, S., Mahurin, S. M., Dai, S. & Jiang, D. E. Design of Graphene/Ionic Liquid Composites for Carbon Capture. *ACS Applied Materials and Interfaces* **13,** 17511–17516. ISSN: 19448252. doi:10.1021/ACSAMI.1C01242/ASSET/IMAGES/LARGE/AM1C01242_0008.JPEG (Apr. 2021).

52. Mileo, P. G., Cho, K. H., Chang, J. S. & Maurin, G. Water adsorption fingerprinting of structural defects/capping functions in Zr–fumarate MOFs: a hybrid computational-experimental approach. *Dalton Transactions* **50,** 1324–1333. ISSN: 1477-9234. doi:10.1039/D0DT03705B (Feb. 2021).

53. Ohba, T. & Kaneko, K. Cluster-associated filling of water molecules in slit-shaped graphitic nanopores. *https://doi.org/10.1080/00268970701192081* **105,** 139–145. ISSN: 00268976. doi:10.1080/00268970701192081 (Jan. 2010).

54. Puibasset, J. & Pellenq, R. J. M. Grand Canonical Monte Carlo Simulation Study of Water Adsorption in Silicalite at 300 K. *Journal of Physical Chemistry B* **112,** 6390–6397. ISSN: 15206106. doi:10.1021/JP7097153 (May 2008).

55. Zhang, J., Clennell, M. B., Liu, K., Dewhurst, D. N., Pervukhina, M. & Sherwood, N. Molecular dynamics study of CO2 sorption and transport properties in coal. *Fuel* **177,** 53–62. ISSN: 0016-2361. doi:10.1016/J.FUEL.2016.02.075 (Aug. 2016).

56. Sarkisov, L., Centineo, A. & Brandani, S. Molecular simulation and experiments of water adsorption in a high surface area activated carbon: Hysteresis, scanning curves and spatial organization of water clusters. *Carbon* **118,** 127–138. ISSN: 0008-6223. doi:10.1016/J.CARBON.2017.03.044 (July 2017).

57. Ghasemzadeh, H., Babaei, S., Tesson, S., Azamat, J. & Ostadhassan, M. From excess to absolute adsorption isotherm: The effect of the adsorbed density. *Chemical Engineering Journal* **425,** 131495. ISSN: 13858947. doi:10.1016/j.cej.2021.131495 (Dec. 2021).

58. Liu, B., Babaei, S., Bai, L., Tian, S., Ghasemzadeh, H., Rashidi, M. & Ostadhassan, M. A dilemma in calculating ethane absolute adsorption in shale gas reservoirs: A theoretical approach. *Chemical Engineering Journal* **450,** 138242. ISSN: 1385-8947. doi:10.1016/J.CEJ.2022.138242 (Dec. 2022).

59. Frenkel, Daan, B. S. *Understanding molecular simulation: from algorithms to applications. Vol. 1. Elsevier* 638. ISBN: 9780080519982 (2001).

60. Torres-Knoop, A., Balaji, S. P., Vlugt, T. J. & Dubbeldam, D. A comparison of advanced monte carlo methods for open systems: CFCMC vs CBMC. *Journal of Chemical Theory and Computation* **10,** 942–952. ISSN: 15499626. doi:10.1021/CT4009766/SUPPL_FILE/CT4009766_SI_001.PDF (Mar. 2014).

61. Gonçalves, D. V., Paiva, M. A., Oliveira, J. C., Bastos-Neto, M. & Lucena, S. M. Prediction of the monocomponent adsorption of H2S and mixtures with CO2 and CH4 on activated carbons. *Colloids and Surfaces A: Physicochemical and Engineering Aspects* **559,** 342–350. ISSN: 18734359. doi:10.1016/j.colsurfa.2018.09.082 (2018).

62. Pršlja, P., Lomba, E., Gómez-Álvarez, P., Urbič, T. & Noya, E. G. Adsorption of water, methanol, and their mixtures in slit graphite pores. *The Journal of Chemical Physics* **150,** 024705. ISSN: 0021-9606. doi:10.1063/1.5078603 (Jan. 2019).

63. Hao, Y., Yuan, L., Li, P., Zhao, W., Li, D. & Lu, D. Molecular Simulations of Methane Adsorption Behavior in Illite Nanopores Considering Basal and Edge Surfaces. *Energy and Fuels* **32,** 4783–4796. ISSN: 15205029. doi:10.1021/ACS.ENERGYFUELS.8B00070/SUPPL_FILE/EF8B00070_SI_004.XYZ (Apr. 2018).

64. Madero-Castro, R. M., Vicent-Luna, J. M., Peng, X. & Calero, S. Adsorption of Linear Alcohols in Amorphous Activated Carbons: Implications for Energy Storage Applications. *ACS Sustainable Chemistry and Engineering* **41,** 46. ISSN: 21680485. doi:10.1021/acssuschemeng.1c06315 (2021).

65. Bahamon, D., Ogungbenro, A. E., Khaleel, M., Abu-Zahra, M. R. & Vega, L. F. Performance of Activated Carbons Derived from Date Seeds in CO2 Swing Adsorption Determined by Combining Experimental and Molecular Simulation Data. *Industrial and Engineering Chemistry Research* **59,** 7161–7173. ISSN: 15205045. doi:10.1021/acs.iecr.9b05542 (Apr. 2020).

66. Chowdhury, S. & Balasubramanian, R. Three-Dimensional Graphene-Based Porous Adsorbents for Postcombustion CO2 Capture. *Industrial and Engineering Chemistry Research* **55,** 7906–7916. ISSN: 15205045. doi:10.1021/ACS.IECR.5B04052/ASSET/IMAGES/LARGE/IE-2015-04052D_0011.JPEG (July 2016).

67. Pang, Y., Hu, X., Wang, S., Chen, S., Soliman, M. Y. & Deng, H. Characterization of adsorption isotherm and density profile in cylindrical nanopores: Modeling and measurement. *Chemical Engineering Journal* **396,** 125212. ISSN: 1385-8947. doi:10.1016/J.CEJ.2020.125212 (Sept. 2020).

68. Gu, S., Gao, B., Teng, L., Li, Y., Fan, C., Iglauer, S., Zhang, D. & Ye, X. Monte Carlo Simulation of Supercritical Carbon Dioxide Adsorption in Carbon Slit Pores. *Energy and Fuels* **31,** 9717–9724. ISSN: 15205029. doi:10.1021/ACS.ENERGYFUELS.7B01344/ASSET/IMAGES/LARGE/EF-2017-01344U_0013.JPEG (Sept. 2017).

69. Vishnyakov, A., Ravikovitch, P. I. & Neimark, A. V. Molecular level models for CO2 sorption in nanopores. *Langmuir* **15,** 8736–8742. ISSN: 07437463. doi:10.1021/LA990726C/ASSET/IMAGES/LARGE/LA990726CF00006.JPEG (Dec. 1999).

70. Samios, S., Stubos, A. K., Papadopoulos, G. K., Kanellopoulos, N. K. & Rigas, F. The Structure of Adsorbed CO2 in Slitlike Micropores at Low and High Temperature and the Resulting Micropore Size Distribution Based on GCMC Simulations. *Journal of Colloid and Interface Science* **224,** 272–290. ISSN: 0021-9797. doi:10.1006/JCIS.1999.6683 (Apr. 2000).
71. Bhatia, S. K., Tran, K., Nguyen, T. X. & Nicholson, D. High-pressure adsorption capacity and structure of co2 in carbon slit pores: Theory and simulation. *Langmuir* **20,** 9612–9620. ISSN: 07437463. doi:10.1021/LA048571I (Oct. 2004).
72. Liu, X., Sim, A. H. H. & Fan, C. Low temperature adsorption of CO2 in carbonaceous wedge pores: a Monte Carlo simulation study. *Adsorption* **28,** 231–247. ISSN: 15728757. doi:10.1007/S10450-022-00363-X/FIGURES/16 (Aug. 2022).
73. Chen, H., Guo, Y., Du, Y., Xu, X., Su, C., Zeng, Z. & Li, L. The synergistic effects of surface functional groups and pore sizes on CO2 adsorption by GCMC and DFT simulations. *Chemical Engineering Journal* **415,** 128824. ISSN: 1385-8947. doi:10.1016/J.CEJ.2021.128824 (July 2021).
74. Zhou, S., Guo, C., Wu, Z., Wang, M., Wang, Z., Wei, S., Li, S. & Lu, X. Edge-functionalized nanoporous carbons for high adsorption capacity and selectivity of CO2 over N2. *Applied Surface Science* **410,** 259–266. ISSN: 0169-4332. doi:10.1016/J.APSUSC.2017.03.136 (July 2017).
75. Li, Q., Xu, W., Liang, X., Liu, B., Wu, Q., Zeng, Z., Li, L. & Ma, X. Specific alkali metal sites as CO2 traps in activated carbon with different pore size for CO2 selective adsorption: GCMC and DFT simulations. *Fuel* **325,** 124871. ISSN: 00162361. doi:10.1016/j.fuel.2022.124871 (Oct. 2022).
76. Dang, Y., Zhao, L., Lu, X., Xu, J., Sang, P., Guo, S., Zhu, H. & Guo, W. Molecular simulation of CO2/CH4 adsorption in brown coal: Effect of oxygen-, nitrogen-, and sulfur-containing functional groups. *Applied Surface Science* **423,** 33–42. ISSN: 0169-4332. doi:10.1016/J.APSUSC.2017.06.143 (Nov. 2017).
77. Khosrowshahi, M. S., Abdol, M. A., Mashhadimoslem, H., Khakpour, E., Emrooz, H. B. M., Sadeghzadeh, S. & Ghaemi, A. The role of surface chemistry on CO2 adsorption in biomass-derived porous carbons by experimental results and molecular dynamics simulations. *Scientific Reports 2022 12:1* **12,** 1–19. ISSN: 2045-2322. doi:10.1038/s41598-022-12596-5 (May 2022).
78. Ma, X., Yang, Y., Wu, Q., Liu, B., Li, D., Chen, R., Wang, C., Li, H., Zeng, Z. & Li, L. Underlying mechanism of CO2 uptake onto biomass-based porous carbons: Do adsorbents capture CO2 chiefly through narrow micropores? *Fuel* **282,** 118727. ISSN: 0016-2361. doi:10.1016/J.FUEL.2020.118727 (Dec. 2020).
79. Wang, S., Lu, L., Wu, D., Lu, X., Cao, W., Yang, T. & Zhu, Y. Molecular Simulation Study of the Adsorption and Diffusion of a Mixture of CO2/CH4 in Activated Carbon: Effect of Textural Properties and Surface Chemistry. *Journal of Chemical and Engineering Data* **61,** 4139–4147. ISSN: 15205134. doi:10.1021/ACS.JCED.6B00554/ASSET/IMAGES/LARGE/JE-2016-00554P_0010.JPEG (Dec. 2016).
80. Wei, D., Ma, X., Yang, T., Liu, B., Jiang, H., Yang, Y. & Li, L. N-doping porous carbon with rich narrow micropores for highly efficient CO2 selective adsorption: Insight from experimental and theoretical study. *Applied Surface Science* **605,** 154777. ISSN: 01694332. doi:10.1016/j.apsusc.2022.154777 (Dec. 2022).

81. Meconi, G. M. & Zangi, R. Adsorption-induced clustering of CO2 on graphene. *Physical Chemistry Chemical Physics* **22,** 21031–21041. ISSN: 1463-9084. doi:10.1039/D0CP03482G (Sept. 2020).

82. Ohba, T. & Kaneko, K. Initial filling mechanism of predominant water adsorption on hydrophobic slit-shaped carbon nanopores. *Journal of Physics: Conference Series* **177,** 012001. ISSN: 1742-6596. doi:10.1088/1742-6596/177/1/012001 (June 2009).

83. Striolo, A., Chialvo, A. A., Cummings, P. T. & Gubbins, K. E. Water adsorption in carbon-slit nanopores. *Langmuir* **19,** 8583–8591. ISSN: 07437463. doi:10.1021/la0347354 (Sept. 2003).

84. Liu, J. C. & Monson, P. A. Does water condense in carbon pores? *Langmuir* **21,** 10219–10225. ISSN: 07437463. doi:10.1021/la0508902 (Oct. 2005).

85. Müller, E. A., Rull, L. F., Vega, L. F. & Gubbins, K. E. Adsorption of water on activated carbons: A molecular simulation study. *Journal of Physical Chemistry* **100,** 1189–1196. ISSN: 00223654. doi:10.1021/jp952233w (1996).

86. McCallum, C. L., Bandosz, T. J., McGrother, S. C., Muller, E. A. & Gubbins, K. E. Molecular model for adsorption of water on activated carbon: Comparison of simulation and experiment. *Langmuir* **15,** 533–544. ISSN: 07437463. doi:10.1021/la9805950 (1999).

87. Wongkoblap, A. & Do, D. D. Adsorption of water in finite length carbon slit pore: Comparison between computer simulation and experiment. *Journal of Physical Chemistry B* **111,** 13949–13956. ISSN: 15206106. doi:10.1021/JP0747297/ASSET/IMAGES/LARGE/JP0747297F00011.JPEG (Dec. 2007).

88. Liu, L., Zeng, W., Tan, S., Liu, M. & Do, D. D. Microscopic insights into water adsorption in carbon nanopores – the role of acidic and basic functional groups and their configurations. *Physical Chemistry Chemical Physics* **23,** 18369–18377. ISSN: 1463-9084. doi:10.1039/D1CP02308J (Sept. 2021).

89. Liu, L., Zeng, Y., Tan, S. J., Xu, H., Do, D. D., Nicholson, D. & Liu, J. On the mechanism of water adsorption in carbon micropores – A molecular simulation study. *Chemical Engineering Journal* **357,** 358–366. ISSN: 1385-8947. doi:10.1016/J.CEJ.2018.09.160 (Feb. 2019).

90. Liu, L., Zeng, W., Tan, S. (, Liu, M. & Do, D. D. On the characterization of bimodal porous carbon via water adsorption: The role of pore connectivity and temperature. *Carbon* **179,** 477–485. ISSN: 00086223. doi:10.1016/j.carbon.2021.04.041 (July 2021).

91. Do, D. D., Johnathan Tan, S. L., Zeng, Y., Fan, C., Nguyen, V. T., Horikawa, T. & Nicholson, D. The interplay between molecular layering and clustering in adsorption of gases on graphitized thermal carbon black - Spill-over phenomenon and the important role of strong sites. *Journal of Colloid and Interface Science* **446,** 98–113. ISSN: 0021-9797. doi:10.1016/J.JCIS.2015.01.028 (May 2015).

92. Takamatsu, H. & Ohba, T. Water Adsorption Control by Surface Nanostructures on Graphene-Related Materials by Grand Canonical Monte Carlo Simulations. *Langmuir* **37,** 14646–14656. ISSN: 15205827. doi:10.1021/acs.langmuir.1c02372 (Dec. 2021).

93. Kumar, K. V., Preuss, K., Guo, Z. X. & Titirici, M. M. Understanding the Hydrophilicity and Water Adsorption Behavior of Nanoporous Nitrogen-Doped Carbons. *Journal of Physical Chemistry C* **120,** 18167–18179. ISSN: 19327455. doi:10.1021/ACS.JPCC.6B06555/ASSET/IMAGES/LARGE/JP-2016-06555M_0010.JPEG (Aug. 2016).
94. Hill, T. L. Thermodynamics of adsorption. *Trans. Faraday Soc.* **47,** 376–380. doi:10.1039/TF9514700376 (0 1951).
95. Everett, D. H. The thermodynamics of adsorption. Part II.—Thermodynamics of monolayers on solids. *Trans. Faraday Soc.* **46,** 942–957. doi:10.1039/TF9504600942 (0 1950).
96. Young, D. M. & Crowell, A. D. *Physical adsorption of gases* (Butterworths, 1962).
97. Myers, A. L. Thermodynamics of adsorption in porous materials. *AIChE Journal* **48,** 145–160. ISSN: 00011541. doi:10.1002/aic.690480115 (1 Jan. 2002).
98. Myers, A. L. & Monson, P. A. Adsorption in porous materials at high pressure: Theory and experiment. *Langmuir* **18,** 10261–10273. ISSN: 07437463. doi:10.1021/la026399h (Dec. 2002).
99. Al-Muhtaseb, S. A. & Ritter, J. A. Roles of Surface Heterogeneity and Lateral Interactions on the Isosteric Heat of Adsorption and Adsorbed Phase Heat Capacity. doi:10.1021/jp984110s (1999).
100. Ismail, A. B., Li, A., Thu, K., Ng, K. C. & Chun, W. On the thermodynamics of refrigerant + heterogeneous solid surfaces adsorption. *Langmuir* **29,** 14494–14502. ISSN: 07437463. doi:10.1021/la403330t (47 Nov. 2013).
101. Chua, H. T., Ng, K. C., Chakraborty, A. & Oo, N. M. Thermodynamic property fields of an adsorbate-adsorbent system. *Langmuir* **19,** 2254–2259. ISSN: 07437463. doi:10.1021/la0267140 (6 2003).
102. Chakraborty, A., Saha, B. B., Koyama, S. & Ng, K. C. On the thermodynamic modeling of the isosteric heat of adsorption and comparison with experiments. *Applied Physics Letters* **89,** 171901. ISSN: 00036951. doi:10.1063/1.2360925 (17 Oct. 2006).
103. Chakraborty, A., Saha, B. B., Koyama, S. & Ng, K. C. Specific heat capacity of a single component adsorbent-adsorbate system. *Applied Physics Letters* **90.** ISSN: 00036951. doi:10.1063/1.2731438 (17 2007).
104. Chakraborty, A., Saha, B. B., Ng, K. C., Koyama, S. & Srinivasan, K. Theoretical insight of physical adsorption for a single-component adsorbent + adsorbate system: I. thermodynamic property surfaces. *Langmuir* **25,** 2204–2211. ISSN: 07437463. doi:10.1021/la803289p (4 Feb. 2009).
105. Rahman, K. A., Loh, W. S. & Ng, K. C. Heat of Adsorption and Adsorbed Phase Specific Heat Capacity of Methane/Activated Carbon System. *Procedia Engineering* **56,** 118–125. ISSN: 1877-7058. doi:10.1016/J.PROENG.2013.03.097 (Jan. 2013).
106. Azahar, F. H. M., Mitra, S., Yabushita, A., Harata, A., Saha, B. B. & Thu, K. Improved model for the isosteric heat of adsorption and impacts on the performance of heat pump cycles. *Applied Thermal Engineering* **143,** 688–700. ISSN: 13594311. doi:10.1016/j.applthermaleng.2018.07.131 (Oct. 2018).

107. Saha, B. B., Chakraborty, A., Koyama, S., Yoon, S. H., Mochida, I., Kumja, M., Yap, C. & Ng, K. C. Isotherms and thermodynamics for the adsorption of n-butane on pitch based activated carbon. *International Journal of Heat and Mass Transfer* **51,** 1582–1589. ISSN: 00179310. doi:10.1016/j.ijheatmasstransfer.2007.07.031 (7-8 2008).

108. Rahman, K. A., Chakraborty, A., Saha, B. B. & Ng, K. C. On thermodynamics of methane + carbonaceous materials adsorption. *International Journal of Heat and Mass Transfer* **55,** 565–573. ISSN: 00179310. doi:10.1016/j.ijheatmasstransfer.2011.10.056 (4 Jan. 2012).

109. Singh, V. K. & Kumar, E. A. Experimental investigation and thermodynamic analysis of CO2 adsorption on activated carbons for cooling system. *Journal of CO2 Utilization* **17,** 290–304. ISSN: 2212-9820. doi:10.1016/J.JCOU.2016.12.004 (Jan. 2017).

110. Pal, A., Rocky, K. A. & Saha, B. B. Thermodynamic analysis of promising biomass-derived activated carbons/CO2 based adsorption cooling systems. *Journal of CO2 Utilization* **46,** 101457. ISSN: 22129820. doi:10.1016/j.jcou.2021.101457 (Apr. 2021).

111. Rupam, T. H., Islam, M. A., Pal, A., Chakraborty, A. & Saha, B. B. Thermodynamic property surfaces for various adsorbent/adsorbate pairs for cooling applications. *International Journal of Heat and Mass Transfer* **144,** 118579. ISSN: 00179310. doi:10.1016/j.ijheatmasstransfer.2019.118579 (Dec. 2019).

112. Rocky, K. A., Pal, A., Moniruzzaman, M. & Saha, B. B. Adsorption characteristics and thermodynamic property fields of polymerized ionic liquid and polyvinyl alcohol based composite/CO2 pairs. *Journal of Molecular Liquids* **294,** 111555. ISSN: 0167-7322. doi:10.1016/J.MOLLIQ.2019.111555 (Nov. 2019).

113. Ye, L., Islam, M. A., Rupam, T. H., Jahan, I. & Saha, B. B. Study on the adsorption characteristics of Maxsorb III/HFO-1234ze(E) pair for adsorption refrigeration applications. *International Journal of Refrigeration* **146,** 248–260. ISSN: 0140-7007. doi:10.1016/J.IJREFRIG.2022.11.005 (Feb. 2023).

114. Myers, A. L. Characterization of nanopores by standard enthalpy and entropy of adsorption of probe molecules. *Colloids and Surfaces A: Physicochemical and Engineering Aspects* **241,** 9–14. ISSN: 0927-7757. doi:10.1016/J.COLSURFA.2004.04.004 (July 2004).

115. Han, B., Chakraborty, A. & Saha, B. B. Isosteric Heats and Entropy of Adsorption in Henry's Law Region for Carbon and MOFs Structures for Energy Conversion Applications. *International Journal of Heat and Mass Transfer* **182,** 122000. ISSN: 00179310. doi:10.1016/j.ijheatmasstransfer.2021.122000 (Jan. 2022).

116. Walton, K. S. & LeVan, M. D. Adsorbed-phase heat capacities: Thermodynamically consistent values determined from temperature-dependent equilibrium models. *Industrial and Engineering Chemistry Research* **44,** 178–182. ISSN: 08885885. doi:10.1021/ie049394j (Jan. 2005).

117. Schwamberger, V. & Schmidt, F. P. Estimating the heat capacity of the adsorbate-adsorbent system from adsorption equilibria regarding thermodynamic consistency. *Industrial and Engineering Chemistry Research* **52,** 16958–16965. ISSN: 08885885. doi:10.1021/ie4011832 (Nov. 2013).

118. Campbell, C. T. & Sellers, J. R. The entropies of adsorbed molecules. *Journal of the American Chemical Society* **134,** 18109–18115. ISSN: 15205126. doi:10.1021/ja3080117 (Oct. 2012).
119. Sghaier, W., Ben Torkia, Y., Bouzid, M. & Ben Lamine, A. Thermodynamic analysis of cooling cycles based on statistical physics modeling of ethanol adsorption isotherms. *International Journal of Refrigeration* **141,** 119–131. ISSN: 01407007. doi:10.1016/j.ijrefrig.2022.05.022 (Sept. 2022).
120. Sakoda, A. & Suzuki, M. Fundamental study on solar powered adsorption cooling system. *JOURNAL OF CHEMICAL ENGINEERING OF JAPAN* **17,** 52–57. ISSN: 00219592. doi:10.1252/jcej.17.52 (Feb. 1984).
121. Alsaman, A. S., Askalany, A. A., Harby, K. & Ahmed, M. S. Performance evaluation of a solar-driven adsorption desalination-cooling system. *Energy* **128,** 196–207. ISSN: 0360-5442. doi:10.1016/J.ENERGY.2017.04.010 (June 2017).
122. Chan, K. C., Tso, C. Y., Wu, C. & Chao, C. Y. Enhancing the performance of a zeolite 13X/CaCl2–water adsorption cooling system by improving adsorber design and operation sequence. *Energy and Buildings* **158,** 1368–1378. ISSN: 03787788. doi:10.1016/j.enbuild.2017.11.040 (Jan. 2018).
123. Xu, J., Pan, Q., Zhang, W., Liu, Z., Wang, R. & Ge, T. Design and experimental study on a hybrid adsorption refrigeration system using desiccant coated heat exchangers for efficient energy utilization. *Renewable and Sustainable Energy Reviews* **169,** 112890. ISSN: 1364-0321. doi:10.1016/J.RSER.2022.112890 (Nov. 2022).
124. Pan, Q. W., Liu, L., Wang, B., Xu, J. & Ge, T. S. Design and experimental study on a small-scale silica gel/water adsorption chiller with heat and mass recovery scheme for solar energy use. *Solar Energy* **252,** 91–100. ISSN: 0038092X. doi:10.1016/j.solener.2023.01.052 (Mar. 2023).
125. Fan, W., Chakraborty, A. & Kayal, S. Adsorption cooling cycles: Insights into carbon dioxide adsorption on activated carbons. *Energy* **102,** 491–501. ISSN: 03605442. doi:10.1016/j.energy.2016.02.112 (2016).
126. Solovyeva, M. V., Gordeeva, L. G., Krieger, T. A. & Aristov, Y. I. MOF-801 as a promising material for adsorption cooling: Equilibrium and dynamics of water adsorption. *Energy Conversion and Management* **174,** 356–363. ISSN: 0196-8904. doi:10.1016/J.ENCONMAN.2018.08.032 (Oct. 2018).
127. Rupam, T. H., Tuli, F. J., Jahan, I., Palash, M. L., Chakraborty, A. & Saha, B. B. Isotherms and kinetics of water sorption onto MOFs for adsorption cooling applications. *Thermal Science and Engineering Progress* **34,** 101436. ISSN: 2451-9049. doi:10.1016/J.TSEP.2022.101436 (Sept. 2022).
128. Loh, W. S., El-Sharkawy, I. I., Ng, K. C. & Saha, B. B. Adsorption cooling cycles for alternative adsorbent/adsorbate pairs working at partial vacuum and pressurized conditions. *Applied Thermal Engineering* **29,** 793–798. ISSN: 13594311. doi:10.1016/j.applthermaleng.2008.04.014 (2009).
129. Miyazaki, T. & El-sharkawy, I. I. *Optimized performance of one-bed adsorption cooling system* in *15th International Refrigeration and Air Conditioning Conference* (2014), 1–7.

130. Chua, H. T., Ng, K. C., Malek, A., Kashiwagi, T., Akisawa, A. & Saha, B. B. Modeling the performance of two-bed, sillica gel-water adsorption chillers. *International Journal of Refrigeration* **22,** 194–204. ISSN: 0140-7007. doi:10.1016/S0140-7007(98)00063-2 (May 1999).
131. Askalany, A. A., Saha, B. B., Ahmed, M. S. & Ismail, I. M. Adsorption cooling system employing granular activated carbon-R134a pair for renewable energy applications. *International Journal of Refrigeration* **36,** 1037–1044. ISSN: 01407007. doi:10.1016/j.ijrefrig.2012.11.009 (2013).
132. Miyazaki, T., Akisawa, A. & Saha, B. B. The performance analysis of a novel dual evaporator type three-bed adsorption chiller. *International Journal of Refrigeration* **33,** 276–285. ISSN: 01407007. doi:10.1016/j.ijrefrig.2009.10.005 (2010).
133. Li, X. H., Hou, X. H., Zhang, X. & Yuan, Z. X. A review on development of adsorption cooling—Novel beds and advanced cycles. *Energy Conversion and Management* **94,** 221–232. ISSN: 0196-8904. doi:10.1016/J.ENCONMAN.2015.01.076 (Apr. 2015).
134. Sidhareddy, M., Tiwari, S., Phelan, P. & Bellos, E. *Comprehensive review on adsorption cooling systems and its regeneration methods using solar, ultrasound, and microwave energy* Feb. 2023. doi:10.1016/j.ijrefrig.2022.10.025.
135. Wu, J. W., Hu, E. J. & Biggs, M. J. Thermodynamic cycles of adsorption desalination system. *Applied Energy* **90,** 316–322. ISSN: 03062619. doi:10.1016/j.apenergy.2011.04.049 (Feb. 2012).
136. Wu, J. W., Biggs, M. J., Pendleton, P., Badalyan, A. & Hu, E. J. Experimental implementation and validation of thermodynamic cycles of adsorption-based desalination. *Applied Energy* **98,** 190–197. ISSN: 03062619. doi:10.1016/j.apenergy.2012.03.022 (Oct. 2012).
137. Ng, K. C., Thu, K., Saha, B. B. & Chakraborty, A. Study on a waste heat-driven adsorption cooling cum desalination cycle. *International Journal of Refrigeration* **35,** 685–693. ISSN: 01407007. doi:10.1016/j.ijrefrig.2011.01.008 (May 2012).
138. Thu, K., Ng, K. C., Saha, B. B., Chakraborty, A. & Koyama, S. Operational strategy of adsorption desalination systems. *International Journal of Heat and Mass Transfer* **52,** 1811–1816. ISSN: 00179310. doi:10.1016/j.ijheatmasstransfer.2008.10.012 (Mar. 2009).
139. Mitra, S., Kumar, P., Srinivasan, K. & Dutta, P. Simulation study of a two-stage adsorber system. *Applied Thermal Engineering* **72,** 283–288. ISSN: 13594311. doi:10.1016/j.applthermaleng.2014.04.023 (Nov. 2014).
140. Mitra, S., Kumar, P., Srinivasan, K. & Dutta, P. Performance evaluation of a two-stage silica gel + water adsorption based cooling-cum-desalination system. *International Journal of Refrigeration* **58,** 186–198. ISSN: 01407007. doi:10.1016/j.ijrefrig.2015.06.018 (Oct. 2015).
141. Mitra, S., Kumar, P., Srinivasan, K. & Dutta, P. Development and performance studies of an air cooled two-stage multi-bed silica-gel + water adsorption system. *International Journal of Refrigeration* **67,** 174–189. ISSN: 01407007. doi:10.1016/j.ijrefrig.2015.10.028 (July 2016).

142. Mitra, S., Thu, K., Saha, B. B., Srinivasan, K. & Dutta, P. Modeling study of two-stage, multi-bed air cooled silica gel + water adsorption cooling cum desalination system. *Applied Thermal Engineering* **114,** 704–712. ISSN: 13594311. doi:10.1016/j.applthermaleng.2016.12.011 (2017).

143. Chen, W. D. & Chua, K. J. Parameter analysis and energy optimization of a four-bed, two-evaporator adsorption system. *Applied Energy* **265,** 114842. ISSN: 03062619. doi:10.1016/j.apenergy.2020.114842 (May 2020).

144. Han, B. & Chakraborty, A. Highly efficient adsorption desalination employing protonated-amino-functionalized MOFs. *Desalination* **541,** 116045. ISSN: 0011-9164. doi:10.1016/J.DESAL.2022.116045 (Nov. 2022).

145. Han, B. & Chakraborty, A. Evaluation on the performances of adsorption desalination employing functionalized metal-organic frameworks (MOFs). *Applied Thermal Engineering* **218,** 119365. ISSN: 1359-4311. doi:10.1016/J.APPLTHERMALENG.2022.119365 (Jan. 2023).

146. Alsaman, A. S., Askalany, A. A., Ibrahim, E. M., Farid, A. M., Ali, E. S. & Ahmed, M. S. Characterization and cost analysis of a modified silica gel-based adsorption desalination application. *Journal of Cleaner Production* **379,** 134614. ISSN: 0959-6526. doi:10.1016/J.JCLEPRO.2022.134614 (Dec. 2022).

147. Riaz, N., Sultan, M., Miyazaki, T., Shahzad, M. W., Farooq, M., Sajjad, U. & Niaz, Y. A review of recent advances in adsorption desalination technologies. *International Communications in Heat and Mass Transfer* **128.** ISSN: 07351933. doi:10.1016/j.icheatmasstransfer.2021.105594 (Nov. 2021).

148. Asfahan, H. M., Sultan, M., Miyazaki, T., Saha, B. B., Askalany, A. A., Shahzad, M. W. & Worek, W. Recent development in adsorption desalination: A state of the art review. *Applied Energy* **328,** 120101. ISSN: 0306-2619. doi:10.1016/J.APENERGY.2022.120101 (Dec. 2022).

149. Thu, K., Yanagi, H., Saha, B. B. & Ng, K. C. Performance investigation on a 4-bed adsorption desalination cycle with internal heat recovery scheme. *Desalination* **402,** 88–96. ISSN: 0011-9164. doi:10.1016/J.DESAL.2016.09.027 (Jan. 2017).

150. Saha, B. B., Chakraborty, A., Koyama, S., Srinivasan, K., Ng, K. C., Kashiwagi, T. & Dutta, P. Thermodynamic formalism of minimum heat source temperature for driving advanced adsorption cooling device. *Applied Physics Letters* **91,** 111902. ISSN: 0003-6951. doi:10.1063/1.2780117 (Sept. 2007).

151. Saha, B. B., El-Sharkawy, I. I., Chakraborty, A., Koyama, S., Banker, N. D., Dutta, P., Prasad, M. & Srinivasan, K. Evaluation of minimum desorption temperatures of thermal compressors in adsorption refrigeration cycles. *International Journal of Refrigeration* **29,** 1175–1181. ISSN: 0140-7007. doi:10.1016/J.IJREFRIG.2006.01.005 (Nov. 2006).

152. Srinivasan, K., Dutta, P., Saha, B. B., Ng, K. C. & Prasad, M. Realistic minimum desorption temperatures and compressor sizing for activated carbon + HFC 134a adsorption coolers. *Applied Thermal Engineering* **51,** 551–559. ISSN: 13594311. doi:10.1016/j.applthermaleng.2012.09.028 (2013).

153. Muttakin, M., Mitra, S., Thu, K., Ito, K. & Saha, B. B. Theoretical framework to evaluate minimum desorption temperature for IUPAC classified adsorption isotherms. *International Journal of Heat and Mass Transfer* **122,** 795–805. ISSN: 00179310. doi:10.1016/j.ijheatmasstransfer.2018.01.107 (2018).

154. Bagheri, M. H. & Schiffres, S. N. Ideal Adsorption Isotherm Behavior for Cooling Applications. *Langmuir* **34,** 1908–1915. ISSN: 15205827. doi:10.1021/ACS.LANGMUIR.7B03989/SUPPL_FILE/LA7B03989_SI_001.PDF (Feb. 2018).

155. Jiang, Y., Bagheri, M. H., Loibl, R. T. & Schiffres, S. N. Thermodynamic limits of adsorption heat pumps: A facile method of comparing adsorption pairs. *Applied Thermal Engineering* **160,** 113906. ISSN: 1359-4311. doi:10.1016/J.APPLTHERMALENG.2019.113906 (Sept. 2019).

156. Hua, W. S., Xu, H. J. & Xie, W. H. Review on adsorption materials and system configurations of the adsorption desalination applications. *Applied Thermal Engineering* **204.** ISSN: 13594311. doi:10.1016/j.applthermaleng.2021.117958 (Mar. 2022).

157. Wang, X., Chua, H. T. & Ng, K. C. Experimental investigation of silica gel–water adsorption chillers with and without a passive heat recovery scheme. *International Journal of Refrigeration* **28,** 756–765. ISSN: 0140-7007. doi:10.1016/J.IJREFRIG.2004.11.011 (5 Aug. 2005).

158. Wang, X. & Chua, H. T. A comparative evaluation of two different heat-recovery schemes as applied to a two-bed adsorption chiller. *International Journal of Heat and Mass Transfer* **50,** 433–443. ISSN: 0017-9310. doi:10.1016/J.IJHEATMASSTRANSFER.2006.08.003 (3-4 Feb. 2007).

159. Thu, K., Saha, B. B., Chakraborty, A., Chun, W. G. & Ng, K. C. Study on an advanced adsorption desalination cycle with evaporator–condenser heat recovery circuit. *International Journal of Heat and Mass Transfer* **54,** 43–51. ISSN: 0017-9310. doi:10.1016/J.IJHEATMASSTRANSFER.2010.09.065 (1-3 Jan. 2011).

160. Thu, K., Yanagi, H., Saha, B. B. & Ng, K. C. Performance analysis of a low-temperature waste heat-driven adsorption desalination prototype. *International Journal of Heat and Mass Transfer* **65,** 662–669. ISSN: 0017-9310. doi:10.1016/J.IJHEATMASSTRANSFER.2013.06.053 (Oct. 2013).

161. Thu, K., Chakraborty, A., Kim, Y. D., Myat, A., Saha, B. B. & Ng, K. C. Numerical simulation and performance investigation of an advanced adsorption desalination cycle. *Desalination* **308,** 209–218. ISSN: 0011-9164. doi:10.1016/J.DESAL.2012.04.021 (Jan. 2013).

162. Thu, K., Kim, Y.-D., Myat, A., Chakraborty, A. & Ng, K. C. Performance investigation of advanced adsorption desalination cycle with condenser-evaporator heat recovery scheme. *Desalination and Water Treatment* **51,** 150–163. ISSN: 19443986. doi:10.1080/19443994.2012.693659 (2013).

163. Wang, R. Z. Performance improvement of adsorption cooling by heat and mass recovery operation. *International Journal of Refrigeration* **24,** 602–611. ISSN: 0140-7007. doi:10.1016/S0140-7007(01)00004-4 (7 July 2001).

164. Akahira, A., Alam, K. C., Hamamoto, Y., Akisawa, A. & Kashiwagi, T. Mass recovery adsorption refrigeration cycle—improving cooling capacity. *International Journal of Refrigeration* **27,** 225–234. ISSN: 0140-7007. doi:10.1016/J.IJREFRIG.2003.10.004 (3 May 2004).

165. Akahira, A., Alam, K. C., Hamamoto, Y., Akisawa, A. & Kashiwagi, T. Mass recovery four-bed adsorption refrigeration cycle with energy cascading. *Applied Thermal Engineering* **25,** 1764–1778. ISSN: 1359-4311. doi:10.1016/J.APPLTHERMALENG.2004.10.006 (11-12 Aug. 2005).

166. Thu, K., Saha, B. B., Mitra, S. & Chua, K. J. *Modeling and Simulation of Mass Recovery Process in Adsorption System for Cooling and Desalination* in *Energy Procedia* **105** (2017), 2004–2009. doi:10.1016/j.egypro.2017.03.574.

167. Muttakin, M., Islam, M. A., Malik, K. S., Pahwa, D. & Saha, B. B. Study on optimized adsorption chiller employing various heat and mass recovery schemes. *International Journal of Refrigeration* **126,** 222–237. ISSN: 0140-7007. doi:10.1016/J.IJREFRIG.2020.12.032 (June 2021).

168. Amirfakhraei, A., Zarei, T. & Khorshidi, J. Advanced heat and mass recovery design in a two bed adsorption desalination system. *Applied Thermal Engineering* **198.** ISSN: 13594311. doi:10.1016/j.applthermaleng.2021.117494 (Nov. 2021).

169. Aristov, Y. I. Adsorptive transformation of ambient heat: A new cycle. *Applied Thermal Engineering* **124,** 521–524. ISSN: 13594311. doi:10.1016/j.applthermaleng.2017.06.051 (2017).

170. Tokarev, M. M., Gordeeva, L. G., Grekova, A. D. & Aristov, Y. I. Adsorption cycle “heat from cold” for upgrading the ambient heat: The testing a lab-scale prototype with the composite sorbent CaClBr/silica. *Applied Energy* **211,** 136–145. ISSN: 03062619. doi:10.1016/j.apenergy.2017.11.015 (Feb. 2018).

171. Aristov, Y. I. A new adsorptive cycle "HeCol" for upgrading the ambient heat: The current state of the art. *International Journal of Refrigeration* **105,** 19–32. ISSN: 0140-7007. doi:10.1016/J.IJREFRIG.2018.12.015 (Sept. 2019).

172. HAMAMOTO, Y. Thermodynamic Analysis of Adsorption Heat Transformer Cycle using Low Heat Capacity Adsorption Reactor and a Proposal of Heat Recovery. *Transactions of the Japan Society of Refrigerating and Air Conditioning Engineers,* 21. ISSN: 1344-4905. doi:10.11322/TJSRAE.21-45DE_OA (2022).

173. Chandra, I. & Patwardhan, V. S. Theoretical studies on adsorption heat transformer using zeolite-water vapour pair. *Heat Recovery Systems and CHP* **10,** 527–537. ISSN: 08904332. doi:10.1016/0890-4332(90)90203-V (5-6 Jan. 1990).

174. Seo, S., Kawakami, H., Miksik, F., Takata, N., Thu, K. & Miyazaki, T. Thermodynamic analysis and impact of thermal masses on adsorption cycles using MaxsorbIII/R245fa and SAC-2/R245fa pairs. *International Journal of Refrigeration* **123,** 52–62. ISSN: 01407007. doi:10.1016/j.ijrefrig.2020.12.005 (2021).

175. Engelpracht, M., Gibelhaus, A., Seiler, J., Graf, S., Nasruddin, N. & Bardow, A. Upgrading Waste Heat from 90 to 110 °C: The Potential of Adsorption Heat Transformation. *Energy Technology* **9,** 2000643. ISSN: 2194-4296. doi:10.1002/ENTE.202000643 (1 Jan. 2021).

176. El-Dessouky, H. T. & Ettouney, H. M. Multiple-effect evaporation desalination systems. thermal analysis. *Desalination* **125,** 259–276. ISSN: 0011-9164. doi:10.1016/S0011-9164(99)00147-2 (Nov. 1999).

177. El-Dessouky, H. T. & Ettouney, H. M. *Fundamentals of Salt Water Desalination* doi:10.1016/B978-0-444-50810-2.X5000-3 (Elsevier, 2002).

178. Saidur, R., Bakthavatchalam, B., Habib, K. & Basrawi, F. *Numerical Analysis of Humidification Dehumidification Desalination System* tech. rep. 1 (2019), 9–17.

179. Andrés-Mañas, J. A., Roca, L., Ruiz-Aguirre, A., Acién, F. G., Gil, J. D. & Zaragoza, G. Application of solar energy to seawater desalination in a pilot system based on vacuum multi-effect membrane distillation. *Applied Energy* **258,** 114068. ISSN: 03062619. doi:10.1016/j.apenergy.2019.114068 (Jan. 2020).

180. Youssef, P. G., Al-Dadah, R. K. & Mahmoud, S. M. *Comparative analysis of desalination technologies* in *Energy Procedia* **61** (Jan. 2014), 2604–2607. doi:10.1016/j.egypro.2014.12.258.

181. Shahzad, M. W., Burhan, M., Ang, L. & Ng, K. C. *Energy-water-environment nexus underpinning future desalination sustainability* 2017. doi:10.1016/j.desal.2017.03.009.

182. Thu, K., Kim, Y.-D., Amy, G., Chun, W. G. & Ng, K. C. A synergetic hybridization of adsorption cycle with the multi-effect distillation (MED). *Applied Thermal Engineering* **62,** 245–255. ISSN: 13594311. doi:10.1016/j.applthermaleng.2013.09.023 (Jan. 2014).

183. Shahzad, M. W., Thu, K., Saha, B. B. & Ng, K. C. An Emerging Hybrid Multi-Effect Adsorption Desalination System. *Evergreen* **1,** 30–36. doi:10.5109/1495161 (2014).

184. Kim, Y.-D., Thu, K., Ng, K. C., Amy, G. L. & Ghaffour, N. A novel integrated thermal-/membrane-based solar energy-driven hybrid desalination system: Concept description and simulation results. *Water Research* **100,** 7–19. ISSN: 18792448. doi:10.1016/j.watres.2016.05.002 (Sept. 2016).

185. Askalany, A. A. Innovative mechanical vapor compression adsorption desalination (MVC-AD) system. *Applied Thermal Engineering* **106,** 286–292. ISSN: 1359-4311. doi:10.1016/J.APPLTHERMALENG.2016.05.144 (Aug. 2016).

186. Askalany, A. A. & Ali, E. S. A new approach integration of ejector within adsorption desalination cycle reaching COP higher than one. *Sustainable Energy Technologies and Assessments* **41,** 100766. ISSN: 2213-1388. doi:10.1016/J.SETA.2020.100766 (Oct. 2020).

187. Ali, E. S., Mohammed, R. H., Qasem, N. A., Zubair, S. M. & Askalany, A. Solar-powered ejector-based adsorption desalination system integrated with a humidification-dehumidification system. *Energy Conversion and Management* **238.** ISSN: 01968904. doi:10.1016/j.enconman.2021.114113 (June 2021).

188. Ahmed, F. E., Hashaikeh, R. & Hilal, N. Hybrid technologies: The future of energy efficient desalination – A review. *Desalination* **495,** 114659. ISSN: 00119164. doi:10.1016/j.desal.2020.114659 (2020).

189. Goh, P. S., Kang, H. S., Ismail, A. F. & Hilal, N. The hybridization of thermally-driven desalination processes: The state-of-the-art and opportunities. *Desalination* **506,** 115002. ISSN: 0011-9164. doi:10.1016/J.DESAL.2021.115002 (June 2021).

190. Khawaji, A. D., Kutubkhanah, I. K. & Wie, J. M. Advances in seawater desalination technologies. *Desalination* **221,** 47–69. ISSN: 00119164. doi:10.1016/j.desal.2007.01.067 (Mar. 2008).

191. Kamali, R. K., Abbassi, A. & Sadough Vanini, S. A. A simulation model and parametric study of MED-TVC process. *Desalination* **235,** 340–351. ISSN: 00119164. doi:10.1016/j.desal.2008.01.019 (Jan. 2009).

192. Alarcón-Padilla, D. C. & García-Rodríguez, L. Application of absorption heat pumps to multi-effect distillation: a case study of solar desalination. *Desalination* **212,** 294–302. ISSN: 00119164. doi:10.1016/j.desal.2006.10.014 (June 2007).

193. Srinivas, G., Sekar, S., Saravanan, R. & Renganarayanan, S. Studies on a water-based absorption heat transformer for desalination using MED. *Desalination and Water Treatment* **1,** 75–81. ISSN: 19443986. doi:10.5004/dwt.2009.110 (2009).

194. Ameri, M., Mohammadi, S. S., Hosseini, M. & Seifi, M. Effect of design parameters on multi-effect desalinationsystem specifications. *Desalination* **245,** 266–283. ISSN: 00119164. doi:10.1016/j.desal.2008.07.012 (Sept. 2009).

195. Thu, K., Kim, Y.-D., Amy, G., Chun, W. G. & Ng, K. C. A hybrid multi-effect distillation and adsorption cycle. *Applied Energy* **104,** 810–821. ISSN: 03062619. doi:10.1016/j.apenergy.2012.12.007 (2013).

196. Shahzad, M. W., Thu, K., Kim, Y.-D. & Ng, K. C. An experimental investigation on MEDAD hybrid desalination cycle. *Applied Energy* **148,** 273–281. ISSN: 03062619. doi:10.1016/j.apenergy.2015.03.062 (June 2015).

197. Ng, K. C., Thu, K., Oh, S. J., Ang, L., Shahzad, M. W. & Ismail, A. B. *Recent developments in thermally-driven seawater desalination: Energy efficiency improvement by hybridization of the MED and AD cycles* Jan. 2015. doi:10.1016/j.desal.2014.10.025.

198. Thu, K., Kim, Y. D., Shahzad, M. W., Saththasivam, J. & Ng, K. C. Performance investigation of an advanced multi-effect adsorption desalination (MEAD) cycle. *Applied Energy* **159,** 469–477. ISSN: 03062619. doi:10.1016/j.apenergy.2015.09.035 (Dec. 2015).

199. Atkins, P., De Paula, J. & Keeler, J. *Atkins' Physical Chemistry: Thermodynamics and Kinetics* ISBN: 9780198817895 (Oxford University Press, 2018).

200. Van Koningsveld, H., Van Bekkum, H. & Jansen, J. C. On the location and disorder of the tetrapropylammonium (TPA) ion in zeolite ZSM-5 with improved framework accuracy. *Acta Crystallographica Section B* **43,** 127–132. ISSN: 1600-5740. doi:10.1107/S0108768187098173 (Apr. 1987).

201. Eddaoudi, M., Kim, J., Rosi, N., Vodak, D., Wachter, J., O'Keeffe, M. & Yaghi, O. M. Systematic design of pore size and functionality in isoreticular MOFs and their application in methane storage. *Science* **295,** 469–472. ISSN: 00368075. doi:10.1126/SCIENCE.1067208/SUPPL_FILE/SUPPT1.EDDAOUDI.PDF (Jan. 2002).

202. Chui, S. S., Lo, S. M., Charmant, J. P., Orpen, A. G. & Williams, I. D. A chemically functionalizable nanoporous material [Cu3(TMA)2 (H2O)3](n). *Science* **283,** 1148–1150. ISSN: 00368075. doi:10.1126/SCIENCE.283.5405.1148/SUPPL_FILE/986116S4_THUMB.GIF (Feb. 1999).

203. Dubbeldam, D., Calero, S. & Vlugt, T. J. iRASPA: GPU-accelerated visualization software for materials scientists. *Molecular Simulation* **44,** 653–676. ISSN: 10290435. doi:10.1080/08927022.2018.1426855 (May 2018).

204. Mayo, S. L., Olafson, B. D. & Goddard, W. A. DREIDING: A generic force field for molecular simulations. *Journal of Physical Chemistry* **94,** 8897–8909. ISSN: 00223654. doi:10.1021/j100389a010 (1990).

205. Rappé, A. K., Casewit, C. J., Colwell, K. S., Goddard, W. A. & Skiff, W. M. UFF, a Full Periodic Table Force Field for Molecular Mechanics and Molecular Dynamics Simulations. *Journal of the American Chemical Society* **114,** 10024–10035. ISSN: 15205126. doi:10.1021/JA00051A040 (Dec. 1992).

206. Pham, T., Forrest, K. A., Tudor, B., Elsaidi, S. K., Mohamed, M. H., McLaughlin, K., Cioce, C. R., Zaworotko, M. J. & Space, B. Theoretical investigations of CO2 and CH4 sorption in an interpenetrated diamondoid metal-organic material. *Langmuir* **30,** 6454–6462. ISSN: 15205827. doi:10.1021/LA500967W/SUPPL_FILE/LA500967W_SI_002.ZIP (June 2014).

207. Martín-Calvo, A., García-Pérez, E., García-Sánchez, A., Bueno-Pérez, R., Hamad, S. & Calero, S. *Effect of air humidity on the removal of carbon tetrachloride from air using Cu-BTC metal-organic framework* in *Physical Chemistry Chemical Physics* **13** (The Royal Society of Chemistry, May 2011), 11165–11174. doi:10.1039/c1cp20168a.

208. Martin, M. G. & Siepmann, J. I. Transferable potentials for phase equilibria. 1. United-atom description of n-alkanes. *Journal of Physical Chemistry B* **102,** 2569–2577. ISSN: 15206106. doi:10.1021/jp972543+ (1998).

209. Potoff, J. J. & Siepmann, J. I. Vapor-liquid equilibria of mixtures containing alkanes, carbon dioxide, and nitrogen. *AIChE Journal* **47,** 1676–1682. ISSN: 00011541. doi:10.1002/aic.690470719 (July 2001).

210. Dubbeldam, D., Calero, S., Ellis, D. E. & Snurr, R. Q. RASPA: Molecular simulation software for adsorption and diffusion in flexible nanoporous materials. *Molecular Simulation* **42,** 81–101. ISSN: 10290435. doi:10.1080/08927022.2015.1010082 (2016).

211. García-Pérez, E., Parra, J. B., Ania, C. O., Dubbeldam, D., Vlugt, T. J., Castillo, J. M., Merkling, P. J. & Calero, S. Unraveling the argon adsorption processes in MFI-type zeolite. *Journal of Physical Chemistry C* **112,** 9976–9979. ISSN: 19327447. doi:10.1021/jp803753h (July 2008).

212. Babarao, R., Hu, Z., Jiang, J., Chempath, S. & Sandler, S. I. Storage and separation of CO2 and CH4 in silicalite, C168 schwarzite, and IRMOF-1: A comparative study from Monte Carlo simulation. *Langmuir* **23,** 659–666. ISSN: 07437463. doi:10.1021/la062289p (Jan. 2007).

213. Polat, H. M., Zeeshan, M., Uzun, A. & Keskin, S. Unlocking CO2 separation performance of ionic liquid/CuBTC composites: Combining experiments with molecular simulations. *Chemical Engineering Journal* **373,** 1179–1189. ISSN: 13858947. doi:10.1016/j.cej.2019.05.113 (Oct. 2019).

214. Vlugt, T. J., García-Pérez, E., Dubbeldam, D., Ban, S. & Calero, S. Computing the Heat of Adsorption using Molecular Simulations: The Effect of Strong Coulombic Interactions. *Journal of Chemical Theory and Computation* **4,** 1107–1118. ISSN: 15499618. doi:10.1021/CT700342K (July 2008).

215. Cruz, A. J., Pires, J., Carvalho, A. P. & De Carvalho, M. B. Physical adsorption of H2S related to the conservation of works of art: The role of the pore structure at low relative pressure. *Adsorption* **11,** 569–576. ISSN: 09295607. doi:10.1007/S10450-005-5614-3/METRICS (Nov. 2005).

216. Mooney, D. A., Müller-Plathe, F. & Kremer, K. Simulation studies for liquid phenol: properties evaluated and tested over a range of temperatures. *Chemical Physics Letters* **294,** 135–142. ISSN: 0009-2614. doi:10.1016/S0009-2614(98)00860-4 (Sept. 1998).

217. Islam, M. A., Pal, A. & Saha, B. B. Experimental study on thermophysical and porous properties of silica gels. *International Journal of Refrigeration* **110,** 277–285. ISSN: 01407007. doi:10.1016/j.ijrefrig.2019.10.027 (Feb. 2020).

218. Jin, S. X., Yu, Q. F., Li, M., Sun, S. N., Zhao, H., Huang, Y. W. & Fan, J. Quantitative evaluation of carbon materials for humidity buffering in a novel dehumidification shutter system powered by solar energy. *Building and Environment* **194,** 107714. ISSN: 0360-1323. doi:10.1016/J.BUILDENV.2021.107714 (May 2021).

219. Saren, S., Mitra, S., Miksik, F., Miyazaki, T., Ng, K. C. & Thu, K. Impacts of the internal heat recovery scheme on the performance of an adsorption heat transformer cycle for temperature upgrade. *International Communications in Heat and Mass Transfer* **144,** 106774. ISSN: 0735-1933. doi:10.1016/J.ICHEATMASSTRANSFER.2023.106774 (May 2023).

220. Mistry, K. H., Antar, M. A. & Lienhard V, J. H. An improved model for multiple effect distillation. *Desalination and Water Treatment* **51,** 807–821. doi:10.1080/19443994.2012.703383 (2013).

221. Ozawa, S., Kusumi, S. & Ogino, Y. Physical adsorption of gases at high pressure. IV. An improvement of the Dubinin—Astakhov adsorption equation. *Journal of Colloid and Interface Science* **56,** 83–91. ISSN: 0021-9797. doi:10.1016/0021-9797(76)90149-1 (1 July 1976).

222. Dubinin, M. M. i. Physical adsorption of gases and vapors in micropores. *Progress in surface and membrane science* **9,** 1–70 (1975).

223. Woo, S.-Y., Lee, H.-S., Ji, H. & Kim, Y.-D. Adsorption Isotherm Model for Analyzing the Adsorption Characteristics of Water Vapor to Commercially Available Silica Gel Adsorbents for Adsorption Desalination Applications. *Cite This: J. Chem. Eng. Data* **66,** 1144–1156. doi:10.1021/acs.jced.0c00927 (2021).

224. Mohammed, R. H., Mesalhy, O., Elsayed, M. L., Su, M. & Chow, L. C. Revisiting the adsorption equilibrium equations of silica-gel/water for adsorption cooling applications. *International Journal of Refrigeration* **86,** 40–47. ISSN: 0140-7007. doi:10.1016/J.IJREFRIG.2017.10.038 (Feb. 2018).

225. Saha, B. B., Jribi, S., Koyama, S. & El-Sharkawy, I. I. Carbon Dioxide Adsorption Isotherms on Activated Carbons. *Journal of Chemical and Engineering Data* **56,** 1974–1981. ISSN: 0021-9568. doi:10.1021/je100973t (5 2011).

226. Uddin, K., Pal, A. & Saha, B. B. Improved CO2 adsorption onto chemically activated spherical phenol resin. *Journal of CO2 Utilization* **41,** 101255. ISSN: 2212-9820. doi:10.1016/J.JCOU.2020.101255 (Oct. 2020).

227. Wei Benjamin Teo, H., Chakraborty, A. & Fan, W. Improved adsorption characteristics data for AQSOA types zeolites and water systems under static and dynamic conditions. *Microporous and Mesoporous Materials* **242,** 109–117. ISSN: 13871811. doi:10.1016/j.micromeso.2017.01.015 (Apr. 2017).